



ALADIN-HIRLAM Newsletter

No. 14, January 29th, 2020

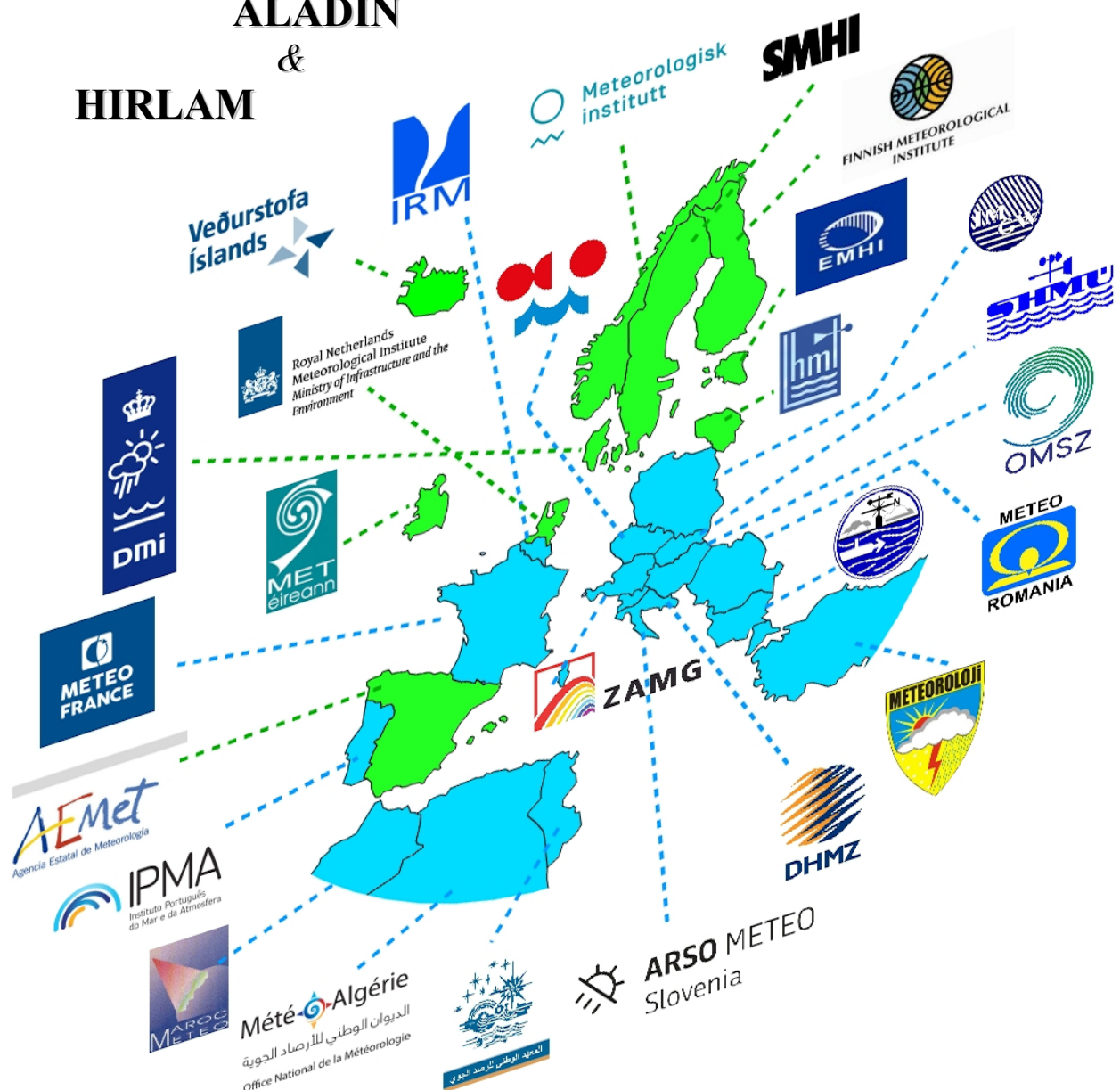
2019 Grand Tour

of

ALADIN

&

HIRLAM



ALADIN Programme, c/o P. Termonia, IRM, Avenue Circulaire 3, 1180 Bruxelles, Belgium

HIRLAM-C Programme, c/o J. Onvlee, KNMI, P.O. Box 201, 3730 AE De Bilt, The Netherlands

CONTENT

Introduction	4
Editorial : Achievements and successes in 2019	5
Events announced for 2020 (and later on)	6
Grand Tour of ALADIN and HIRLAM	8
<ul style="list-style-type: none"> • Algeria : Running ALADIN Dust configuration over Northern Africa, Middle East and Europe • Austria : C-LAEF and AROME-RUC – New operational systems in Austria • Belgium : Data assimilation and Seamless short-term ensemble prediction at RMIB • Croatia : Highlights of the NWP activities at the Croatian Meteorological and Hydrological Service • Czech Rep : ALARO-1 Non Hydrostatic Operational Application at 2.3 km. • Denmark : NWP progress report 2019 from DMI • Finland : Selected NWP-related research at FMI • France : Surface precipitation type forecasts in AROME-France • Hungary : On the way towards the AROME nowcasting system in Hungary • Ireland : Met Éireann Updates • Morocco : Some numerical weather prediction activities in Moroccan Meteorological Service in 2019 • Netherlands : Wind turbine parameterisation in HARMONIE-AROME • Netherlands: Use of wind information from Harmonie-Arome in high-resolution applications: crosswind and fuel consumption on motorways • Poland : Aladin in Poland – 2019 • Portugal : 2019 ALADIN Highlights for IPMA, I.P. • Romania : ALADIN activities in Romania • Slovakia : ALADIN related activities @SHMU (2019) • Slovenia : ALADIN highlights in Slovenia in 2019 • Spain : A major update in AEMET operational suite including radar reflectivity, ASCAT data, humidity in the large scale blending and assimilation of screen level variables in 3DVar • Sweden : SMHI ALADIN/HIRLAM 2019 Main Activities • Turkey : Implementation of CANARI in AROME TURKEY 	 8 12 17 22 32 39 44 58 65 70 79 82 98 102 108 113 115 124 128 138 151
Patrick Samuelsson et al : HIRLAM experience with ECOCLIMAP Second Generation	154
Ulf Andrae et al : A continuous EDA based ensemble in MetCoOp	189
ALADIN-HIRLAM Newsletters : previous issues	200

Introduction

Welcome to the combined 14th edition Newsletter of the HIRLAM and ALADIN consortia.

This first 2020 edition is a **big Tour d'ALADIN & HIRLAM** as it was presented to our Directors at their last meetings in Istanbul on 16-17 December 2019: [the 5th joint ALADIN GA & HIRLAM-C Council](#), [the 24th ALADIN GA](#) and the 8th HIRLAM-C Council. Highlights are listed in the [Edito](#).



The delegations at the joint ALADIN GA & HIRLAM C, Istanbul, 17 Dec. 2019

We hereby thank all those that contributed to this Newsletter with their articles.

Last but not least, a [summary list of upcoming events, planned for the near future](#) is available.

Enjoy reading the fourteenth ALADIN-HIRLAM Newsletter. For additional article information please contact the article author(s) directly.

Patricia and Frank

Further consortia information needed? Check the [ALADIN](#) and [HIRLAM](#) websites or contact us.

Edito : Achievements and successes in 2019

Patricia Pottier

At [the joint meeting of the ALADIN and HIRLAM Directors](#), on behalf of ALADIN, LACE and HIRLAM, Piet reported on the realisation of the 2019 Rolling Work Plan and illustrated it with concrete examples of important achievements in 2019:

- The long standing developments on Vertical Finite Elements were ported to the IFS and allowed to reduce temperature Biases in the tropopause.
- A grid-point solver has been developed as an alternative to the spectral one. The scalability was tested and it was proved that it performs better than the spectral one. Tests were performed in the full AROME setup, albeit on a single core. The tests confirmed that the performance is comparable to the one of the spectral approach.
- An overview was given of the status of the operational implementations of the data assimilation systems in the LACE countries. Good progress was reported on the DasKIT program. The ALH community as a whole is increasingly investigating non-standard (crow-sourced) observations.
- Some major works were carried out in the tuning of the ALARO physics (as part of the increase of the resolution in CHMI).
- During the last year increasingly more attention has been payed to postprocessing and diagnostics. This includes to use of big data and machine-learning techniques in Morocco.
- New versions of the LAEF system have been presented, leading to an improved forecast of a flash flood in Turkey.
- A growing amount of attention is being paid within the ALH community to work on issues of code efficiency and portability to new types of hardware (scalability, code optimization, single precision, dependence on architecture ...).

The chairs of the joint Assembly, Marianne Thyrring and Martin Benko thanked Piet for this report, congratulated all Members for these developments that contribute to the ALADIN-LACE-HIRLAM common success and asked them to pass on their congratulations to all their scientists.

This Newsletter is aimed at presenting more in details the major achievements of the 26 ALADIN-HIRLAM Partners over 2019.

Events announced for 2020 (and further near future)

The Newsletters presents a static overview (twice a year) with upcoming meetings for the (near) future time frame. For actual updates (year round) please check the [ALADIN](#) / [HIRLAM](#) websites and the [LACE](#) website.

1 ALADIN/HIRLAM related meetings

- [ALADIN-HIRLAM strategy meeting](#), Toulouse, 3-4 February 2020
- [Jean-François Geleyn tribute day](#), Toulouse, 6 February, 2020 : [registration](#) for participants in Toulouse or remotely (a web-conference will be opened)
- [30th ALADIN Wk & HIRLAM ASM 2020](#), Ljubljana, 30 March – 2 April 2020 : [registration open till 15 February](#) !...
- [28th ALADIN LTM meeting](#), March 30 or 31 2020, Ljubljana
- [HMG-CSSI meeting](#), April 2-3, 2020, Ljubljana
- [10th Joint PAC-HAC meeting](#), Oslo, 14-15 May 2020
- [25th ALADIN GA, HIRLAM Council, LACE Council, 6th Joint ALADIN GA and HIRLAM Council](#), Madrid, 25-26 June 2020
- [EWGLAM/SRNWP meeting](#), Brussels, 28 September - 1st October 2020
- [29th ALADIN LTM meeting](#), Brussels, 28 or 29 September 2020
- [11th Joint PAC-HAC meeting](#), Madeira, 20-21 October 2020 (date to be confirmed)
- [26th ALADIN GA, HIRLAM Council, LACE Council, 7th Joint ALADIN GA and HIRLAM Council](#), France (Paris or Toulouse, t.b.d.), 26-27 November 2020

*A tribute to
Jean-François Geleyn*

6 February 2020

Météo-France Conference Centre
Toulouse, France



Joint 30th ALADIN Workshop & HIRLAM ASM 2020

Ljubljana

host: ARSO Meteo Slovenia

Monday 30 March - Thursday 2 April 2020

followed by the

HMG-CSSI meeting on Thursday 2 – Friday 3 April

Please [register](#)

30th ALADIN Wk & HIRLAM ASM
Ljubljana, 30 March - 3 April 2020

Email

Name

First

Last

National Met Service/Country

I propose a presentation, preferably in session:

Title of the presentation :

If possible, I propose a 2nd presentation, preferably in session:

Title of the 2nd presentation :

I propose a poster : please give the Title (or the Titles in case of more than one poster)

ARSO METEO
Slovenian Environment Agency

2 ALADIN/HIRLAM Working Weeks / Days

Following information is available as per end of January 2020:

- 2020 Joint LACE Data Assimilation & [DAsKIT Working Days](#), date tbd, Vienna
- Spring DA working week, 27 April – 1 May, Copenhagen, Denmark.
- EPS working week, 11-15 May 2020, Innsbruck, Austria.
- Surface Working Week, 8-12 June 2020, Madrid, Spain.

3 Regular group video meetings

Regular group video meetings (google hangouts) take place on several topics (from both ALADIN and HIRLAM site). Outcomes are noted as very valuable. If you like more details how to organize please contact Roger Randriamiampianina, Daniel Santos Munoz or Patrick Samuelsson. Reports of these meetings are available on the [HIRLAM wiki](#) pages (registration needed).

Maria Monteiro (ALADIN DA coordinator) has established regular [specific regular video-conferences with DAsKIT countries](#) (ALADIN DA starter countries).

4 About the past joint ALADIN – HIRLAM events

During the second semester of 2019, the PM's presented the consortia at the EWGLAM/SRNWP meeting (30 September – 4 October, Sofia). Furthermore, the 9th joint HAC/PAC met on 5 November in Toulouse and the 5th joint ALADIN GA and HIRLAM Council took place on December 17 in Istanbul.

The minutes of these meetings, after validation, are available on line at the ALADIN website and can be downloaded:

- [joint ALADIN Workshops & HIRLAM All Staff Meetings](#),
- [minutes of the HMG/CSSI meetings](#),
- [minutes of HAC/PAC meetings](#),
- [minutes and presentations : joint ALADIN General Assemblies and HIRLAM Councils](#)

Running ALADIN Dust configuration over Northern Africa, Middle East and Europe.

Abdenour AMBAR and Mohamed MOKHTARI

Introduction

The prediction of atmospheric cycle of desert dust aerosols at the Algerian national office of Meteorology (ONM) is based on ALADIN Dust configuration (M.Mokhtari et al, 2012). It is running operationally, twice a day (00h and 12h) and provide aerosols optical depth and concentrations of mineral aerosols over Algerian domain.

This short paper will describe briefly a new ALADIN Dust configuration over a large domain which covers Northern Africa, Middle East and Europe. This configuration, was prepared in order to participate to the WMO SDS-WAS dust forecasts ensemble. A short overview about the WMO SDS-WAS will be presented in this paper.

About the WMO SDS-WAS

The *SDS-WAS* (Sand and Dust Storm Warning Advisory System) has been established by the WMO in order to develop, refine and provide a basis for distributing to the global community products that are useful in reducing the adverse impacts of sands and dust storms (SDS) and to assess impacts of the SDS process on society and nature (S.Nikovic et al., 2014). The SDS-WAS mission is to enhance the ability of countries to deliver timely and quality sand and dust storm forecasts, observations, information and knowledge to users through an international partnership of research and operational communities.

The SDS-WAS operates as an international hub of researchers, operational centres and end-users and is organised through regional nodes. Three nodes are currently in operation:

- Regional Node for Asia, coordinated by a Regional Center in Beijing, China, hosted by the China Meteorological Administration.
- Regional Node for Northern Africa, Middle East and Europe (NAMEE), coordinated by a Regional Center in Barcelona, Spain, hosted by the State Meteorological Agency of Spain (AEMET) and the Barcelona Supercomputing Center (BSC).
- Regional Node for Pan-America, coordinated by a Regional Center in Bridgetown, Barbados, hosted by the Caribbean Institute for Meteorology and Hydrology.

The Regional Center for Northern Africa, Middle East and Europe of the WMO SDS-WAS (<http://sds-was.aemet.es>), hosted by Spain, is managed by a consortium of AEMET and BSC. It was established in April 2010 to coordinate the SDS-WAS activities within this region. The Regional Centre soon evolved into a structure that hosted international and interdisciplinary research cooperation between numerous organisations in the region and beyond, including national meteorological services, environmental agencies, research groups and international organisations (S.Bassart et al., 2019).

ALADIN Dust configuration over NAMEE domain

A new ALADIN Dust configuration has been prepared over a larger domain covering Northern Africa, Middle East and Europe to provide daily dust forecasts to the SDS-WAS ensemble system. This configuration is based on cycle CY43T2bf.09, with 25km of horizontal resolution and 70 vertical level. For the LBC and initial conditions, coupling files are used from ARPEGE.

Tab.01: ALADIN Dust configuration for NAMEE domain

Model	ALADIN	
Cycle	CY43T2bf.09	
Horizontal resolution	25km	
Vertical levels	70 levels	
Grid	262 x 342	
Area	Latitude	0° - 65° N
	Longitude	25° W - 60° E
Boundaries	ARPEGE	
Forecasts	72 hours at 00UTC	
Time steps	420 s	

Currently, this new configuration is running pre-operationally, it is planned to switch to operational (once a day at 00h) in order to participate in the WMO SDS-WAS ensemble dust forecasts and then becoming available daily on the SDS-WAS website.

Hereafter, some examples of surface dust concentrations and aerosols optical depth (AOD) outputs. A fully verification study should be conducted with significant scores to better understand the behaviour of this configuration compared to the observations (mainly with Aeronet data) and to the other participating models in the SDS-WAS ensemble dust forecasts.

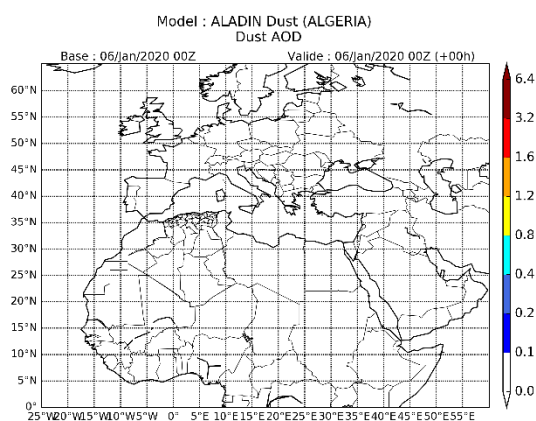


Fig.01: Dust AOD initial file for ALADIN Dust (06/01/2020 at 00UTC).

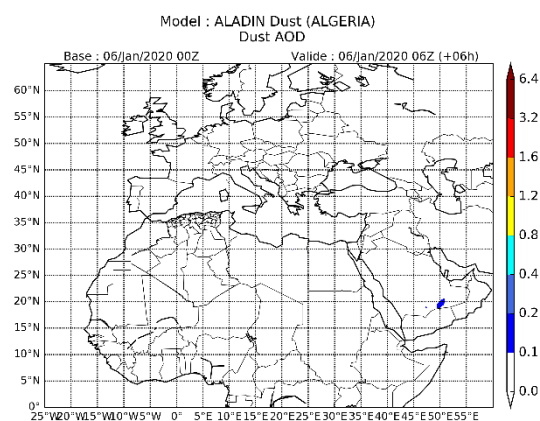


Fig.02: Dust AOD simulated by ALADIN Dust (06/01/2020 at 06UTC).

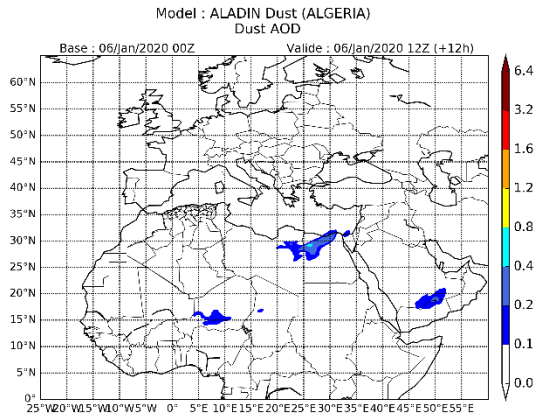


Fig.02: Dust AOD simulated by ALADIN Dust (06/01/2020 at 12UTC).

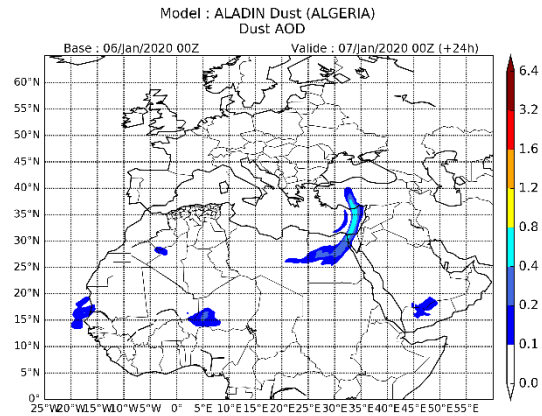


Fig.04: Dust AOD simulated by ALADIN Dust (07/01/2020 at 00UTC).

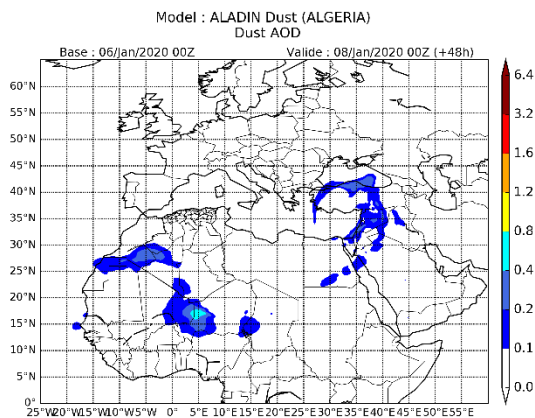


Fig.05: Dust AOD simulated by ALADIN Dust (08/01/2020 at 00UTC).

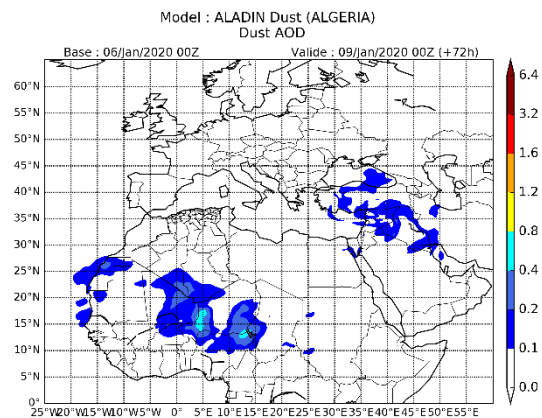


Fig.06: Dust AOD simulated by ALADIN Dust (09/01/2020 at 00UTC).

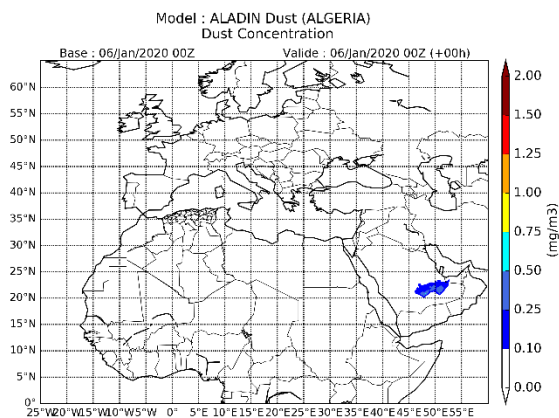


Fig.07: Dust surface concentration initial file for ALADIN Dust (06/01/2020 at 00UTC).

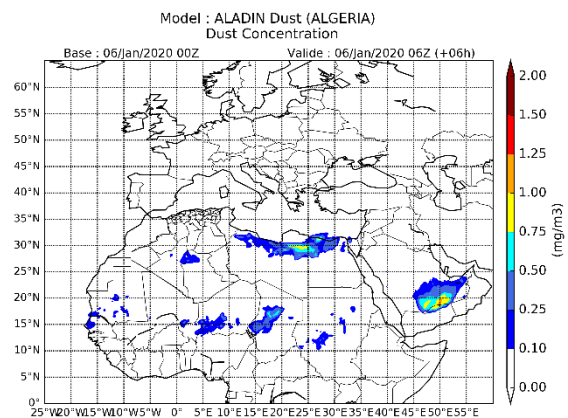


Fig.08: Dust surface concentration simulated by ALADIN Dust (06/01/2020 at 06UTC).

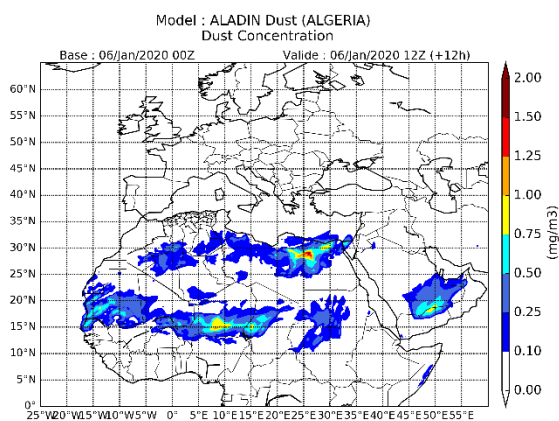


Fig.09: Dust surface concentration simulated by ALADIN Dust (06/01/2020 at 12UTC).

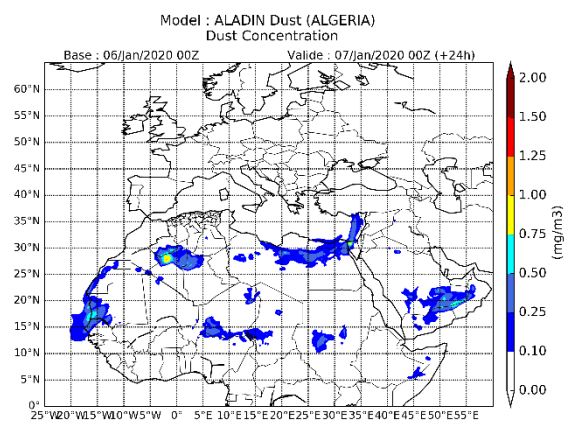


Fig.10: Dust surface concentration simulated by ALADIN Dust (07/01/2020 at 00UTC).

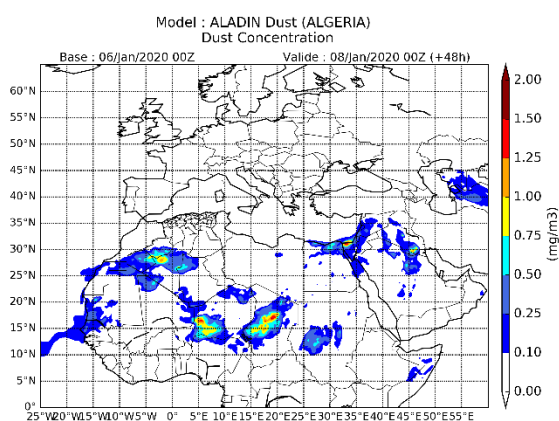


Fig.11: Dust surface concentration simulated by ALADIN Dust (08/01/2020 at 00UTC).

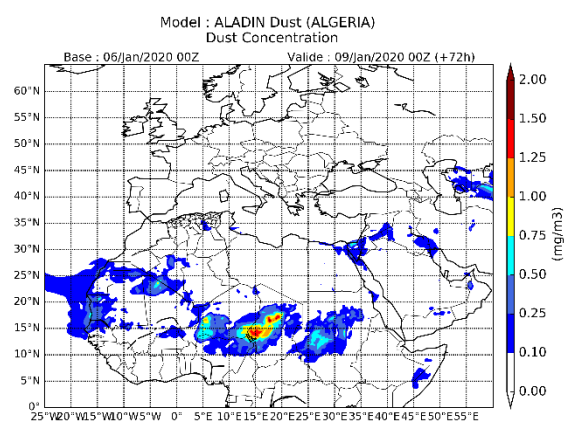


Fig.12: Dust surface concentration simulated by ALADIN Dust (09/01/2020 at 00UTC).

References

M. Mokhtari, L. Gomes, P. Tulet, and T. Rezoug (2012): Importance of the surface size distribution of erodible material: an improvement on the Dust Entrainment And Deposition (DEAD) Model, *Geosci. Model Dev.*, 5, 581–598, 2012, doi:10.5194/gmd-5-581-2012.

Slobodan Nickovic, Emilio Cuevas, Jose Baldasano, Enric Terradellas, Tetsuo Nakazawa, Alexander Baklanov (2014): SDS-WAS Science and Implementation Plan: 2011-2015, World Meteorological Organization, Geneva (2014).

Sara Basart, Slobodan Nickovic, Enric Terradellas, Emilio Cuevas, Carlos Pérez García-Pando, Gerardo García-Castrillo, Ernest Werner and Francesco Benincasa (2019): The WMO SDS-WAS Regional Center for Northern Africa, Middle East and Europe. E3S Web of Conferences; Les Ulis Vol. 99, Les Ulis: EDP Sciences. (2019) DOI:10.1051/e3sconf/20199904008.

C-LAEF and AROME-RUC – New operational systems in Austria

Christoph Wittmann, Clemens Wastl, Florian Meier

1 Introduction

The year 2019 brought major operational changes at ZAMG in Austria. During the last years a lot of effort was invested to complete the AROME based forecast chain. In addition to the existing deterministic 2.5km/90L system AROME-Aut, two new applications have been developed and finally put to operations in late 2019: The ensemble system C-LAEF and the nowcasting system AROME-RUC. The following sections briefly describe the main characteristics of the new systems.

2 C-LAEF (Convection permitting Limited Area Ensemble Forecasting)

In the past years the convection permitting ensemble forecasting C-LAEF which is based on the AROME model has been developed at ZAMG. In autumn 2019 this system has become operational. C-LAEF is running 4 times a day on the ECMWF HPC with lead times between 6h (06 and 18 UTC), 48h (12 UTC) and 60h (00UTC). The ensemble comprises 16 members (+ 1 unperturbed control) using the first 16 out of a total of 51 members of ECMWF-ENS for the boundary conditions with a coupling frequency of 3 hours. The horizontal resolution is 2.5km and 90 vertical levels are used (more details can be found in Table 1).

Uncertainties in the initial conditions are represented by a combination of EDA (ensemble data assimilation), sEDA (surface ensemble data assimilation) and Ensemble-Jk. In Ensemble-Jk small-scale perturbations coming from 3D-Var EDA and large-scale perturbations coming from the driving model are blended. Model error is represented by a combination of tendency perturbation approach (for radiation, shallow convection and microphysics) and parameter perturbations in the turbulence scheme.

Domain		Model characteristics		LBC	
Grid points:	600x432	Code version:	CY40T1	Coupl. model:	IFS Ensemble
Horizon. resolution:	2.5km	Time step:	60s	Coupl. frequency:	3h
Levels:	90	Integration time:	60h (00 UTC), 48h (12 UTC), 6h (06, 18 UTC)	Retrieval:	Internet/ RMDCN
Grid:	linear	Physics:	AROME/Meso-NH incl. stophy	Archive:	local + MARS (08/2019)
Orography:	mean	Dynamics:	non-hydrostatic		
		Initialization:	CANARI/OIMAIN, 3DVAR EDA + surface EDA + Ensemble JK		

Table 1: C-LAEF Main characteristics.

To increase the application of the C-LAEF ensemble system at the forecasting offices, several probabilistic products and maps have been developed in a close cooperation between model developers and forecasters. Figure 1 shows a C-LAEF 6-panel tailored to warning applications in summertime convective situations. The upper left panel shows the probability of lightning for different thresholds (low - yellow, medium - orange, high - red), the upper center panel the diagnostic probability of hail and the upper right panel the predicted maximum 3h gusts. In the lower row the C-LAEF median of 3h accumulated precipitation (left), 3h sunshine duration (center) and cloudiness (right) are shown.

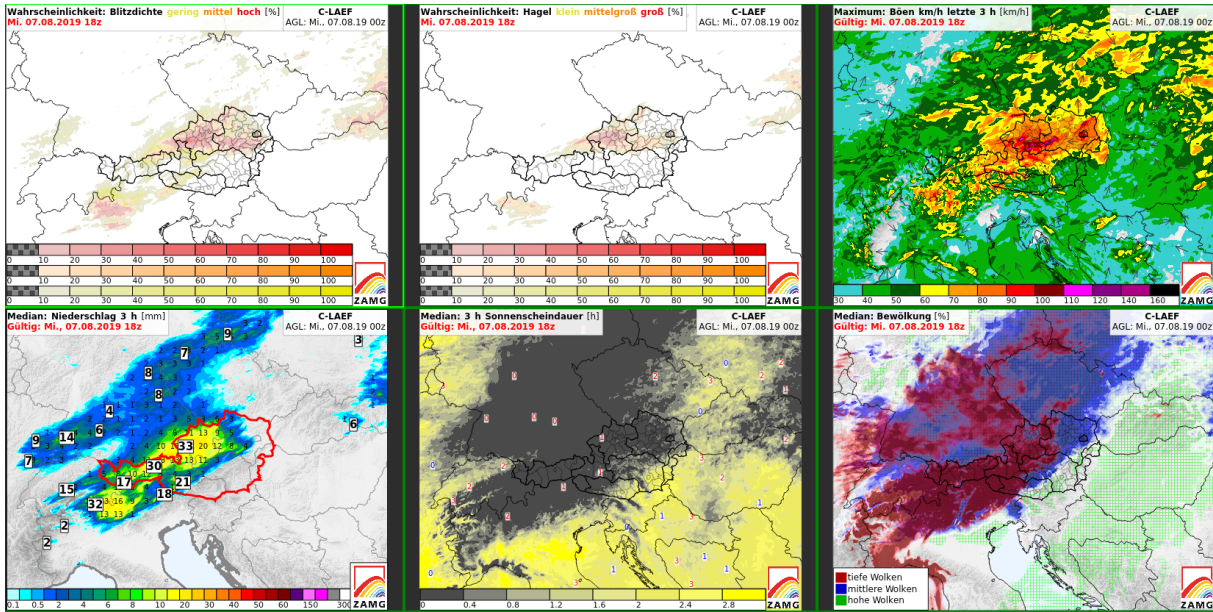


Fig. 1: C-LAEF panel used by the operational forecasters at ZAMG for a thunderstorm warning situation at August 8th, 2019.

Continuous verification of C-LAEF versus the ECMWF-ENS has clearly shown the benefit of a convection permitting EPS (Fig. 2).

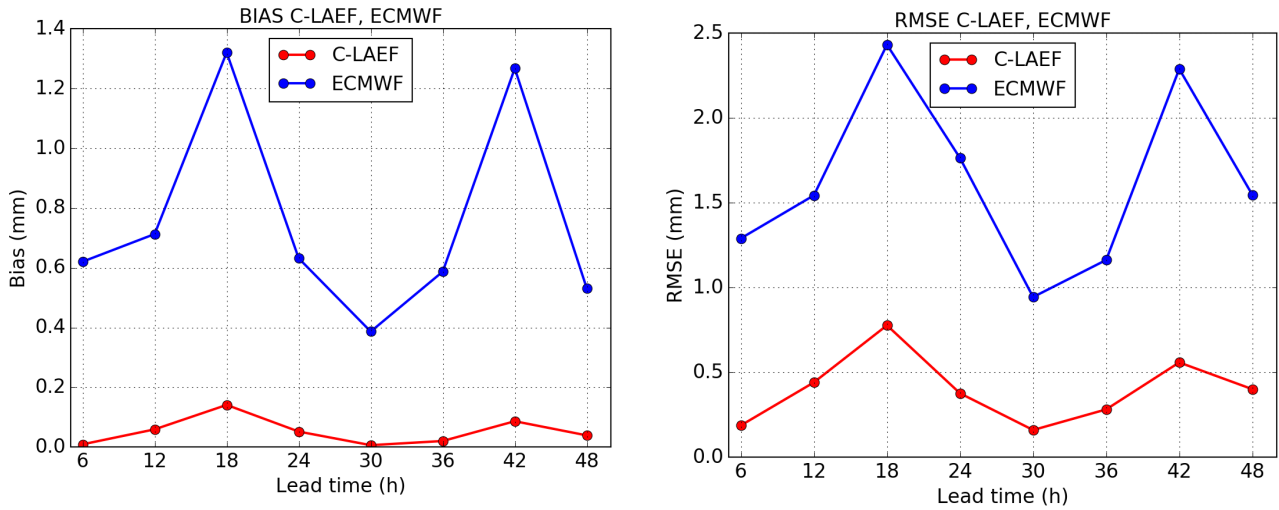


Fig. 2: Precipitation verification of C-LAEF (red) and ECMWF (blue) at all Austrian stations for August 2019. The left panel shows the precipitation BIAS, the right panel the RMSE.

3 AROME-RUC - Nowcasting version of AROME

ROME-RUC is similar to the French AROME-PI (Auger 2015) an hourly available system with 1.2km/L90 grid space. However, there are several technical differences: The hourly lateral boundaries come from AROME-Aut 2.5km instead of global model Arpège. It is an hourly cycled system, because the 3-hourly cycling frequency of AROME-Aut would in case of a rapid refresh cause a rather old first guess and its downscaling from 2.5km to 1.2km additional unwanted spin-up (see last Newsletter), which is not the case in France due to hourly cycling and same resolution in non-nowcasting version of AROME, there.

AROME-RUC Domain & Topography

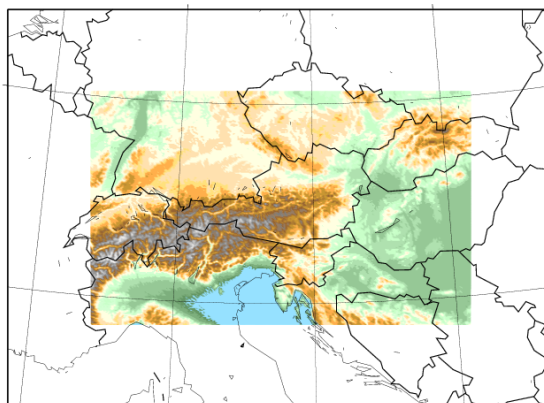
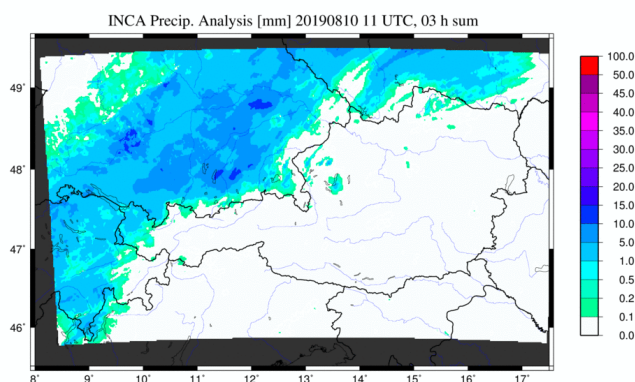


Fig. 3: AROME-RUC domain (coloured) inside AROME-Aut domain (white)

The assimilation window is extended backward (-90min-+25min) and the cut off time is extended to +25min to have enough observations for cycling. It was also found that the observation error and quality control cut off limit of Doppler winds needed re-tuning (see Figure 4) and that a two step IAU for spin-up reduction is needed. Furthermore there is additional latent heat nudging of precipitation analyses and forecasts from conventional analysis and nowcasting system INCA and FDDA nudging of AWS observations up to +30min integration time. Results are available about 1 hour after initialisation time.

The two step IAU leads to the fact that two one hour forecasts valid at the same time are available for each AROME-RUC run, where one is running freely when nudging period is exceeded, while the other one is pushed against the +1h 3D analysis. This can be used to calculate differences of the day and to add them to the static B-Matrix differences made from one month AROME-RUC-EDA by rerunning FSTAT every 6h. This dynamic B does not significantly change the shape of the B-Matrix compared to the static version, but slightly reduces the standard deviations (see Fig. 3.) Compared to the downscaling and 2.5km version standard deviation is higher and there is more power on the large wavenumbers, which is in agreement with findings in other institutes.



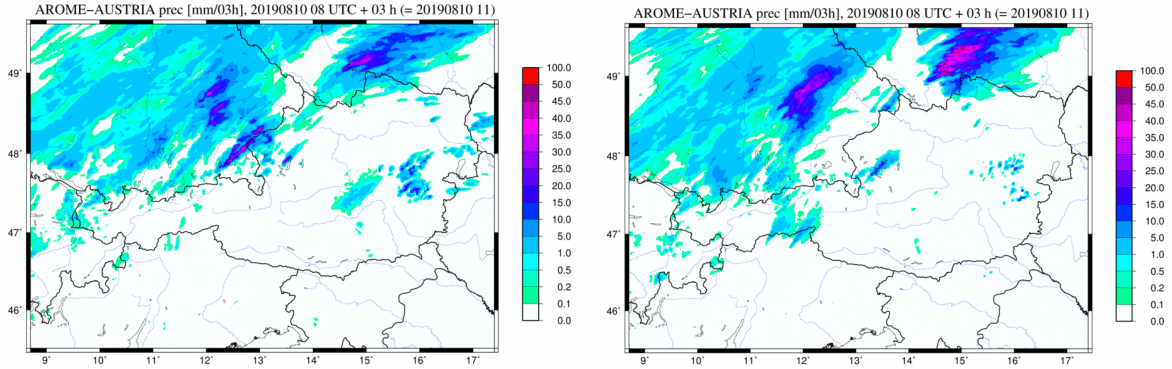


Fig. 4: Effect of modified Doppler wind quality control: 3h precipitation at 11 UTC on 10th August 2019. Precipitation analysis from INCA (top), AROME-RUC standard setting (bottom left) and new setting with VARQC on and higher Doppler observation error (bottom right). The erroneous convection over Eastern Austria is almost suppressed.

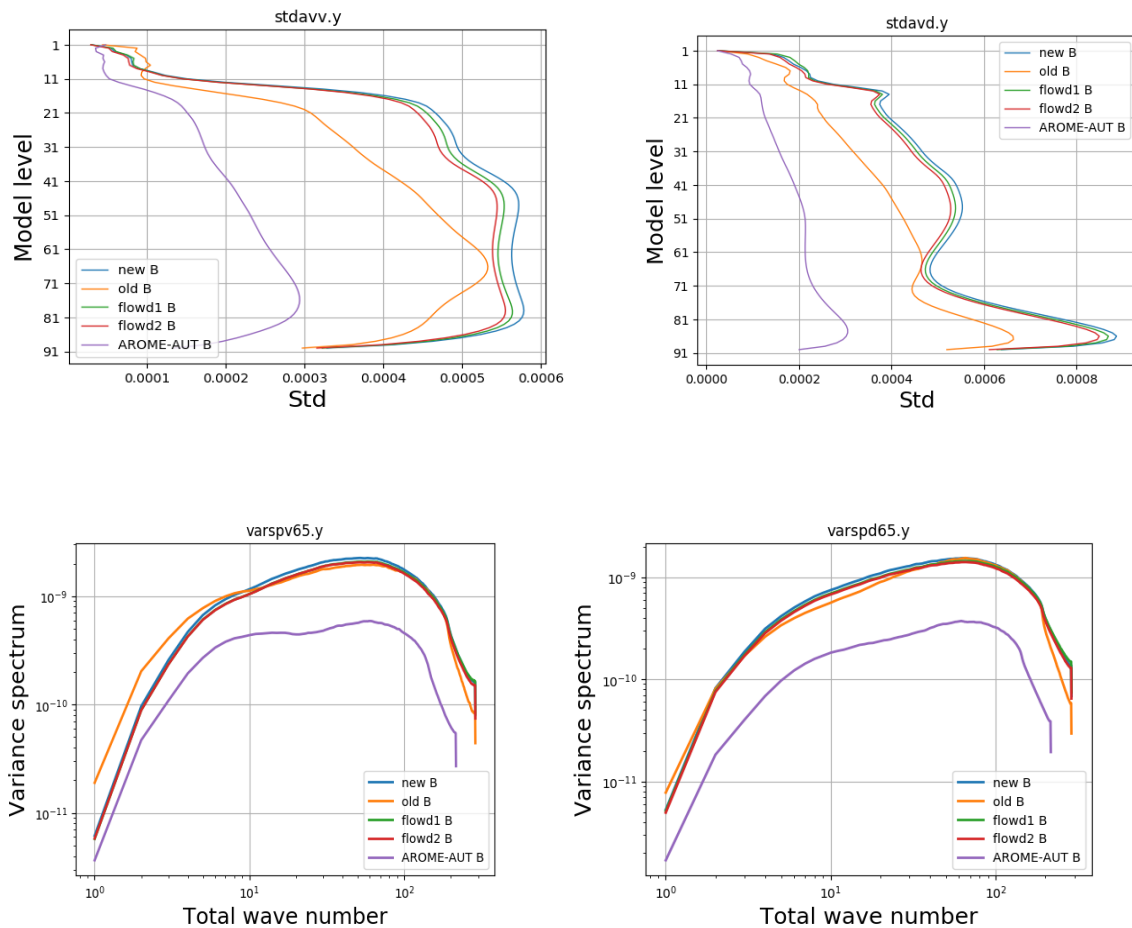


Fig. 5: Background error correlation matrix statistics for vorticity (left) and divergence (right) standard deviation (top) and variance spectrum (bottom). Comparison of AROME-Aut 2.5km (violet) and AROME-RUC 1.2km (downscaling of CLAEF EPS yellow), static AROME-RUC EDA based (blue) and including differences of the day (green, red).

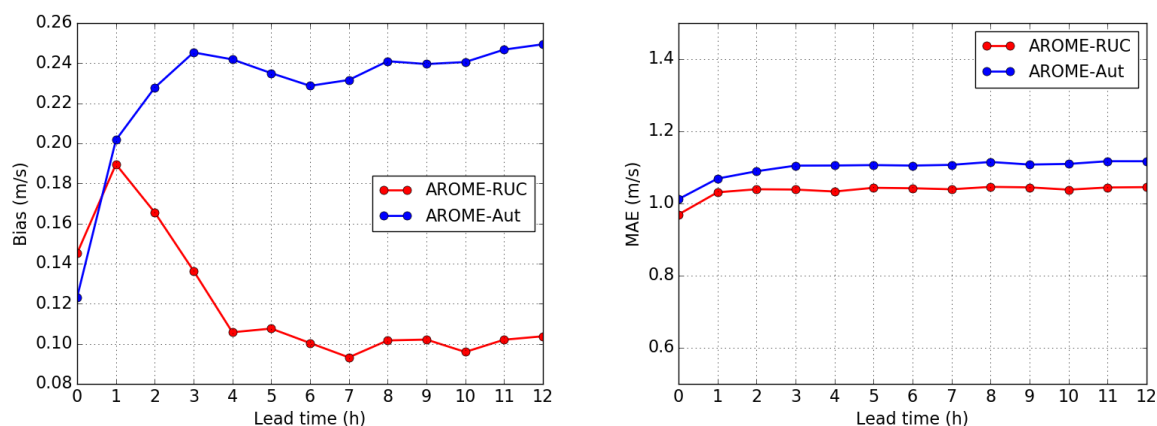


Fig. 6: Verification of 10m windspeed against Austrian surface stations. AROME-RUC (red) and AROME-Aut (blue), bias (left) and MAE (right) in September 2019 as function of leadtime. Average over 8 runs per day and 30 days for both AROME versions.

Verification shows that compared to the current operational AROME-Aut system the biggest benefit of AROME-RUC can be seen in the scores for wind speed and precipitation. An example can be seen in Figure 6.

4 Outlook

Beside the continuation of developments for AROME-Aut, AROME-RUC and C-LAEF it is a major target for 2020 to increase the number of applications for the new operational systems in downstream applications and the ZAMG forecast and warning system in general. This includes e.g. the coupling of AROME-RUC and C-LAEF to the current analysis and nowcasting system INCA and its ensemble version EnINCA. Further it is planned to position C-LAEF as the major contributor for the ZAMG warning system.

L. Auger, O. Dupont, S. Hagelin, P. Brousseau and P. Brovelli, 2015: AROME-NWC: a new nowcasting tool based on an operational mesoscale forecasting system. Q. J. R. Meteor. Soc., 141(690), 1603–1611.

Data assimilation and Seamless short-term ensemble prediction at RMIB

Lesley De Cruz, Idir Dehmous, Alex Deckmyn

1 Introduction

The density of meteorological observations and the amount of novel data sources have been increasing steadily in recent years. Likewise, more computational power is available than ever before: not just for data processing and numerical weather prediction (NWP), but also for impact modelling. Along with these rising trends in both data availability and modelling capabilities, the requirements for operational forecasting systems are shifting. This shift is apparent from the smartphone user who expects near-real-time updates, to the hydrologist or wind energy provider who needs ensemble predictions to estimate uncertainty. The focus is moving from traditional deterministic forecasts towards probabilistic, convection-permitting and rapidly updating forecasting systems. The basic building blocks such as nowcasting systems and convection-permitting NWP are present at RMIB but an integrated, seamless product is lacking.

In this article we describe recent work at RMIB to develop such an integrated system. In the first section we describe the basic structure of the system that we hope to achieve. Then we focus on an important ingredient that was lacking up to now. Operational NWP models are still running in downscaling mode. In the framework of the Data Assimilation Starter's Kit (DASKit) we have implemented an experimental data assimilation cycle for which we show some first results.

2 Project IMA

2.1 Introduction

With project IMA (Japanese for "soon" or "now"), the RMIB aims to address this need for a seamless product by combining data-driven probabilistic short-term predictions with convection-permitting NWP models. The goal is to have a seamless high-resolution probabilistic short-term forecast (24 hours). An effective transfer from research to operations is prepared by involving end users early, quality assurance through probabilistic verification (based on HARP), and the robustness of the operational system (based on EcFlow).

2.2 Structure

The first building block of IMA is the Short-Term Ensemble Prediction System for Belgium: STEPS-BE (Seed et al., 2013; Foresti et al., 2016). The success of this state-of-the-art nowcasting system lies in its treatment of the different scales present in precipitation as separate autoregressive processes. It takes into account the multifractal theory of precipitation by Lovejoy and Schertzer (2006), by decomposing the observed fields into a "cascade" of different scales. Such a cascade decomposition is obtained by Gaussian filtering in Fourier space of the observed radar rainfall fields. To generate an ensemble, stochastic noise is added to each spatial scale independently, and in accordance with the observed spatio-temporal properties and autoregressive parameters of each scale.

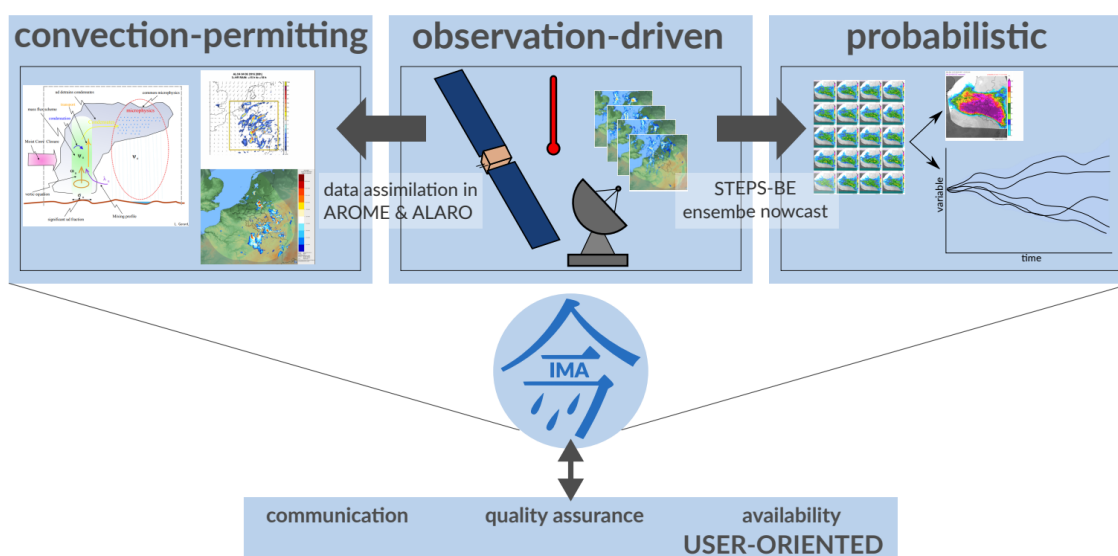


Figure 1: Structure of IMA

STEPS-BE features an adaptive skill-dependent blending with precipitation output from a Mini-EPS of NWP models. INCA-BE will also be combined with the members of the Mini-EPS in order to generate a probabilistic forecast for all variables.

The STEPS-BE nowcasting system has a timestep of 5 minutes. In order to enable dynamic blending with an NWP ensemble, the model output frequency also needed to be increased. We have therefore implemented a feature for ALARO and AROME to extract specific fields with the frequency of a single model timestep. Details such as which fields to extract, the output format (FA or netCDF), domain, time window and frequency can be set using a new namelist entry (namsteps). In our set-up, the ALARO and AROME models running at 1.3km horizontal resolution have a 45" second timestep, which is re-aggregated to 5 minutes afterwards.

The multimodel Mini-EPS will consist of an ALARO-AROME 2+2(lagged)-member ensemble running at 1.3km resolution, with a 3-hourly data assimilation cycle. This will also be our first trial of an ALARO-AROME ensemble running at a spatial resolution of 1.3km.

For best results, these high resolution models should be run with a data assimilation cycle. In the next section, we describe the current progress on this matter.

3 Data Assimilation progress

3.1 Introduction

Currently, at RMIB we run ALARO at 4km and 1.3km in downscaling mode (thus depending on the Arpège coupling for the data assimilation).

Therefore the implementation of Data Assimilation is an important part of the IMA project. In the first stages of development, we have had a lot of support from the DAsKit (Data Assimilation Starter's Kit) special program.

3.2 CANARI+OIMAIN surface analysis for AROME

A pre-operational suite was built and is running in real-time testing mode using synop data for surface analysis of the surface and soil fields (T2m , H2m ,Ts , Tg , Ws and Wg) with the CANARI_Oimain technique based on cy43t2 of the ARPEGE/ALADIN code. The analysis is performed every 3 hours and a forecast is produced every 6 hours with a 48-hour forecast range. The spatial resolution of the AROME model is 1.3km and it get its lateral boundary conditions files from ALARO 4.0km (Operational at RMIB) with a one-hour frequency. The ISBA fields are added from climatological files to the first guess at every analysis time and the SST (Sea Surface Temperature) is updated from the ARPEGE model coupling files. The suite is running and maintained using ecFlow scripting and the interactive user interface. The plots below show the bias of T2m in three different months (August, October and December 2019) for 00h runtime compared with operational model ALARO 1.3km.

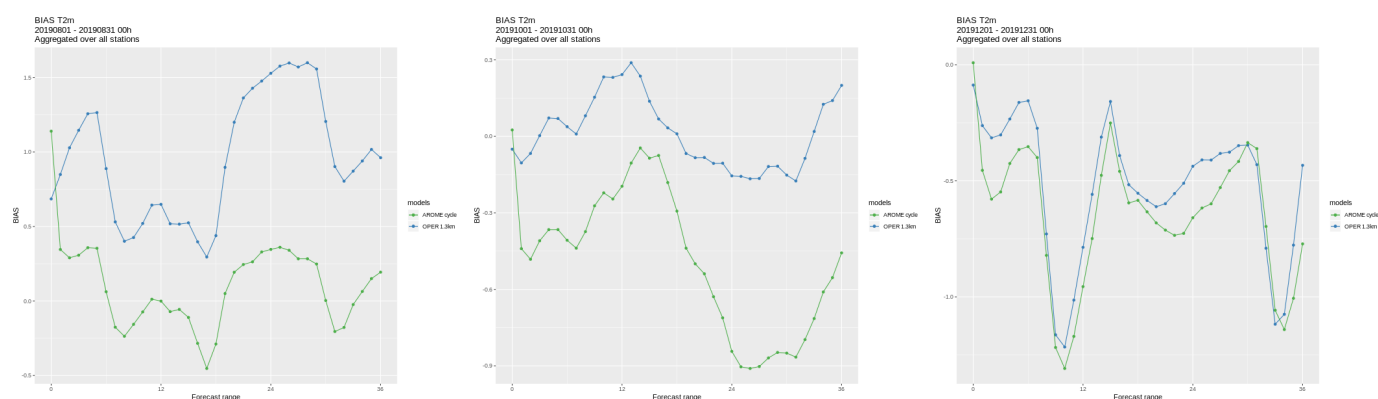


Figure 2: T2m bias scores for the operational Alaro-1.3km and the experimental Arome-1.3 cycle.

3.3 3DVAR setup for the three models at RMIB (ALARO 4.0km, ALARO 1.3km and AROME 1.3km)

In the last quarter of 2019, the data assimilation team started to focus on the building of an operational 3DVAR cycle for the three models used at RMIB. The main set-up is now done and scripts for the different configurations are written: Bator for the conversion of observations to ODB, screening for observations thinning and filtering and finally minimisation to get the new initial state (analysis).

The Bator namelists are set up in order to perform a geographical selection by introducing the extent of each model domain (namelist Bator_lamflag). The minimization namelists are tuned by setting up the REDNMC parameter to 1.0 (default value in namelist NAMJG) and switching off the keys related to satellite data processing and the VarBC method. Finally, the analysis is computed by the Quasi-Newton method which corresponds to M1QN3 minimizer (Yessad 2008).

Another fundamental ingredient of a complete 3DVAR setup is the B matrix. This was computed and diagnosed for the three models by taking two forecast periods (from 01-02-2019 to 28-02-2019 and 01-08-2019 to 31-08-2019) by spreading the forecasts every 3 days. Furthermore, the B matrices for the three models are computed using the NMC method (Parrish and Derber 1992).

Some B matrix diagnostics for ALARO (4.0km , 1.3km) and AROME 1.3km are presented on the figures below. Currently, the synop (land + automatic) are the only type of observation that is being used, the main aim is to get a stable 6-hour 3DVAR cycle running on a ecFlow environment.

In the future we plan to use other types of observation (AMDAR, GNSS and MODE-S) and increase the

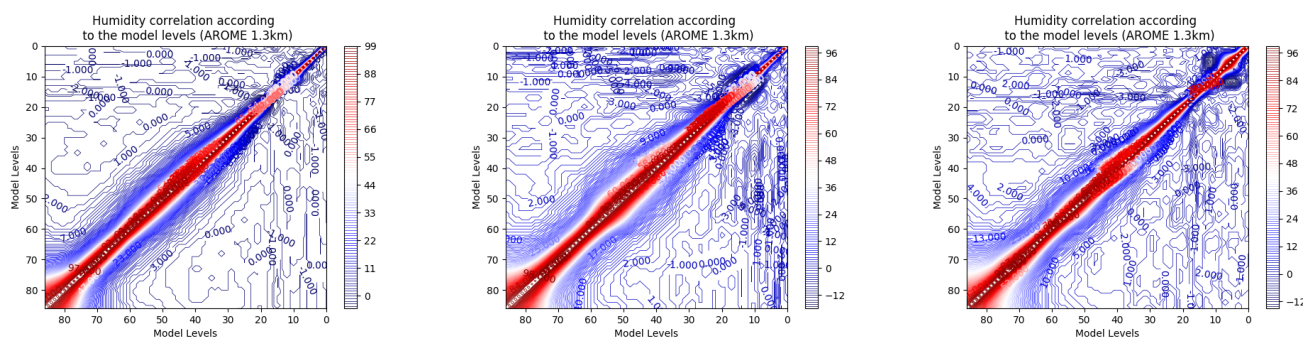


Figure 3: Specific humidity covariances according to model levels.

frequency of the analysis time to 3-hourly cycling with 6 hours runtime forecast.

4 Future plans

Below is an overview of the current and future operational system at RMIB.

- **Q1 2020:** Added to current set-up:
 - AROME 1.3km with SURFEX 3-hourly surface data assimilation cycle, 6-hourly forecasts
 - Complete rewrite of scripting system for robustness and maintainability Using latest version of ECMWF's EcFlow system
- **Q2-3 2020:** Project IMA v.1: Seamless probabilistic forecasts from 5 minutes to 24h.
 - Mini-EPS: ALARO 1.3km with ISBA & AROME 1.3km with SURFEX, with surface data assimilation
 - Blending with ensemble nowcasting: STEPS-BE (pr) / INCA-BE (T2m, RH2m, \dot{A}_{ϵ})
- **Late 2020:**
 - Mini-EPS v2: ALARO 1.3km with SURFEX & AROME 1.3km with SURFEX
 - 3-hourly upper-air data assimilation (3DVar), 6-hourly forecasts

5 References

- Foresti, L., Reyniers, M., Seed, A., Delobbe, L., 2016: Development and verification of a real-time stochastic precipitation nowcasting system for urban hydrology in Belgium. *Hydrology and Earth System Sciences* 20: 505-527.
- Seed, A.W., Pierce, C.E., Norman, K., 2013: Formulation and evaluation of a scale decomposition-based stochastic precipitation nowcast scheme. *Water Resources Research* 49(10), 6624-6641.
- Lovejoy, S., and D. Schertzer, 2006: Multifractals, cloud radiances and rain. *Journal of Hydrology* 322.1-4, 59-88.
- Parrish, D.F. and J.C. Derber, The National Meteorological Center's spectral statistical interpolation analysis system. *Mon. Wea. Rev.* 120 1747-1763, 1992.

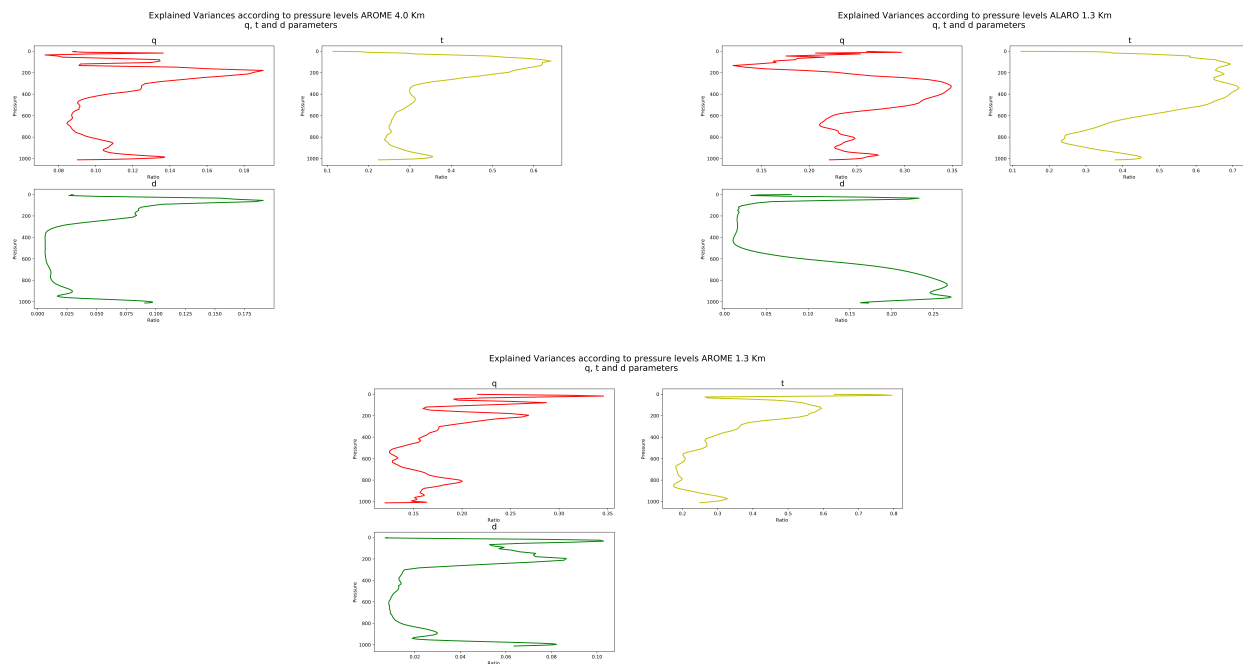


Figure 4: Explained variances for the parameters Humidity (Red), Temperature (Yellow) and Divergence (Green)

Yessad, K., Meteo-France/CNRM/GMAP/ALGO Minimization in the cycle 32 of ARPEGE/IFS, 2008.

Highlights of the NWP activities at the Croatian Meteorological and Hydrological Service

Iris Odak Plenković, Mario Hrastinski, Alica Bajić, Kristian Horvath, Endi Keresturi, Kristina Kozić, Ines Muić, Suzana Panežić, Antonio Stanešić, Ana Šljivić, Martina Tudor

1 Introduction

In 2019 several activities regarding research and operations were performed at Croatian Meteorological and Hydrological Service (DHMZ). We have started with the implementation of new export cycle 43 and in parallel considerable work has been done in order to switch operations from the current 8-km model setup to a 4-km model setup. As part of this activity new setup of dynamical adaptation was developed and more details about this can be found in the next section. Also, one of our main focuses is the development of post-processing methods that can enhance forecast in complex terrain. Thus, the analog-based method was extended to new variables and locations and also more details can be found in the next section.

2 Highlighted activities

Analog-based method

Even at the sub-kilometer grid spacing, state-of-the-art mesoscale models still exhibit considerable errors, especially in complex terrain (Horvath et al., 2012). This is particularly relevant for operational weather prediction systems that are constrained by the available computing resources. It is thereby useful to develop post-processing methods that reduce starting model errors at locations where measurements are available, besides improving the model itself (e.g., using higher resolution or improved parameterization package).

The analog-based method is a point-based post-processing approach built on finding the most similar past numerical weather predictions (analogs) over several variables (predictors) and forming an analog ensemble (AnEn) out of the corresponding observations. Analogs are found independently for every forecast time and location, narrowing the search around particular time of a day by a time window. The verifying observations of the best-matching analogs are the members of AnEn. The assumption is that the errors of the good (quality) analog forecasts are likely to be similar to the error of the current forecast (Delle Monache et al., 2011 and 2013).

The analog-based method is thoroughly tested, for the first time over a coastal region characterized by complex topography in Croatia (Odak Plenković et al., 2018). From the end of November 2016 until August 2019 the analog-based method is used to provide forecast of wind speed for 16 locations. The operational analog-based method uses four 2 km HRDA operational output products as predictor variables: wind speed and direction, vorticity and divergence. The analog-based 3-hourly wind speed output (up to +72 hours) is visualized by box-plot figures, representing 15-members ensemble.

The new algorithms are now developed to expand the number of locations and the forecast variables. All the existing algorithms are translated into Python programming language in 2018 /19.

The pre-selected data includes the measurements (temperature, wind speed, and gusts) and ALADIN-HR4 -38v1 (A4) 00 UTC forecasts at approximately 60 stations. Basic quality control is applied at the measured data, after which 63 locations are used for wind and 49 for temperature forecasting. The data is then divided into training (yr. 2016-2017) and testing (yr. 2018). Since there seem to be improvements if more than 4 predictor variables are used, the ALADIN-HR4 model (4-km horizontal grid spacing) is used as a raw model (up to 13 predictor variables).

Three different analog-based method experiments are tested, producing 15 analog ensemble members. The experiments differ on the number of predictor variables used. For wind speed and gust forecasting the experiments are listed below:

- **ANrr** – using 8 predictor variables: wind speed, direction and gusts, temperature, relative humidity, pressure, precipitation and total cloud cover forecasts from model ALADIN-HR4 -38v1
- **ANr** – in addition to the ANrr predictor variables, global and diffuse radiation predictor variables are also used
- **AN** – using all the predictor variables as ANr plus additional cloud cover predictors: low, middle and high cloud cover (13 predictors total).

All available predictor variables are weighted the same at the moment (weight equals 1), and 15 AnEn members are produced. The time window used to find the most similar analogs is defined by one time step before and after the lead time of interest.

For the temperature forecasting, it has been noticed that the analog-based method is very easily over-fitted. Therefore, two additional experiments using fewer predictors are tested:

- **ANtt** – using only 4 predictors total: temperature, wind speed, global radiation, and cloud cover
- **ANt** – pressure, relative humidity and diffuse radiation predictors are added to ANtt set of predictors (7 predictors total).

The temperature predictor variable is weighted using 1.0 value, while the other predictor variables are weighted using 0.3 value. The time window used to find the most similar analogs is defined by one time step before and after the lead time of interest. The **ANr** and **ANtt** are assessed as the most successful experiments. Therefore, they are implemented as a part of the forecasting system, in operational test mode from August 2019. The setup includes 15 members wind speed, wind gusts and temperature ensemble predictions with the hourly resolution, up to 72 h ahead (Figure 1).

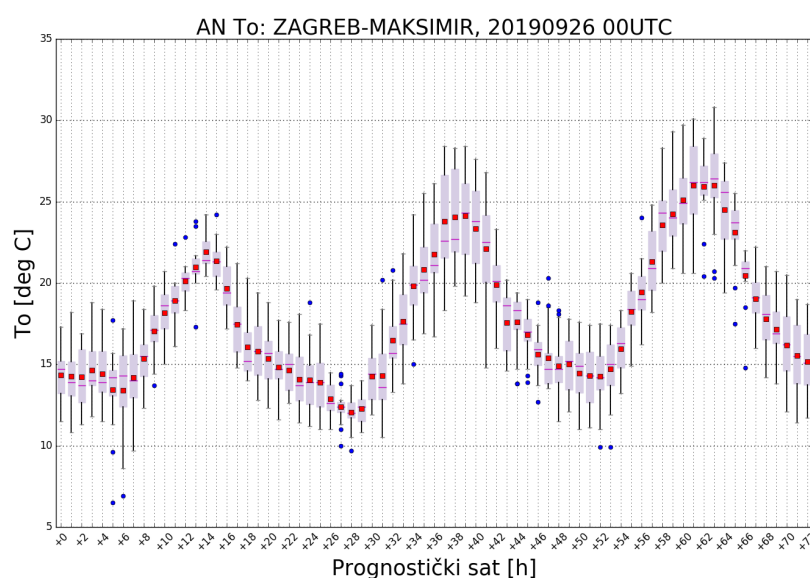


Figure 1: The example of analog-based ensemble forecast output for temperature at Zagreb-Maksimir station at 26th of September, 2019.

All analog-based experiments for the wind speed and exhibit better results when compared to the starting ALADIN-HR4 model (Tables 1. and 2.). The bias is generally small for all available forecasts, both ALADIN-HR4 model and AnEn mean. The (Pearson) correlation coefficient is higher after post-processing, while the average root mean square error (RMSE) is lower. The ANr and ANrr results are almost identical. However, using even more predictors does not seem to produce further improvements.

The ensemble verification measures, such as Brier skill score (BSS) for wind exceeding 10 m/s or continuous rank probability score (CRPS) show almost identical result for ANr and ANrr as well, while the AN experiment is less successful. Additionally, reducing the number of predictor variables seem to decrease the ensemble spread.

Table 1: The overall values of several verification metrics for three different analog-based experiments compared to the ALADIN-HR4 wind speed (V) forecast at 63 locations in Croatia, 2018.

V	AN	ANr	ANrr	ALADIN-HR4
Bias [m/s]	-0.06	-0.03	-0.02	0.29
Corr. coeff.	0.79	0.80	0.80	0.69
RMSE [m/s]	1.71	1.69	1.69	2.16
Spread [m/s]	1.80	1.75	1.74	x
BSS za V>10 m/s	0.41	0.43	0.43	x
CRPS[m/s]	0.84	0.83	0.83	x

Table 2: The overall values of several verification metrics for three different analog-based experiments compared to the ALADIN-HR4 wind gust (VMAX) forecast at 63 locations in Croatia, 2018.

VMAX	AN	ANr	ANrr	ALADIN-HR4
Bias [m/s]	-0.11	-0.07	-0.03	0.08
Corr. coeff.	0.81	0.82	0.82	0.71
RMSE [m/s]	3.01	2.97	2.97	3.84
Spread [m/s]	3.12	3.03	3.00	x
BSS za V>10 m/s	0.47	0.48	0.49	x
CRPS[m/s]	1.47	1.45	1.45	x

The AN, ANr and ANrr wind speed and gusts forecast RMSE does not differ significantly for any lead time available (Figure 2). It seems that ANr and ANrr exhibit slightly smaller RMSE values than AN. All analog-based experiments keep the ALADIN-HR4 RMSE daily cycle.

Since it is very important to analyze the forecast accuracy depending on different thresholds, the Brier skill score (BSS) depending on threshold value is used. The differences among analog based experiments increase for higher than 2-3 m/s thresholds (Figure 3). Similarly to previously shown results, the ANr and ANrr experiments seem to be more successful than AN.

Finally, the spatial distribution of error is investigated using CRPS. The results are shown for ANr experiment, while the results for AN and especially ANrr are barely distinguishable (Figure 4). For both wind speed and gusts analog-based forecast is more accurate at nearly-flat continental terrain situated more inland than at coastal and mountain complex area, as expected.

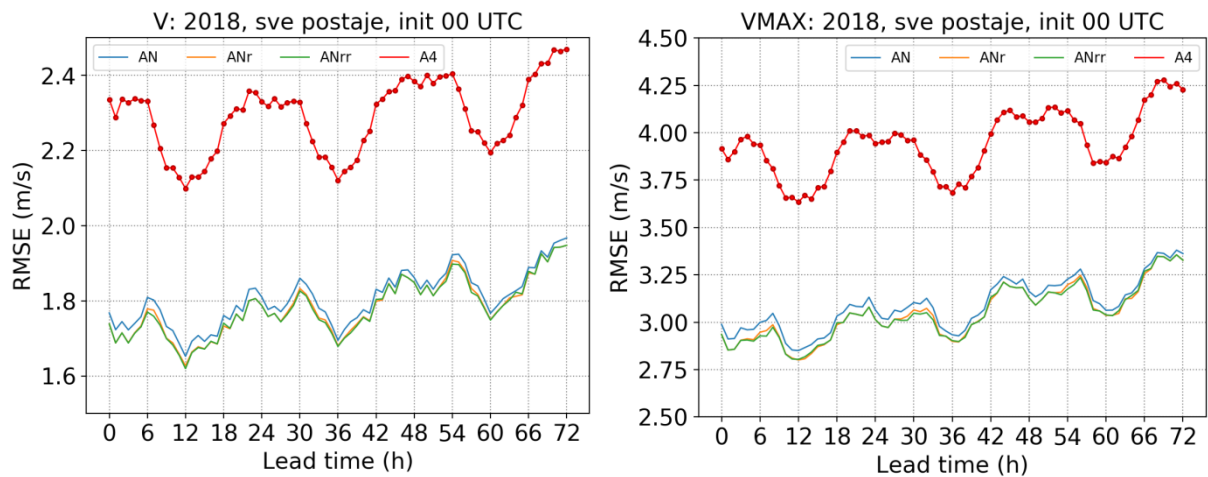


Figure 2: RMSE scores for wind speed (V) and gusts ($VMAX$) analog based forecasts compared to ALADIN-HR4 ($A4$) starting model at 63 locations (yr. 2018). The markers are set for the results significantly different from the AN forecast (95 % confidence level).

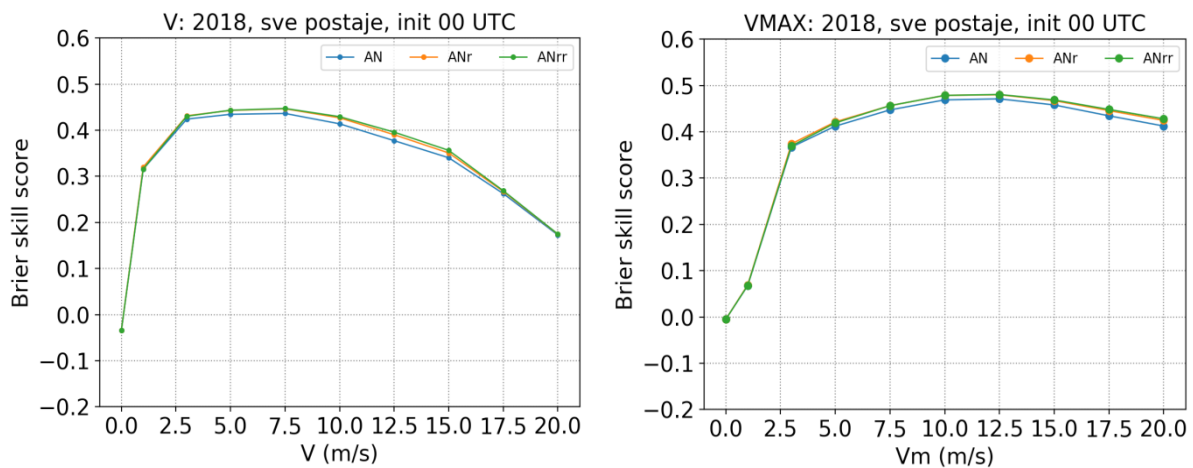


Figure 3: Brier skill score for wind speed (V) and gusts ($VMAX$) analog based forecasts (to exceed threshold value), compared to ALADIN-HR4 ($A4$) starting model at 63 locations (yr. 2018). The markers are set for the results significantly different from the AN forecast (95 % confidence level).

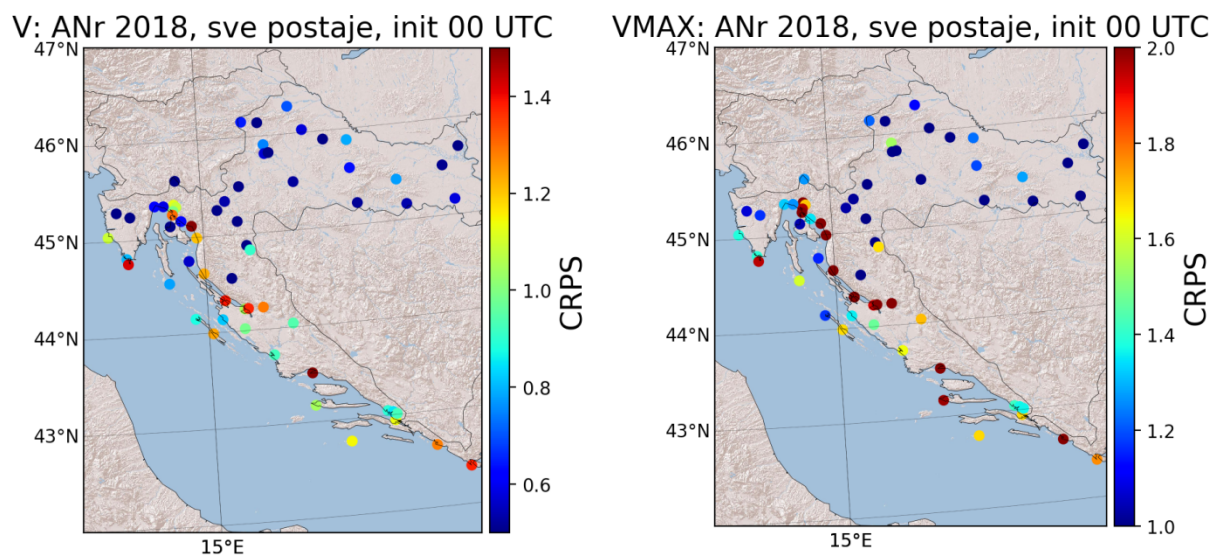


Figure 4: Continuous rank probability score for wind speed (V) and gusts ($VMAX$) analog based ANr experiment at 63 locations (yr. 2018).

In addition to forecasting the wind speed and gusts, the temperature is also forecasted by the analog-based method. Since quality temperature measurements are not available for all the stations, only 49 stations are used. Compared to wind forecasting, the AN, ANr and ANrr are not as successful: if several overall values of verification metrics are compared (Table 3), it can be seen that the error is larger than for the starting model ALADIN-HR4. Since the variability of the temperature is much smaller than for the wind and a big part of that variability can be described with the climatological cycle (daily, yearly etc.). Therefore, it is more prone to over-fitting. That is why two additional experiments are included, using less predictors and different weights, with the temperature being the most important predictor. Result show that with this approach analog-based method outperforms starting model. Additionally, unlike AN, ANr and ANrr, ANt exhibits similar or smaller error measured by RMSE than the starting ALADIN-HR4 model, especially during nighttime (Figure 5). Furthermore, ANtt shows improvement for all lead times. The benefit of using less predictors (i.e. ANt and ANtt) is apparent for all temperature thresholds tested, exhibiting higher BSS. The ANtt BSS is very similar to ANt BSS for the higher threshold, while it yields higher score for the lower thresholds.

Table 3: The overall values of several verification metrics for three different analog-based experiments compared to the ALADIN-HR4 temperature (T) forecast at 49 locations in Croatia, 2018.

T	AN	ANr	ANrr	ANt	ANtt	ALADIN-HR4
Bias [°C]	0.33	0.25	0.37	0.21	0.13	-0.35
Corr	0.92	0.94	0.94	0.98	0.98	0.97
RMSE [°C]	3.60	3.26	3.20	1.99	1.93	2.20
Spread [°C]	4.26	3.88	3.97	2.35	2.94	x
BSS za $T > 20$ °C	0.70	0.72	0.72	0.80	0.81	x
CRPS	1.90	1.73	1.71	1.09	1.03	x

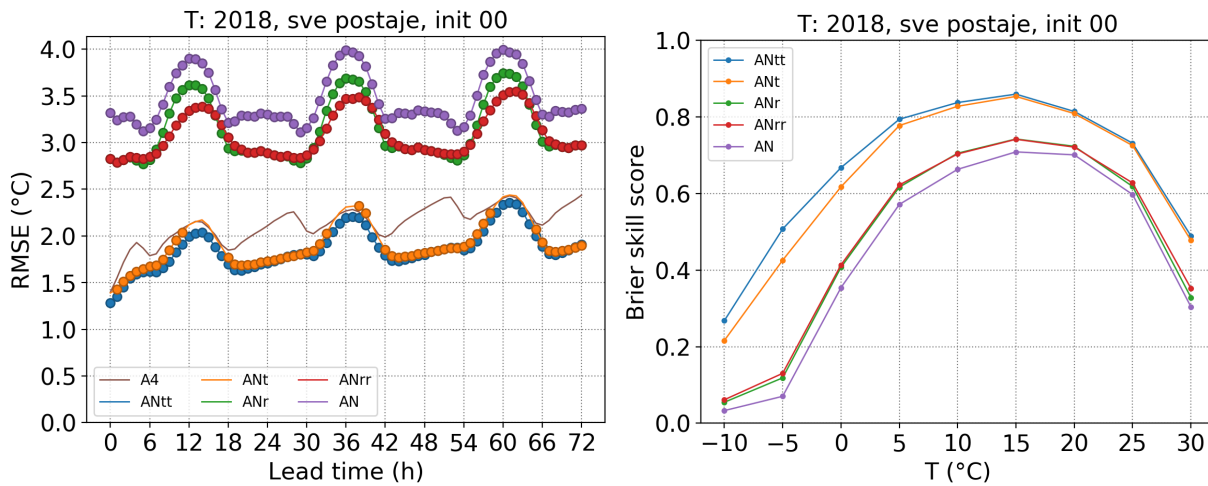


Figure 5, Left: RMSE scores for temperature (T) analog based forecasts compared to ALADIN-HR4 (A4) starting model. The markers are set for the results significantly different from the AN forecast (95 % confidence level). Right: The Brier skill score for temperature analog based forecasts. The results include data at 49 stations during 2018.

Finally, the CRPS shows that analog-based forecast produces the best results at coastal maritime region (Figure 6). The mountain complex area seems to be the least predictable one, resulting in the lowest CRPS as expected. This is the small area with the high altitudes, with distinctive mountain climatology (unlike surrounding area).

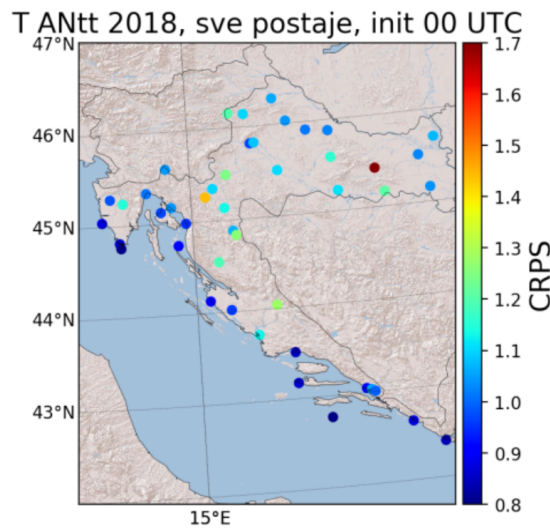


Figure 6: Continuous rank probability score for temperature analog based ANtt experiment at 49 locations (yr. 2018).

The new Dynamical Adaptation (DA) configuration

At DHMZ we run operationally Dynamical Adaptation (DA; e.g. Žagar and Rakovec 1999., Ivatek-Šahdan and Tudor 2004.) of the ALADIN-HR8 wind forecast to 2 km grid, utilizing hydrostatic dynamical core. The DA is run four times daily (00, 06, 12 and 18 UTC) at 15 vertical levels with 60 s time-step. During the procedure each (hourly) input file is run for 30 time-steps in advance to obtain refined and computationally efficient wind forecast.

Since the ALADIN-HR8 configuration will be switched-off soon, there is a need to couple DA to the ALADIN-HR4 configuration. Here we present novelities and preliminary results of the new DA configuration.

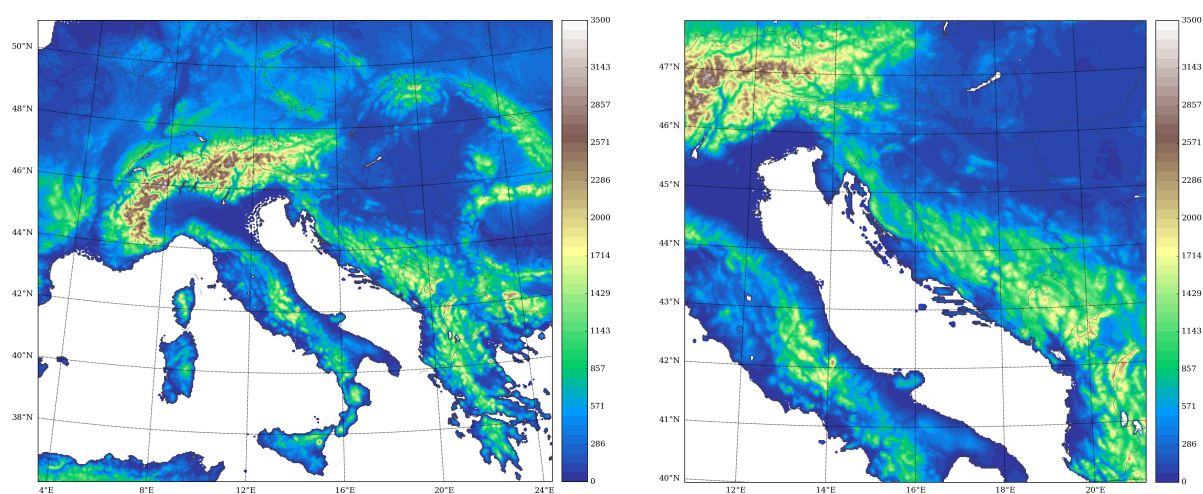


Figure 7: Orography of the model domain for ALADIN-HR8/ALADIN-HR4 configurations (left) and ALADIN-DA2 configuration (right).

The domain of the new DA configuration covers the same area as its predecessor, i.e. it consists of 439x439 grid points covering the broader area around Croatia (Figure 7.). However, the number of vertical levels is increased to 32. To decrease the impact of vertical interpolations on near surface wind, the first model is lowered to ~10 m (previously it was at ~17 m). Trying to achieve the balance between cost-effectiveness and performance we created several DA configurations which match the levels of ALADIN-HR4 up to certain height:

- **HRDG** – configuration with 44 vertical levels based on CY29T2 which preserves the levels of the ALADIN-HR4 configuration up to ~3000 m
- **HRDH** – configuration with 24 vertical levels based on CY29T2 which preserves the levels of the ALADIN-HR4 configuration up to ~700 m
- **HRDI** – configuration with 32 vertical levels based on CY29T2 which preserves the levels of the ALADIN-HR4 configuration up to ~1500 m
-

Additionally, we created the control **HR42** configuration which preserves the levels of ALADIN-HR8 configuration, but it is coupled to ALADIN-HR4. Both ALADIN-HR4 and ALADIN-HR8 are based on CY38T1. Three experiments and control were run during the February 2019. for the 00 UTC run and compared against ALADIN-HR4 (CRO4) and ALADIN-DA2 (HRDA) configurations. The scores for February are shown on Figure 8. Based on scores and computation time HRDI configuration is chosen as the best candidate to replace the currently operational HRDA.

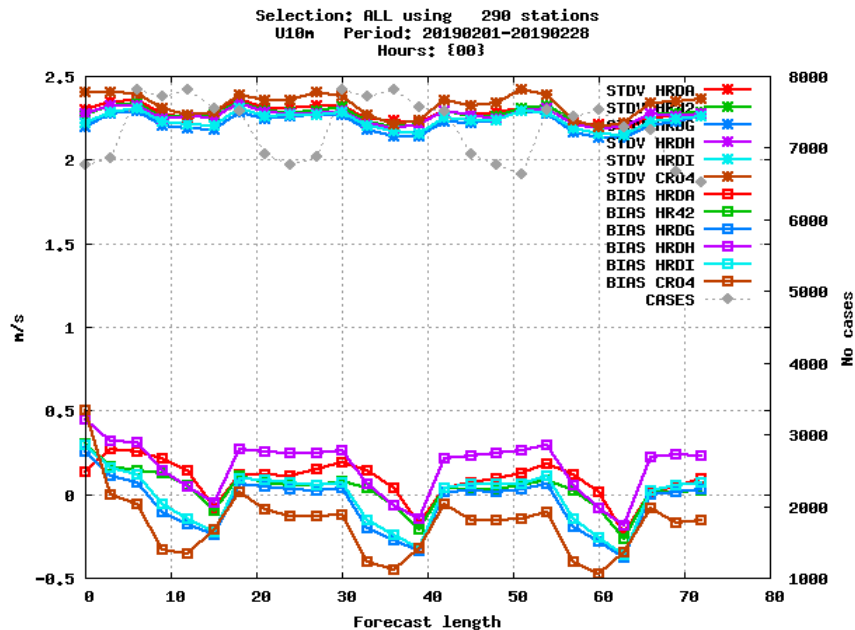


Figure 8. Comparison of 10m wind speed BIAS and STDEV for different experimental dynamical adaptation configurations (HR42, HRDG, HRDH and HRDI) against currently operational ALADIN-HR4 (CRO4) and ALADIN-DA2 (HRDA).

After that we utilized new climate files prepared by Suzana Panežić, based on her work in Toulouse during the January 2019 (HRDJ experiment). Those were also used for creation of DA at 1 km grid spacing (HRDK experiment). The number of vertical levels and domain size for HRDK are the same as for HRDI configuration.

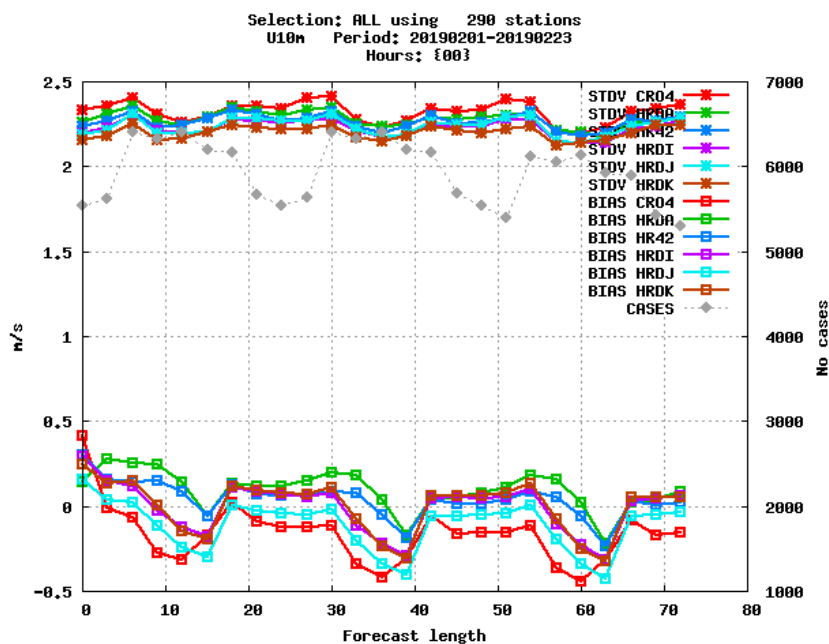


Figure 9. Comparison of 10m wind speed BIAS and STDEV for different experimental dynamical adaptation configurations (HR42, HRDI, HRDJ and HRDK) against currently operational ALADIN-HR4 (CRO4) and ALADIN-DA2 (HRDA).

Overall the scores for HRDK are comparable to HRDI (Figure 9.) and HRDJ. However, when verification is performed using only Croatian stations the scores for HRDK are worse (Figure 10.). As a result of better performance at Croatian stations (not shown here), HRDJ configuration is chosen over HRDI to replace HRDA.

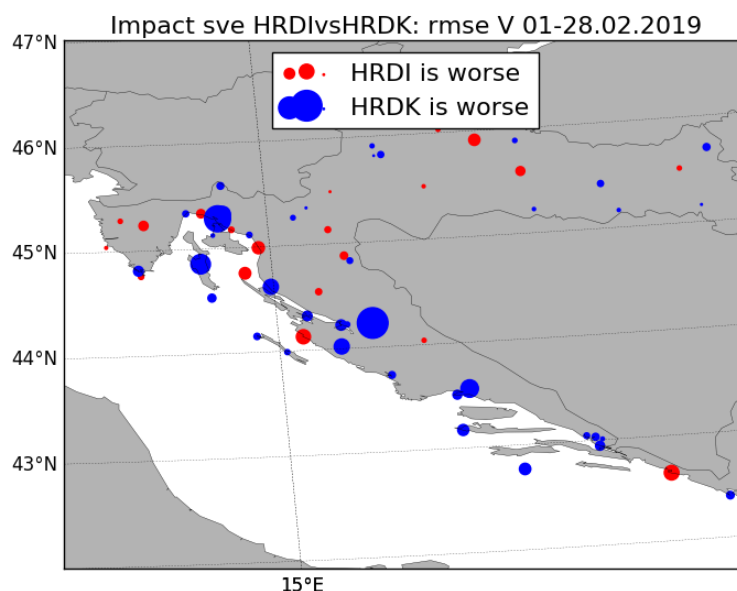


Figure 10. Comparison of 10m wind speed RMSE for HRDI and HRDK configurations using only Croatian stations.

Currently there is an ongoing work on tuning of wind gusts. After that the longer period run of HRDJ configuration will be prepared and configuration will enter into the parallel run. Obviously, this configuration is rather outdated and needs to be upgraded. First of all it has to be arranged to work on a higher cycle (preferably CY43T2) and switched to non-hydrostatic dynamical core. Furthermore, with the desired increase in resolution we need climate files with up to date orography and roughness length fields. Finally, we need to upgrade our computing resources. Additionally, we will focus on improving the wind forecast by using post-processing methods. These methods are even less computationally demanding than the DA. Therefore, the development of these methods is not limited by the status of current computing resources.

3 References

Delle Monache, L., Nipen, T., Liu, Y., Roux, G., Stull, R., 2011: Kalman filter and analog schemes to post-process numerical weather predictions. *Monthly Weather Review*, 139, 3554-3570.

Delle Monache, L., Eckel, T., Rife, D., Nagarajan, B., 2013: Probabilistic weather prediction with an analog ensemble. *Monthly Weather Review*, 141, 3498-3516.

Horvath, K., Koracin, D., Vellore, R., Jiang, J., Belu, R., 2012: Sub-kilometer dynamical downscaling of near-surface winds in complex terrain using WRF and MM5 mesoscale models. *Journal of Geophysical Research*, 117, D11111, 19 pp.

Odak Plenković, I., L. Delle Monache, K. Horvath, and M. Hrastinski, 2018: Deterministic Wind Speed Predictions with Analog-Based Methods over Complex Topography. *Journal of Applied Meteorology and Climatology*, 57, 2047–2070 (<https://doi.org/10.1175/JAMC-D-17-0151.1>).

Ivatek-Šahdan, S., and M. Tudor, 2004: Use of high-resolution dynamical adaptation in operational suite and research impact studies. *Meteor. Z.*, 13, 99-108.

Žagar, M., and J. Rakovec, 1999: Small-scale surface wind prediction using dynamic adaptation. *Tellus*, 51A, 489-504.

ALARO-1 Non Hydrostatic Operational Application at 2.3 km

Radmila Brožková

1 Introduction

Following quite an important increase of computer power coming with the new supercomputer, CHMI could pursue its plans in terms of the main operational application of the ALADIN System. The goal was to go to a double of the horizontal resolution, implying also the use of the non-hydrostatic dynamical core. We also wished to keep the same physical size of the model domain, since we consider this aspect quite important. Too small domains would not allow the model to develop its solution properly. In addition, over a small domain, the number of available observations would be far too reduced at the same time for a meaningful data assimilation and verification allowing for tuning the model setup.

2 Model domain and Dynamical core choices

The new horizontal resolution is 2.325 km, which is practically doubling the previous grid size of 4.710 km. In number of grid points it represents 1080 x 864, having 11 points in the extension zone in each direction. For the coupling zone we have decided to keep its physical size, passing from the traditional width of 8 points to 16 points. In vertical, we keep 87 levels. Another portion of computer power goes to the deployment of the non-hydrostatic dynamical core.

To establish the orography and land-sea mask, we use now the GMTED2010 topographic database; see Fig 1. Since we use still ISBA surface scheme operationally, the other surface characteristics are computed by the standard e923 procedure from the previous databases. We need to note one important aspect – the sub-grid-scale topographic characteristics, such as orographic roughness, we computed from the previous database GTOPO30. We applied orographic roughness reduction and smoothing as usual to get good screen level scores, namely of wind at 10 m. On the other hand we have separated the thermal roughness from the orographic one and adapted the surface calculations in ALARO-1 accordingly.

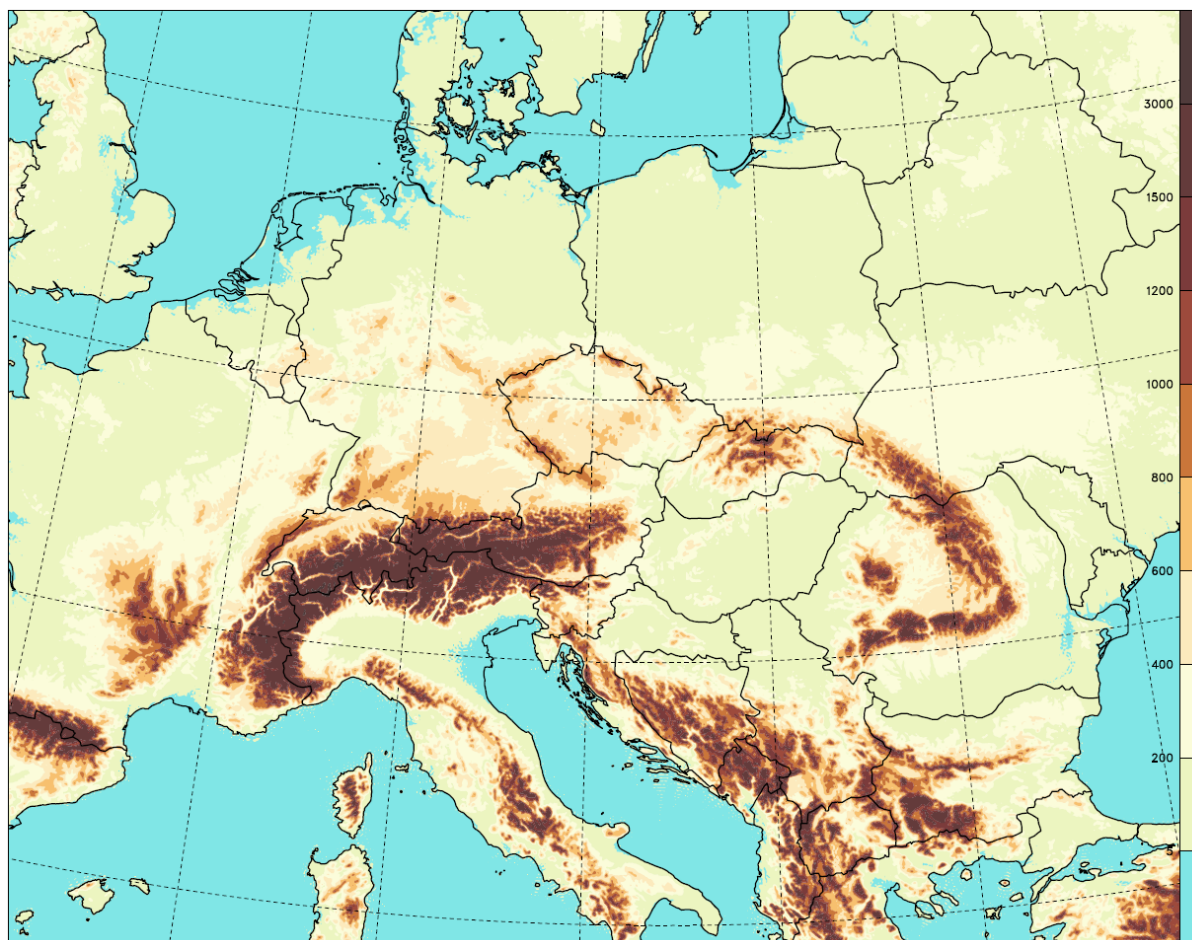


Figure 1: Orography of the current ALADIN domain at the resolution of 2.3 km with the quadratic truncation applied.

Regarding the model dynamics setup, we have been investigating the best compromise between the time-step length and number of the semi-implicit solver iterations. The result is to use 90 s long time-step and one iteration of the solver.

Further, we have retuned spectral horizontal diffusion to control properly the kinetic energy spectra cascade. We recall that we use a combination of the SLHD local grid-point horizontal diffusion and the spectral one. The spectral diffusion acts mainly in the stratosphere, and only this part, including the vertical profile of its activity needed to be touched.

While going to higher resolution with steeper orography it becomes necessary to improve the localisation of origin points of semi-Lagrangian trajectories. We have now four iterations to get the origin points positions; the calculation is cheap and fast.

A complete and detailed description of the dynamical setup can be found in the research report Smolíková, 2019.

3 Parameterizations

Here we mention very briefly, which schemes in the ALARO-1 physics had to be revised and or retuned. With higher resolution, we describe further part of atmospheric circulation spectra, and hence we move the limit of what is still sub-grid-scale and what becomes resolved.

First question was whether we need still to use the parameterizations of unresolved orography, which is shortly called as gravity wave drag, although it is not only about gravity waves generated by the orographic torque. In literature it is discussed that the limit to need the parameterization is somewhere between 4 to 3 km. Experimentally, we found that from the point of view of model scores, it is better to keep this parameterization still active, albeit it is retuned to reduce its effects. We believe that to get rid completely of this parameterization we have to address the orographic roughness computation, first to base it on more precise topographic database GMTED2010 and then to revise its way of smoothing. Otherwise, the option of having thermal roughness separated from the orographic one is now operational, see for example the presentation at ALADIN-HIRLAM workshop 2018.

Regarding the parameterization of the moist deep convection, the 3MT scheme is still active at the resolution of 2.325 km since we are not yet out from the grey zone. We retuned only the efficiency of downdraft accordingly to the mesh-size refinement.

Most of our attention has been devoted to the scheme computing cloudiness for the radiation scheme. Here cloudiness originating from all considered processes is combined, i.e. from the grid-scale condensation, shallow convection and moist deep convection (updraft and detrained cloud). In ALARO we have not yet unified the grid-scale condensation computation between the adjustment and the radiation cloud scheme, since there are several ingredients that need to be addressed first. We have however made steps going to the right direction. First, we have introduced the scale awareness to the radiation cloud scheme, adjusting the critical relative humidity profile, which is done in the adjustment. By doing so, we reduced excessive amount of mid-level cloudiness. Further, we got rid of the algorithm keeping resulting cloudiness away from its limit values 0 and 1. Finally, we have retuned the parameter of the simple algorithm mimicking the shallow convection cloudiness to increase the amount of sub-inversion clouds.

4 Cycling and Data Assimilation

For the surface data assimilation, we have not made any change when going to the higher resolution. We may revise some tunings when implementing higher density of additional surface stations.

To get the upper-air initial condition, we use the BlendVAR algorithm. Indeed, here we have retuned the cut-off blending truncation and digital filters accordingly to the horizontal resolution change. The result of the blending step is an input to the 3DVAR scheme. There it has been of course necessary to create new background covariations matrix. This has been done by the dynamical adaptation of the ARPEGE global model assimilation ensemble. The background term is retuned now by the coefficient 0.25. Further, observation error of brightness temperatures is also changed.

Currently, in the upper-air assimilation we use pressures from ground stations, radio soundings, aircraft observations AMDAR, MODE-S MRAR, MODE-S EHS, AMV and SEVIRI from Meteosat 11. The cycling is still 6 h for the time being. When going to the higher resolution and the non hydrostatic core, we examined the spin-up effect, which reduces compared to the previous version, see Fig. 2. We see as well that the spin-up is well away after 2 hours of integration, which opens the way to the planned 3 h cycling instead of 6 h.

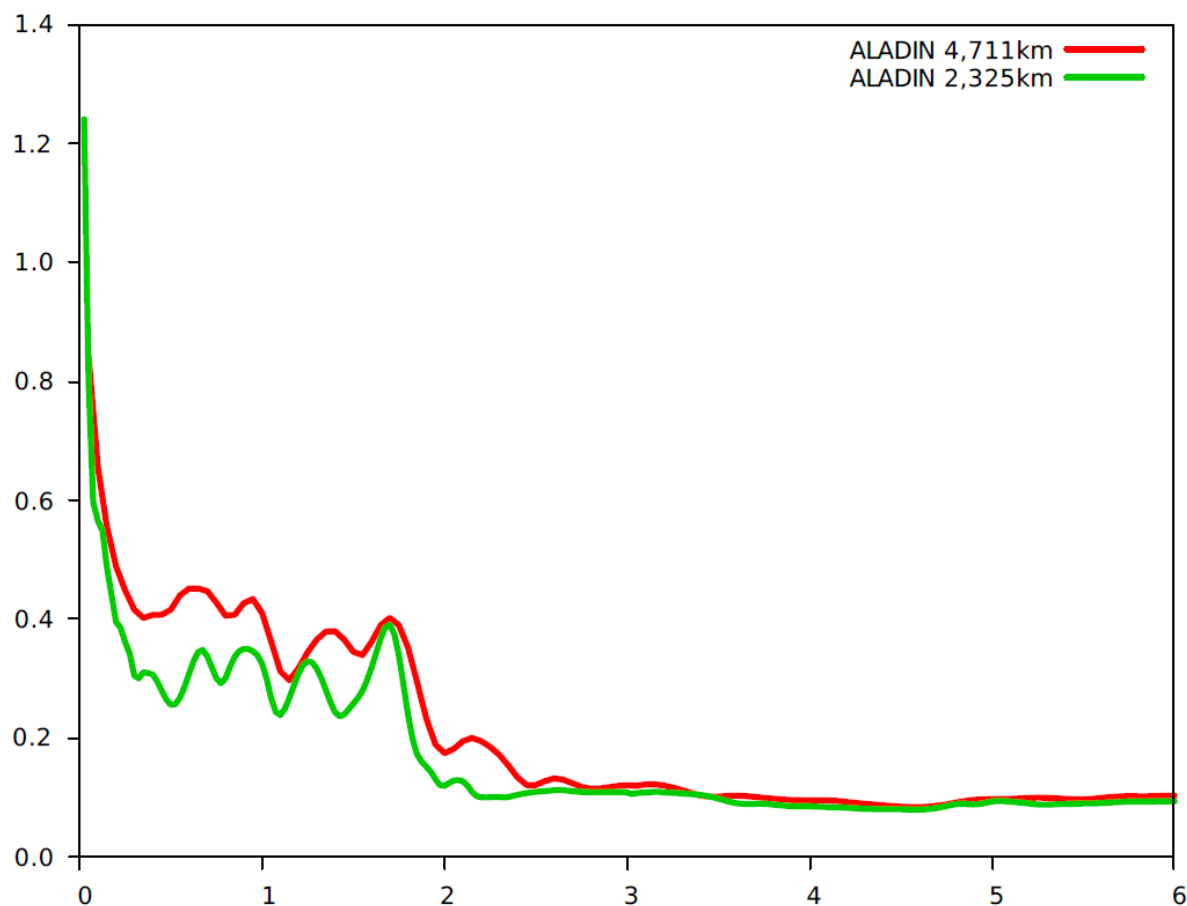


Figure 2: Domain mean quadratic tendency of surface pressure [hPa/h] in function of forecast length in hours (horizontal axis).

5 New products and results

As expected, the high resolution model version improves the scores, some of them quite significantly. This is true namely for the screen level parameters like wind, temperature and humidity. An example of 10 m wind better quality is shown on Fig. 3.

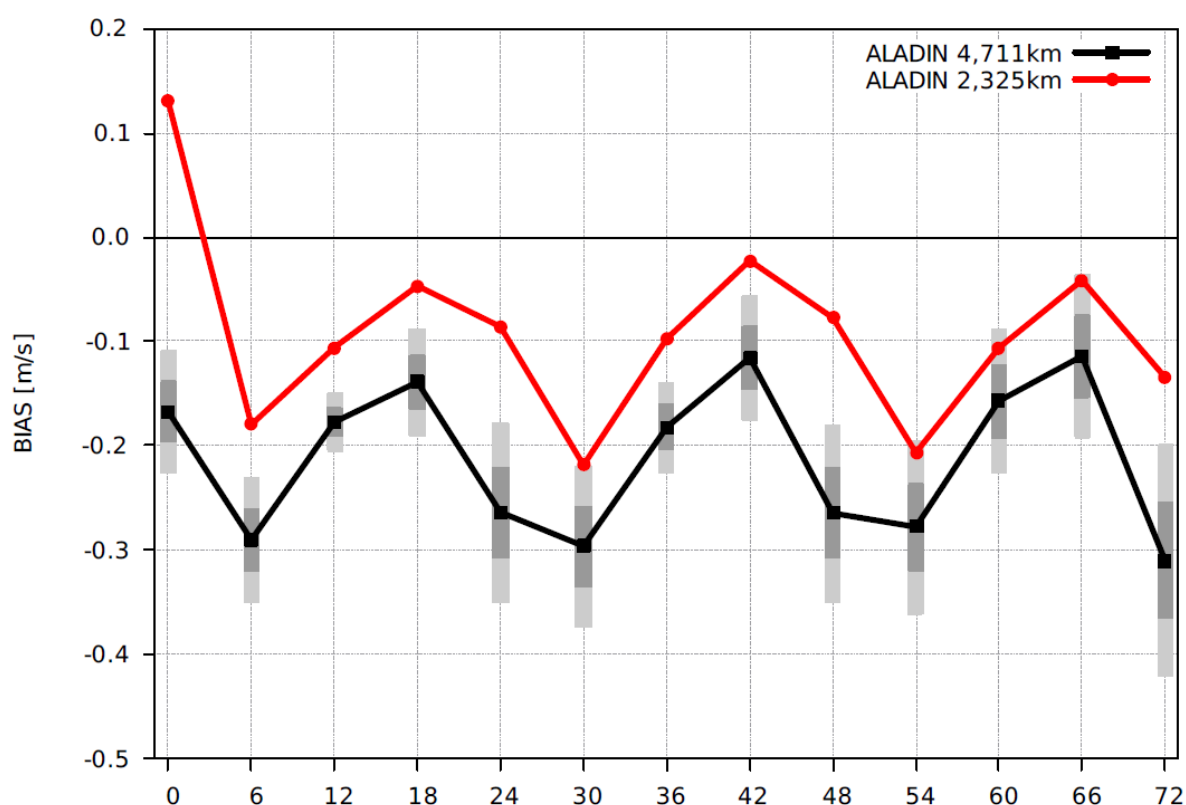


Figure 3: Bias of 10m wind (m/s), averaged from 0h UTC forecast over period 14/05-31/05/2018. Black line – reference, with confidence intervals of $\pm \sigma$ (app 68 %, dark bars) and $\pm 2 \sigma$ (app 95 %, light grey bars); red-line – new resolution.

Another nice result is that the model captures better summer convective events as well. This is demonstrated on the case of 20th May 2019, as shown on Fig.4, where the high resolution model simulates the small scale convective line crossing South Moravia and North Austria.

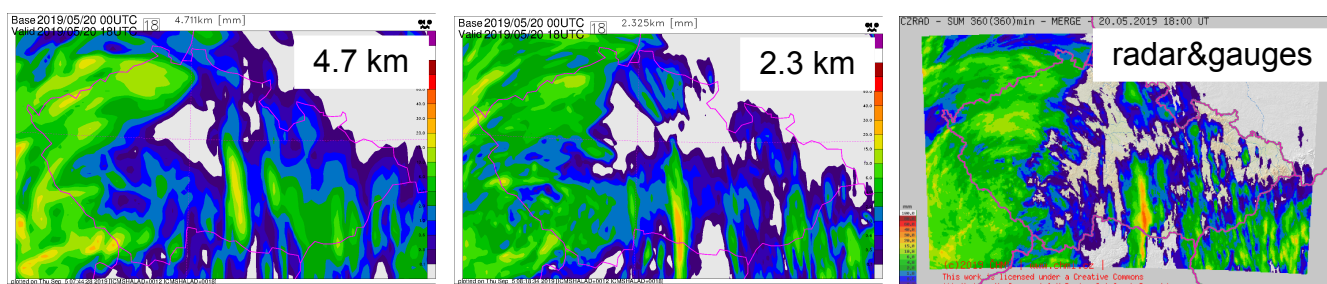


Figure 4: 6h precipitation sum forecast (from +12 h to +18 h) starting from the analysis at 0 h of 20 May 2019. Left: previous resolution run; middle: new high resolution run; right: verifying observations combining radar estimates and rain gauges.

We have profited from the high resolution version to introduce a couple of new products important for both general and the aviation forecasting. In the list we can mention the visibility, simulations of radars reflectivity, satellite brightness temperature, index of human being thermal comfort and so on. Fig. 5 shows the product of radars maximal reflectivity forecast compared to the OPERA product.

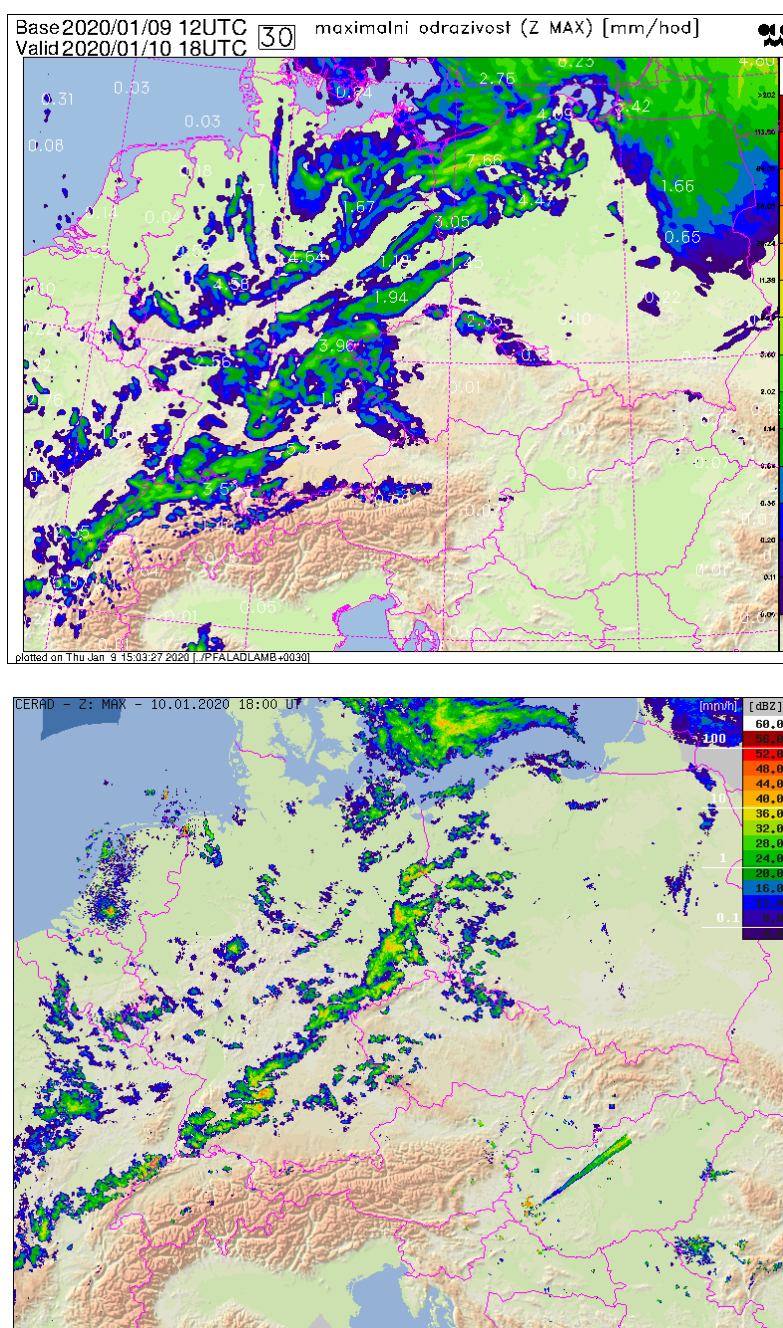


Figure 5: Radar reflectivity forecast at +30 h starting from the analysis at 12 h of 9 January 2020 (upper panel) compared to the observed reflectivity provided by the OPERA product completed by the radars in Salzburg and Vienna (lower panel).

Finally, we would like to acknowledge especially the help of Météo-France for providing us in advance the code to determine precipitation types. Like that we could prepare a patch available for the export cycle CY43T2bf10 to share it with ALADIN partners who have this library level installed. We also profited from the work done by Polish and Slovenian colleagues and their proposal for tuning graupel and hail thresholds in ALARO-1. Here below Fig. 6 shows the freezing rain forecast example.

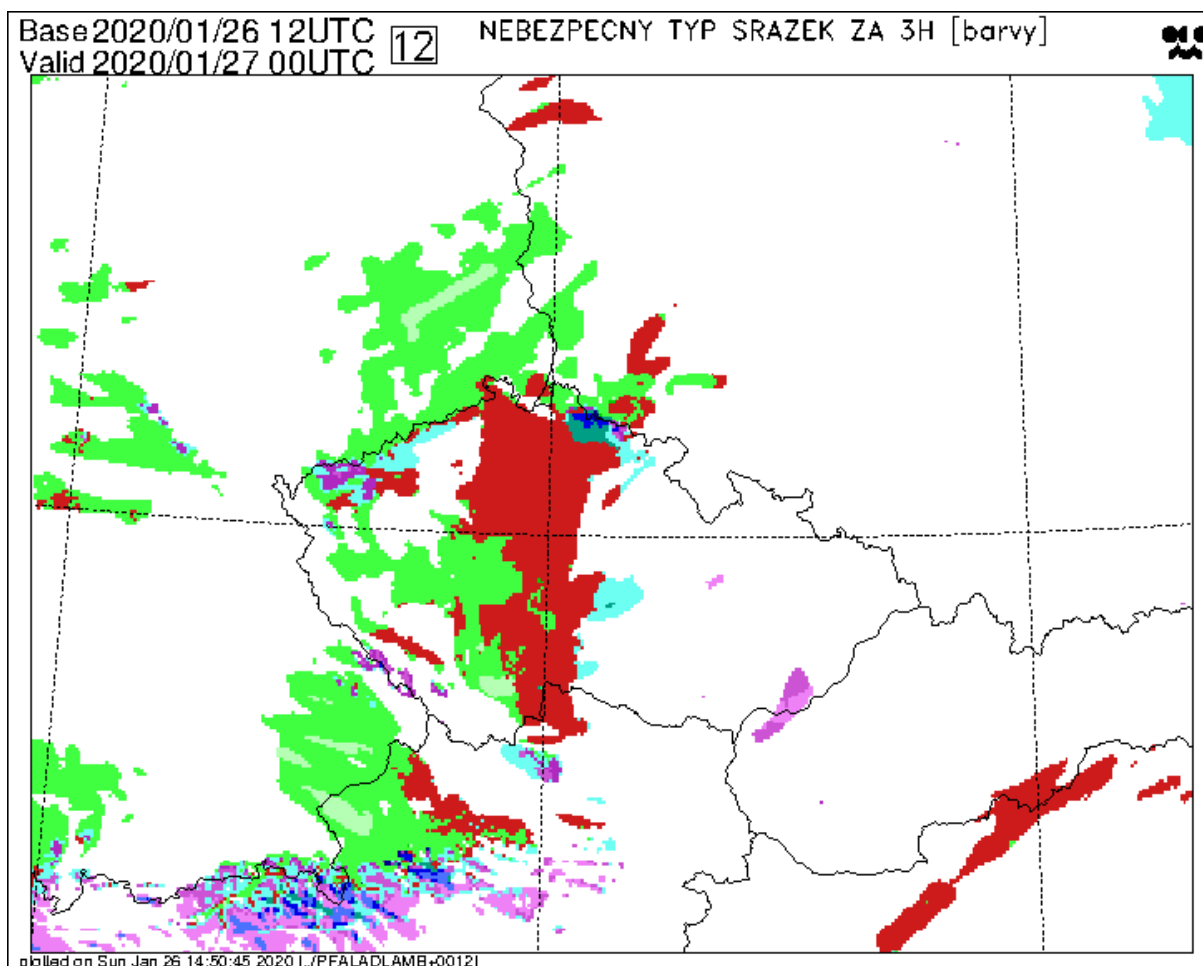


Figure 6: The most dangerous precipitation type occurrence over past three hours, forecast at +12 h starting from the analysis at 12 h of 26 January 2020. Red color denotes freezing rain.

6 References

Brožková, R., Bučánek, A., Mašek, J., Smolíková, P. a Trojáková, A., 2019: Nová provozní konfigurace modelu ALADIN ve vysokém rozlišení. Meteorologické zprávy, 72, 129-139.

Smolíková, P., 2019: Dynamical Parameters for the New Operational Application of the ALADIN System at CHMI Aiming to Use Nonhydrostatic Equations at a 2.325 km Horizontal Resolution. CHMI Technical Document TD000102.

NWP progress report 2019 from DMI

Bent Hansen Sass, Xiaohua Yang, Henrik Feddersen, Kristian Pagh Nielsen & DMI NWP team

1 Introduction

This summary of evolution in NWP systems at DMI is limited to provide first a very brief summary of the present Harmonie-Arome based systems at DMI, as available in 2019. Next the status of the DMI Harmonie ensemble prediction system is described. It has become possible to verify precipitation from ensembles using precipitation analyses. An example is shown to outline how probabilities from the ensemble may be used as guidance to forecasters. Moreover, a status is given on current developments at DMI regarding spatial verification of precipitation. A link is provided to the HARP based verification of precipitation. This enables easy monitoring of scores computed with HARP. Finally some ongoing research is mentioned regarding modified diagnostics of temperature and humidity in the stable planetary boundary layer. The new framework is under test in Harmonie-Arome. It shows significant impacts relative to the currently used diagnosis of temperature and humidity at the 2m level. Due to the links of these parameters to the current surface analysis the possible impact may also become significant in a surface assimilation framework. Work on these topics is expected to continue into 2020.

2 DMI progress on operational setups

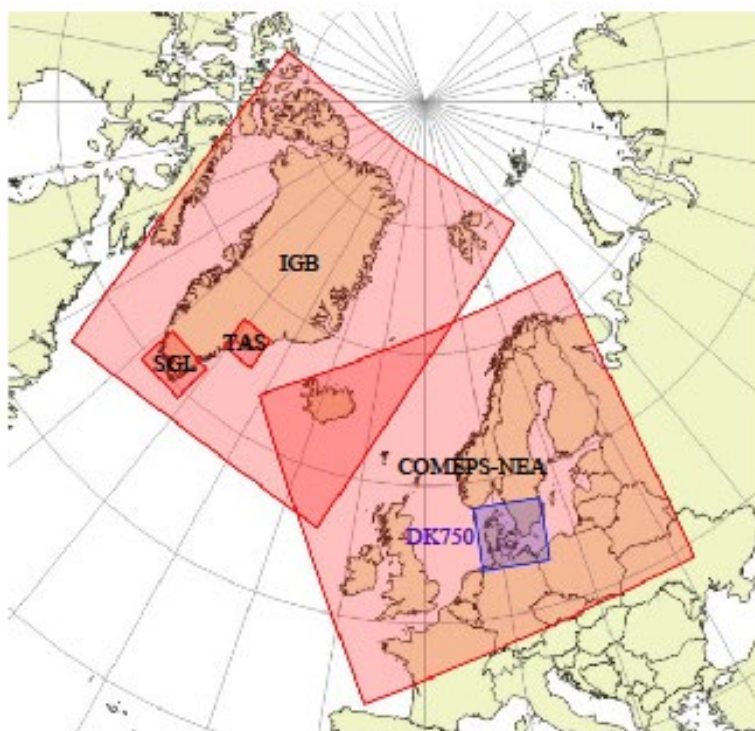


Figure 1: Operational model areas developed during 2019 at DMI. – IGB (1280*1080, 2.5km), COMECS-NEA (1200*1080, 2.5 km), SGL (600*480, 750m), TAS (400*400, 750m), DK750 (800*720, 750m)

The ensemble technique, high resolution and rapid updating nowcasting continue to be the focus areas in research and operational NWP activities at Danish Meteorological Institute. During the past year, DMI has upgraded its innovative, COntinuous Mesoscale Ensemble Prediction System (COMEPS) into Version 3, extending the hourly updating, 2.5 km resolution EPS system to an extensive forecast area so as to be merged with deterministic forecast system NEA. Progress has been made on the development of hectometric scale Harmonie-Arome. As a result two 750-m grid NWP setups were operationalized ('SGL' and 'TAS' in Figure 1), e.g. to address the major forecast challenge for storm situations in coastal Greenland. Routine verification shows that for some locations the sub-km grid resolution has a significant and positive impact. At 2.5 km resolution there is significant overprediction at a number of locations, i.e. many false alarms of near surface strong winds, in a number of weather situations where the sub-km implementations produce results in (much) better agreement with observations. The sub-km model still forecasts very high winds when they occur. Intensive efforts are ongoing with high resolution ensemble nowcasting which assimilates high resolution and high density observation data such as crowdsource data ('DK750' model covering Denmark).

3 COMECS related developments

COMECS is DMI's operational version of HarmonEPS. It has been operational since 2017; the latest major upgrade was in 2019 when the domain size was increased to that of NEA for all ensemble members. COMECS comprises three HarmonEPS systems that run independently of each other and contribute members to the COMECS ensemble. All three control runs run 3D-VAR data assimilation using 3-hourly cycling, but shifted one hour from each other. That is, new observations are assimilated every hour in overlapping data assimilation windows. In addition to the control runs three perturbed members are run every hour, and the perturbed members for the six latest runs are collected to form an 18+1 member ensemble, where 15 of 18 perturbed members are time-lagged, and the last, unperturbed member is the latest of the three control members. The initial and lateral boundary condition perturbations are based on the SLAF technique (Ebisuzaki and Kalnay, 1991) as implemented in HarmonEPS (Frogner et al., 2019). In addition, stochastic perturbations are applied to a number of surface variables, such as roughness, albedo, SST, soil temperature and soil moisture, and the perturbed members are run with different combinations of physics settings, including alternative turbulence and shallow convection schemes.

The advantages of a continuously updated ensemble system are, compared to the traditional update every six hours:

- assimilation of new data every hour;
- more even distribution of the computational load during the day;
- reduced forecast jumpiness;
- the time-lagging contributes to the ensemble spread which is traditionally smaller than that of a perfect ensemble.

The main disadvantage is obviously

- the use of time-lagged members whose quality a-priori is poorer than non-lagged members.

For probabilistic products one can argue that the members should be weighted according to their lag, but in COMECS all members are treated equally. In any case, the use of time-lagged members result in more book keeping.

Postprocessing of COMEPS includes calculation of upscaled precipitation probabilities based on neighbourhood methods and percentiles for a number of parameters such as precipitation, visibility, cloud base height and wind gust. Both upscaled probabilities and percentiles are used regularly by duty meteorologists at DMI. Figures 2 and 3 show an example of both upscaled probabilities of precipitation exceeding 15mm/3h (showing the fraction of members that exceeds the threshold somewhere in a 15 grid box (37.5km) radius around each grid point) and the 90th percentile for 6h accumulated rainfall (no upscaling) for the same convective situation. Both of the plots indicate where there is a risk of showers, and the hope is that the two types of plots can supplement each other.

In 2020 we expect to upgrade the Harmonie version of COMEPS to cy43h1.2, and COMEPS will be nested in IFSENS of ECMWF instead of using the SLAF perturbations.

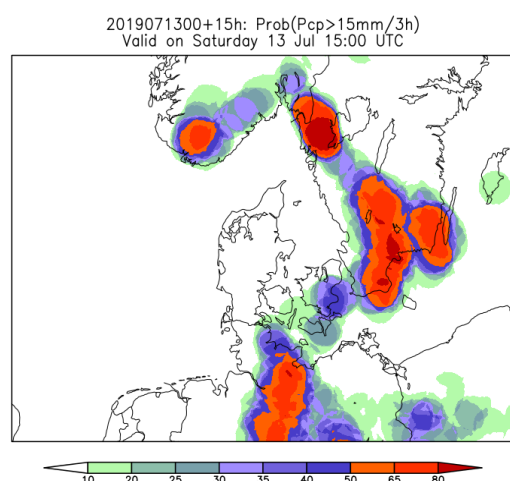


Figure 2: Upscaled probability map for precipitation exceeding 15 mm/3h rainfall

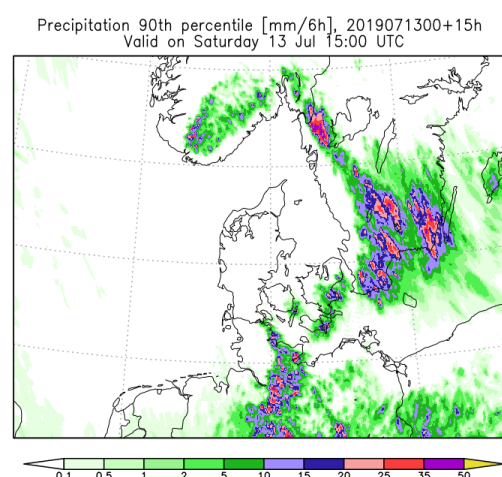


Figure 3: 90th percentile of 6h accumulated rainfall for the same convective situation as in Figure 2.

Spatial ensemble verification

The use of upscaled precipitation probabilities has made it more necessary to develop spatial verification methods for ensemble forecasts. A question that often arises, is at what (upscaled) probability level should a meteorologist take action and, e.g., issue a warning ?

Verification based on rain gauge observations are inadequate to answer that question. Instead we use a surface quantitative precipitation estimate (SQPE) based on radar reflectivities that are calibrated using rain gauge observations. By upscaling both probability forecasts and observations and varying the probability level we can calculate verification scores. For example, if we choose a probability level = 50% in Figure 2, we predict the event in the orange and red parts of plot, which we will then verify against our SQPE upscaled to the same scale. If we use a lower probability level, we will be more likely to predict the event and get more hits. But we will also get more false alarms. On the other hand, if we use a higher probability level, we will fail to forecast more events, but get less false alarms. So the challenge is to find a suitable balance between hits, misses and false alarms. A simple score that does that is the threat score which is simply the number of hits divided by the sum of hits, misses and false alarms.

As an example, Figure 4 shows the threat score as a function of probability level and upscaling neighbourhood size for a lead time of 15h for August 2019 in Denmark.

For low probability levels the threat score is dominated by many false alarms, while for high probability levels it is dominated by many misses. The best threat scores are obtained for probability levels between 20 and 30%. The scales indicated in Figure 4 are the length of a side in a square used in the spatial verification. For the two smallest scales there is practically no difference between the scores as they are both smaller than the size of one model grid box. The upscaling used to produce Figure 2 corresponds to the blue curve (scale=75km) in Figure 4. It should be noted that a verification period of only one month may not be sufficient to obtain robust results for 15mm/3h which is a relatively rare event, and that the threat score is chosen here as an example because of its simplicity, not because it is found to be the best score from which to choose an optimal probability level.

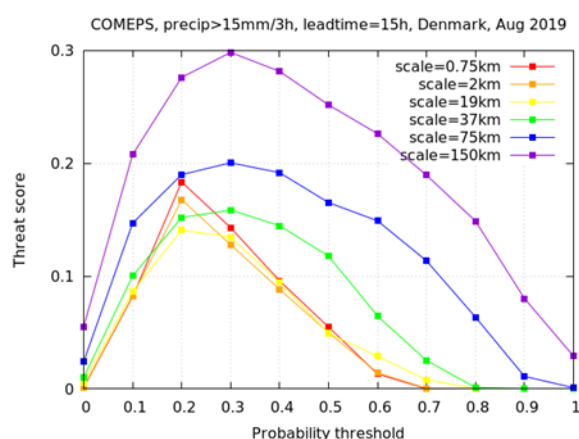


Figure 4: Threat score as function of probability threshold and neighborhood scale

4 Spatial verification of precipitation

Work has continued to make use of the HARP verification system (see QA1, QA2 in the HIRLAM-ALADIN Rolling Work plan). HARP spatial is now used for verifying precipitation over Denmark, thanks to the routine precipitation analysis product (SQPE) by the Radar group in DMI. Routine spatial results have been produced tentatively for verification of precipitation since July 2019. The results may be inspected at <https://shiny.hirlam.org/comepshf/spatial/>. The verification options will be upgraded further in the future.

Ideas are emerging at DMI with regard to some sort of version control for HARP developments. These ideas need to be discussed further in the community around HARP. It seems possible to set up a docker installation for HARP. The main ideas focus on the possibility to protect HARP-developments against externally changing R-libraries. This way forward could make installations easier.

Finally, the spatial scheme under development to verify the ability of a NWP model to forecast local extremes (Sass, 2019) has progressed further. It can operate on model input field(s) and analysis field(s). A publication is under preparation.

5 Developments of near surface diagnostics in the stable boundary layer

An alternative diagnosis of 2m temperature and humidity in the stable boundary layer is being tested for use in the SURFEX part of the Harmonie-Arome model system. The new formulation is based on Nielsen (2017) which is documenting a new iterative method for calculating turbulent surface fluxes in the stable boundary layer. However, the framework may be used to diagnose temperature and humidity near the surface, e.g. at 2m. The framework is developed in combination with a proposal of Zilitinkevich et al. (2013) and experimental results of Beljaars and Holtslag (1991)

In several situations where currently used diagnostics of 2m temperature show a significantly negative bias the new scheme provides results in better agreement with corresponding observations. More studies to confirm the statistical significance of the preliminary results are planned for 2020. Continued studies seem relevant for another reason since the scheme provides a framework for modifying surface fluxes. This in turn may affect the structure of the stable boundary layer. The contact point at DMI for tests and further studies is Kristian P. Nielsen (kpn@dm.dk).

6 References

- Beljaars, A.C.M., and A.A.M Holtslag, 1991: Flux parameterizations over land surfaces for atmospheric models. *J. Appl. Meteorol.* **30**, 327-341.
- Ebisuzaki, W., and E. Kalnay, 1991: Ensemble experiments with a new lagged average forecasting scheme. *WMO Research Activities in Atmospheric and Oceanic Modeling*, **15**, 308 pp.
- Frogner, I., U. Andrae, J. Bojarova, A. Callado, P. Escribà, H. Feddersen, A. Hally, J. Kauhanen, R. Randriamampianina, A. Singleton, G. Smet, S. van der Veen, and O. Vignes, 2019: HarmonEPS—The HARMONIE Ensemble Prediction System. *Wea. Forecasting*, **34**, 1909–1937, <https://doi.org/10.1175/WAF-D-19-0030.1>
- Nielsen, N. Woetmann, 2017: Turbulent surface fluxes in the stably stratified atmospheric boundary layer obtained by an analytic solution of a cubic equation involving a bulk Richardson number. *DMI Rapport No. 17-24*, <https://www.dmi.dk/publikationer>
- Sass, B. Hansen, 2019: SLX Verification Scheme, *ALADIN-HIRLAM Newsletter, NL13*, Aug. 2019, 37-40.
- Zilitinkevich, S.S., T. Elperin, N. Kleerorin, I. Roga chevskii, and I Esau, 2013: A Hierarchy of Energy- and Flux-Budget (EFB) Turbulence Closure Models for Stably-Stratified Geophysical Flows. *Boundary-Layer Meteorol.*, **146**, 341-373. DOI 10.1007/s10546-012-9768-8

Selected NWP-related research at FMI

Carl Fortelius*, Bin Cheng, Erik Gregow, Ekaterina Kurzeneva, Laura Rontu, and David Schönach

1 Introduction

This report summarizes some of the research and development related to NWP and the ALADIN-HIRLAM system involving FMI scientists during 2019. Our main operational implementation of the HARMONIE-AROME system, i.e. the MetCoOp ensemble system MEPS is described elsewhere in this issue.

2 Nowcasting developments for MetCoOp-Nowcasting (MNWC) Erik Gregow and David Schönach

2.1 MetCoOp-Nowcasting (MNWC) pre-operational model setup at FMI

The MetCoOp HARMONIE-AROME Nowcasting is running at FMI supercomputer in a pre-operational manner (MNWC-preop; branches/MetCoOp/harmonNWC-40h1.2_preop). The first-guess information (both surface and upper-air) are coming from MEPS-control member, but there is a plan to use cycled input from MNWC-preop itself. MNWC-preop produce 3D-output of 15-minute interval in Grib2 format and surface files in Grib1. A separate stream of fast delivered GNSS data are used, at this stage only from Sweden.

2.2 MNWC development: MSG cloud-ingest

The cloud ingest method is implemented in the MNWC-preop suite, which modifies the initial-state of the humidity and the 3D cloud-structures (developments based on Van der Veen, 2013). An update to the method combines the NWCSAF cloud information with Synop observations and a first-guess field from MEPS (control run), in order to create a better cloud-base estimate. Here we make use of GridPP-system to interpolate the observed cloud-base information from Synop to correct the first-guess cloud-base field from MEPS.

Apart from correcting the cloud information, this method also give an impact to the precipitation. For example, correct placement of convective precipitation is being initialized (Figure 1; see south Finland) but, on the other hand, there are cases with over-prediction of precipitation (Figure 2; see south Finland).

There is a need to fine tune the cloud ingest method, taking into account the variability of humidity at different vertical layers. To address this problem, planned developments include a better technique how to detect cloud-layers within the 3D-column, and by that, dampen the false triggering of precipitation and reduce the moisture bias (as seen in verification, not shown here).

*Corresponding author carl.fortelius@fmi.fi

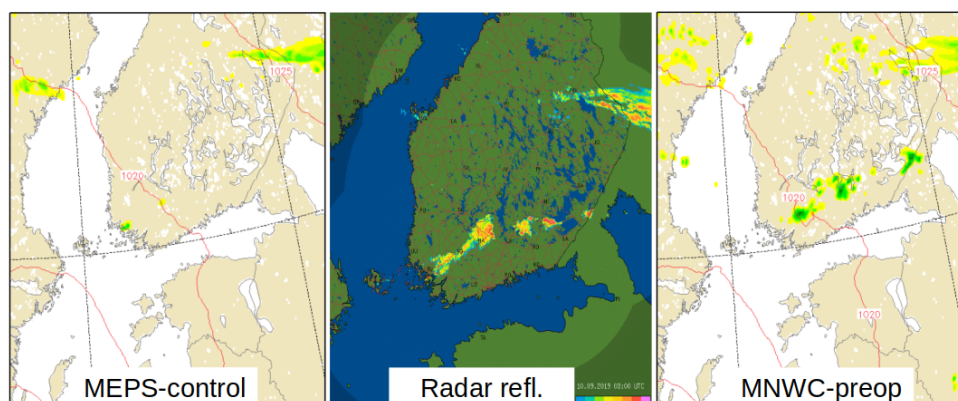


Figure 1: Comparison between MEPS control run (left), MNWC-preop (right) and the radar reflectivity (middle). Forecast initial time: 10 September 2019 at 00Z, valid time 03Z (+3h fc.)

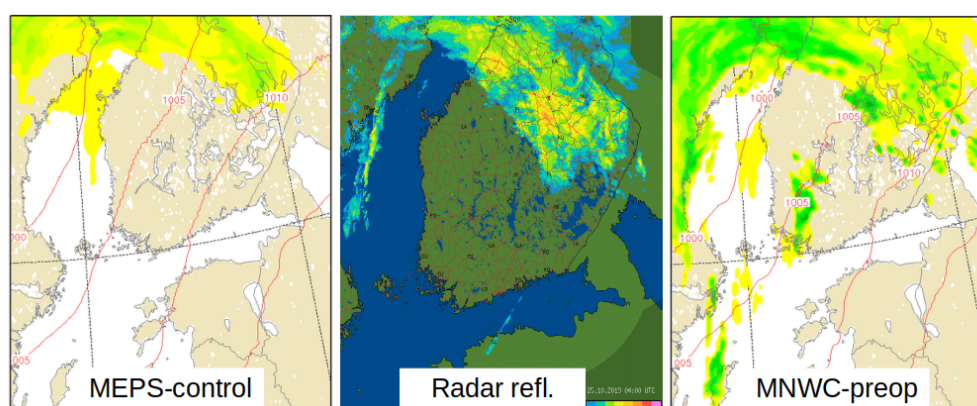


Figure 2: Comparison between MEPS control run (left), MNWC-preop (right) and the radar reflectivity (middle). Forecast initial time: 25 September 2019 at 00Z, valid time 04Z (+4h fc.)

2.3 MNWC development: Atmospheric Motion Vectors (AMV)

The AMV are derived from satellites by tracking clouds or water vapor features in consecutive satellite images (Hautecoeur and Borde, 2017). The AMV developments from AROME-Arctic branch (see report by Randriamampianina, 2017) have been merged to MNWC code version. Three different AMVs have been used for experimental runs; Polar orbiting (Metop-A/B/C), geostationary (MSG) satellites (both products from EUMETSAT) and NWCSAF High-Resolution Wind product, which itself is based on MSG measurements. The data is derived from FMI's satellite department, where the NWCSAF data is produced locally using own software.

The combination of polar-orbiting and geostationary satellites is potentially very beneficial for the MetCoOp domain, which currently reaches as far as 74.1°N, because their geographical coverage complete each other. See Figure 3, where an example date of the locations of AMVs is plotted for the Metop-C and the MSG satellite. The verification score shows neutral impact for a two week period, with no changes at the surface and indifferent changes in the vertical profiles of wind-speed and wind-direction (Figure 4). The AMV development is going to be implemented into the MNWC-preop in near future.

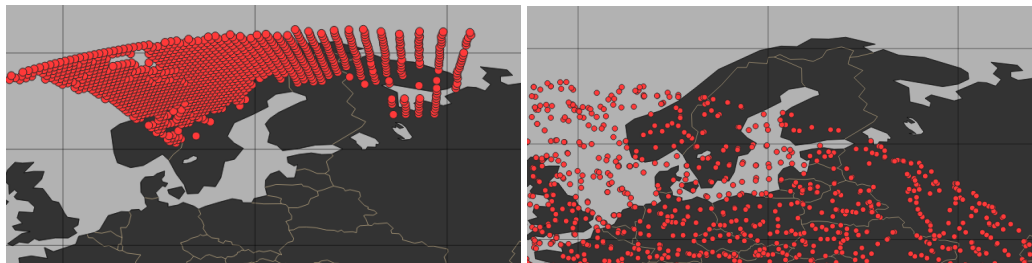


Figure 3: Locations of AMVs of polar-orbiting Metop-C (left) and geostationary MSG (right) satellite for date: 20190715, 19Z.

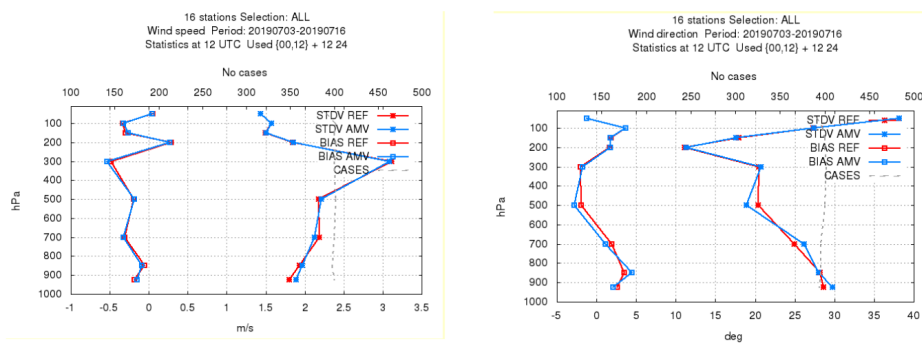


Figure 4: Standard verification of AMV experiment (AMV) vs. reference exp. (REF) for profiles of windspeed and winddirection for period: 20190703 - 20190716.

3 On mapping of lakes and verification of lake parametrization in NWP

Ekaterina Kurzeneva

Separation between inland and ocean water on physiography maps used in NWP remains a serious problem. For example, many efforts were needed in ECOCLIMAP SG land cover map developments (ECOCLIMAP, 2019) to separate between inland and ocean water on the basic land cover map of ESA CCI (<https://www.esa-landcover-cci.org/>). An accurate separation is important in NWP, to avoid extrapolation of the sea surface temperature deep into the continent in the case of miss-classification of e. g. river and sea water. A novel algorithm to separate between inland and ocean water on the gridded map was proposed, implemented in the ECMWF numerical forecasting system IFS, and described in the paper by Choulga et al., 2019. As a first step, this algorithm uses the flood-filling algorithm, described e. g. in the IFS documentation (ECMWF, 2017). It separates oceans from lakes, however yet allows deep penetration of ocean water the into land through river estuaries on high (1 km or less) resolution maps. The new algorithm allows to separate narrow rivers or bays from large water bodies. This algorithm is based on physical and geographical rather than geometrical features and contains 2 parameters which should be defined beforehand by relying on expert opinion. These are the window width W and the number of iterations L . These parameters are regionally and grid dependent. The algorithm is illustrated by Fig.5. On the figure, $W=1$ and $L=2$.

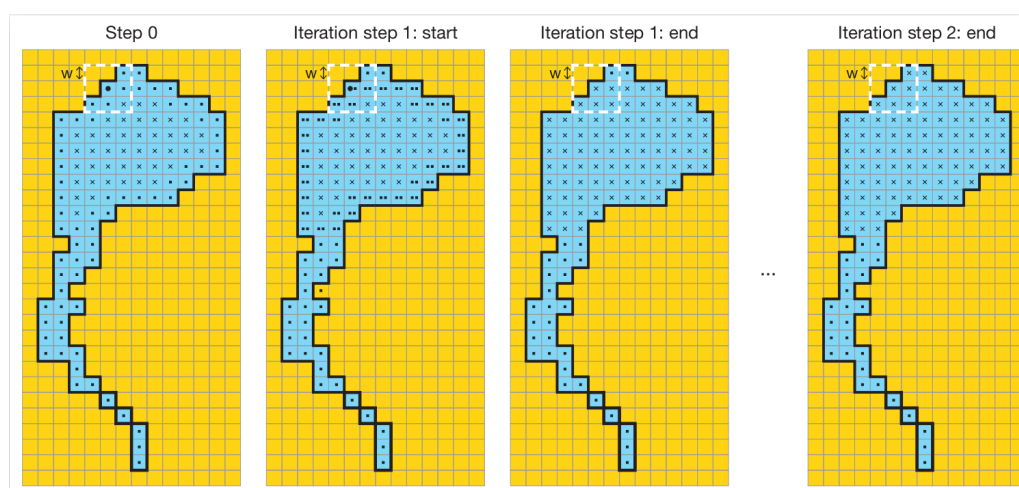


Figure 5: Steps of the pixel-by-pixel water separation algorithm. W window width, \cdot — water grid box has not only water points in its checking window; x — water grid box has only water points in its checking window; $\cdot\cdot$ — water grid box has at least one x in its checking window; yellow colour indicates land, and blue indicates water.

Step 0 of the algorithm starts by working from the results of the basic flood-filling algorithm. In this case the basic flood-filling algorithm should be applied so that it creates an individual water body mask. Step 0 is shown in Fig. 1, left plot. At Step 0, each water pixel is marked with x if all pixels within the moving window of the W width are water, or if at least one pixel in this window is non-water. Next starts the iteration phase that will be repeated L times. At the beginning of each iteration, pixels with \cdot are checked again with the moving window of the W width if around the pixel in question there is at least one x pixel, it is marked with a dot (\cdot); see Fig. 1, second from left plot. At the end of each iteration all \cdot pixels are changed into x and the next iteration starts if required; see Fig. 1, third from left plot. At the end of the iteration phase the considered water body will be divided into several ones; see Fig. 1, right plot x pixels will mark the main part of the water body and \cdot pixels will mark the narrow rivers or bays. This algorithm was applied in Choluga et al. (2019) to separate automatically large rivers from the ocean to stop deep penetration of the ocean into the land on the 1 km resolution land cover map. This algorithm may be applied in the future, for example, for increasing the

resolution of the global lake database (Choluga et al., 2014) or for corrections of ECOCLIMAP SG, if needed. The study by Choluga et al. (2019) contains also interesting findings concerning a verification of the lake parameterization within NWP. In this study, the lake model FLake (Mironov, 2008), which is used to parameterize lakes in many NWP and climate models, was run offline with the forcing from ERA5 (C3S, 2017), for the period of 5 years (2010-2014). Modelling results were compared with lake water surface temperature and ice observations over 27 lakes in Finland, collected by Finnish Environmental Institute. Verification results were dependent on seasons of lake mixing, namely (i) spring mixing, (ii) autumn mixing, and (iii) summer stratified periods. Seasonal verification allowed to understand better the sources of different errors. For example, it allowed to find a cold bias in autumn over Finland in ERA5 forcing data.

4 Six years of operational FLake in HIRLAM NWP model

Laura Rontu

In the study by (Rontu et al., 2019a), *in-situ* lake observations from the Finnish Environment Institute were used for validation of the HIRLAM NWP model, which is applied operationally in the Finnish Meteorological Institute. HIRLAM contains Freshwater Lake prognostic parametrizations and an independent objective analysis of lake surface state. We focused on comparison of observed and forecast lake surface water temperature, ice thickness and snow depth in the years 2012 - 2018. Because the HIRLAM system was unmodified during this period, a long uniform dataset was available for evaluation of the performance of FLake integrated into an operational NWP model. On the other hand, no conclusions about the impact of the lake surface state on the operational forecast of the near-surface temperatures, cloudiness or precipitation can be drawn because of the lack of alternative forecasts (without FLake) for comparison.

Forecast freeze-up dates were found to correspond the observations well, typically within a week. The forecast ice thickness tended to be overestimated, still the break-up dates over most of the lakes occurred systematically several weeks too early. Practically no forecast snow was found on the lake ice, although the snow parametrization by FLake was included in HIRLAM. The reason for the incorrect behaviour was related to a too large critical value to diagnose snow existence that prevented the accumulation of snow on lake ice. It can be concluded that a realistic parametrization of snow on lake ice is important in order to describe correctly the lake surface state in spring.

Validation of lake surface state within the MetCoOp operational HARMONIE-AROME is only starting. First findings show that there is snow on lakes, but we do not yet know how realistic the snow cover is and what might be the impact of lakes on the winter-time weather forecast by the model.

5 Renewing aerosol radiative transfer in ALADIN-HIRLAM

Laura Rontu

Aerosol impact on SW radiation flux and near-surface temperature was studied in three-dimensional climate and NWP model simulations (Rontu et al., 2019b) that applied the default IFSRADIO and a version of ACRANEB for the radiation parametrizations. It was shown that the update of the input aerosol climatology from the default Tegen AOD550 to simplified CAMS-based AOD550 did not lead to significant changes in the climate simulations. Near-real-time CAMS aerosol concentration was introduced in a Saharan dust case study. Desert dust mass extinction coefficient at 550 nm was used to convert the mass mixing ratio to AOD550. The prescribed wavelength-dependencies for AOD, SSA and ASY were retained and the default IFSRADIO used for the radiation calculations. In this case of large mineral dust load the results showed good correspondence with local temperature and radiation observations in spite of the simplified treatment of the aerosol optical properties (Figure 6).

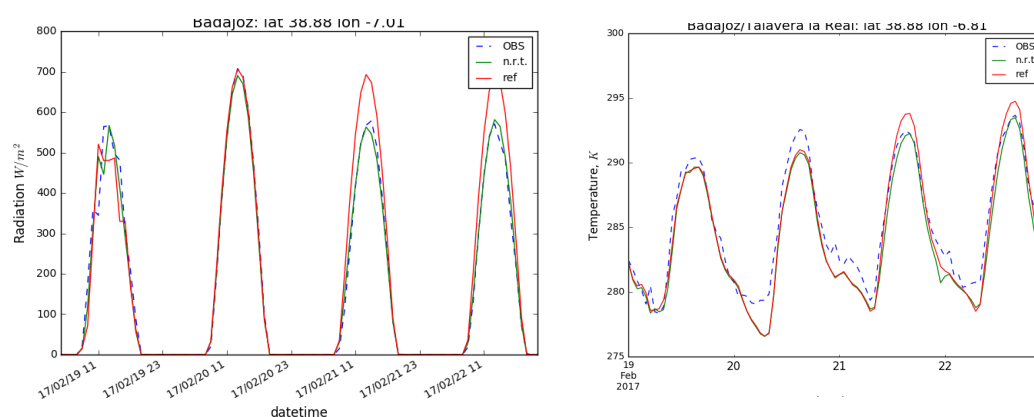


Figure 6: One-hour average global radiation (Wm^{-2}) for Badajoz station from 19th until 22nd of February: the reference experiment (red), CAMSNRT experiment (green) and observations (dashed blue) (left Figure) and the screen-level temperature at the automatic station Talavera la Real, Badajoz (right).

The next step in renewal of the HARMONIE-AROME aerosol radiative transfer parametrizations will be the combination of the up-to date data on aerosol concentration based on CAMS reanalysis, or near-real time data, to the new aerosol inherent optical properties. Humidity available during the NWP model run can be used to obtain the optical properties AOD, SSA and ASY for the aerosol mixture in the model's three-dimensional grid. These are meant for use as input to any radiation scheme available in ALADIN-HIRLAM system. At the first step, we will introduce them to HLRADIA, the simplest radiation scheme available in this framework, using the approach originally prepared for Enviro-HIRLAM (Baklanov et al. , 2017a). We will test the impact of the update within MUSC, the single-column version of ALADIN-HIRLAM system.

6 Observations of snow and ice in the Arctic Ocean and Arctic lake for NWP model assimilation and validation

Bin Cheng

In order to improve numerical weather predication (NWP) models performance in the Polar regions, snow and ice data are vitally important for a) NWP models validation; b) for better understand snow and ice physical processes within the NWP models and c) assimilation of snow and ice data in NWP models.

SIMBA is a thermistor string-based ice mass balance (IMB) buoy (SIMBA-IMB, Jackson et al., 2013). It measures high-resolution (2cm) vertical environment temperature (SIMBA-ET) profiles (4 times a day) through the air-snow-ice-water column. In addition, SIMBA measures the heating temperature (SIMBA-HT) applying a small identical heating element on each sensor. The heating interval usually lasts for 60 s and 120 s. The temperature data is used to derive snow depth and ice thickness. SIMBA uses GPS module to measure positions. The Iridium satellite is used for data transmission. The SIMBA data products are: air temperature; snow/ice temperature; ocean/lake temperature below ice bottom; Snow depth and ice thickness derived from temperature measurements. the SIMBA-IMB has a lower cost, allowing deployment in large numbers, e.g., across the Arctic Ocean. This reduces the risk of failure of an observation campaign (Thompson et al., 2019). SIMBA data have been used for snow depth and ice thickness monitoring and energy balance studies in seasonally ice-covered lakes and seas, as well as in polar oceans (Cheng et al. (2014); Hoppmann et al (2015); Provost et al. (2017); Lei et al. (2012)).

6.1 SIMBA in the Arctic Ocean

A total 15 SIMBA buoys have been deployed in the Arctic Ocean during the Chinese National Arctic Research Expedition (CHINARE) 2018 and the Nansen and Amundsen Basins Observational System (NABOS) 2018 field expeditions in late autumn. In 2019 several field campaigns, i.e. CAATEX and MOSAiC have been carried out and a large number of SIMBA buoys have been deployed in the ice field. Figure 7 shows the drift trajectories of those SIMBA buoys.

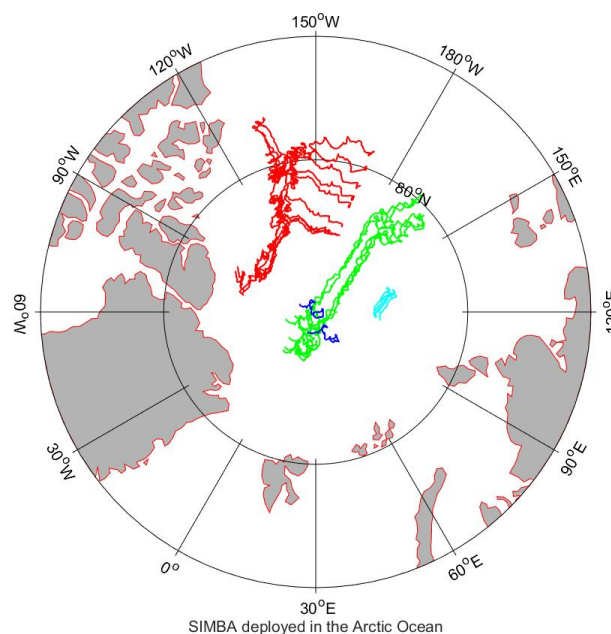


Figure 7: The drift trajectories (until 8, November 2019) for selected 22 SIMBA buoys deployed in the Arctic Ocean in the past two years via several international field campaigns: CHINARE2018 (red); NABOS2018 (green); CAATEX2019 (blue) and MOSAiC2019 (light blue). Most of the SIMBA buoys are still working.

Retrieval snow depth and lake ice thickness from SIMBA data was a manual process (Cheng et al., 2014). A SIMBA-algorithm was developed by Liao et al (2018) and used to extract snow depth and ice thickness from SIMBA-ET data. The algorithm was targeted for SIMBA data obtained from Arctic Ocean where the snow/ice interface remained unchanged. Figure 8 gives one SIMBA example result. The algorithm works well in cold condition but becomes less reliable in warmer conditions where the vertical temperature gradient is reduced.

6.2 SIMBA in the Arctic lake

FMI deployed SIMBA buoy in an Arctic lake (Fig. 9) for the past 10 winter seasons.

Lake ice is thinner than the Arctic perennial ice. Snow layer may actively contribute to ice thickness via snow-ice and superimposed ice formation. As a result, the snow-ice interface is a moving boundary. The SIMBA algorithm (Liao et al, 2018) must be adapted in order to detect snow depth and ice thickness with a moving snow/ice interface. A new SIMBA algorithm designed to retrieve snow depth and ice thickness for lake condition is developed. The SIMBA-ET and SIMBA-HT are both applied. The first- and second-order spatial derivatives (FOD/SOD) of SIMBA-ET, i.e. temperature changes, in 2 cm fixed distance were calculated to identify the air/snow, snow/ice and ice/water interfaces. A manuscript (Cheng et al, 2020) has been submitted to *Annals of Glaciology* (AoG). Figure 10 gives one example of lake SIMBA temperature field and its derived snow depth and ice thickness.

In order to assess the reliability of snow/ice interface detection, we retrieved snow depth and ice thickness from SIMBA ET measurements in 2011/2012, when the snow depth and ice thickness were manually observed biweekly. The SIMBA observations and manual data analyses for winter 2011/2012 was discussed in (Cheng et al., 2014). The interfaces and thicknesses detected by manual analyses and by the method presented in this study are shown in Figure 11. The results based on the two methods are in good agreement, especially the upward motion of snow/ice interface. This indicated that the analyses method described in this study is capable to derived snow and ice thickness in boreal lake from SIMBA measurement where a moving snow/ice interface was evident.

We are processing SIMBA data for both Arctic Ocean and Arctic lake deployment. The temperature data are valuable for NWP model validation. Challenges remain for making the reliable snow depth and ice thickness in warm conditions. During the melting season (AugustSeptember in the Arctic), the in-ice temperature gradient at the ice base may be too small due to the impact of brine channels creating a skeleton layer leading to an underestimation of the total ice thickness.

After quality control, the SIMBA buoy data will be available for ALADIN-HIRLAM community for NWP model validation, process studies and data assimilation.

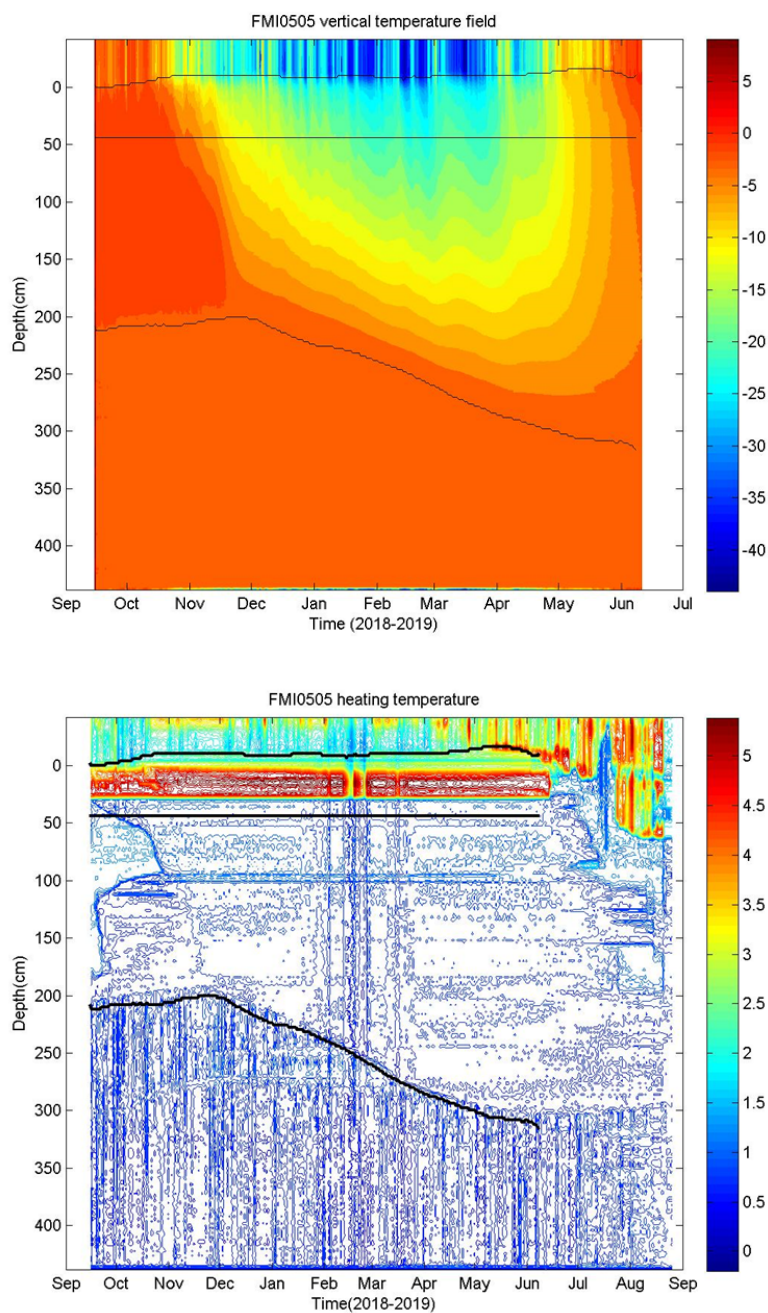


Figure 8: a) SIMBA temperature field. The black lines are snow surface (top), Initial freeboard (middle) and ice bottom (bottom). Zero level refers to initial snow/ice interface. b) SIMBA heating temperature field. The black lines in b) were derived by SIMBA algorithm. This SIMBA buoy (FMI0505) was deployed during NOBAS2018.

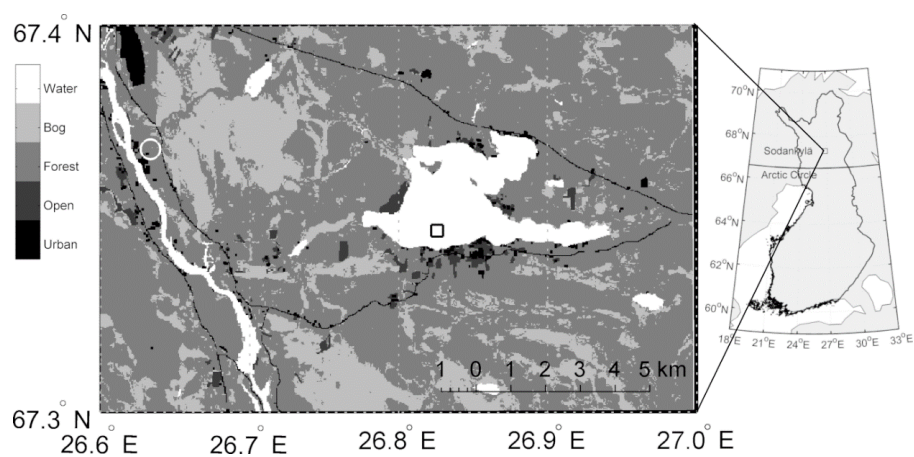


Figure 9: Map of Lake Orajärvi, where the black square marks the SIMBA site, where the water depth was 5.2 m and the white circle marks the Sodankylä weather station, 10 km east from the lake, at the Finnish Meteorological Institute (FMI) Arctic Space Centre (<http://fmiaarc.fmi.fi/>) (ARC) 120 km north of the Arctic Circle.

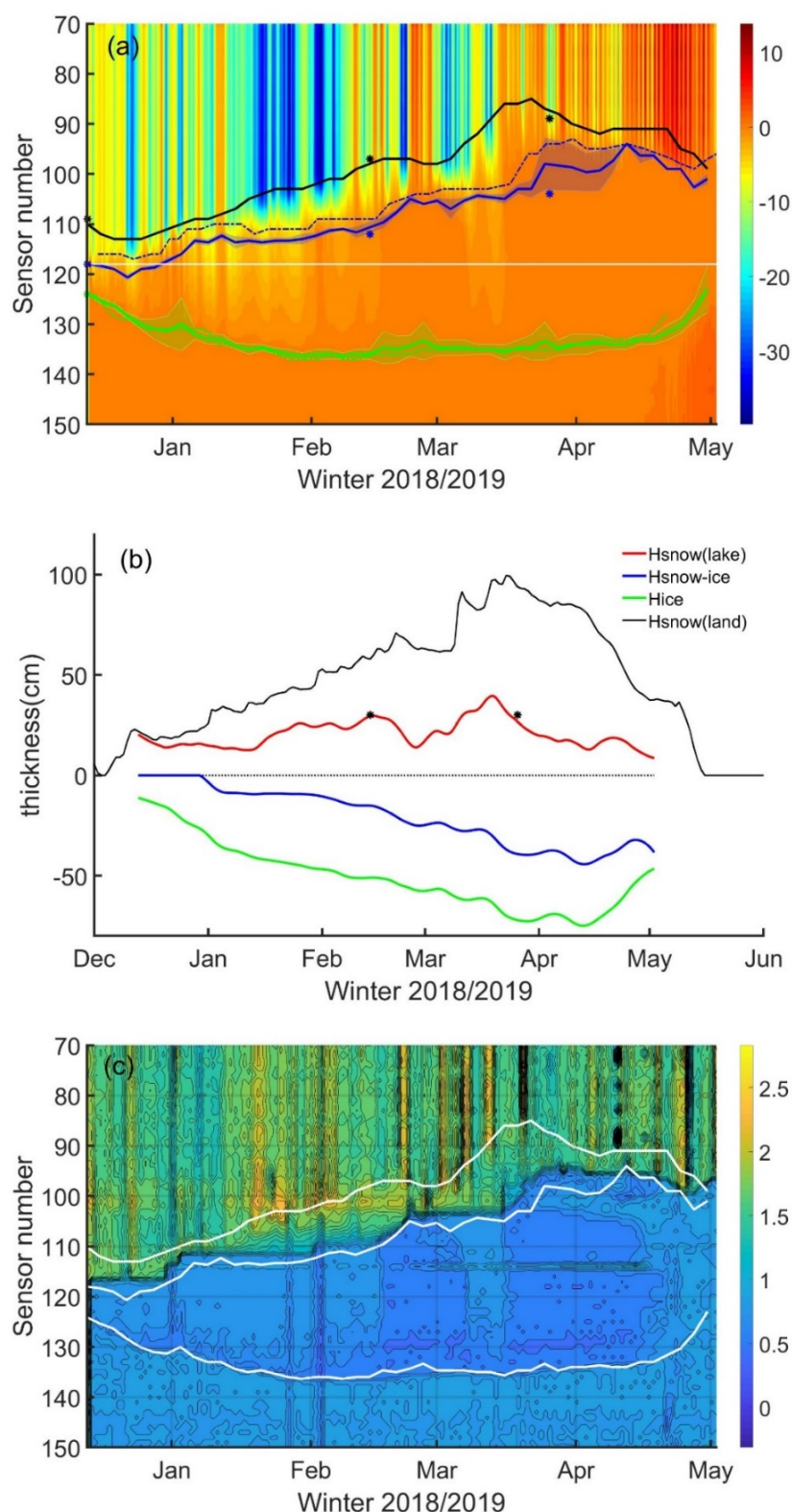


Figure 10: a) Evolution of air/snow (black), snow/ice (blue) and ice/water (green) interfaces identified from SIMBA-ET. The dashed black line is the interface obtained from SIMBA-HT field. The asterisks (*) represent sensor positions for snow and ice surface when SIMBA was deployed and for ice surface when SIMBA was recovered. The background contour plot is the SIMBA-ET temperature field measured between sensors 70 and 150. The white line was the original snow/ice interface. b) Time series of snow depth, snow-ice and total ice thickness using snow/ice interface as the zero-reference level. The black line marks the snow depth on land. c) Time series of SIMBA-HT field recorded after 60 s heating. The white lines are interfaces derived from SIMBA-ET field.

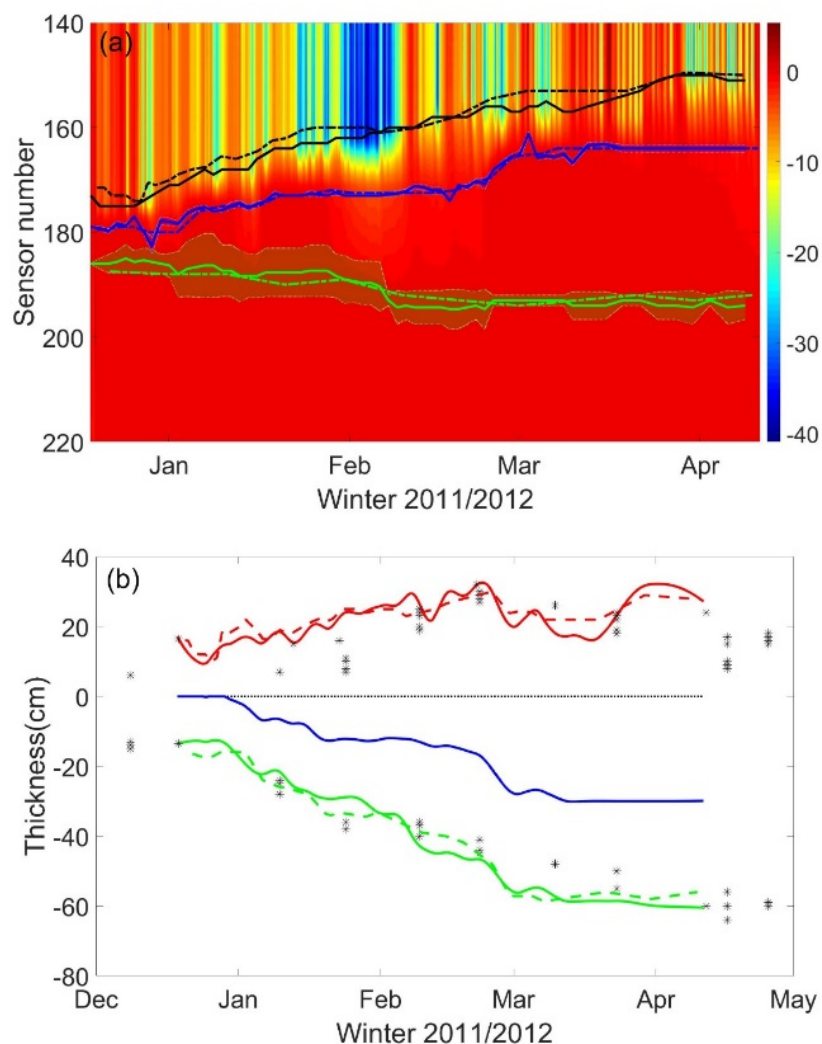


Figure 11: a) SIMBA ET temperature field for 2011/2012 ice season. The evolution of snow surface, snow/ice interface and ice bottom are marked as black, blue and green lines. The solid lines are obtained from this study and dashed lines are manual analyses. b) SIMBA ET derived snow (red), snow-ice (blue) and total ice thickness (green). The snow/ice interface is used as zero reference level. The symbols are in situ snow and ice thickness measurements in the lake. The solid lines are obtained from this study and dashed lines are identified manually.

References

- Baklanov, A., D. Brunner, G. Carmichael, J. Flemming, S. Freitas, / M. Gauss, Ø. Hov, R. Mathur, K.H. Schlünzen, C. Seigneur, and B. Vogel, 2017: Key Issues for Seamless Integrated Chemistry Meteorology Modeling. *Bull. Amer. Meteor. Soc.*, 98, 22852292, <https://doi.org/10.1175/BAMS-D-15-00166.1>
- Cheng, B., T. Vihma, L. Rontu, A. Kontu, H.K. Pour, C. Duguay and J. Pulliainen (2014) Evolution of snow and ice temperature, thickness and energy balance in Lake Orajärvi, northern Finland. *Tellus A: Dynamic Meteorology and Oceanography*, 66(1): 21564.
- Cheng, Y and others, (2020) Snow/ice interface detection from high-resolution vertical temperature profiles measured by ice mass-balance buoys on an Arctic lake. Submitted to AoG.
- Choulga, M., E. Kourzeneva, G. Balsamo, S. Boussetta, and N. Wedi, 2019: Upgraded global mapping information for earth system modelling: an application to surface water depth at the ECMWF, *Hydrol. Earth Syst. Sci.*, 23, 40514076, <https://doi.org/10.5194/hess-23-4051-2019>
- Choulga, M., E. Kourzeneva, E. Zakharova and A. Doganovsky, 2014: Estimation of the mean depth of boreal lakes for use in numerical weather prediction and climate modeling. *Tellus A* 2014, 66, 21295, <http://dx.doi.org/10.3402/tellusa.v66.21295>
- C3S (Copernicus Climate Change Service), 2017: ERA5: Fifth generation of ECMWF atmospheric reanalyses of the global climate, Copernicus Climate Change Service Climate Data Store (CDS), available at: <https://cds.climate.copernicus.eu/cdsapp#!/home> (last access: 23 September 2019)
- ECMWF, 2017: IFS Documentation: CY43R3 Part IV: Physical processes, ECMWF, 4, available at: <https://www.ecmwf.int/node/17736> (last access: 23 September 2019), 2017
- ECOCLIMAP 2019: ECOCLIMAP-SG: technical documentation. Available from https://opensource.umr-cnrm.fr/attachments/download/2059/doc_ecosg.pdf
- Hautecoeur, O. and Borde, R: Derivation of Wind Vectors from AVHRR/MetOp at EUMETSAT. *J. Atmos. Oceanic Technol.*, 34, 16451659, 2017. <https://doi.org/10.1175/JTECH-D-16-0087.1>
- Hoppmann, M., M. Nicolaus, P.A. Hunkeler, P. Heil, L.K. Behrens, G. König-Langlo and R. Gerdes (2015) Seasonal evolution of an ice-shelf influenced fast-ice regime, derived from an autonomous thermistor chain. *Journal of Geophysical Research: Oceans*, 120(3): 1703-1724.
- Jackson, K., J. Wilkinson, T. Maksym, D. Meldrum, J. Beckers, C. Haas and D. Mackenzie (2013) A Novel and Low-Cost Sea Ice Mass Balance Buoy. *Journal of Atmospheric and Oceanic Technology*, 30(11): 2676-2688.
- Lei, R., M. Leppäranta, B. Cheng, P. Heil and Z. Li (2012) Changes in ice-season characteristics of a European Arctic lake from 1964 to 2008. *Climatic Change*, 115(3-4): 725-739.
- Liao, Z., B. Cheng, J. Zhao, T. Vihma, K. Jackson, Q. Yang, Y. Yang, L. Zhang, Z. Li, Y. Qiu and X. Cheng (2018) Snow depth and ice thickness derived from SIMBA ice mass balance buoy data using an automated algorithm. *International Journal of Digital Earth*, 12(8): 962-979.
- Mironov, D., 2008: Parameterization of lakes in numerical weather prediction. Description of a lake model, COSMO Technical Report, 11, 141
- Provost, C., N. Sennéchaël, J. Miguet, P. Itkin, A. Rösel, Z. Koenig, N. Villacieros-Robineau and M.A. Granskog (2017) Observations of flooding and snow-ice formation in a thinner Arctic sea-ice regime during the N-ICE2015 campaign: Influence of basal ice melt and storms. *Journal of Geophysical Research: Oceans*, 122(9): 7115-7134.

- Randriamampianina, R. et al.: Impact of Atmospheric Motion Vectors (AMV) on rapid update cycling (RUC) and rapid-refresh (RR) systems, 2017.
- Rontu, L., Eerola, K., and Horttanainen, M., 2019a: Validation of lake surface state in the HIRLAM v.7.4 numerical weather prediction model against in situ measurements in Finland, *Geosci. Model Dev.*, 12, 37073723, <https://doi.org/10.5194/gmd-12-3707-2019>.
- Rontu, L., Pietikäinen, J.-P., and Martin Perez, D., 2019b: Renewal of aerosol data for ALADIN-HIRLAM radiation parametrizations, *Adv. Sci. Res.*, 16, 129136, <https://doi.org/10.5194/asr-16-129-2019>.
- Thompson, P., K. Jackson and B. Cheng (2019) Measuring Arctic Ice, *Sea Technology*, Vol. 60, No. 2
- Van der Veen, S. H.: Improving NWP Model Cloud Forecasts Using Meteosat Second Generation Imagery. *Mon. Wea. Rev.*, 141, 15451557, 2013.

Surface precipitation type forecasts in AROME-France

Ingrid Dombrowski-Etchevers, Yann Seity

1 Introduction

Snow, hail or freezing precipitation are weather phenomena that are dangerous for the safety of people and properties. They significantly impact the activities of our fellow citizens by disrupting the movement of trains, air and road traffic. Snow or hail can damage homes, buildings or crops. The current society is increasingly weather-sensitive and these phenomena must be forecasted enough in advance to inform the population.

On the other hand, forecasters have access to more models and more fields provided by the models. Determining the type of precipitation inside the model can facilitate their decision-making.

In a first part, this article explains how the surface precipitation types (noted SPTYPE) is determined in AROME. Then, the second part contains two examples of cases over France, but also the application of the diagnostic of SPTYPE in other countries of the consortium. Finally, the article ends with the conclusion and the outlook about the SPTYPE, but also on other diagnostics for forecasters.

2 Precipitation type : method

The precipitation type discrimination is done in two steps in the NWP model:

- First, an algorithm is called at each time step in the model physics, in order to determine instantaneous SPTYPE (section 2.1).
- Next, at user defined specific time, two fields are produced: the most frequent SPTYPE and the most severe SPTYPE over given time period (noted TPERIOD, one hour for instance). The intermittent nature of the precipitation is also determined (section 2.2).

2.1 Instantaneous SPTYPE

Complex microphysics like Milbrandt and Yau (2005) can be used to determine the SPTYPE in NWP models. But when the model microphysical scheme is simpler, the forecasted temperature profiles are used (Bourgouin (2000) ; Gascón et al. (2018)). To improve surface precipitation discrimination, some authors use the wet-bulb temperature (noted T^w) profiles (Ramer (1993) or Schuur et al. (2012)). In our method, we propose to use the surface fluxes of each hydrometeor (rain, snow, graupel) provided by the microphysics of the model (according to Reeves et al. (2016)) in addition to the wet-bulb temperature profile.

The algorithm called at each time step in `apl_rome.F90` subroutine is described by the decision tree presented in figure 1. This algorithm determines 11 types of precipitation: drizzle, rain, rain and snow mixed, sleet/moist snow, wet snow, dry snow, small hail, hail, freezing rain, ice pellets (when the cooling in low layers is too significant to have freezing rain) and freezing drizzle (light supercooled liquid precipitation)

The hail and small hail are determined using the operational hail diagnostic developed by Yann Seity. This hail diagnostic is based on the vertical integral of the amount of graupel.

For the others precipitation type, the $T'w$ at 2-meters level and the $T'w$ profiles are used as explained in the decision tree.

The diagnostic of freezing rain is based on the computation of areas between iso- $T'w = 0^{\circ}\text{C}$ and the profile of $T'w$.

The diagnostic of freezing drizzle is based on the work of Quéno et al. (2018). It uses the profile of $T'w$ and the liquid water content in low layers.

At the end, when the $T'w$ is above 0°C , it is the distribution of the precipitating fluxes of the rain, snow and graupel hydrometeors which determines the rainy or snowy nature of the precipitation.

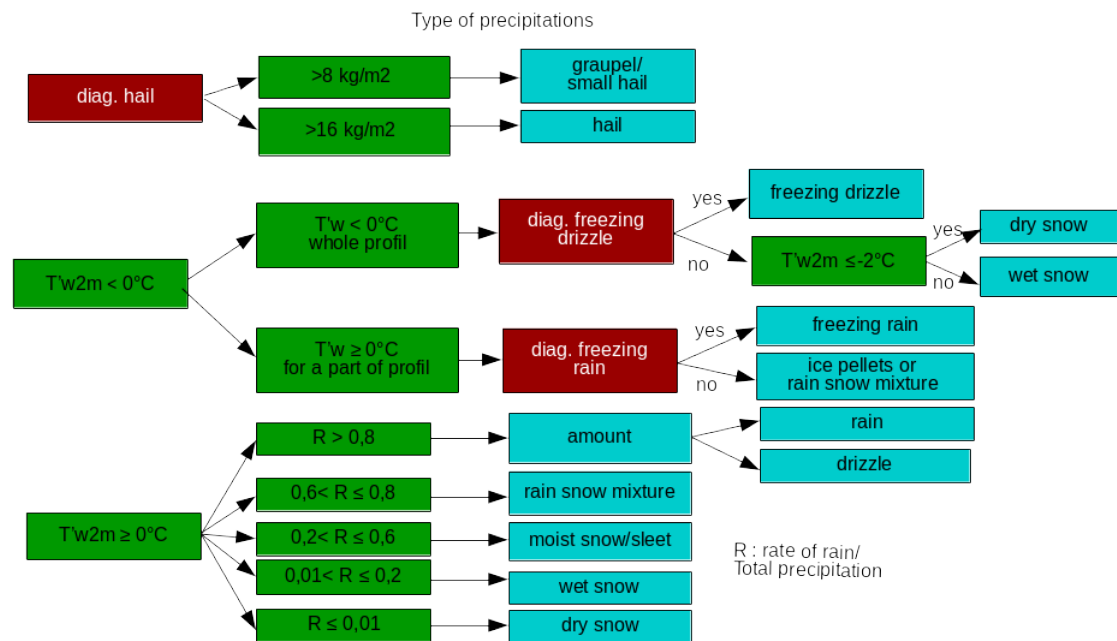


Figure 1: Decision tree for precipitation type

2.2 Produced SPTYPE in output files

Instantaneous SPTYPE computed at each time step are stored in memory for a defined TPERIOD (72 time steps for one hour of forecast for AROME). Two fields of SPTYPE are produced : the most frequent SPTYPE and the most severe SPTYPE over TPERIOD. Fields are valid over the previous TPERIOD (rather than instantaneous) in order to provide the most complete information possible (Hail does not necessarily fall during the round TPERIOD, and snowfall does not start necessarily at the round TPERIOD, for instance).

To determine the most severe SPTYPE, priority rules are applied. They were established by the forecasters themselves and given in the table 1.

For the most frequent SPTYPE, the frequency of each SPTYPE is calculated over TPERIOD. So we get the most common. In the case of a draw, we apply the priority rules of the most severe type.

Most severe	Freezing rain
	Freezing drizzle
	Hail
	Moist snow/sleet
	Wet snow
	Dry snow
	Small hail/graupel
	Ice pellets
	Rain and snow mixture
∨	Rain
Least severe	Drizzle

Table 1: Priority of precipitation types

3 Applications

SPTYPE diagnostic have been operational since the beginning of July 2019. They were qualitatively assessed on around thirty weather-sensitive days (snow, hail or freezing precipitation) between December 2018 and December 2019. For this comparison, we used the data fusion product (mixture of several observed data - radar data, rain gauges, temperatures, etc - and analysed data of NWP) called HYDRE. It discriminates surface precipitation and soil conditions. We present in sections 3.1 and 3.2, two cases to illustrate the contribution of SPTYPE diagnostic. A systematic and quantitative evaluation (scores) is under development: SPTYPE will be compared with the SYNOP stations observed data.

3.1 Freezing rain

The first case presented concerns freezing precipitation. The 25th of January, surface temperatures were cold in eastern FRANCE as the diurnal maximums temperature remains negative. On the night of January 25 to 26, a warm front arrived over France. This warm and moist air above the cold low layers led to some freezing rain phenomenon. On the figure 2, the SPTYPE diagnostic from AROME for the 26th of January at 04TU highlights this phenomenon. It is in agreement with HYDRE for the same time (figure 3).

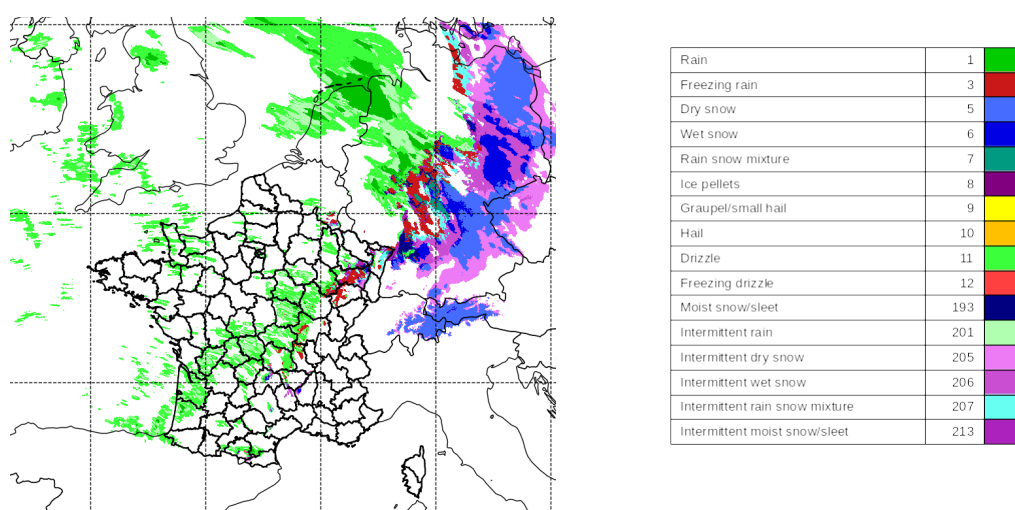


Figure 2: The most frequent SPTYPE during the previous hour forecasted for the 26th of January at 04TU

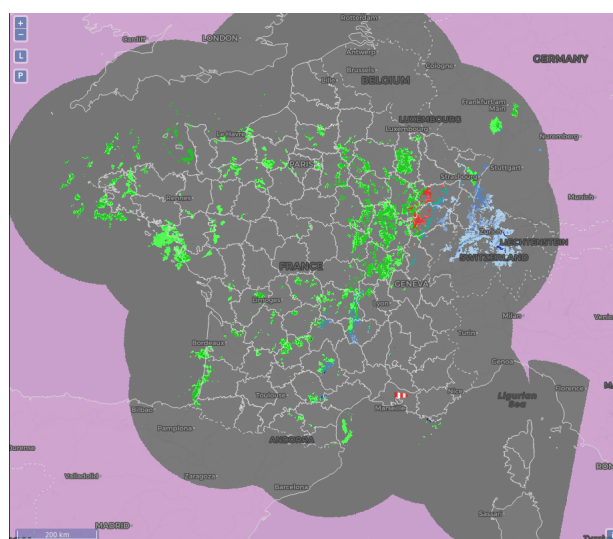


Figure 3: Precipitation type by HYDRE for the 26th of January at 04TU. The colors palette is the same for AROME

3.2 Snow and hail

The most frequent SPTYPE of the 14th November 2019 is presented on the figure 4. A cold drop over France is associated with a low pressure area. An occluded front is crossing the country from West to East. The temperatures are cold and the air moist. It is snowing (in blue shades) on the mountains, but on the lowlands too, like in the Rhone valley. In the Mediterranean, the cold front is active with hail thunderstorms forecasted and observed (in yellow and orange). It is in agreement with HYDRE for the same time (figure 5).

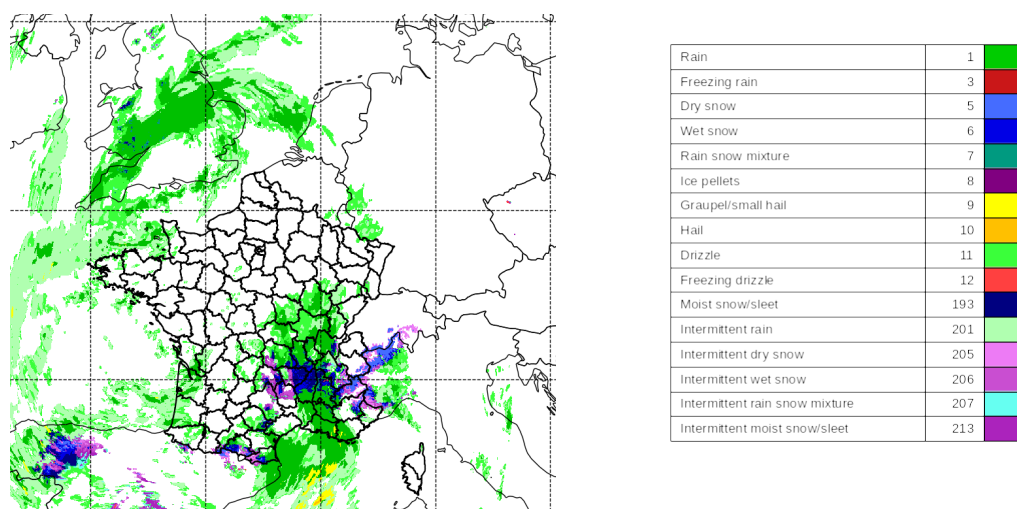


Figure 4: The most frequent SPTYPE during the previous hour forecasted for the 14 th November at 13TU

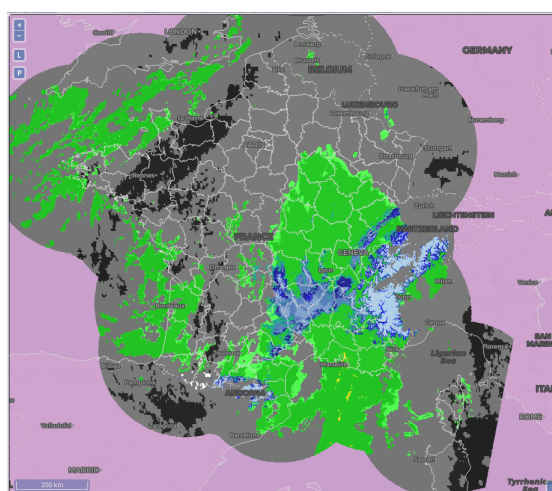


Figure 5: Precipitation type by HYDRE for for the 14 th November at 13TU. The colors palette is the same for AROME

3.3 In other countries

The development of the diagnostic of precipitation types only started in summer 2018 in AROME. The first version was delivered for operational model in April 2019. However, it has already been shared with several members of the ALADIN-HIRLAM consortium who have given feedback on their use. An example is presented on the figure 6. It comes from Piotr Sekuła's report, available in ALADIN's website.

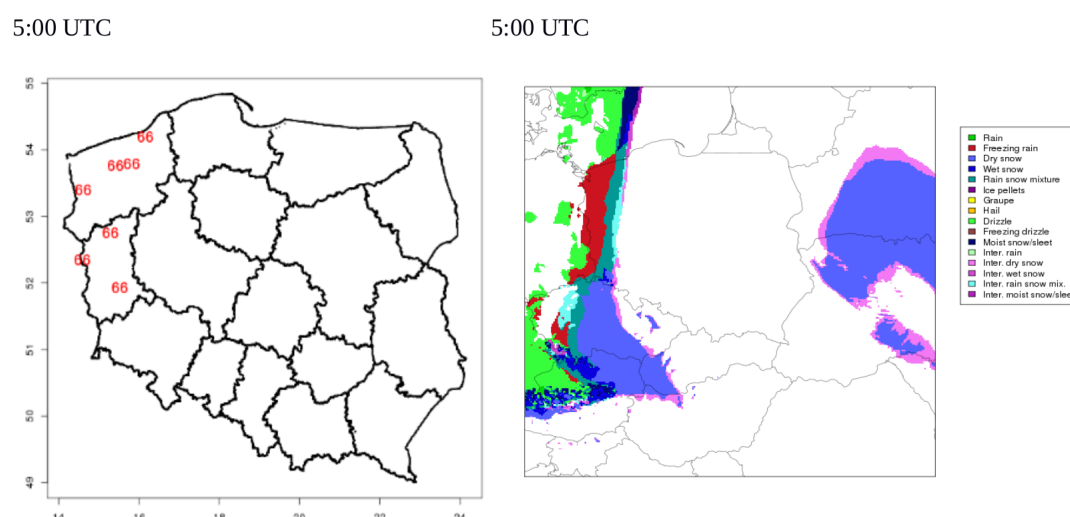


Figure 6: Precipitation type (right) and locations of observed freezing rain over Poland the 1st of December 2018 by Piotr Sekuła

4 Conclusions and outlook

A surface precipitation types discrimination algorithm has been implemented in the physics of the AROME model. It is based on the wet-bulb temperature (at 2 meters and profile) and on the microphysics of the model via the distribution of the precipitating fluxes of hydrometeors, rain, snow and graupel.

The first results show good agreement from a qualitative point of view with the observations. The current winter season will provide additional feedback from forecasters. In addition, a quantitative method of comparison between observations and forecasts of surface precipitation types is still being developed.

This same diagnostic is also integrated into ARPEGE physics. It also seems to have worked well, even if the intermittent nature of precipitation is poorly assessed and hail is not available yet.

Simultaneously two other diagnostics were integrated into the models:

- visibility with the minimum visibility due to clouds (fog) and the minimum visibility due to precipitation over a time period. For visibility diagnostic, we based ourselves on the work of Sami Niemelä and Sander Tijm, in particular.
- the altitude of the top of convection in ARPEGE developed by Olivier Jaron

In AROME the altitude at the top of convection is under development. This diagnostic could be integrated into the discrimination of surface precipitation types : the convective nature of a precipitation would replace the intermittent nature. This would be more in agreement with observations.

To end with the diagnostics, the lightning density developed by Christoph Wittmann and Jure Cedilnik is now available in the common code. For our part, S. Radanovics is calibrating the coefficients of this diagnostic and will assess it.

We would like to thank those who interacted with us for the development and evaluation of this new diagnostic and other. In alphabetical order : Radmila Brozková, Christine Bruschi, Philippe Cau, Odile Coudert, Jure Cedilnik, Ryad El Khatib, Daniel Heral, Najla Marass, Karine Maynard, Sami Niemelä, Neva Pristov, Leonard Roger, Piotr Sekuła, Andre Simon, Sander Tijm and Christoph Wittmann.

5 References

References

- Bourgouin, P., 2000: A method to determine precipitation types. *Weather and Forecasting*, **15** (5), 583–592, doi:10.1175/1520-0434(2000)015<0583:AMTDPT>2.0.CO;2.
- Gascón, E., T. Hewson, and T. Haiden, 2018: Improving predictions of precipitation type at the surface: Description and verification of two new products from the ECMWF ensemble. *Weather and Forecasting*, **33** (1), 89–108, doi:10.1175/WAF-D-17-0114.1.
- Milbrandt, J. A., and M. K. Yau, 2005: A multimoment bulk microphysics parameterization. part I: Analysis of the role of the spectral shape parameter. *Journal of the Atmospheric Sciences*, **62** (9), 3051–3064, doi:10.1175/JAS3534.1.
- Quéno, L., V. Vionnet, F. Cabot, D. Vrécourt, and I. Dombrowski-Etchevers, 2018: Forecasting and modelling ice layer formation on the snowpack due to freezing precipitation in the pyrenees. *Cold Regions Science and Technology*, **146**, 19 – 31, doi:https://doi.org/10.1016/j.coldregions.2017.11.007, URL <http://www.sciencedirect.com/science/article/pii/S0165232X1730054X>.
- Ramer, J. A., 1993: An empirical technique for diagnosing precipitation type from model output. *Preprints*, Amer. Meteor.Soc., Vienna, Fifth Int. Conf. on Aviation Weather Systems, 227–230.
- Reeves, H. D., A. V. Ryzhkov, and J. Krause, 2016: Discrimination between winter precipitation types based on spectral-bin microphysical modeling. *Journal of Applied Meteorology and Climatology*, **55** (8), 1747–1761, doi:10.1175/JAMC-D-16-0044.1.
- Schuur, T. J., H.-S. Park, A. V. Ryzhkov, and H. D. Reeves, 2012: Classification of precipitation types during transitional winter weather using the RUC model and polarimetric radar retrievals. *Journal of Applied Meteorology and Climatology*, **51** (4), 763–779, doi:10.1175/JAMC-D-11-091.1.

On the way towards the AROME nowcasting system in Hungary

Katalin Jávorné Radnóczy, Anikó Várkonyi, Gabriella Szépszó

1 Introduction

Currently, AROME cy40t1 and ALARO cy40t1 are both used in the operational numerical weather prediction (NWP) in Hungary. AROME/HU (Szintai et al., 2015) runs 8 times per a day up to 36-48 hours at 2.5 km horizontal resolution using 60 vertical levels over a domain including the Carpathian Basin (*Figure 1*). The initial conditions are prepared by optimal interpolation on the surface and local 3D-Var assimilating SYNOP, TEMP, AMDAR, GNSS ZTD measurements and Mode-S MRAR data from the Slovenian network. The hydrometeors and snow evolve through the data assimilation (DA) cycle. Hourly lateral boundary conditions (LBCs) are taken from the ECMWF HRES forecast in time lagged mode.

In spring 2019, a considerable upgrade of the high-performance computing system was realized in Hungary. In the new HPE Apollo 6000 server, 8 nodes are dedicated to the operational runs and further 12 nodes are used for NWP-related research. Each single node has two Intel XeonE5-2698, 2.2 GHz processors with 2x20 cores. This capacity allows us to make preparatory steps to design an AROME-based nowcasting system. To eliminate some instabilities occurring in the stratosphere with 60 vertical levels, we achieved some test experiments using 90 levels and the predictor-corrector scheme. To increase the vertical resolution, the background error covariances need to be re-calculated, thus some B-matrix computation experiments are carried out using the ensemble data assimilation (EDA) technique. We started to investigate the impact of hourly data assimilation cycle with testing different cut-off time configurations and frequency of the surface assimilation. At the same time, in agreement with forecasters' request we developed a convection-permitting ensemble prediction system (EPS) based on AROME. AROME-EPS is not the first limited area EPS in Hungary, as ALARO-EPS (Horányi et al., 2011) is in operation since 2009: it runs at 18 UTC up to 60 hours every day downscaling 11 members of the ECMWF ENS (since 2015; Szűcs et al., 2016) at 8 km resolution over a Central European domain.

In this paper, the preliminary outcomes are shown for the test experiments of the rapid update cycle (RUC) in Section 2, AROME-EPS and its first verification results are introduced in Section 3.

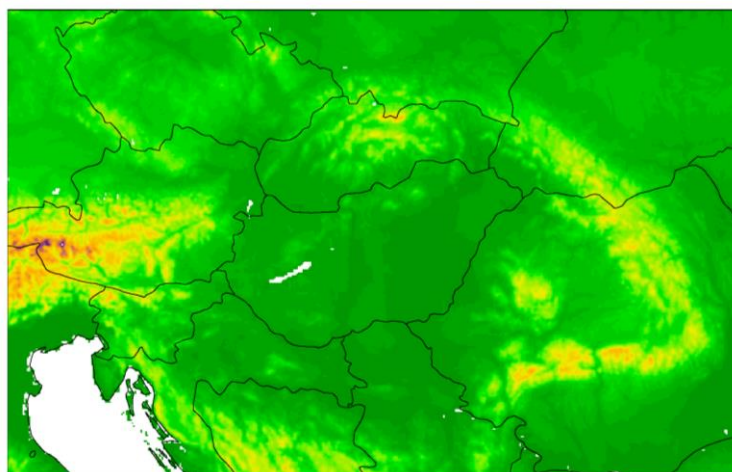


Figure 1: Integration domain of operational AROME/HU.

2 AROME rapid update cycle experiments

The main goal of these experiments was to employ more observations with reduced representativity error in time, which would serve as a basis to enhance data assimilation by including radar data assimilation in the near future. The RUC experiments were based on AROME operational configuration but applied 1-hour assimilation window length instead of 3 hours used in the operational DA cycle.

Experiments

Experiments were achieved for two 30-day periods: a winter period covering 08/01/2017–06/02/2017 and an early summer period of 04/05/2019–02/06/2019 including numerous thunderstorm activities in the model domain. All model runs had started at 00, 06, 12, 18 UTC and performed a 12-hour forecast range. The assimilation cycle was started six days before the first forecast in order to provide appropriate first guess field at the beginning of the periods. Some modifications were made with respect to the operational configuration: the atmospheric assimilation frequency was set to 1 hour with +/-30 minutes cut-off time, meanwhile 1, 3 and 6 hourly surface data assimilation frequency were applied. In the last two cases (*AROME_combo_1hourly_surf3*, *AROME_combo_1hourly_surf6*) whenever surface data was not taken into account for hourly assimilation, first guess fields were used. The following four configurations were tested for both periods:

- *AROME_3hourly* represents the original settings of operational AROME;
- *AROME_1hourly* represents 1 hourly data assimilation cycle for 3D-Var and surface data;
- *AROME_combo_1hourly_surf3* consists of a combination of 1 hourly cycle for 3D-Var and 3 hourly cycle for surface data;
- *AROME_combo_1hourly_surf6* consists of a combination of 1 hourly cycle for 3D-Var and 6 hourly cycle for surface data;

In case of *AROME_combo_1hourly_surf3*, the effect of cut-off time modification was also evaluated using -45/+15 minutes in the assimilation window.

Evaluation and conclusions

To evaluate the results two different verification approaches were applied. Standard verification measures (RMSE, bias) were used for surface parameters (*Figures 2 and 3*), and the so-called SAL verification method was used for precipitation (*Table 1*). The SAL method (Wernli et al., 2008) provides an objective quality measure for precipitation forecasts compared to radar observations as three distinct components (structure, amplitude and location) are considered. In order to get a comprehensive picture of all the three components, the central statistic approach was applied (*Table 1*): better performing cases are closer to the center, therefore a given percentage of cases (5%, 10%, 20%, 50%) can be covered by a shorter radius.

According to the results so far, we assume that *AROME_1hourly* performs better than *AROME_3hourly* in case of 2-metre temperature. Higher accuracy were provided by reduction of surface assimilation frequency (*AROME_combo_1hourly_surf3*, *AROME_combo_1hourly_surf6*). The results show a bigger difference between the performances of configurations in January compared to May. Meanwhile, considering precipitation there is no significant difference between the configurations as SAL verification shows balanced performance for each setting (*Table 1*).

The 15-minute shift in the cut-off time does not show substantial impact on the forecasts (*Figure 4*) which is an important information to design the operational configuration later.



Figure 2: RMSE of 2-metre temperature in the function of lead time in the winter period.

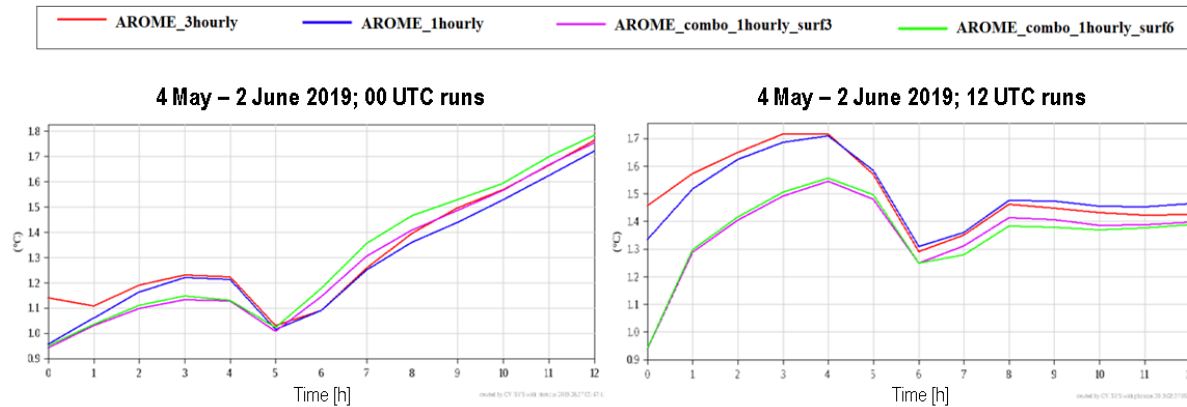


Figure 3: RMSE of 2-metre temperature in the function of lead time in the early summer period.

Table 1: Lower radius values in SAL method indicate better performance on precipitation forecasts.

	00 UTC				06 UTC			
	5%	10%	20%	50%	5%	10%	20%	50%
AROME_3hourly	0,282	0,391	0,570	0,992	0,382	0,475	0,666	1,037
AROME_1hourly	0,276	0,365	0,506	1,075	0,297	0,454	0,666	1,026
AROME_combo_1hourly_surf3	0,274	0,373	0,578	1,117	0,325	0,492	0,652	1,051
AROME_combo_1hourly_surf6	0,261	0,410	0,570	1,128	0,369	0,484	0,655	1,016
	12 UTC				18 UTC			
	5%	10%	20%	50%	5%	10%	20%	50%
AROME-3hourly	0,366	0,447	0,665	1,096	0,357	0,534	0,684	1,157
AROME-1hourly	0,358	0,450	0,625	1,052	0,379	0,514	0,768	1,216
AROME-1hourly_surf3	0,307	0,424	0,648	1,094	0,369	0,484	0,643	1,159
AROME-1hourly_surf6	0,302	0,442	0,647	1,111	0,314	0,446	0,642	1,216

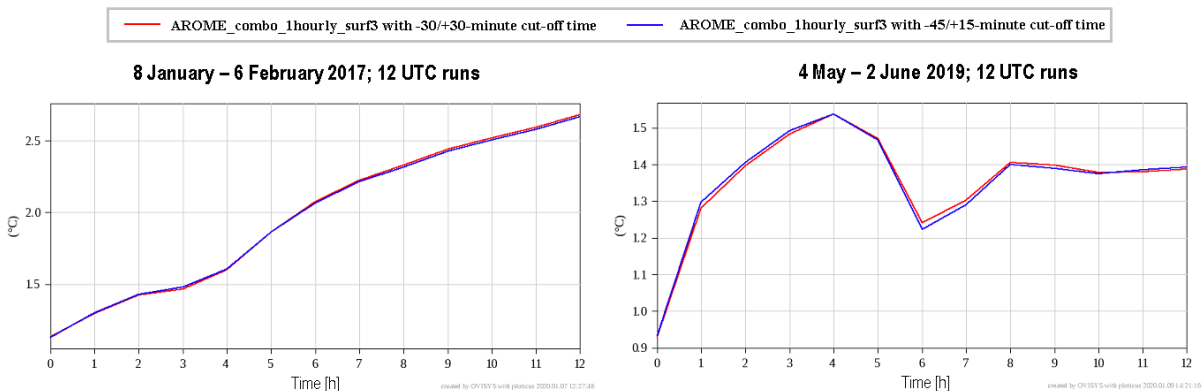


Figure 4: RMSE of 2-metre temperature using different cut-off time for both verification periods.

3 AROME-EPS

Description

AROME-EPS runs once a day, similarly to operational ALARO-EPS. Some main features are kept: it is an 11-member forecast coupled to 18 UTC ECMWF ENS with a frequency of 3 hours. However, we changed some important attributes: the new ensemble runs at horizontal resolution of 2.5 km over a domain covering the Carpathian Basin (*Figure 1*). The forecasts are initialized at 00 UTC and range up to 48 hours. AROME-EPS still does not include assimilation cycle: initialization uses guess (hydrometeors) and surface analysis of “deterministic” AROME, upper air fields are downscaled from LBCs. The test version are available for forecasters, through HAWK visualization system since May 2019.

Results

Comparison of AROME-EPS and ALARO-EPS was made for the period of 28 May – 19 June 2019. This period was partly dry and warm, but heavy precipitation induced by convection also occurred in a part of Hungary on most days. (Precipitation locally exceeded even 50 mm on 3 days.) The results show that while forecasts of geopotential, wind and cloud parameters clearly improve in AROME ensemble, the results for humidity, temperature and precipitation have varying performance (*Figure 5*). Verification of control member shows similar results.

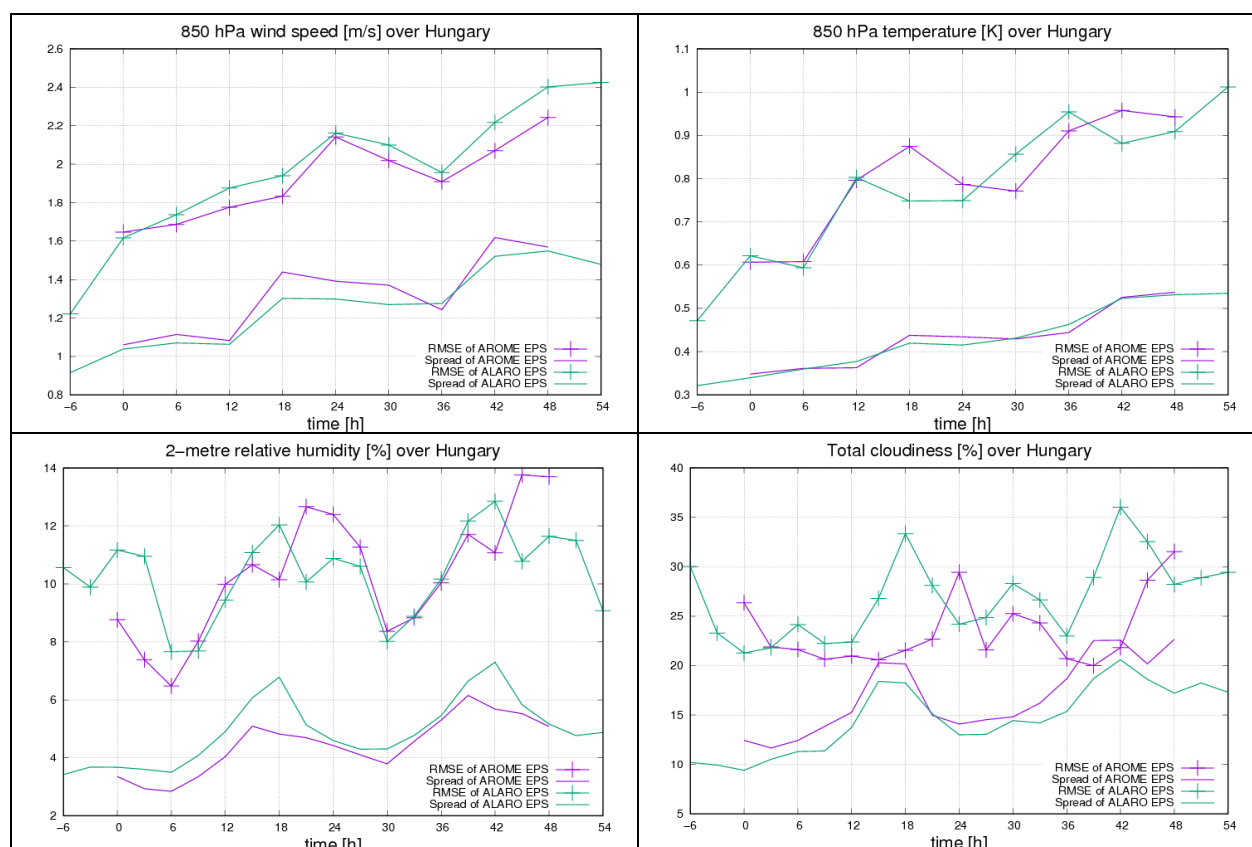


Figure 5: RMSE (+ symbols) and spread (solid line) of AROME-EPS (purple) and ALARO-EPS (green). The verification reference was ECMWF analysis in case of upper air parameters (top panels) and Hungarian station data in case of surface fields (lower panels).

4 Outlook

The hourly update of the initial conditions has benefit in case of observation types the data of which are available with high density and without significant delay in time. Assimilation of the hourly SYNOP data has already proven to have significant effect on the forecast quality, however, we plan to implement further observations into RUC, as radar data and Mode-S MRAR data from the Hungarian traffic controller. We will continue the next experiments with reduced surface assimilation frequency found optimal above.

AROME-EPS is going to move from pre-operational to operational status in the beginning of February 2020. As next step, we would like to introduce not only local data assimilation to initialize the control forecast, but also local perturbations to be generated by EDA and stochastic physics. Intensive verification of AROME-EPS will continue on longer periods applying more ensemble verification methods as well as through case studies.

5 References

Horányi, A., Mile, M., Szűcs, M., 2011: Latest developments around the ALADIN operational short-range ensemble prediction system in Hungary. *Tellus* 63A, 642–651.

Szintai, B., Szűcs, M., Randriamampianina, R., Kullmann, L., 2015: Application of the AROME non-hydrostatic model at the Hungarian Meteorological Service: physical parametrizations and ensemble forecasting. *Időjárás* 119, 2, 241–265.

Szűcs, M., Sepsi, P., Simon, A., 2016: Hungary's use of ECMWF ensemble boundary conditions. *ECMWF Newsletter* 148, 24–30.

Wernli, H., Paulat, M., Hagen, M., Frei, C., 2008: SAL – A Novel Quality Measure for the Verification of Quantitative Precipitation Forecasts. *Mon. Wea. Rev.* 136, 4470–4487, <https://doi.org/10.1175/2008MWR2415.1>.

Met Éireann Updates

Geoffrey Bessardon, Colm Clancy, Conor Daly, Rónán Darcy, Emily Gleeson, Alan Hally, Eoin Whelan

1 Introduction

Cycle 40h1 of HARMONIE-AROME has been operational at Met Éireann since May 2018, with the short-range Irish Regional Ensemble Prediction System (IREPS) running since October 2018. Details of this configuration may be found in a previous newsletter (Clancy et al., 2019). In August 2019, a technical upgrade to this operational NWP suite was carried out. This is described in detail in Section 2. In November, the SAPP system from ECMWF was made operational for the pre-processing of observations; details are given in Section 3. Recent work on model physiography is discussed in Section 4, while some information on MUSC development is provided in Section 5. Finally, updates on the MÉRA reanalysis project are given in Section 6.

2 Operational Upgrade

A technical upgrade to the operational suite (o-suite) was carried out in August 2019. The changes applied are summarised in Table 1 and are described in more detail below.

Table 1: Summary of changes in the technical upgrade

Model component	Description
Dynamics	Adjust vertical momentum equation
Dynamics	Change spectral grid from linear to quadratic
Data assimilation	Assimilate radiances from AMSU-A, MHS and IASI satellite instruments
Data assimilation	Assimilate METOP-C ASCAT winds
Ensemble	Update SLAF coefficients, SLAFLAG values and surface perturbations

2.1 Forecast model

During winter 2018/2019 noise patterns were observed in the MSLP forecasts produced by our operational HARMONIE-AROME. Investigations revealed that these could be removed by changing two parameters related to the form of the vertical momentum equation: i.e. changing {LGWADV, LRDBBC} from their default {FALSE, TRUE} to {TRUE, FALSE}. These latter values are already in use at Météo France and a number of ALADIN countries. The effects of these changes can be clearly seen from experiments shown in Fig. 1. Longer tests were carried out with these changes, and showed no significant differences in forecast quality.

A further dynamics change was also tested: replacing the default linear spectral grid with the quadratic grid. This results in a saving of approximately 13% in CPU time, which allows for more rapid forecast production. Experiments carried out during the period of a high-impact storm event (February 2014, with Storm Darwin) showed no significant reduction in accuracy.

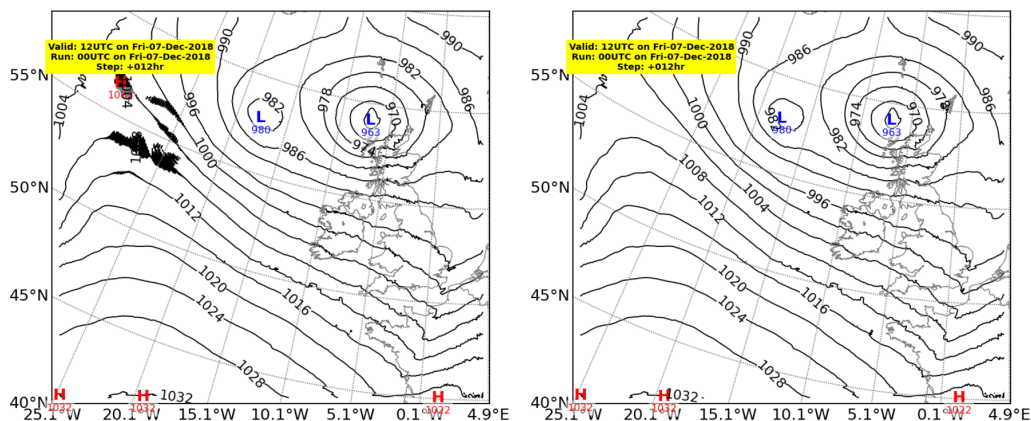


Figure 1: Plots of MSLP before (left) and after (right) the changes made to HARMONIE-AROME (40h1.1) following experiments with {LGWADV,LRDBBC} options. Left: default {FALSE,TRUE}. Right: {TRUE,FALSE}.

2.2 Data Assimilation

The technical upgrade also brought the assimilation of radiance data from the AMSUA-A, MHS and IASI instruments on board EUMETSAT and NOAA polar orbiting satellites. Met Éireann receives satellite data used in NWP via the EUMETSAT Advanced Retransmission Service (EARS) Regional Service. Figure 2 shows typical data coverage for AMSU-A and IASI observations.

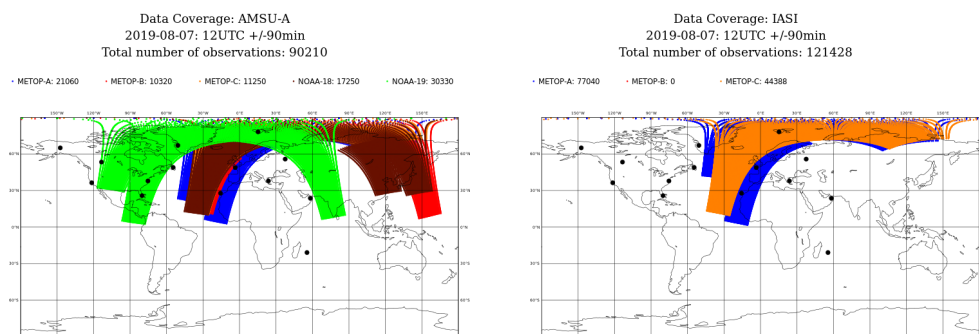


Figure 2: Data coverage of AMSU-A (left) and IASI (right) observations for 1200 UTC 7th August 2019. The black dots indicate the location of EARS receiving stations.

It is assumed by many data assimilation algorithms that observations have unbiased (Gaussian) errors. However, it is known that satellite observation errors have biases that must be corrected before use in NWP. HARMONIE-AROME uses a technique known as Variational Bias Correction (VarBC) (Auligné et al., 2007) to correct satellite observation biases. VarBC coefficients are calculated over a suitable period (typically one month) and then corrections are applied to radiance observations as part of the HARMONIE-AROME 3D-Var minimization process. Further details on the application of VarBC in the HARMONIE-AROME system are available Arriola et al. (2016). VarBC coefficients for AMSU-A, MHS and IASI data assimilated in the operational domain were calculated during August 2018. Appropriate blacklisting of satellites was applied taking orbit times into account. As the operational domain is mainly ocean, radiance data over land was also blacklisted. Examples of time-series of the convergence of VarBC corrections applied to radiance data are shown in Fig. 3.

Following the calculation of VarBC coefficients for the operational domain a one month test period was used to validate model performance with the assimilation of AMSU-A, MHS and IASI observations in the HARMONIE-AROME 3D-Var data assimilation system. A control experiment (varbc_met_radass) assimilating only conventional and ASCAT observations ran for August 2018. An experiment (varbc_met_radass),

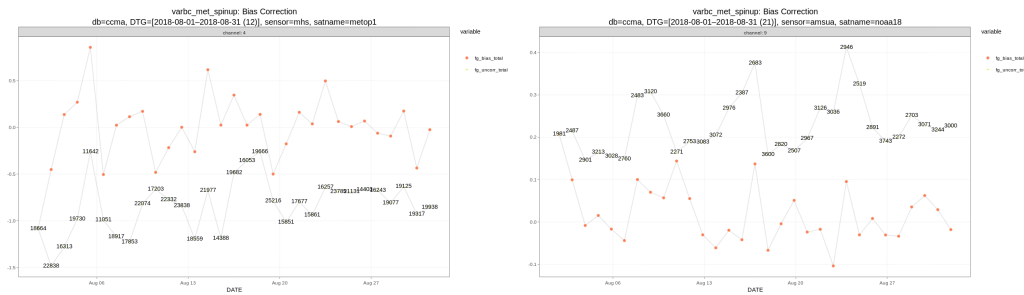


Figure 3: Time-series of average first-guess departures for Metop-B MHS Channel 4 (left) and NOAA-18 AMSU-A Channel 9 are show. "Raw" (green dots, numbers) and bias corrected (orange dots) departures are illustrate the benefits of applying VarBC to the data.

producing 24 hour forecasts at 0000 UTC and 1200 UTC, assimilating radiance data also ran for the same period. Forecasts produced by both experiment were then validated using SYNOP and TEMP observations. There was a slight positive improvement in scores MSLP and results for near-surface parameters were neutral, Fig. 4. There were improvements in forecasts of geopotential heights and humidity parameters in the middle atmosphere, Fig.5.

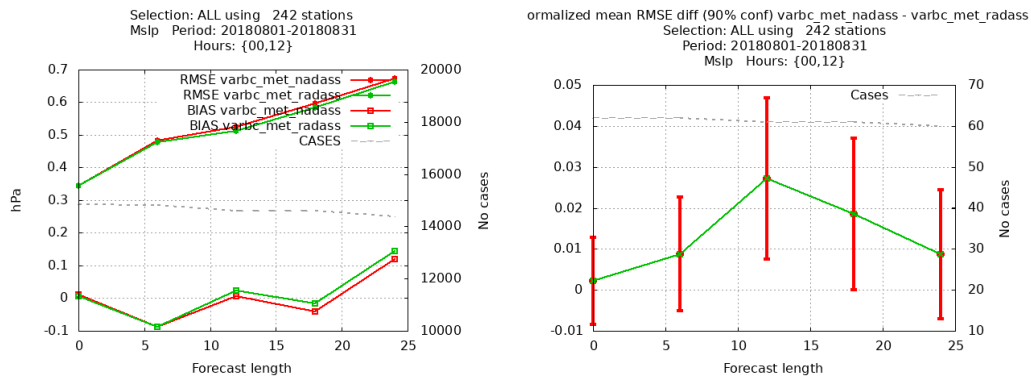


Figure 4: Validation of MSLP forecasts compared to SYNOP observations (right) and the significance of these results (right). Control (conventional + ASCAT) statistics are shown in red and radiance experiment statistics are shown in green.

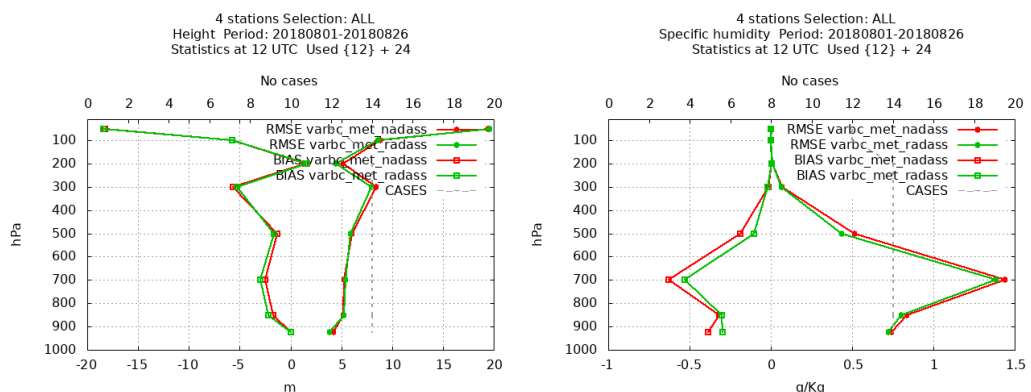


Figure 5: Validation of geopotential (left) and humidity (right) forecasts compared to TEMP observations. Control (conventional + ASCAT) statistics are shown in red and radiance experiment statistics are shown in green.

Metop-C was launched on the 7th November 2018. Data from Metop-C data are currently (August 2019) in

trial dissemination mode. Radiance data (AMSU-A, MHS and IASI) have been blacklisted. ASCAT data will be assimilated as these data are considered to be unbiased. The assimilation of Metop-C radiances will be introduced at a later date.

2.3 Deterministic Verification

The deterministic configuration of the technical upgrade (e-suite) was put into parallel operational and cycled for a number of months to spin up the surface processes. The main parallel test period covered June and July 2019, with 48-hour forecasts beginning at 0000 UTC and 1200 UTC. Figure 6 shows sample surface verification scores for 10 m wind speed and 2 m temperature parameters. Some minor differences are visible but overall the average forecast quality is comparable, with no obvious degradation from the use of the quadratic grid. Verification of some vertical profiles is given in Fig. 7. Results are, again, broadly neutral. Perhaps the most notable feature is an improvement in upper level relative humidity (bottom panels), due to the assimilated radiance observations that provide information at these levels.

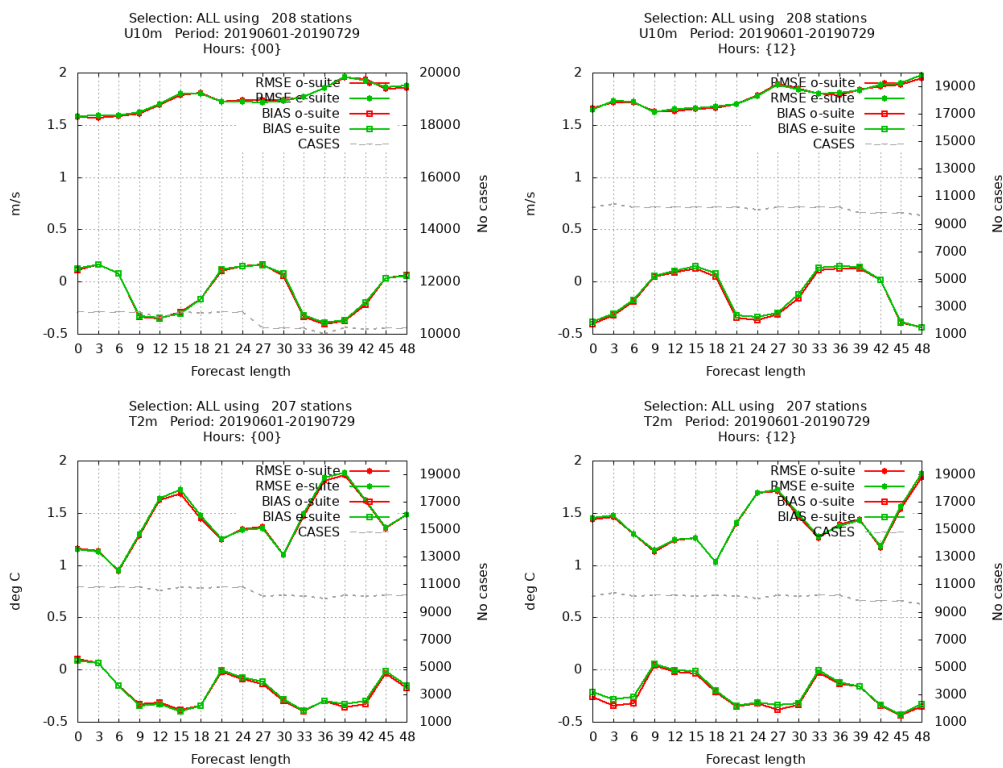


Figure 6: Point verification of the o-suite (red) and the e-suite (green) for the test period in June and July 2019. Forecasts begin at 0000 UTC (left) and 1200 UTC (right). Parameters shown are 10 m wind-speed (above) and 2 m temperature (below).

2.4 Ensemble System

Testing on a number of aspects related to the IREPS configuration was undertaken in order to pinpoint potential useful technical upgrades to the o-suite. The implementation of the perturbed analysis (PertAna) approach of representing initial condition uncertainty was investigated but discounted due to unacceptable noise patterns developing in the first few hours of the forecast.

Modifications were restricted to changes in the SLAF perturbation coefficients, SLAFLAG values and surface perturbations. The SLAF coefficients control the scaling applied to the difference between the two lagged

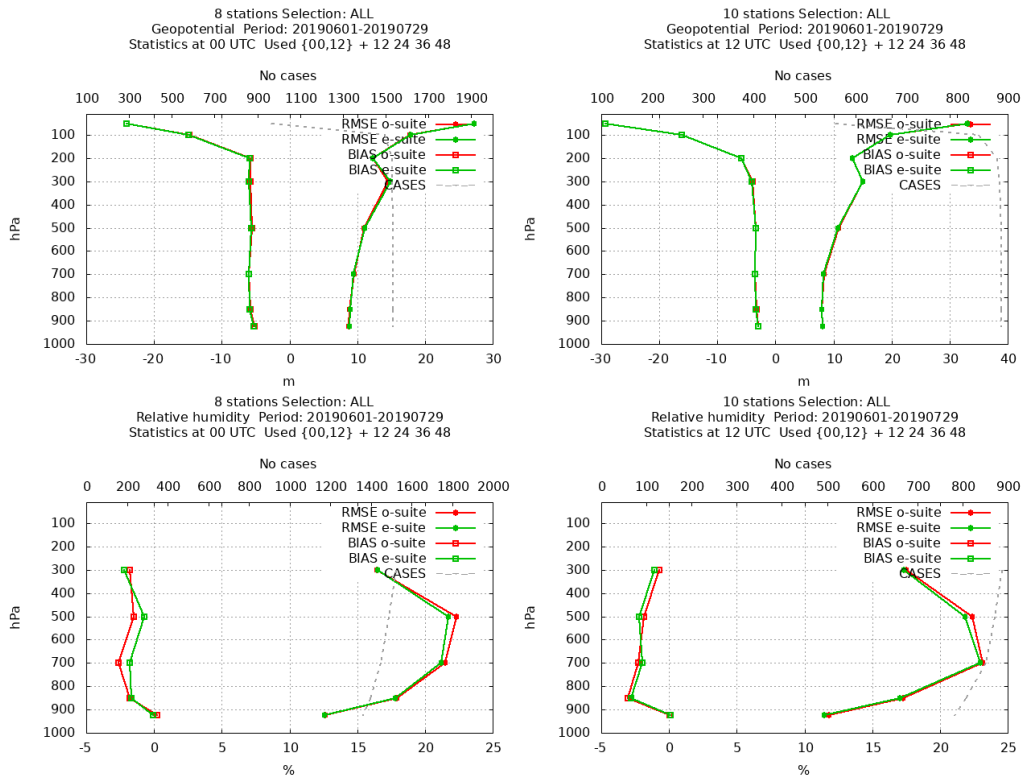


Figure 7: Vertical profile verification of the o-suite (red) and the e-suite (green) for the test period in June and July 2019. Verification is for forecasts valid at 0000 UTC (left) and 1200 UTC (right). Parameters shown are geopotential (above) and relative humidity (below).

forecasts which are valid at the same time. The SLAFLAG values determine the number of hours lag between the two forecasts. Table 2 shows the updates applied to the SLAF coefficients and SLAFLAG values.

Table 2: Previous and updated SLAF coefficient and SLAFLAG values for IREPS

Member	Old SLAF coeff	New SLAF coeff	Old SLAFLAG	New SLAFLAG
0	0.0	1.0	0	0
1	1.75	1.60	6	12
2	-1.75	-1.60	6	12
3	1.5	1.4	12	18
4	-1.5	-1.4	12	18
5	1.2	1.2	18	24
6	-1.2	-1.2	18	24
7	1.0	1.0	24	30
8	-1.0	-1.0	24	30
9	0.9	0.86	30	36
10	-0.9	-0.86	30	36

Perturbations of the snow depth parameter, vegetation fraction, leaf area index (LAI) and soil thermal coefficient were deactivated. The mean bias (Fig.8) in 2 m temperature, 10 m wind speed and 2 m relative humidity, shows the positive impact of these modifications. The 3 parameters result in a lower mean bias compared to the reference experiment. This is particularly important for 2 m temperature given that HARMONIE-AROME cycle 40h1.1 suffers from a negative 2 m temperature bias over Ireland.

IREPS continues to add significant value over IFSSENS as demonstrated by the spread/skill score plot for 10m-wind in Fig.9.

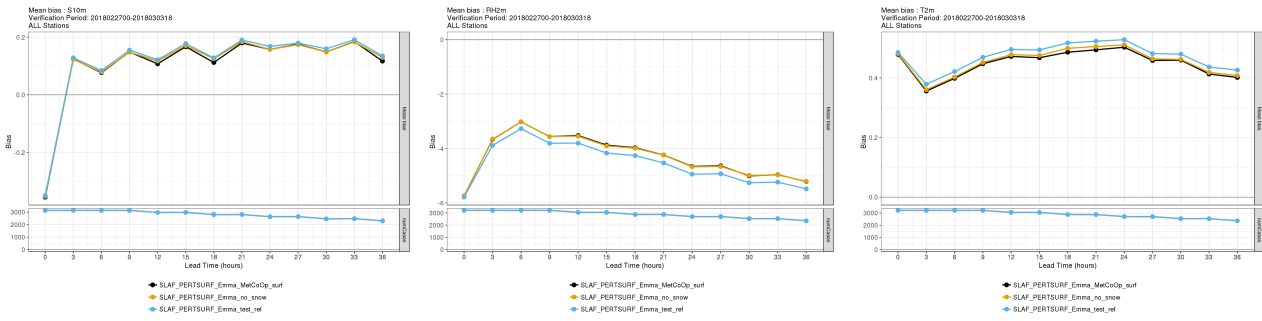


Figure 8: Mean bias in 10 m wind speed, 2 m relative humidity and 2 m temperature for experiments related to modifications in the surface perturbations. The updated surface perturbation set-up is shown in black, a reference experiment is in blue and an experiment with no perturbations to the snow depth parameter is in orange.

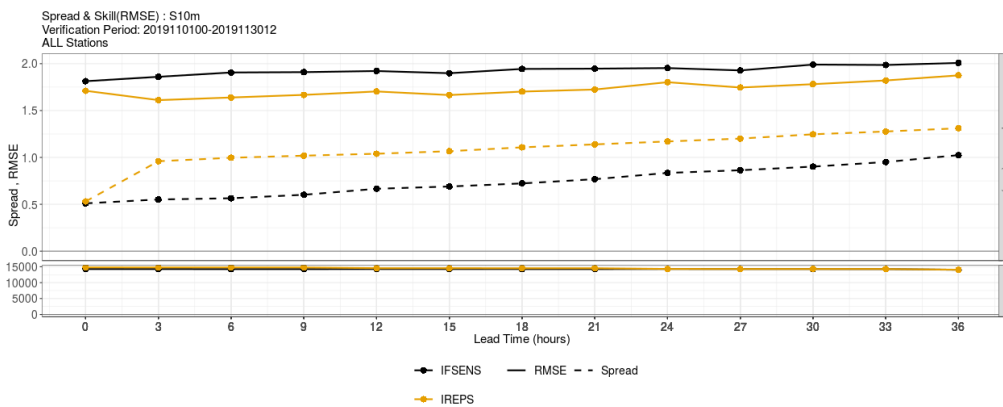


Figure 9: Spread-skill scores for IREPS (orange) and IFSENS (black) for 10m-wind speed for the month of November 2019.

3 Implementation of SAPP

3.1 Introduction

Met Éireann has used the Automatic Data Extraction system (ADE) to produce observational (BUFR) data readable by our operational NWP systems. The ADE was developed in the 1990’s and is based on software developed by ECMWF supplemented by local adaptations and quality control functions. With the changes in formats used to transmit data on the GTS (TAC to BUFR) and the availability of new observational data streams the rigidity of the ADE design was apparent and was hindering progress with our operational NWP system development.

In May 2016 Met Éireann contacted ECMWF staff requesting access to a copy of their SAPP (Scalable Acquisition and Pre-Processing) System. A series of video meetings followed and Met Éireann hosted a SAPP workshop in 2017 which was attended by ECMWF staff and HIRLAM colleagues. In 2018 ECMWF Council approved a new Optional Programme to make SAPP available to Member and Co-operating States. During 2018 and 2019 Met Éireann staff (Eoin Whelan, Sarah Gallagher, Rónán Darcy and James Brennan) installed and developed the SAPP system for operational use.

The SAPP system has provided Met Éireann a robust flexible framework for processing and monitoring ob-

servations used in NWP. With SAPP more conventional observations are now available for operational data assimilation. New observation types, such as wind profiler and GNSS, are also available for testing and planned use in the next version of IREPS.

3.2 Operational implementation

ECMWF have provided the SAPP system as a virtual machine (VM). Two instances of SAPP (vsapp02a/b) have been installed in Met Éireann's virtual environment and have been running in pre-operational mode since June 2019. Both VMs process conventional observational data received from the GTS. The extraction of data for use in operational NWP has been tailored to Met Éireann's needs. A "short cut-off" (sc) stream has been implemented for use by IREPS and "nowcast" (nc) data stream has been implemented for a planned HARMONIE based nowcasting system to be developed in 2020. The use of BUFR data produced by SAPP was made operational for the 1200 UTC forecast on 19 November 2019.

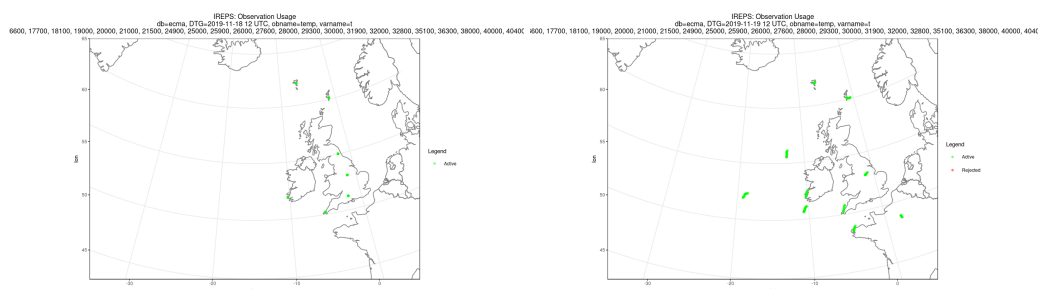


Figure 10: Radiosonde temperature observations assimilated by IREPS on the 18th (left) using ADE BUFR and (right) on the 19th using SAPP BUFR

4 Surface

A summary of recent preliminary work in the area of physiography, carried out by staff working at Met Éireann may be found at: <https://hirlam.org/trac/attachment/wiki/Meetings/Surface/Surface201911/nwp-note-201907.pdf>

As this is the first time we have looked at the physiography-related datasets over Ireland, we began by comparing the sand and clay maps in HARMONIE-AROME Cycle 43 FAO, SOILGRIDS, HWSO) with a locally available dataset created by an Irish organisation called Teagasc. As the local dataset only covers the Republic of Ireland, with Northern Ireland excluded, it was necessary to blend the local dataset with the maps available over the HARMONIE-AROME experiment area for our tests. We also looked at the ECOCLIMAP-SG land cover dataset and LAI input.

A brief summary of our findings to date is given below. More extensive testing is planned for the coming months using off-line SURFEX. We are also looking for other local datasets that could potentially be of use and we are investigating the possibility of using machine learning to extract useful parameters from mapping imagery such as Google Street View and OpenStreetMap.

1. Soil & Clay: As the SOILGRID and SOILGRID-BLEND (where SOILGRID-BLEND = SOILGRID + local data) soil and clay maps are similar, and significantly different to the lower resolution FAO maps, the SOILGRID maps can be considered to be of superior quality. The SOILGRID-BLEND maps provide additional local information, not included in SOILGRID, and are therefore the preferred choice. Testing using SURFEX in offline mode has commenced to get a better handle on sensitivities.

2. Land Cover: The water, urban and nature fractions in the ECOCLIMAP-SG land cover dataset are much

more realistic than in ECOCLIMAP2.5plus. For instance, in SG the Shannon Estuary is now clearly accounted for. All of Ireland's cities are larger than before, consistent with the growth that has taken place over recent decades. The land-sea mask seems to be much improved in general with more of the islands around the coast being resolved. Initial comparisons between SG and a small subset of the Ordnance Survey Ireland Prime 2 dataset have been made but so far no 3D or offline SURFEX runs have been made. It is not trivial to map the cover types in Prime 2 to those in SG to aid comparisons so this work is on-going.

3. Leaf Area Index: The climatologies of LAI used in HARMONIE-AROME are not sufficient for years that vary greatly from normal. An example of this occurred during the summer of 2018 when Ireland suffered a serious drought which resulted in the normally green island, turning a shade of brown. Figure 11 shows the large difference between the LAI in July 2018 and that of the climatologies used in HARMONIE-AROME and highlights the need for assimilating LAI data rather than using climatologies. Offline experiments are underway to investigate the differences between using satellite LAI for 2018 compared to multiyear climatologies.

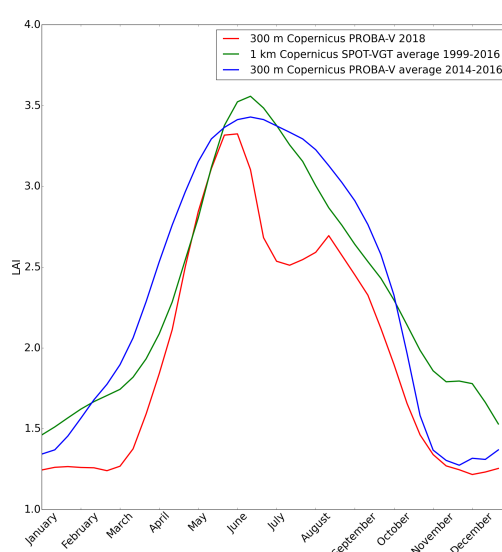


Figure 11: Annual cycle of mean LAI over Ireland plotted using: 300 m LAI data for 2018 from the Copernicus PROBA-V satellite (red), the Copernicus satellite SPOT-VGT LAI data averaged over the period 1999-2016 (green), the Copernicus satellite 300 m LAI data averaged over the period 2014-2016 (blue).

5 MUSC

The scripts that we have developed to run test cases of MUSC in HARMONIE-AROME Cycle 43 are document on the hirlam.org wiki under <https://hirlam.org/trac/wiki/HarmonieSystemDocumentation/MUSC>. Stephen Outten, who works at NERSC in Norway, developed a virtual box version of MUSC. Details about the installation of this are also provided on the MUSC wiki page. Further test cases will be added over the coming months.

6 MÉRA

With the completion of ERA-Interim in late 2019 the production of the MÉRA high resolution reanalysis for Ireland (Whelan et al. 2018, Gleeson et al. 2017) completed in early 2020. The dataset extends from January 1981 to August 2019. A user workshop was hosted by Met Éireann (<https://www.met.ie/science/events/mera->

workshop-2019) last May and invited presentations by representatives from Copernicus reanalysis projects were included on the programme. Presentation slides and the workshop proceedings are available on the website.

A new Irish reanalysis project, MÉRA-2, is planned for the coming years which will involve use of ECMWF ERA5 boundary conditions, a new version of HARMONIE-AROME and other useful upgrades.



Figure 12: MÉRA users workshop May 2019, National Botanic Gardens, Dublin.

7 Summary and Outlook

The past year has seen some significant NWP developments at Met Éireann. Significant work in the area of NWP during 2019, including the assimilation of radiance data and the operational implementation of SAPP, should put Met Éireann on a good footing for the coming years.

Early in 2020 five members of IREPS will start to run operationally on KNMI's HPCF with the other members continuing to run at ECMWF's HPCF. The operational version of HARMONIE-AROME will be upgraded from cycle 40h1.1 to 43h2.1 in the third quarter of 2020. Other planned NWP developments include the implementation of an NWP based nowcasting system, the assimilation of GNSS data and the evaluation of locally received Mode-S observations.

8 References

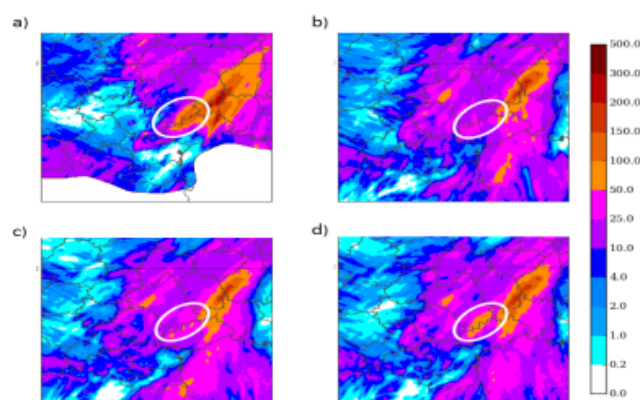
- Arriola, J.S., M. Lindskog, S. Thorsteinsson, and J. Bojarova, 2016: Variational Bias Correction of GNSS ZTD in the HARMONIE Modeling System, *J. Appl. Meteor. Climatol.*, 55, 1259–1276, <https://doi.org/10.1175/JAMC-D-15-0137.1>
- Auligné, T., McNally, A. P. and Dee, D. P., 2007: Adaptive bias correction for satellite data in a numerical weather prediction system, *Q.J.R. Meteorol. Soc.*, 133: 631–642. doi:10.1002/qj.56
- Clancy, C., Daly, C., Darcy, R., Gleeson, E., Hally, A. and Whelan, E., 2019: Met Éireann Updates. ALADIN-HIRLAM Newsletter No. 12.
- Gleeson, E., Whelan, E., and Hanley, J.: Met Éireann high resolution reanalysis for Ireland, *Adv. Sci. Res.*, 14, 49–61, <https://doi.org/10.5194/asr-14-49-2017>, 2017
- Whelan, E., Gleeson, E., Hanley, J., 2018: An Evaluation of MÉRA, a High-Resolution Mesoscale Regional Reanalysis, *J. Appl. Meteor. Climatol.*, 57, 2179–2196, <https://doi.org/10.1175/JAMC-D-17-0354.1>

Some numerical weather prediction activities in Moroccan Meteorological Service in 2019

Moroccan ALADIN team

1 1Dvar + 3Dvar assimilation of radar-gauge precipitation in AROME Framework.

The aim of this work is to investigate the impact of the assimilation of a radar-gauge precipitation analysis in the limited area model AROME . The proposed assimilation method is based on a two-step approach. Firstly, hourly precipitation is assimilated in a 1D-Var system to retrieve temperature and humidity profiles. The input data is provided by the French precipitation analysis ANTILOPE which combines radar and gauge data. The retrieved profiles are then converted to relative humidity profiles and assimilated in the AROME 3D-Var system. This method was applied to a heavy rain event which affected the French Mediterranean regions. The overall results showed a neutral impact for precipitation amounts bellow 10 mm and a positive impact on large amounts. The following paper gives more details on the method and on the results: Sahlaoui, et al 2020[1].



24h accumulated precipitation analysed by ANTILOPE (a) and simulated by AROME (b: No radar reflectivity ,c: operational suite ,d: AssimPrecip)

2 Local validation of Integrated Water Vapour (IWV) from AROME-MOROCCO using GPS-IWV.

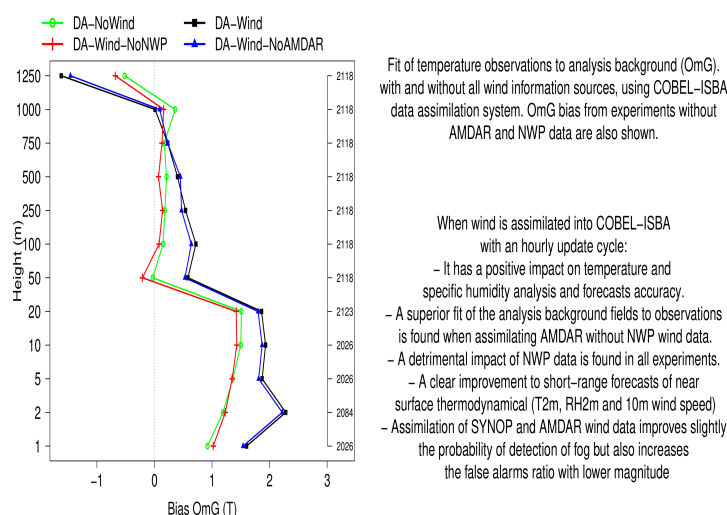
The aim of this work is to quantify locally water vapour from the GPS and to use it in order to validate the Integrated Water Vapor (IWV) forecasted by the AROME-MOROCCO model. The data used are measured by 9 GPS stations in Morocco, and are in near real time processed locally using BERNESE software (Hdidou et al. 2018) [2]. This validation is done through a statistical comparison over du 20th February to 20th March 2018, and through three case studies.

The evaluation results over this month showed a great agreement between GPS observations and 3hour-forecasts of IWV by AROME-MOROCCO, with a small underestimation in the coastal regions and a small overestimation in the continental regions. The mean bias is about 0.4mm.

In the three case studies the initiation of the precipitation events is detected in the time evolution of the measured IWV, opening the way for possible uses in nowcasting.

3 Wind assimilation in COBEL-ISBA using AMDARs, SYNOP observations and AROME

The assimilation impact of wind data from aircraft measurements (AMDAR), surface synoptic observations (SYNOP) and AROME_MOROCCO model, on short-range numerical weather forecasting (up to 12 h) and on the assimilation system, using the one-dimensional fog forecasting model COBEL-ISBA (Code de Brouillard à l'Échelle Locale-Interactions Soil Biosphere Atmosphere), is studied in the present work. The wind data are extracted at Nouasseur airport, Casablanca, Morocco, over a winter period from the national meteorological database. The impact is assessed by performing experiments with data denial tests, configured to be close to the operational settings. The assimilation system estimates the flow-dependent background covariances for each run of the model and takes the cross-correlations between temperature, humidity and wind components into account. When assimilated into COBEL-ISBA with an hourly update cycle, the wind field has a positive impact on temperature and specific humidity analysis and forecasts accuracy. Thus, a superior fit of the analysis background fields to observations is found when assimilating AMDAR without AROME-MOROCCO wind data. The latter has shown a detrimental impact in all experiments. Besides, wind assimilation gave a clear improvement to short-range forecasts of near-surface thermodynamical parameters. Although, assimilation of SYNOP and AMDAR wind measurements slightly improves the probability of detection of fog but also increases the false alarms ratio by a lower magnitude. More details on the method, the experimental design and the results can be found in (Bari 2019) [3].

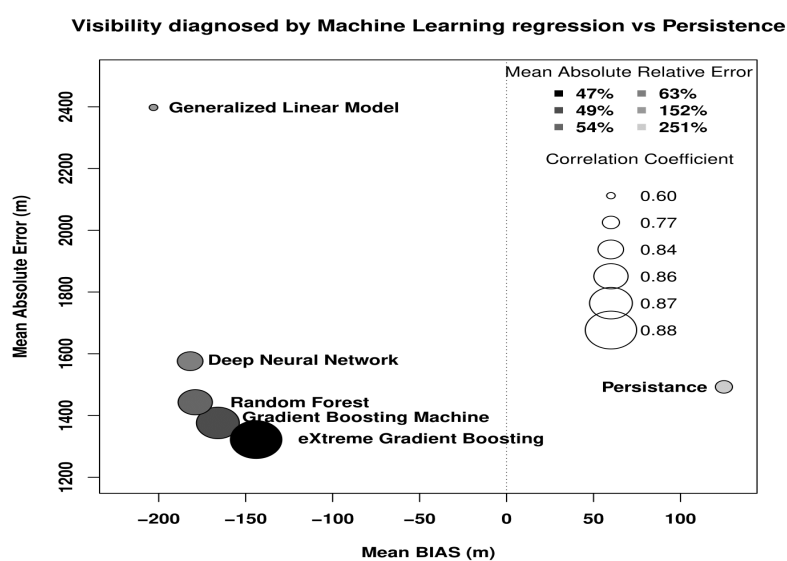


4 Use of Big data and Artificial intelligence in NWP:

Benchmark of the impact of the platform and the machine learning technique on the performance of the model developed: Case of a regression problem

Low visibility has been a challenge for weather forecasters for a long time, due to its negative impact on air, sea and road traffic. Indeed, the human and financial losses attributable to reduced visibility become increasingly important, hence a good forecast of horizontal visibility is of great benefit to meteorological forecasters. So, to cope with this challenge in the area of numerical weather prediction, the potential of Datamining techniques to estimate horizontal visibility has been evaluated in several scientific studies. However, the performance of developed models differs from one study to another due to the variety of Datamining tools and algorithms used. Therefore, the objective of our study is to evaluate the sensitivity of the performance of the developed models to the Datamining platform and al-

gorithm for a regression case which aims to estimate the visibility from the predictions of the operational numerical weather prediction AROME-MOROCCO model. To achieve this goal, we used two types of algorithms : those based on the ensemble methods including gradient boosting, eXtreme gradient boosting and random forest, and those based on deep learning. The algorithms are evaluated under various open source platforms (Scikit-learn, H2O, WEKA, Tensorflow and Keras). In addition, a database covering 3-year of hourly data, and resulting from preprocessing of the raw outputs of AROME-MOROCCO and the observed data, was used in this work. The sampling of these data in 70% for learning and 30% for testing was carried out by guaranteeing the representativeness of the months, the hours and the various classes of visibilities for all the synoptic stations. The results show that the performance of the models based on the ensemble methods is the best whatever the used platform except for Keras where only the Deep Learning was used. On the other hand, the Random Forest algorithm is found as the best estimator of visibility after tuning of hyperparameters for the WEKA and Scikit-learn platforms. However, Gradient boosting machine outperforms the other algorithms for the H2O platform. Besides, the mean squared errors are 1933 m, 1942 m and 1945 m respectively for Gradient Boosting under H2O, Random Forest for Scikit-learn and WEKA. Similarly for the mean absolute error took the following values 1199 m, 1221 m and 1232 m for the same algorithms and platforms.



5 References

- [1] Sahlaoui, Z, Mordane, S, Wattrelot, E, Mahfouf, J.F. Improving heavy rainfall forecasts by assimilating surface precipitation in the convective scale model AROME: A case study of the Mediterranean event of November 4, 2017. *Meteorol Appl.* 2020; 27:e1860. <https://doi.org/10.1002/met.1860>.
- [2] Hdidou, FZ, Mordane, S, Sbi, S. Global positioning systems meteorology over Morocco: accuracy assessment and comparison of zenith tropospheric delay from global positioning systems and radiosondes. *Meteorol Appl.* 2018; 25: 606– 613. <https://doi.org/10.1002/met.1725>
- [3] Bari, D. A Preliminary Impact Study of Wind on Assimilation and Forecast Systems into the One-Dimensional Fog Forecasting Model COBEL-ISBA over Morocco. *Atmosphere.* 2019. 10(10), 615; <https://doi.org/10.3390/atmos10100615>.

Wind turbine parameterisation in HARMONIE-AROME

Bart J.H. van Stratum^{1,*}, Sukanta Basu², Ine L. Wijnant¹, Jan Barkmeijer¹,
Jeanette Onvlee¹, A. Pier Siebesma^{1,2}

¹ Royal Netherlands Meteorological Institute (KNMI), ² Delft University of Technology

* Now at: Wageningen University and Research (bart.vanstratum@wur.nl)

1 Introduction

Offshore wind power production in the European Union (EU) and specifically the North-Sea region is steadily increasing: the Dutch offshore capacity is expected to grow from ± 1 GW in 2019 to ± 11.5 GW in 2030, as part of a total expected increase to ± 70 GW in the entire EU (WindEurope, 2017). Wind turbines produce electric energy by extracting kinetic energy from the atmosphere, thereby decelerating (and agitating) the air. This typically results in a downstream decrease in wind speed and increase in turbulence (e.g. Baidya Roy & Traiteur, 2010; Fitch et al., 2012). As wind farms grow – both in size and number – the impact on weather and climate is expected to become more significant, requiring an adaptation of mesoscale models like HARMONIE-AROME (hereafter: HARMONIE) to account for the influence of wind farms on the local and regional meteorological conditions.

As part of the Dutch Offshore Wind Atlas (DOWA, www.dutchoffshorewindatlas.nl) project, we implemented the wind turbine parameterisation from Fitch et al. (2012) in HARMONIE. In the presence of wind turbines, this parameterisation adds an elevated drag term to the atmosphere, which locally decelerates the flow. The kinetic energy that is extracted from the atmosphere, but not converted into electric power, is used as a source term of turbulence kinetic energy (TKE).

As a first validation of the new wind turbine parameterisation in HARMONIE, four 48-hour experiments were compared to both experiments with the original code of Fitch et al. (2012) in WRF-ARW (hereafter: WRF), and available offshore measurements near the Dutch/Belgium coast.

Next, we repeated 6 months of the DOWA reanalysis with the wind farm parameterisation and all current offshore wind farms in the North-Sea region included. The motivation for this experiment was twofold: first, to more thoroughly validate the wind farm parameterisation. During the chosen period from January to (including) June 2016, two floating lidars were available in the Borssele wind farm zone, one in the Westermost Rough wind farm, with additionally FINO1 tower measurements near the Alpha Ventus wind farm. Since all these measurements are in or near existing wind farms, they are ideal for validating the new wind farm parameterisation. Secondly, the six month experiment allowed us to quantify the impact of the offshore wind farms on the Dutch offshore and coastal meteorological conditions.

The content of this article is as follows: section 2 describes the wind farm parameterisation in HARMONIE, including a description of the code organisation and required input files. Section 3 contains the brief validation of HARMONIE with WRF, followed by the description and analysis of the 6 month HARMONIE reanalysis in section 4.

2 Model description

2.1 HARMONIE-AROME

The wind farm parameterisation is implemented in HARMONIE (cycle 40h1.2tg2), a mesoscale model developed by the ALADIN-HIRLAM consortium, which is operationally used in 10 European countries (Bengtsson et al., 2017). The base version contains several minor modifications, mostly related to the ERA5 boundaries and statistics output (Wijnant et al., 2019), and the data-assimilation (Fischer et al., 2005; Gustafsson et al., 2018) of Mode-S EHS aircraft (e.g. de Haan, 2011, 2016) and *Advanced Scatterometer* (ASCAT) observations. Additional changes related to the wind farm parameterisation are described in the remainder of this section.

2.2 Wind farm parameterisation

This section briefly summarises the wind farm parameterisation from Fitch et al. (2012). For details, see the original publication.

The wind farm parameterisation of Fitch et al. (2012) imposes an elevated momentum sink on the mean flow, where the drag (or thrust) of the individual turbine blades is modelled as a constant (but wind speed dependent) drag force across the area swept by the rotor blades. As the diameter of a wind turbine is about an order of magnitude smaller than the horizontal grid spacing in HARMONIE (currently: 2.5 km), the model accounts for the bulk influence of one or several wind turbines per grid point.

The wind turbine characteristics are defined by the geometry (hub-height z_{hub} and turbine radius r), the cut-in (V_{in}) and cut-out (V_{out}) wind speeds, and by the dimensionless power (C_P) and thrust (C_T) coefficients. The latter two describe – as a function of wind speed V_{hub} at hub height – the fraction of kinetic energy that is extracted from the air (C_T), and the fraction that is converted into electrical energy (C_P). An example of typical C_P and C_T curves is provided in Fig. 1a.

Given the thrust coefficient C_T , the thrust force of a turbine (the force opposite to the flow direction and drag force) is defined as:

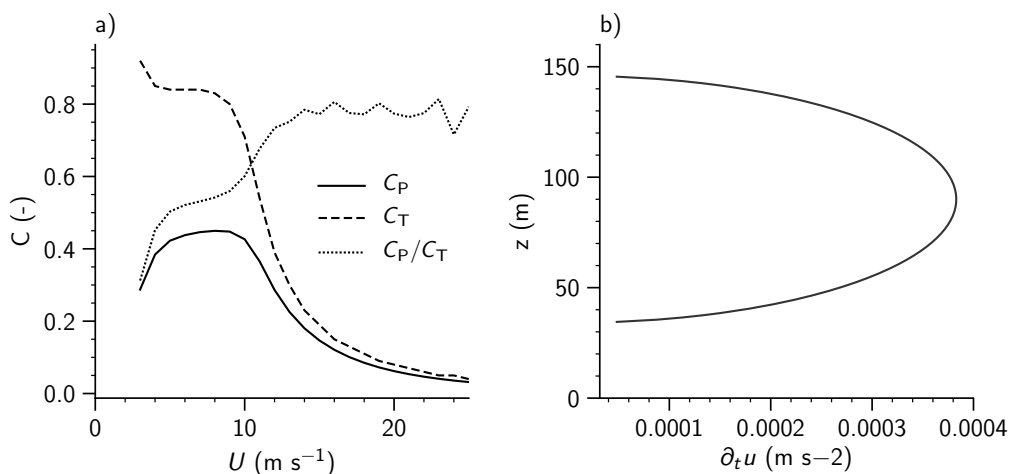


Figure 1: a) Example thrust and power coefficients, from a Vestas V112 turbine. For this model, $V_{\text{in}} = 3 \text{ m s}^{-1}$ and $V_{\text{out}} = 25 \text{ m s}^{-1}$. b) Example of the momentum sink as a function of height, for a wind speed (constant with height) of 15 m s^{-1} , and a turbine with $z_{\text{hub}}=90 \text{ m}$, $r=56 \text{ m}$.

$$\vec{F}_{\text{thrust}} = -\frac{1}{2}\rho C_T |\vec{V}| \vec{V} A_T, \quad [\text{N}] \quad (1)$$

where ρ is the air density (kg m^{-3}), $\vec{V} = (u, v)$ the horizontal wind vector (m s^{-1}), $|\vec{V}| = \sqrt{u^2 + v^2}$, and A_T is the rotor area (m^2). The rate of loss of kinetic energy (KE) then equals:

$$\left. \frac{\partial \text{KE}}{\partial t} \right|_{\text{drag}} = -\frac{1}{2}\rho C_T |\vec{V}|^3 A_T. \quad [\text{J s}^{-1}] \quad (2)$$

In practise, the rotor of a turbine intersects multiple model levels, and Eq 2 (and all equations in the remainder of this section) are solved for each model level k individually, replacing the rotor area A_T with the area intersected by the k -th grid level, and the wind speed $|\vec{V}|$, and density ρ with values from the k -th grid level, indicated where appropriate by a subscript k . As a result, the momentum sink (and TKE source) is elevated and height dependent, as illustrated in Fig. 1b.

In general, the total change in KE of a single grid cell with a volume $\Delta_k = (\Delta x \Delta y \Delta z_k)$ m^3 equals:

$$\left. \frac{\partial \text{KE}_k}{\partial t} \right|_{\text{cell}} = \frac{\partial}{\partial t} \left(\frac{1}{2} \rho_k |\vec{V}_k|^2 \right) \Delta_k = \rho_k |\vec{V}_k| \frac{\partial |\vec{V}_k|}{\partial t} \Delta_k. \quad [\text{J s}^{-1}] \quad (3)$$

Combining Eqs 2 and 3, i.e. setting:

$$\left. \frac{\partial \text{KE}_k}{\partial t} \right|_{\text{cell}} = \left. \frac{\partial \text{KE}_k}{\partial t} \right|_{\text{drag}}, \quad [\text{J s}^{-1}] \quad (4)$$

results, after re-arranging, in an expression for the change in velocity with time:

$$\frac{\partial |\vec{V}_k|}{\partial t} = -\frac{1}{2} C_T |\vec{V}_k|^2 A_k \Delta_k^{-1}, \quad [\text{m s}^{-2}] \quad (5)$$

or, in component form:

$$\frac{\partial u_k}{\partial t} = -\frac{1}{2} C_T u_k |\vec{V}_k| A_k \Delta_k^{-1}, \quad [\text{m s}^{-2}] \quad (6)$$

$$\frac{\partial v_k}{\partial t} = -\frac{1}{2} C_T v_k |\vec{V}_k| A_k \Delta_k^{-1}. \quad [\text{m s}^{-2}] \quad (7)$$

The vertical velocity component is assumed to be unaffected by the wind turbines, and furthermore, drag by the wind turbine tower and nacelle is not included in the parameterisation. The energy that is extracted from the atmosphere, but not converted into electrical energy, is assumed to be converted into turbulence kinetic energy (TKE, per unit mass), i.e. $C_{\text{TKE}} = C_T - C_P$, resulting in:

$$\frac{\partial \text{TKE}_k}{\partial t} = \frac{1}{2} C_{\text{TKE}} |\vec{V}_k|^3 A_k \Delta_k^{-1}. \quad [\text{m}^2 \text{s}^{-2} \text{s}^{-1}] \quad (8)$$

Finally, as a diagnostic quantity, the model outputs the electrical power produced by the wind turbines:

$$P = \frac{1}{2} \rho C_P A_T |\vec{V}_{\text{hub}}|^3 \quad [\text{W}] \quad (9)$$

For a typical offshore wind farm, multiple wind turbines can occupy a single horizontal grid point. Instead of introducing a horizontal wind turbine density – like in Fitch et al. (2012) – Eqs 6 to 9 are repeated for each individual turbine, allowing different turbine types in a single horizontal grid point.

2.3 Code description

The majority of the wind farm parameterisation is implemented in a single Fortran module: (`src/arpifs/module/windfarm_mod.F90`). This module contains two main subroutines, one which handles the initialisation (reading of turbine locations/types/properties, and mapping of the turbines to grid points), and one which calculates the tendencies of u , v and TKE each model time step using Eqs 6, 7 and 8, and the power production using Eq. 9. The wind farm parameterisation is called from:

```
src/arpifs/phys_dmn/apl_arome.F90.
```

2.4 Input files

The wind farm parameterisation requires two sets of input files: one with the latitude, longitude and turbine type of each individual turbine (`wind_turbine_coordinates.tab`), and for each turbine type, a file with the turbine characteristics (`wind_turbine_xxx.tab`). The latter contains information on the turbine geometry, the thrust coefficients used below and above the cut-in and cut-out wind speeds, and a table with the power and thrust coefficients as a function of wind speed. The first and last wind speed included in the table defines the cut-in and cut-out wind speeds. Both file types are currently ASCII files, and need to be present in the `$HM_DATA/climate` directory before the start of the experiment.

3 WRF-HARMONIE intercomparison

3.1 Introduction

As a first validation of the new wind farm parameterisation in HARMONIE, we compared the results with data obtained from the original wind farm parameterisation in WRF. The comparison focussed on the Belgium *Northwind*, *C-Power*, and *Belwind* sites, located approximately 35 km of the Dutch/Belgium coast (Fig. 2). The comparison was mostly aimed at assessing whether the wind farm parameterisation in HARMONIE produces sensible results, i.e. whether HARMONIE produces a similar wake strength, increase in TKE, and power production. Where possible, the results were compared to measurements.

3.2 Model setup

HARMONIE (40h1.2tg2) used the same domain and experimental setup as used in the DOWA reanalysis (2000×2000 km² domain with 65 vertical grid levels, 2.5 km horizontal grid spacing, centred around 51.96°N, 4.9°E).

The WRF experiments were performed using the NOAH land surface model, MYNN2 boundary layer scheme, RRTMG long- and short wave radiation, and the single moment WSM 5-class microphysics scheme. The spatial grid was chosen to match the HARMONIE grid as closely as possible. However, a small spatial shift was still present, influencing the mapping of turbines to individual grid points, as shown in Fig. 3.

The wind turbine coordinates were obtained from Whiffle¹, the turbine characteristics from Delft University of Technology.

Both HARMONIE and WRF used ERA5 for the initial and boundary conditions, and performed 48 hour time integrations, for simplicity without data assimilation. Four periods were considered: 2016-02-01 00 UTC to

¹<http://www.weatherfinecasting.com/>

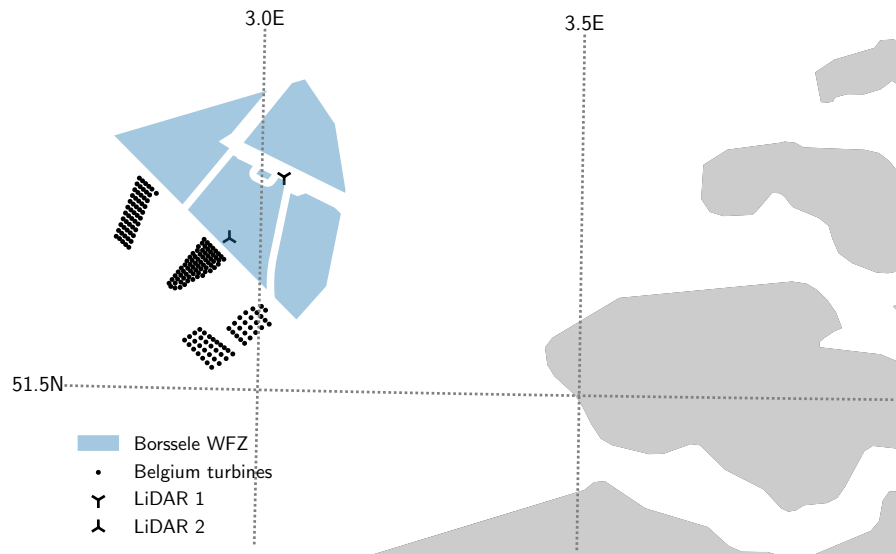


Figure 2: Existing Belgium wind turbines (individual dots), with the future Borssele wind farm zones.

2016-02-03 00 UTC, with both HARMONIE and WRF experiment with and without the wind farm parameterisation, and 2016-08-05 00 UTC to 2016-08-07 00 UTC (stable conditions), 2016-07-07 00 UTC to 2016-07-09 00 UTC (neutral conditions) and 2016-09-30 00 UTC to 2016-10-02 00 UTC (unstable conditions) with only experiments using the wind farm parameterisation. The comparison here focusses mostly on the first time period, as without reference experiments without wind turbines, it is difficult to quantify the impact of the turbine parameterisation.

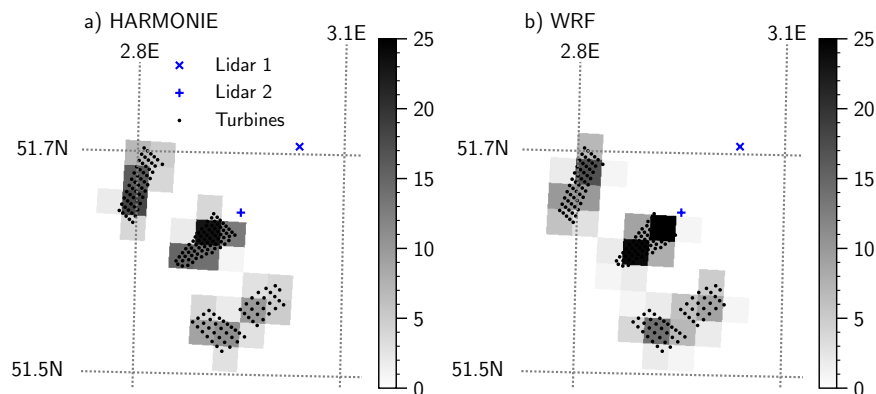


Figure 3: Mapping of wind turbines to grid points; the shading indicates the number of turbines per 2.5×2.5 km² grid point. Both lidars are part of the Borssele metocean campaign by Fugro

3.3 Results

3.3.1 Atmospheric impact of wind turbines

Fig. 4 (a,b) shows time series of the 100m wind speed and TKE, averaged over all grid points with one or more turbines (Fig. 3), for the 2016-02-01 00 UTC to 2016-02-03 00 UTC period. Over the first 24 hours, both

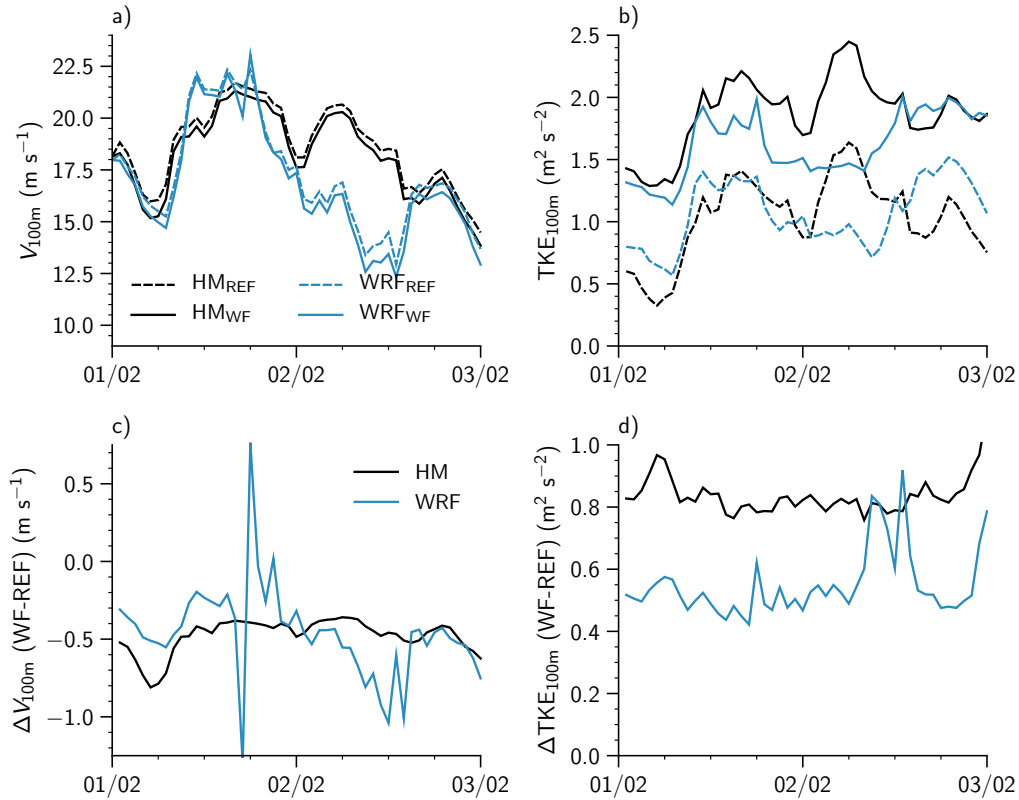


Figure 4: Top: time series of the 100 m wind speed and TKE from HARMONIE (HM) and WRF, with (WF) and without (REF) the wind turbine parameterisation. Bottom: differences between the WF and REF experiments, for both models.

the wind speed and TKE are comparable in HARMONIE and WRF, both for the experiments with (WF) and without (REF) the turbine parameterisation. Including the wind turbine parameterisation decreases the wind speed and increases TKE, as expected. Without data-assimilation or another mechanism to keep the models close to reality, the results start to drift apart over the second 24-hour period, hindering the comparison.

Fig. 4 (c,d) shows the same quantities, but as the difference between the experiments with and without the turbine parameterisation. The decrease in wind speed is similar in HARMONIE and WRF, but the increase in TKE is clearly higher in HARMONIE. This result can be explained by examining the time averaged vertical profiles, as shown in Fig. 5. The decrease in wind speed is comparable in both models, over the entire layer influenced by the wind turbines. However, the increase in TKE shows a different pattern; in HARMONIE the increase is mostly limited to the vertical extent of the wind turbines (~ 0 -200 m), whereas WRF mixes the increase in TKE over a deeper layer. Such differences outside the layer directly influenced by the turbine parameterisation are unlikely to be caused by the turbine parameterisation itself, and are more likely the result of differences in the vertical mixing schemes.

3.4 Power production

Elia (Belgium's transmission system operator) provides time series of the observed total power production (P) of the offshore Belgium wind farms. As the power production scales with the velocity cubed (Eq. 9), it is very sensitive to errors in the modelled wind speed, and as such it is a useful parameter to both validate and compare HARMONIE and WRF.

Figure 6 shows the comparison between the Elia measurements, HARMONIE, and WRF. For all experiments

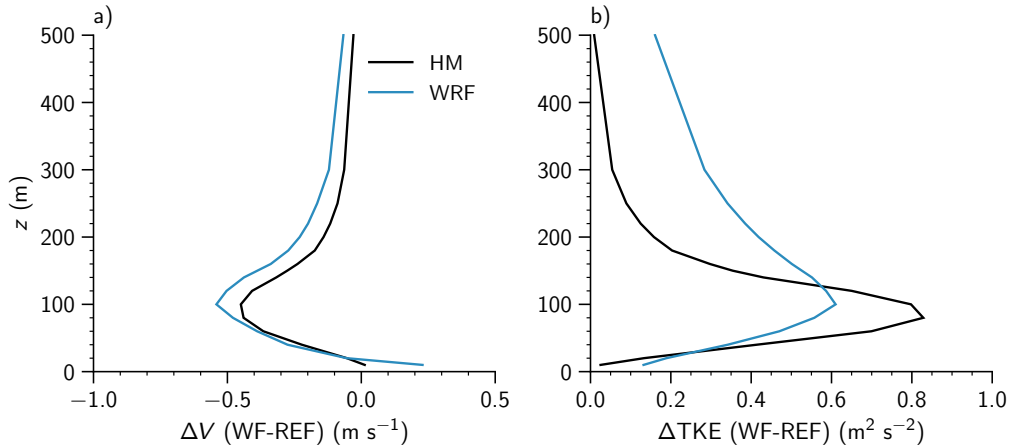


Figure 5: Time averaged vertical profiles of the difference in wind speed and TKE between the experiments with and without the turbine parameterisation.

the power production from the HARMONIE experiments without wind turbines is included as well, which was simply diagnosed offline from the model output using Eq. 9.

During the first time period (01-02-2016 to 03-02-2016), the wind speed was mostly such high that all three wind farms were operating at their peak (rated) power production. Theoretically, the three farms combined can produce ~ 716 MW, which is reproduced by both HARMONIE and WRF. However, the measurements show a clear upper limit of only ~ 650 MW. There are several possible explanations for this discrepancy – e.g. efficiency losses, curtailment, or turbines which were offline for maintenance – but the exact reason for these differences could not be ascertained.

For the other three periods, when the wind farms were not operating at their rated power, the agreement between measurements and the model predictions is better. On average, both HARMONIE and WRF with the wind turbine parameterisation reproduce the observed power production over the entire range from 0 to ~ 600 MW, without showing a clear bias. The power production diagnosed from the HARMONIE experiments without turbine parameterisation (HM_{REF}) shows a clear positive bias compared to the measurements. This indicated that the turbine parameterisation in both WRF and HARMONIE sufficiently reduces the wind speed to produce realistic power production estimates.

3.5 Conclusion

The new wind turbine parameterisation in HARMONIE produces results which are comparable to results obtained from the original parameterisation in WRF. The local decrease in wind speed – caused by the wind turbine parameterisation – is nearly identical in both models, and the decrease in TKE is similar, although with a different distribution with height. Compared to the observed power production data from Elia, both HARMONIE and WRF perform similar. Furthermore, the predicted power production from HARMONIE with wind turbine parameterisation shows a clear improvement compared to the power production calculated from the experiments without wind turbines. Overall, these results gave confidence that the wind turbine parameterisation in HARMONIE is producing sensible results.

4 DOWA reanalysis with wind farms

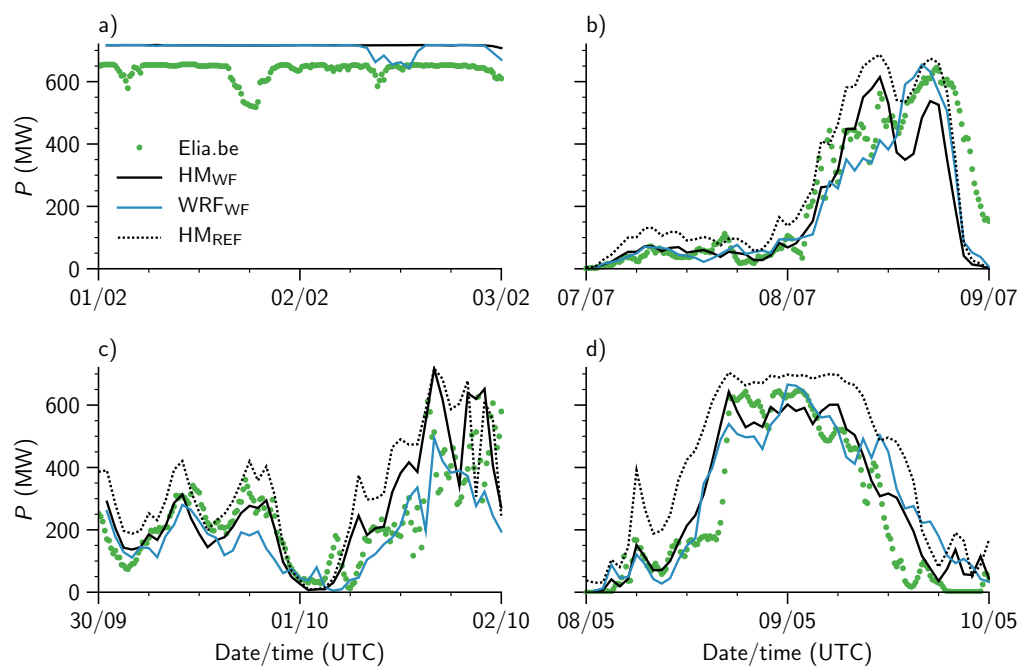


Figure 6: Power production compared to the measurements from Elia.be

4.1 Introduction

To further validate the wind farm parameterisation with offshore measurements, and to quantify the impact of offshore wind farms on a typical HARMONIE experiment, we performed a 6 month reanalysis with all current offshore wind farms in the North-sea region included (Fig. 7).

The experiments were validated with wind speed measurements from two floating wind lidars in the Borssele wind farm zone (BWFZ), one platform mounted wind lidar at Westermost Rough wind farm and one mast mounted cup anemometer at FINO1. The experiments were also validated with power production data from the Belgium wind farms.

This section documents the experimental setup and provides a basic validation of the experiments, a more thorough validation is provided by Ramakrishnan (2019) as part of a MSc thesis at the Delft University of Technology.

4.2 Wind turbine properties and locations

For the Belgium² and Dutch³ wind farms, the exact (individual) turbine coordinates are available, which could directly be used in the experiments. For the other offshore wind farms in the computational domain (Fig. 7), the available information was limited to the wind farm boundaries and the total number of turbines per wind farm. For these sites, the turbine coordinates were first chosen randomly within the wind farm boundary, and next distributed uniformly using an iterative repulsion method (Witkin & Heckbert, 2005), as illustrated in Fig. 8. This random approach to determine the turbine coordinates can be justified by the fact that within the turbine parameterisation, all turbines are mapped to the nearest 2.5×2.5 km grid point, making the exact turbine coordinates less important. The wind farm boundaries were obtained from the *The European Marine Observation and Data Network* (EMODnet)⁴.

²Northwind, C-Power, and Belwind

³Egmond aan Zee, Princes Amalia, Luchterduinen, and Gemini

⁴[https://www.emodnet-humanactivities.eu/search-results.php?dataname=Wind+Farms+\(Polygons\)](https://www.emodnet-humanactivities.eu/search-results.php?dataname=Wind+Farms+(Polygons))

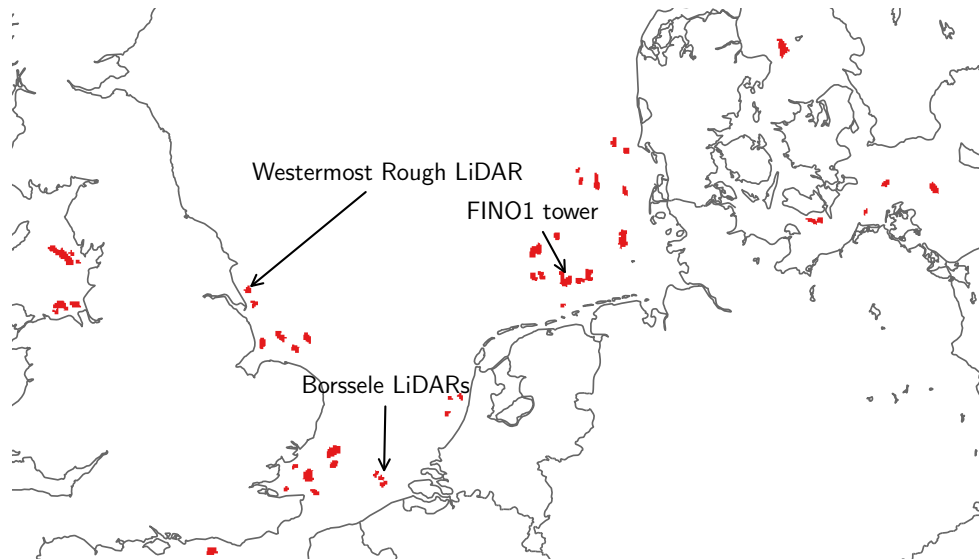


Figure 7: Overview of all (2.5×2.5 km) grid points with one or more wind turbines (red).

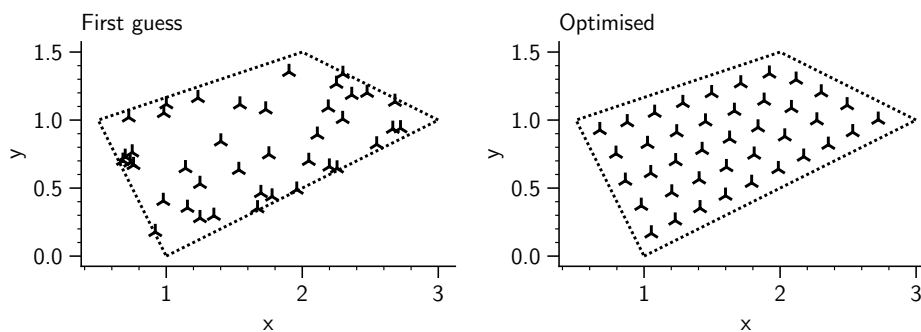


Figure 8: Example of the random placement of wind turbines within a known wind farm boundary, with (left) the first random guess, and (right) the final optimised locations.

The C_P and C_T curves were obtained from various sources, predominantly from windPRO⁵. For a small number of turbines, no C_P and C_T curves were publicly available, those turbines have been replaced with either reference data from literature, or C_P and C_T curves from similar turbines. An overview is provided in Table 1.

4.3 Experiments

The HARMONIE setup is identical to the setup of the original DOWA reanalysis. The experiments run from 01-01-2016 00 UTC to 01-07-2016 00 UTC. This period was chosen because of the availability of two floating lidars in the Borssele wind farm zone⁶, directly north-east of the (Belgium) Northwind wind farm (Fig. 3 & 7). In addition, for this period there are tower measurements from the FINO1 platform⁷, and lidar measurements from the Westermost Rough wind farm⁸.

⁵<https://www.emd.dk/windpro/>

⁶<https://offshorewind.rvo.nl/studiesborssele>

⁷<https://www.fino1.de/en/>

⁸<https://orsted.com/en/Our-business/Offshore-wind/Wind-Data>

Name	N	P (MW)	D (m)	
Siemens SWT-2.3-82	72	2.3	72	
Siemens SWT-2.3-93	202	2.3	93	
Siemens SWT-3.6-107	563	3.6	107	
Siemens SWT-3.6-120	899	3.6	120	
Siemens SWT-4.0-120	78	4.0	120	
Siemens SWT-4.0-130	222	4.0	130	
Siemens SWT-6.0-154	478	6.0	154	(1)
Siemens SWT-7.0-154	47	7.0	154	(1)
Vestas V80-2.0	170	2.0	80	
Vestas V90-3.0	251	3.0	90	
Vestas V112-3.0	188	3.0	112	
Vestas V112-3.3	15	3.3	112	
Vestas V112-3.45	116	3.45	112	
Vestas V164-8.0	139	8.0	164	(2)
Senvion 5	30	5.0	126	
Senvion 6.2	156	6.2	126	
BARD-5.0	80	5.0	126	(3)
Adwen-5.0	202	5.0	116	(3)
Haliade-6	1	6.0	100	
	3908	460×10^3		

Table 1: Overview of the wind turbine types included in the experiments. The total installed power equals $\sum N \times P$. Notes: (1) replaced with 6 MW reference turbine from Bulder et al. (2016), (2) replaced with 8 MW reference turbine from Bulder et al. (2016), (3) replaced with Senvion 5 turbine.

4.4 Validation

The first part of the validation focusses on the offshore lidar and tower measurements. During the chosen period, all lidars had periods with missing data, as summarised in Fig. 9. The lidars in the Borssele wind farm zone (BWFZ) became operational in mid February, and have (overall) a good availability of measurements afterwards. The Westernmost Rough (WMR) lidar became operational in mid January, but only has an overall availability of $\sim 25\%$ (1.5 out of 6 months), which limits its usability.

For all statistical analyses in this section we use collocated data, i.e. missing data in the measurements is removed (or masked) in the model dataset as well. In addition, there is no conditional sampling based on (e.g.) wind direction; all available measurements are always included in the statistics.

4.5 Offshore lidar and tower measurements

4.5.1 Borssele Wind Farm Zone (BWFZ) lidars

As part of the wind resource assessment for the Borssele wind farm zone (BWFZ), Fugro⁹ conducted a metocean campaign using (amongst other observations) two floating lidars. As shown in Fig. 2, both lidars were positioned north-east of the Belgium Northwind wind farm. With prevailing winds from the south-west, these lidar measurements are typically disturbed by the Belgium wind farms, making them ideal for assessing the impact of the wind turbines on the wind field, and the ability of the wind farm parametrisation to reproduce the disturbed wind field due to the wake effect of the wind farm.

Figure 10 shows the time averaged vertical wind speed profiles from the DOWA reanalysis (DOWA), the ex-

⁹www.fugro.com

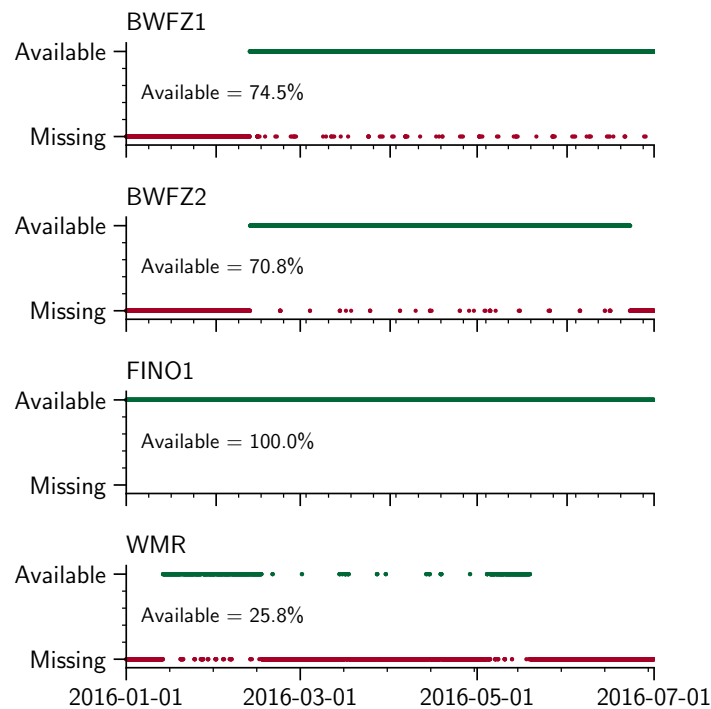


Figure 9: Availability measurements.

periment with the wind farm parameterisation (WFP), and the Borssele lidars.

For both sites the DOWA reanalysis overestimates the wind speed, which is most pronounced for lidar location number two, which is closest to the Belgium wind farms. Enabling the wind farm parameterisation clearly improves the experiments; for location two, the mean profile from HARMONIE matches nearly perfect with the measurements, for location one the model slightly underestimates the wind speed.

4.5.2 FINO1 tower

Approximately 50 km north of the Wadden island Borkum, the FINO1 research site provides continuous meteorological tower measurements at heights of 35 m to 100 m. The tower is situated directly west of the Alpha Ventus wind farm, and north-east of the Borkum Riffgrund wind farm (Fig. 7). Because of the measurement setup, with observations at only one side of the tower, the wind speed measurements need to be corrected to account for upwind blocking, lateral speedup, and downwind wake effects from the mast (Westerhellweg et al., 2012).

Fig. 11a shows the time averaged vertical wind speed profiles, compared to the corrected FINO1 measurements. In line with the results from the Borssele area, the DOWA reanalysis overestimates the wind speed with ~ 0.6 - 0.8 m s^{-1} . With the wind farm parameterisation included, the absolute bias is decreased, but with a negative bias of ~ 0.1 - 0.4 m s^{-1} . This underestimation seems to be partially caused by the mapping of wind turbines to the nearest HARMONIE grid point. In reality the FINO1 tower is west (and with the dominating wind direction: upstream) of the Alpha Ventus wind farm, but in HARMONIE the grid point nearest to FINO1 also houses some of the Alpha Ventus wind turbines, as shown in Fig. 11b. This means that the grid point used for the analysis, directly experiences drag from some of the Alpha Ventus turbines, resulting in a reduced wind speed.

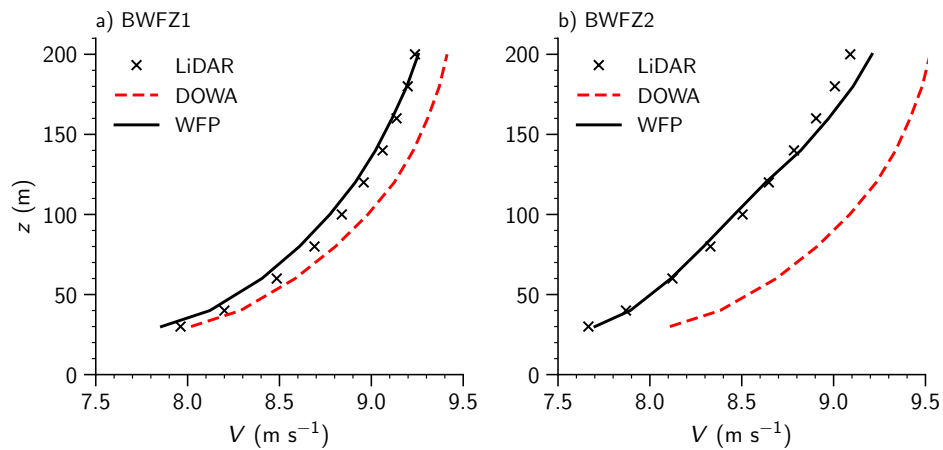


Figure 10: Vertical profiles of wind speed, from the normal DOWA reanalysis (DOWA) and experiment with wind farm parameterisation (WFP), compared to the Borssele lidars.

4.5.3 Westermost Rough lidar

On top of the Westermost Rough wind farm substation (Fig. 7), Ørsted operates a lidar, providing wind speed measurements between 74 m to 324 m height. Unlike the Borssele lidars and FINO1 tower, this lidar is located in the centre of the wind farm, and is therefore always disturbed by the wind turbines. As shown in Fig. 9, the data availability is limited to $\sim 25\%$ of the January to June period, and even less at the three highest measurement heights. Therefore, the analysis here is limited to the lowest 214 m.

Fig. 12 shows the time averaged vertical profiles of the lidar measurements and HARMONIE experiments. As with the FINO1 location, the original DOWA reanalysis overestimates the wind speed, and the experiment with wind turbines has a smaller mean – but negative bias. However, overall the mean bias is relatively small at a maximum of -0.3 m s^{-1} .

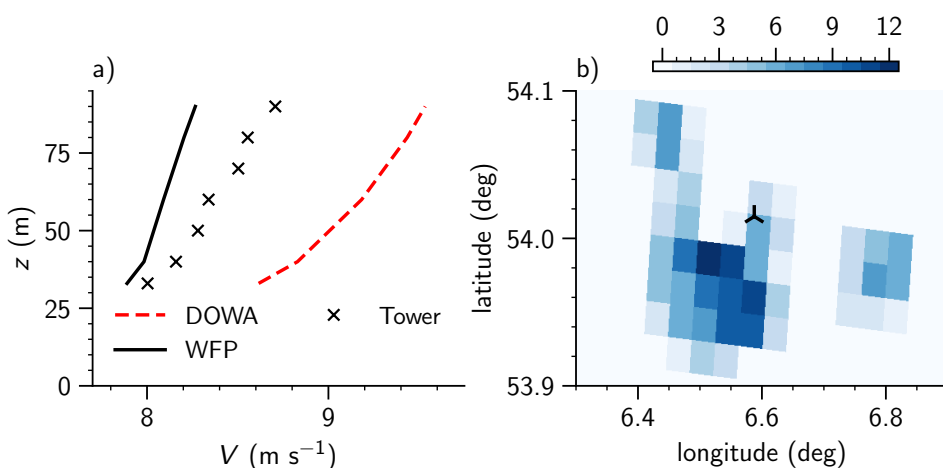


Figure 11: Vertical profiles of wind speed, from the normal DOWA reanalysis (DOWA) and experiment with wind farm parameterisation (WFP), compared to the FINO1 tower.

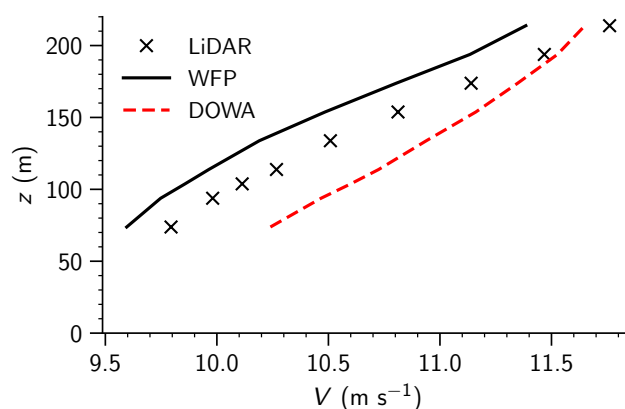


Figure 12: Vertical profiles of wind speed, from the normal DOWA reanalysis (DOWA) and experiment with wind farm parameterisation (WFP), compared to the Westermost rough lidar.

4.6 Power production

As mentioned in section 3, power production is an interesting quantity to use for validation as it scales with the velocity cubed, making it sensitive to biases in wind speed. For the full period considered here, Elia provides power production data for the Belgium offshore wind farms.

Figure 13 shows the comparison between the observed power production and power production obtained from the HARMONIE experiments, both from the normal DOWA reanalysis (DOWA) and experiment with the wind turbine parameterisation (WFP). The bottom panels indicate the absolute and relative differences, averaged over 50 MW bins. The relative bias from the first (0-50 MW) bin should be treated with caution, as conditions where the observed power production equals zero result in an infinitely large relative bias.

The power production calculated offline from the DOWA reanalysis clearly overestimates the production, with absolute biases as large as 150 MW, and for low wind speeds (low power production) relative biases as large as 100%. Including the wind turbine parameterisation clearly improves the power production forecast, reducing the absolute bias to a maximum of 50 MW at high wind speeds, and the relative bias to $\sim 6\%$. There are a few possible causes for this constant relative bias – e.g. efficiency losses in the turbines or power cables, the use of (manufacturers) turbine specifications which are too optimistic, or inaccuracies in the turbine parameterisation – but the exact cause could not be traced.

4.7 Impact wind farms on local meteorological conditions

As has become clear from the validation results, wind turbines have an impact on the (local) wind conditions. In addition, wind turbines generate TKE, which enhances vertical mixing, potentially influencing other quantities like temperature, humidity, or clouds.

In this section we briefly examine the impact of the Dutch offshore wind farms on the local meteorological conditions. In the absence of suitable measurements, the results are limited to comparing just the model results, from the original DOWA reanalysis and the experiments with wind turbines.

Fig. 14 shows the differences in wind speed (V), temperature (T), specific humidity (q) and relative humidity (RH) between the experiments with and without wind turbines. For each wind farm, the statistics were averaged over the HARMONIE grid points which have one or more turbines, and averaged in time.

For wind speed, the elevated drag is clearly visible, with a maximum decrease of -1 m s^{-1} near hub height, but a near-surface decrease which is almost zero. The relatively small wind farms near the Dutch west coast

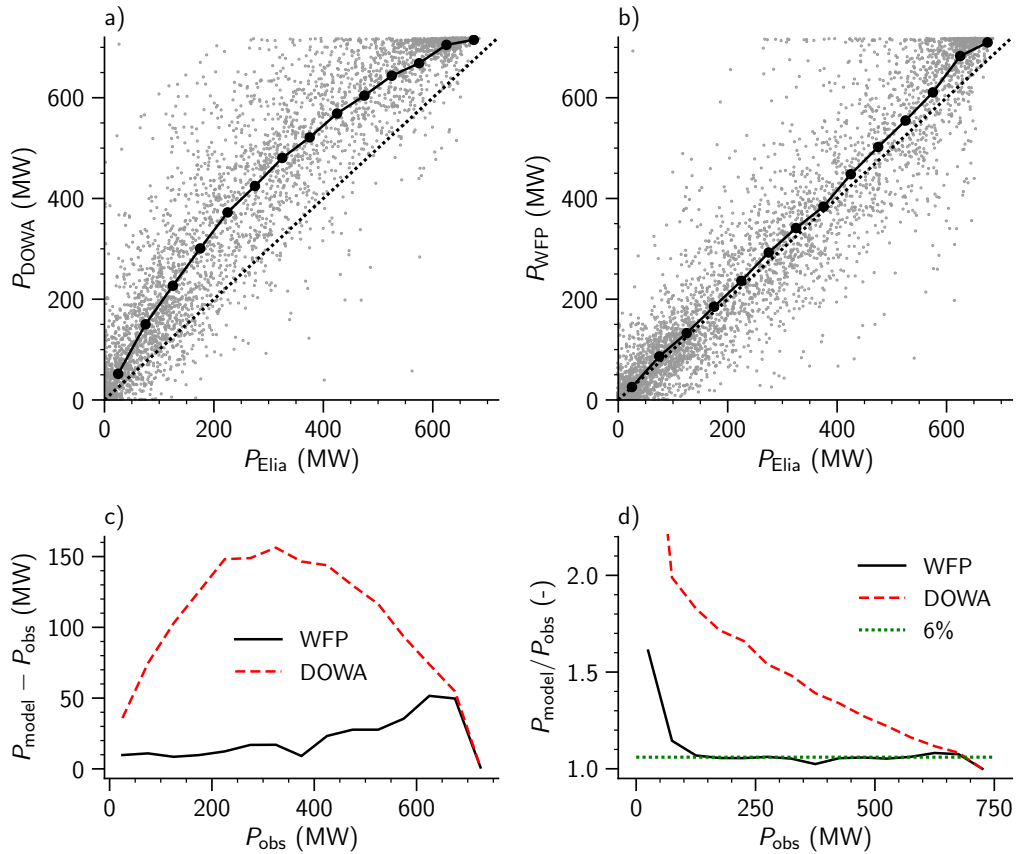


Figure 13: Power production calculated from the (a) normal DOWA reanalysis (REF) and (b) experiment with wind farm parameterisation (WFP), compared to the Elia measurements. The solid black line with markers (top row) indicates the mean of the model data calculated over 50 MW bins. The bottom row shows the absolute (c) and relative (d) error of both model experiments.

(*Egmond aan Zee*; 108 MW, *Princes Amalia*; 120 MW, *Luchterduinen*; 129 MW) have a smaller impact than the larger *Buitengaats* and *ZeeEnergie* (combined called *Gemini*; total of 600 MW) farms.

The enhanced vertical mixing has a weak impact on temperature and specific humidity. For these offshore locations, and for the period considered, the atmosphere is on average stably stratified, with an increase in potential temperature and decrease in specific humidity with height. Additional vertical mixing tends to decrease the stratification, resulting in an increase in temperature and decrease in specific humidity near the surface, and decrease in temperature and increase in specific humidity at 100-150 m height. As a result of the near surface heating and drying, and the cooling and moistening aloft, the relative humidity decreases near the surface, and increases higher up. This could impact the formation of fog or low clouds, although no differences were visible in the cloud fraction output by the cloud scheme.

5 Conclusion

The validation of the six month reanalysis with wind turbines included, indicates that the inclusion of the turbine parameterisation has a positive impact on the predicted wind speeds near (offshore) wind farms. For all locations considered, the absolute bias in wind speed is decreased compared to the original DOWA reanalysis. Furthermore, the predicted power production – compared to observations from Elia – shows a substantial improvement with the turbine parameterisation included.

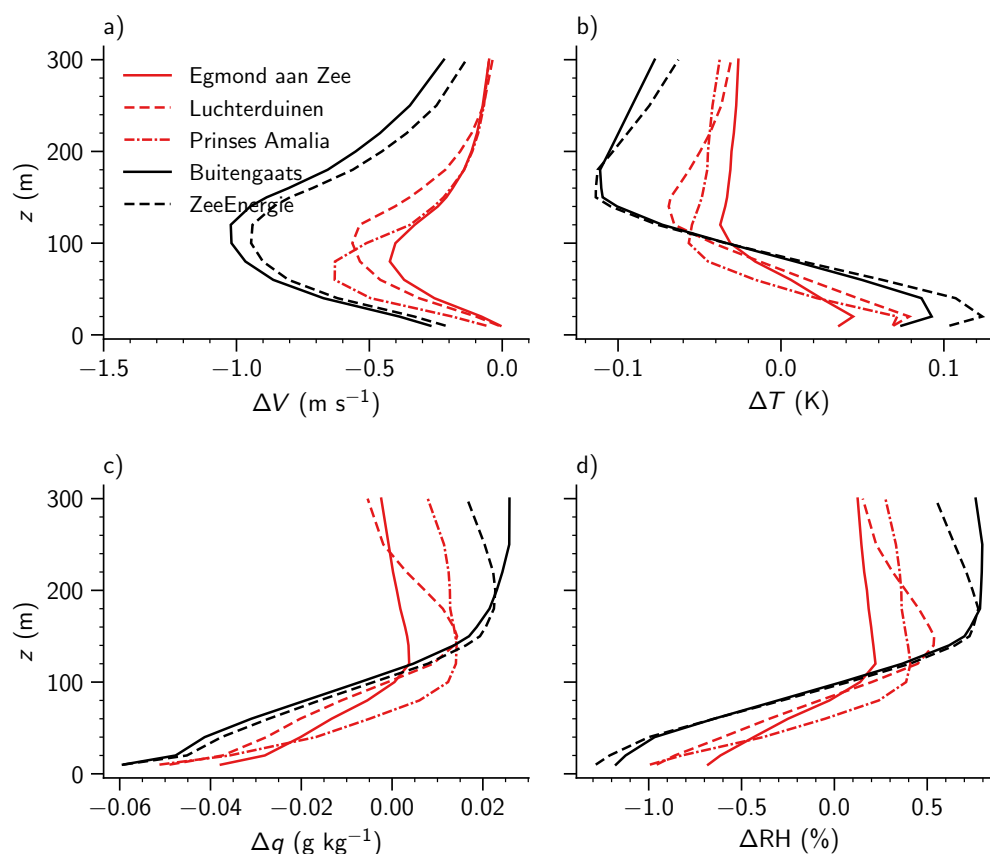


Figure 14: Impact wind turbines on meteorological conditions over the Dutch offshore wind farms.

A brief survey of the impact of wind farms on the local meteorological conditions, indicates that in addition to changes in wind speed, other quantities like temperature or humidity are influenced by wind farms as well.

References

- Baidya Roy, S., & Traiteur, J. J. (2010). Impacts of wind farms on surface air temperatures. *Proceedings of the National Academy of Sciences*, 107(42), 17899–17904.
- Bengtsson, L., Andrae, U., Aspelien, T., Batrak, Y., Calvo, J., de Rooy, W., ... others (2017). The HARMONIE-AROME model configuration in the ALADIN-HIRLAM NWP system. *Monthly Weather Review*, 145(5), 1919–1935.
- Bulder, B., Bot, E., & Marina, A. (2016). *Scoping analysis of the potential yield of the Hollandse Kust (zuid) wind farm sites and the influence on the existing wind farms in the proximity* (Tech. Rep. No. ECN-E-16-021 - 2nd ed.) ECN.
- de Haan, S. (2011). High-resolution wind and temperature observations from aircraft tracked by Mode-S air traffic control radar. *Journal of Geophysical Research: Atmospheres*, 116(D10).
- de Haan, S. (2016). Estimates of Mode-S EHS aircraft-derived wind observation errors using triple collocation. *Atmospheric Measurement Techniques*, 9(8), 4141–4150.

- Fischer, C., Montmerle, T., Berre, L., Auger, L., & Ştefănescu, S. E. (2005). An overview of the variational assimilation in the ALADIN/France numerical weather-prediction system. *Quarterly Journal of the Royal Meteorological Society*, 131(613), 3477–3492.
- Fitch, A. C., Olson, J. B., Lundquist, J. K., Dudhia, J., Gupta, A. K., Michalakes, J., & Barstad, I. (2012). Local and mesoscale impacts of wind farms as parameterized in a mesoscale NWP model. *Monthly Weather Review*, 140(9), 3017–3038.
- Gustafsson, N., Janjić, T., Schraff, C., Leuenberger, D., Weissmann, M., Reich, H., ... others (2018). Survey of data assimilation methods for convective-scale numerical weather prediction at operational centres. *Quarterly Journal of the Royal Meteorological Society*, 144(713), 1218–1256.
- Ramakrishnan, P. (2019). *Evaluation of a wind farm parameterisation in an operational mesoscale model* (Master's thesis, Delft University of Technology, the Netherlands). <https://repository.tudelft.nl>.
- Westerhellweg, A., Neumann, T., & Riedel, V. (2012). "FINO1 mast correction" (Tech. Rep.).
- Wijnant, I. L., van Uft, B., van Stratum, B. J. H., Barkmeijer, J., Onvlee, J., de Valk, S., C. Knoop, ... Klein Baltink, H. (2019). *The dutch offshore wind atlas (DOWA): description of the dataset* (Tech. Rep.). Retrieved from <https://www.dutchoffshorewindatlas.nl/publications>
- WindEurope. (2017). *Wind energy in europe: Scenarios for 2030* (Tech. Rep.).
- Witkin, A. P., & Heckbert, P. S. (2005). Using particles to sample and control implicit surfaces. In *Acm siggraph 2005 courses* (p. 260).

Use of wind information from Harmonie-Arome in high-resolution applications: crosswind and fuel consumption on motorways

Gertie Geertsema⁽¹⁾ and Erik de Graaff⁽²⁾

¹ KNMI, The Netherlands; gertie@knmi.nl,

² M+P consulting engineers, The Netherlands

1 Introduction

A study of the relation between road surface and fuel consumption of traffic included wind measurements *in situ* to disentangle the effect of wind and road surface (de Graaff et al. in preparation). For the experiment a van and truck drove approximately 50 meters apart maintaining a constant speed of 84 km/h using cruise control along the A2 highway near Boxtel in the Netherlands (Figure 1).

Care has been taken not to let other vehicles between the van and the truck. A pole on the van was used to measure the wind speed and the wind direction, fuel consumption was measured in the truck. The route chosen for the experiment has different surroundings, ranging from open spaced agricultural area to solid sound barriers along the highway in an urban area (see Figures 1 and 2). The wind and the fuel consumption were measured during a specific trajet which was traversed several times on days with different meteorological conditions.



Figure 1: Left: The truck in which fuel consumption was measured was preceded at about 50 m by a van with a pole measuring wind parameters. The picture is taken at a stretch of the route with solid sound barriers. Right: location of Harmonie-Arome grid-points (grey balloons) near the A2 highway (blue line) near Boxtel.

It was found that not only a headwind, but also a crosswind causes a substantial increase in fuel consumption. In particular, a preliminary comparison indicates that fuel consumption increases by 16% when the crosswind increases from 0 to 5 m/s (Figure 3).



Figure 2: Pictures of the local roughness along the highway traject. The left picture shows a stretch in a rural area with no barrier, on the right is an example of a barrier of shrubs and trees along the roadside.

Furthermore, it was found that shrubbery or barriers flanking the road reduce the crosswind. Combining these results, a rough estimate indicates that the cost of adding shrubs or barriers can be recuperated in a few years from the reduced fuel consumption and the related CO₂ emission reduction.

Before we embark on a full-scale long-term study of the effect of shrubs and barriers on motorways nationally, we perform in this paper a pilot study to see how well measurements *in situ* can be described with wind speeds and wind velocities from Harmonie-Arome. If this is satisfactory, the wind-roses climatology (tabulated wind speed and wind direction) determined using a 10 year Harmonie dataset (Geertsema and van den Brink, 2014) can be used to identify highways for which addition of shrubs or sound barriers are most effective in reducing longterm CO₂ emission. Simultaneously this study provides a verification of the values obtained by measurements with sensors on top of a pole on a moving van.

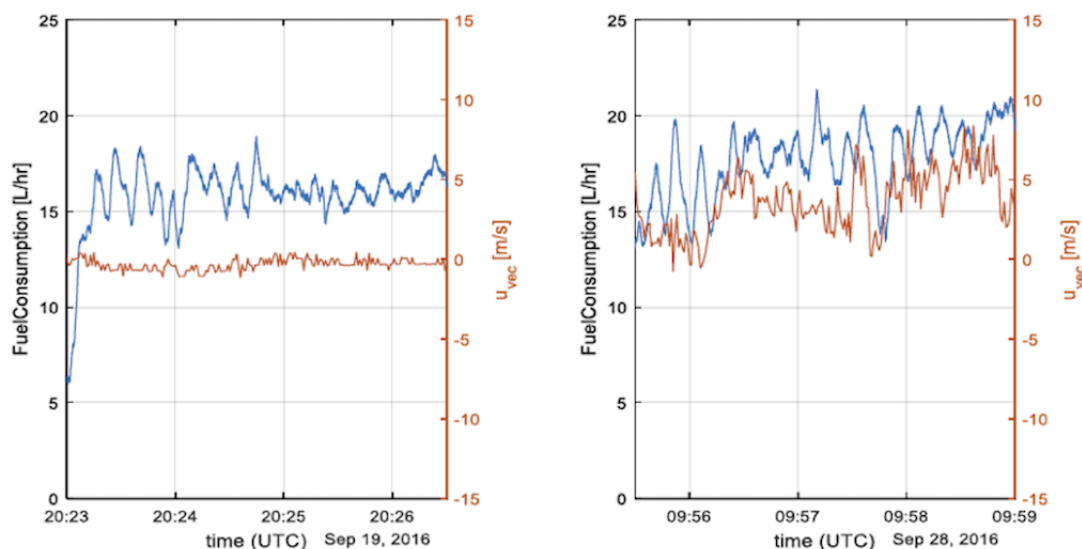


Figure 3: Example of the fuel consumption (blue) and crosswind (red) measurements. The left panel shows measurements on a calm day, the right panel shows the observations on a day with more wind. All other observational conditions (speed, temperature, tail or headwind, etcetera) are comparable.

2 Comparison of Harmonie-Arome wind data with measurements *in situ*

In this pilot project we investigate two data sets in more detail: the evening of 19 September 2016 and the morning of 28 September 2016, for which the crosswind is respectively 0 and 5 m/s (see Table 1). The fuel consumption and the crosswind are shown in Figure 3.

Table 1: Pilot days examined in this paper. Time is given in UTC, for LT (Local Time) add 2 hours. The crosswind from the *in situ* observations and from the Harmonie-Arome modelwind is estimated for the period in column 2 and provided here as an indication.

Date	Time (UTC)	crosswind	
		<i>in situ</i>	model-wind
19 September 2016	20:23 - 20:27	0 m/s	1 m/s
28 September 2016	09:55 - 09:59	5 m/s	4 m/s

The wind observations *in situ* are at approximately 3 meters above surface. Therefore the wind speed from Harmonie-Arome has been translated from the 10 meter model wind to a 3 meter model wind using a neutral logarithmic profile:

$$u(z_2) = u(z_1) \frac{\ln(z_2/z_0)}{\ln(z_1/z_0)} \quad (1)$$

For a multi-year period a neutral profile has been shown to be a good first order estimate. For these heights the wind direction is taken to be constant, that is the wind direction at 3 meter is the same as at 10 meter. The resulting wind speeds and directions are shown for 19 and 28 September 2016 in Figure 4 at two Harmonie-Arome grid-points nearest to the location of the measurements *in situ*.

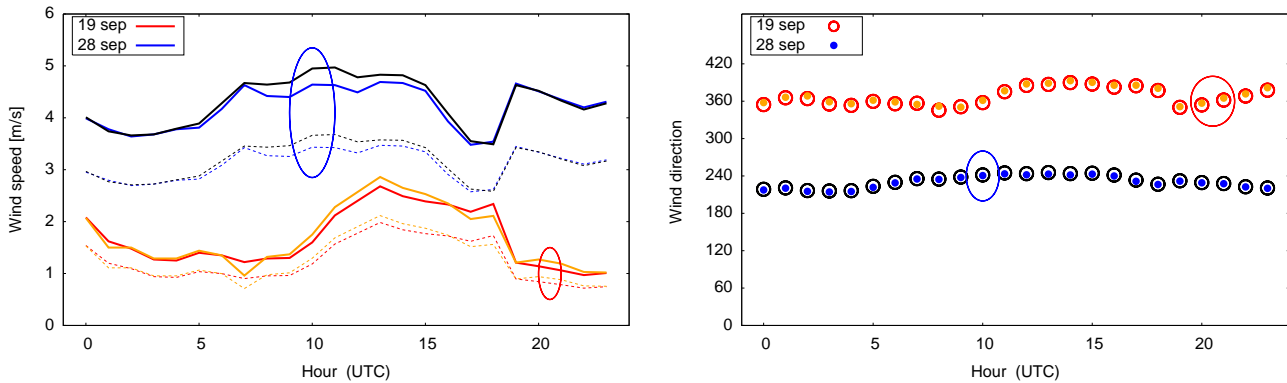


Figure 4: Hourly wind data at two nearby grid-points. For 19 September 2016 the left panel shows the wind speed at the height of 3 meter (dashed lines) and of 10 meter (solid lines). The color red is used for the nearest grid-point at the south side of the observation area, the color orange is used for the nearest grid-point at the north side of the observation area. The right panel shows the wind direction at 10 meter height, the color code is the same. The wind direction at the two grid-points is almost the same. For 28 September 2016 the colors are blue for the grid-points at the south side of the observation area, the black lines (solid and dashed) denote the grid-point at the north side of the observation area. The ellipses indicate the times of the comparison with the *in situ* data.

Information on the orientation of the highway (Figure 1) and the model wind given in Figure 4 can be combined to determine the crosswind. On 19 september 2016 20:00-21:00 UTC the modelled wind direction is North and the wind speed is ± 0.8 m/s which means the crosswind is approximately 0.5 m/s, the same within the error as the velocity measured *in situ*.

On 28 september 2016 10:00 UTC the modelled wind direction is around 240 degrees, which is perpendicular to the road. The wind speed at the two grid-points is 3.4 - 3.7 m/s at 3 meter height and 4.6-5.0 m/s at 10 meter height.

The observed wind speed *in situ* averaged over a few minutes is approximately 4 m/s (Figure 3). Here too the comparison between model crosswind and observed crosswind is satisfactory.

3 Discussion and conclusions

In our comparison between measurements *in situ* and Harmonie-Arome wind parameters atmospheric stability effects are not taken into account. In the calculation of the Harmonie-Arome wind parameters local effects, such as the black surface of the road, the noise barrier and/or the shrubbery and turbulence due to the traffic are not taken into account.

Even so, our results indicate that Harmonie-Arome wind data are in agreement with the wind measurements *in situ* on top of a pole on a moving van. For the comparison the Harmonie-Arome output at 10 meter was used for the wind direction and translated to a 3 meter wind speed using a neutral logarithmic profile assumption.

The good agreement between the two differently obtained windspeeds and wind directions gives confidence that the Harmonie-Arome wind climatology can be used to estimate the longterm average crosswind. The correlation of crosswind with fuel consumption thus makes it possible to use wind-roses climatology to compute the effect of shrubs, trees and barriers on the longterm-averaged reduction in fuel consumption, and the accompanying reduction in CO2 emission along different highways in the Netherlands.

Thus shrubs, trees and barriers are beneficial not just in blocking sound, but also in reducing CO2 emission. A 'back of the envelope' calculation showed that with the present costs of CO2-pollution, the crosswind reduction barrier costs may well be recuperated in a few years. A more detailed calculation can take into account aspects like the form of the barrier, which may consist out of for example brushes, trees and other forms of barrier, as well as maintenance costs. In planning decisions local residents need to be consulted on acceptable barrier forms.

Optimal weather circumstances for experiments such as described here require careful planning. For the campaign which was meant to study specifically the crosswind effect 19 september 2016 was chosen because the weather forecast predicted a constant calm wind on that day, and 28 september because the forecast predicted a constant wind almost perpendicular to the highway, and no significant wind along it. Figure 4 confirms that the campaign periods were well chosen showing also the synergy between weather forecasting and experimental research.

4 References

de Graaff, E., Geertsema, G., Jonker, H., Rentema, D., Fortuin, P., Tollenaar, C., Invloed bermbosschages op zijwind en CO2 emissie vrachtwagens, juni 2020, CROW Infradagen, (in preparation)

Geertsema, G.T., van den Brink, H.W., Windkaart van Nederland op 100 meter hoogte. KNMI Technical Report, TR351, 2014. (url: <http://bibliotheek.knmi.nl/knmipubTR/TR351.pdf>)

Aladin in Poland - 2019

Bogdan Bochenek, Marek Jerczyński, Marcin Kolonko, Piotr Sekuła, Małgorzata Szczęch-Gajewska, Jadwiga Woyciechowska

1 Introduction

Among many other activities, ALADIN group in Poland covered the following: switching to ALARO NHYD as operational suite, analysis of severe weather incident in Suszek (Poland) on 11.08.2017, and exploration of boundary layer in Cracow with the usage of UAV (Unmanned Aerial Vehicle).

2 Non-hydrostatic version of ALARO

Tests

There were several tests conducted, including comparison of CY40 HYD and CY43 NHYD (both export versions) dealt with the aspect of convective precipitation, general 2-week forecasts in winter and summer, corrected parametrization of snow layer, its impact on temperature forecast, and the quality of new low level cloudiness forecast.

Selected results

To estimate influence of the new snow parametrization, the elements of radiation budget were summarized (for the point of given geographical coordinates: lat = 50.0 deg N, lon = 14.4 deg E). The expected effect was improvement of the forecast, and the appropriate diagram is listed below (Fig. 1).

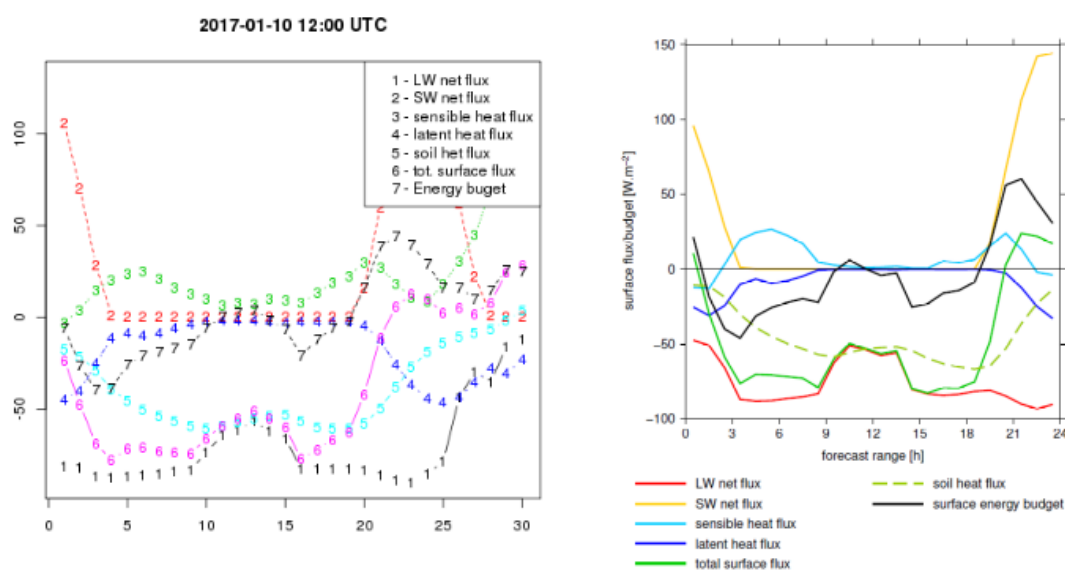


Figure 1: Elements of the radiation budget – on the left hand side, new configuration (CY43 NHYD), on the right hand side – reference suite (CY40 HYD). Both forecasts are for the base date 10.01.2017, 12 UTC.

Another test was made for low level cloudiness. One can notice higher contrast (immediate increases from 0 to 1) for the test forecast and smaller contrast (with intermediate cloudiness values such as 0.5) for the reference forecast.

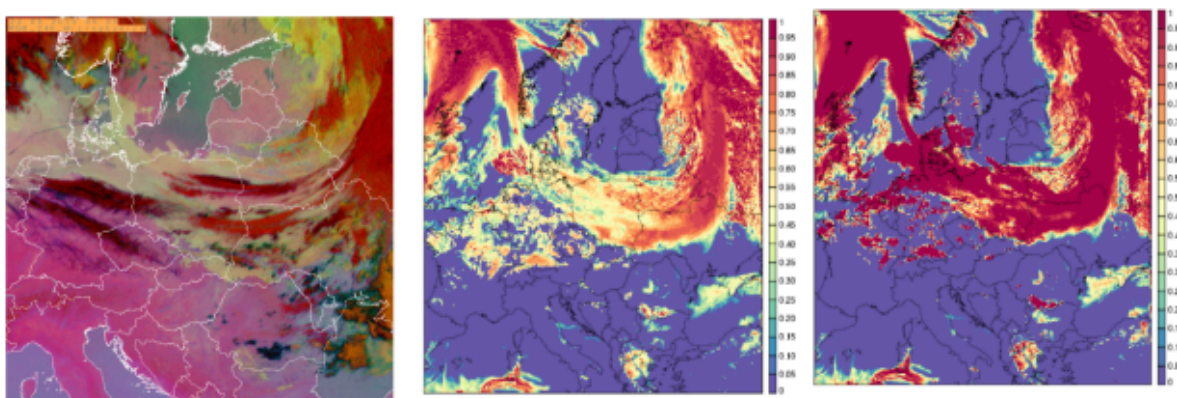


Figure 2: Cloudiness field for: RGB satellite product (microphysics) on the left hand side, reference forecast (middle panel) and tested CY43 NHYD forecast on the right hand side. All data prepared for 22.03.2019, 06 UTC.

3 Case study of severe weather in Poland on 11 Aug 2017

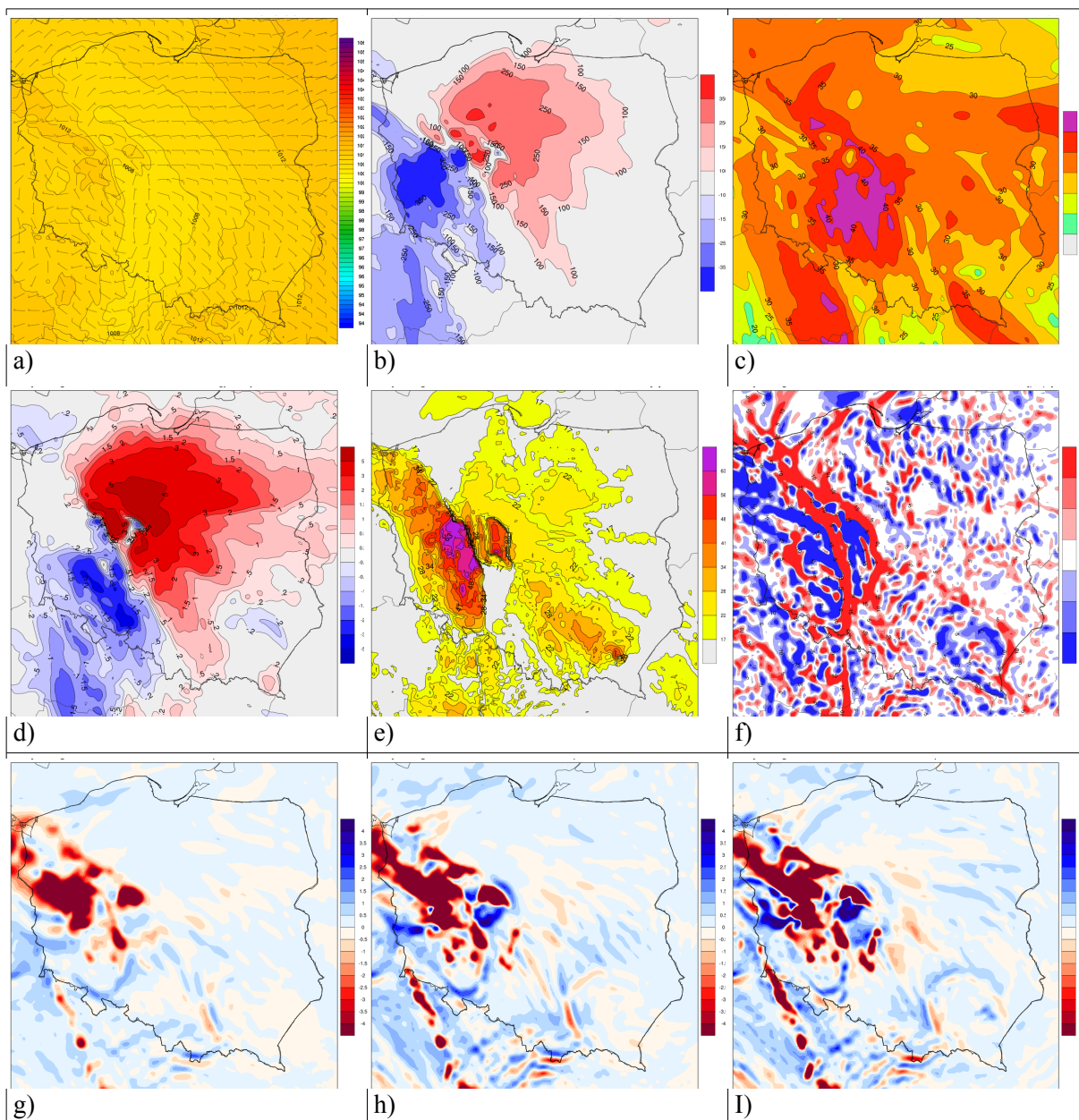
Severe weather case for Suszek

The outbreak of bad weather in Suszek (northern Poland) noticed 6 fatalities, some of them children who were located in the forests at scout camp. There was an issue concerning possible responsibility of forecast service and/or headquarters of the camp who switched mobile phones off and thus ignored a local alarm against strong (over 40 m/s) wind gusts for this region (Pomeranian voivodeship).

Forecast for 11 Aug 2017 afternoon

The wind gust maps and forecast of some storm indexes (such as EHI, SRH 0-3 km, Total Totals, K-index, moisture convergence and vertical speed) for the model (CY40 HYD) runs with the base 10 and 11 Aug 2017 anticipated (at least some of them) the presence of bow echo – meaning strong wind gusts (having the strength of F2-F3 tornado but without circular pattern of pressure). The example forecast maps of that phenomenon are presented on Table 1.

Table 1: Example model maps fro the severe weather outbreak, 11 Aug 2017. Maps for the forecast base 10.08.2017 18 UTC. Upper row: a) Pressure and wind on the surface [hPa]+[kt], b) SRH 0-3km, c) K-index, middle row: d) EHI, e) wind gusts [kt], f) MOCON, bottom row - vertical speed [Pa/s] at: g) 700 hPa h) 850 hPa I) 925 hPa. All maps are results from non-hydrostatic version of ALARO CY43 model and the forecast period is 24h, thus for 11.08.2017, 18 UTC.



Interpretation

There is high sensitivity of storm indices to the extreme situation expected. Actually, it could be named “derecho” as the observed final effect was splitting the bow echo into many sub-centres all of which were sources of serious damage by high-speed horizontal winds.

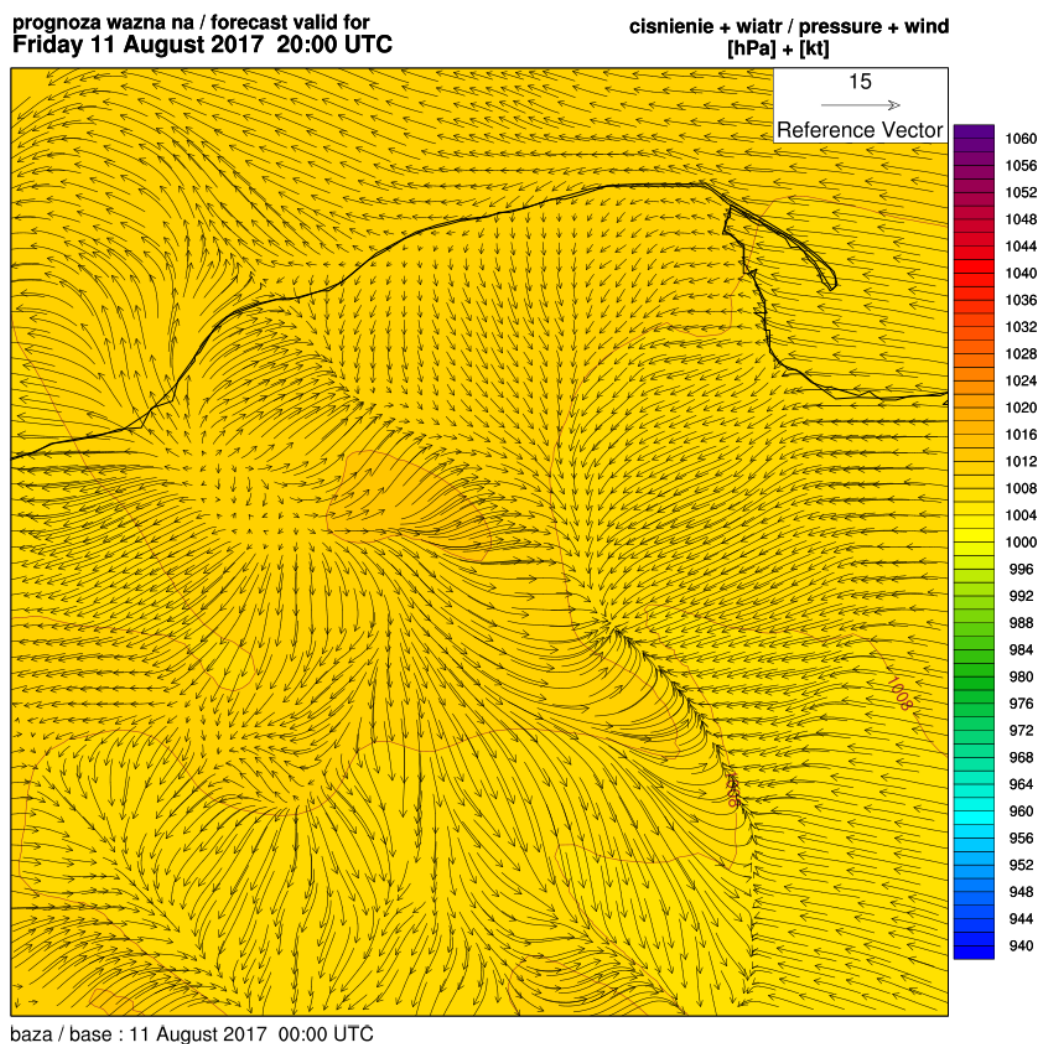


Figure 3: Forecast of msl pressure and wind for 11th of August 2017, showing possible downbursts and chaotic structure of wind (arrows).

4 UAV study of Krakow environmental pollution

Context

Krakow is concerned as the mostly polluted cities in Europe, especially during winter season. For some years there was introduced program of monitoring air quality and replacing old heavy-fraction coal and oil stoves to the new (mostly gas) ones. There were over 25000 stoves replaced in 2019 (according to municipal government flyer) but citizens still cope with pollution from neighbouring villages and distant heavy industry centres in Silesia. It is natural to tend to detect and measure remaining sources of air and ground pollution. Thus the idea of using UAV (called also “drones”) for such task.

Equipment and methodology

Authors (Piotr Sekuła and his collaborators from University of Mining and Metallurgy) used UAV (Unmanned Aerial Vehicle) with the sketch of equipment listed below:

Table 2: General specification of the UAV used for sessions.

Parameter	Model of sensor
Temperature, pressure, humidity	Bosh BME 280
Pm (dust parts per million) concentration	Plantower PMS7003
Global Positioning System	Ublox NEO7M GPS
Memory card	Arduino MKR Zero
Data transmission	Radioline 433 MHz, 10mW
Temperature sensor type	Thermocouple type T
CO2/methane sensor	Picarro
Thermoelement	Adafruit MAX31856
Voltage converter	Step down 5-30V to 5V, max. current 2A

There were 9 flight sessions conducted (including 2 with particular methane fraction measurement) in the vicinity of Krakow. Greenhouse (and other) gas concentrations were measured and visualized. The demanded conditions for such research are: the wind speed less than 25 km/h, no precipitation and no superposition of flight area with any zones reserved for aviation (as “drone” may fly at the height of 1 km above ground level).

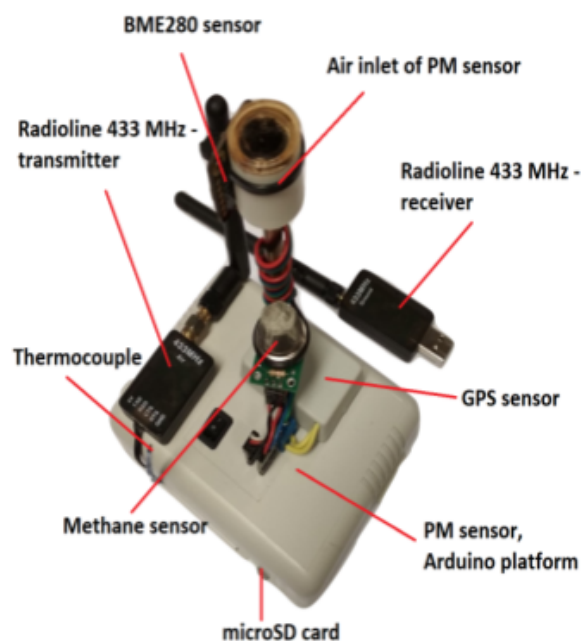


Figure 4: The central part of UAV control unit (with the sensors' description).

Example result

Particularly interesting session took place 7th of March, 2019, which took place in the southern-west part of Krakow. It was later interpreted as the effect of pointlike source of emission (higher PM10 values), and rapid change of circulation during the measurement (thus the position of red and blue line peaks are on different heights).

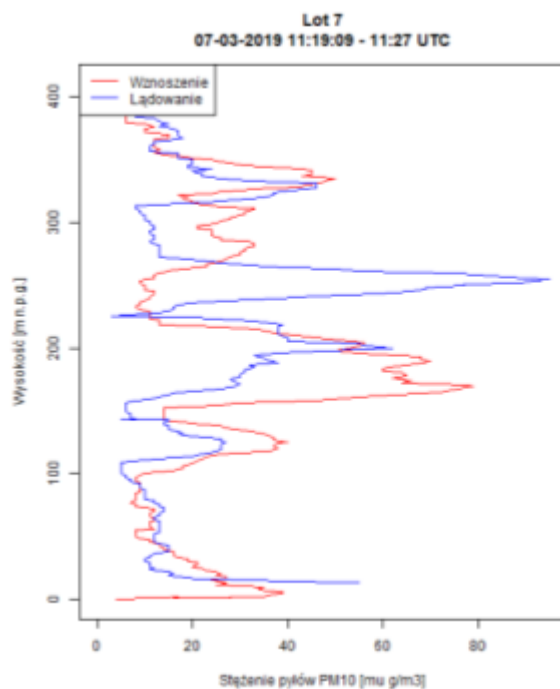


Figure 5: The vertical profile of PM10 particle concentration. Red line marks ascent, blue one – descent of UAV. The vertical axis is meters above ground level. Measurement date 07.03.2019, around 11:30 UTC.

2019 ALADIN Highlights for IPMA, I.P.

Maria Monteiro, João Rio, Vanda Costa, Manuel João Lopes

1 Introduction

Two topics have been given particular attention in Portugal during 2019: the porting and validation of the local AROME operational configurations to CY40T1_bf07, on the three different geographical domains of Mainland (AROME-PT2), and Madeira (AROME-MAD) and Azores (AROME-AZO) Archipelagos; and the implementation of a local Data Assimilation (DA) system to the local AROME-PT2, under the framework of the ALADIN Data Assimilation Strategic Core Programme (here named DAsKIT).

Details on the porting and validation of the local configurations of AROME are described in Section 2 on the operational activities, while the status of the local implementation of the AROME-PT2 DA system is given in Section 3.

2 Operational activities

The ALADIN system code version CY40T1_bf07, commonly accepted as an “export version”, was successfully installed on the local operational machine IBM Power 7⁺ under the AIX 7.1 operating system in June 2019. So far, AROME is locally run in operations by downscaling initial and 3-hour frequency boundary conditions from the ARPEGE operational model. In order to port the actual operational configurations (at CY38T1) to the new code features with impact on the near surface forecasts performance, some tuning had to be made for each geographical domain leading to the adoption of the final switches shown in Table 1.

Table 1: Surface switches for different AROME-Portugal domains.

Configuration/Switches (namelists parameters or schemes)	Mainland (AROME-PT2)	Madeira (AROME-MAD)	Azores (AROME-AZO)
Coupling/LNOTS_L	false	true	true
Model/CANOPY (SBL scheme by Masson et Seity 2009)	false(*)	true	true

(*) when CANOPY was switch off, Geleyn 1988 scheme was adopted.

For each domain, the choices described in Table 1 were based on several spatial and categorical scores performed over near surface forecasts of the AROME model, initialized at 00UTC during specific validation periods. The forecasts were obtained from several model experiments where different combinations of the switches were tested.

Two time intervals were used for this validation: a Winter period, from 10 December 2018 to 10 February 2019; and a Summer period, from 01 August to 09 September 2019. Figures 1-2 illustrate some of the scores for AROME-PT2, while Figures 3-4 illustrate some of the scores for AROME-MAD.

Generally speaking, with the options described above and for the parameters, geographical domains and periods analysed, it was possible to see: i) an overall positive or neutral impact when porting the operational configurations from CY38 to CY40 (see, for instance, blue line or shadow for AROME-PT2 in Figures 1-2; and red line or shadow for AROME-MAD in Figures 3-4); in detail, ii) a wider positive impact during the Winter than over the Summer period (not shown); iii) that 24-hour accumulated precipitation forecasts tend to be more accurate under moderate or heavy rain periods; iv) a positive or neutral impact for the daily maximum temperature while neutral or negative impact for the daily minimum temperature (not shown); and finally, v) a wider positive impact over Madeira than over Azores (not shown).

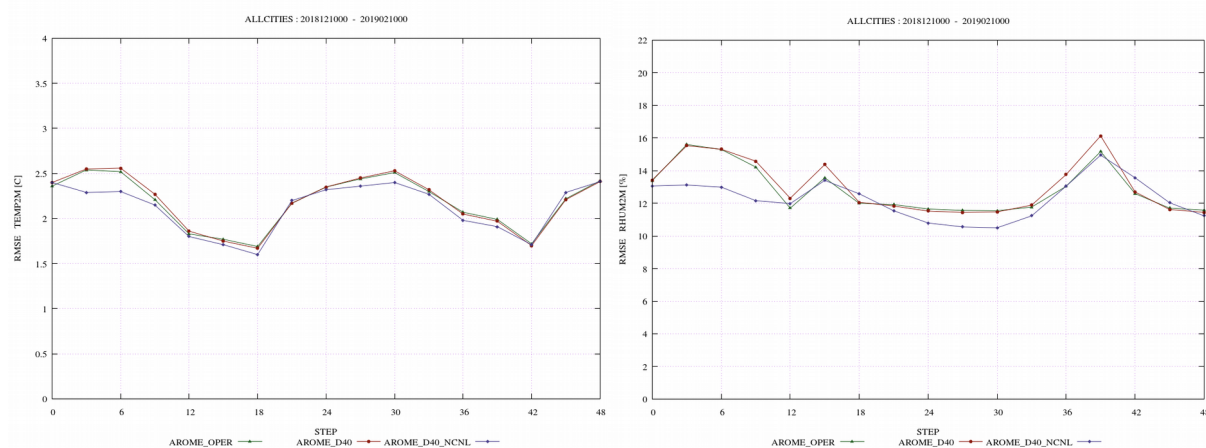


Figure 1: RMSE of AROME-PT2 48-hour forecasts initialized at 00UTC for the 2-metre temperature (left) and the 2-metre relative humidity (right), over a Winter period (2018.12.10-2019.02.10), using different setups: CY38-green; CY40(export)-red; CY40(changed)-blue.

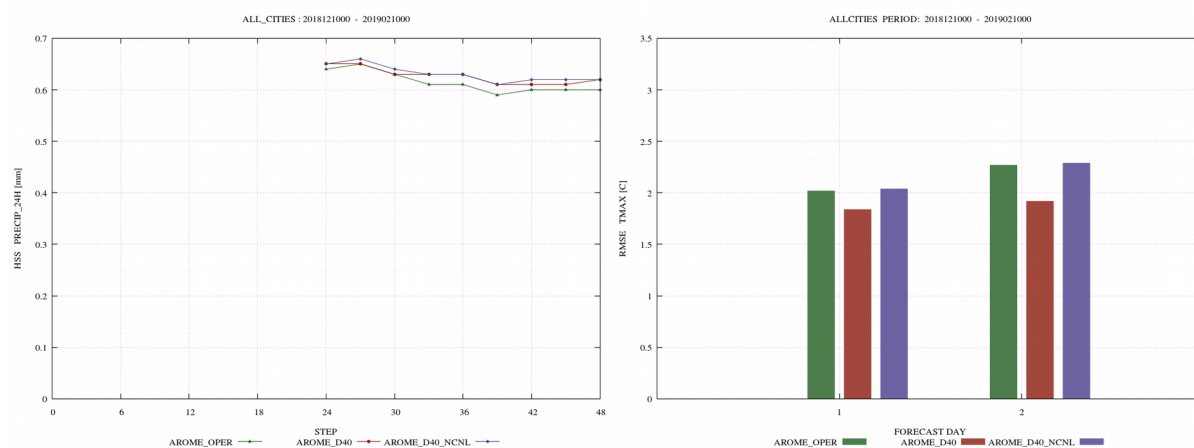


Figure 2: HSS of 24-hour accumulated precipitation (left) and RMSE of daily maximum temperature (right) AROME-PT2 forecasts initialized at 00UTC, over a winter period (2018.12.10-2019.02.10), using different setups: CY38-green; CY40(export)-red; CY40(changed)-blue.

Taking into account the above taken conclusions, an upgrade of the actual operational configurations is foreseen for the first quarter of 2020. Further progress is planned with the new code export version CY43T2_bf10. However, since local operational HPC platform (IBM Power 7⁺) has become obsolete and does not allow the implementation of new FORTRAN features used in CY43, ECMWF HPC computing platforms will be used boosting further progress. In particular, taking into account the actual participation of Portugal in the DAsKIT programme, the implementation of DA procedures in this new cycle will take place.

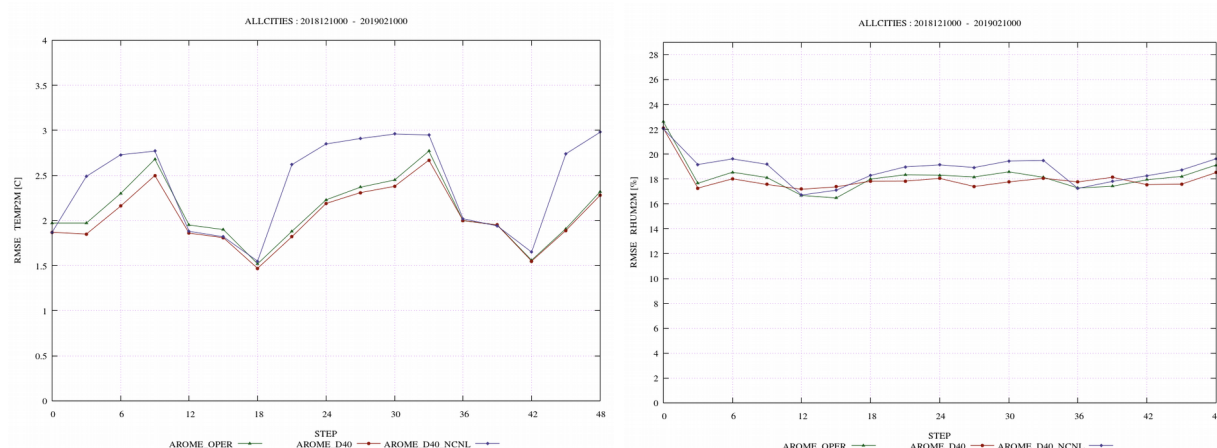


Figure 3: RMSE of AROME-MAD of 48-hour forecasts initialized at 00UTC for the 2-metre temperature (left) and the 2-metre relative humidity (right), over a winter period (2018.1210-2019.02.10), using different setups: CY38-green; CY40(export)-red; CY40(changed)-blue.

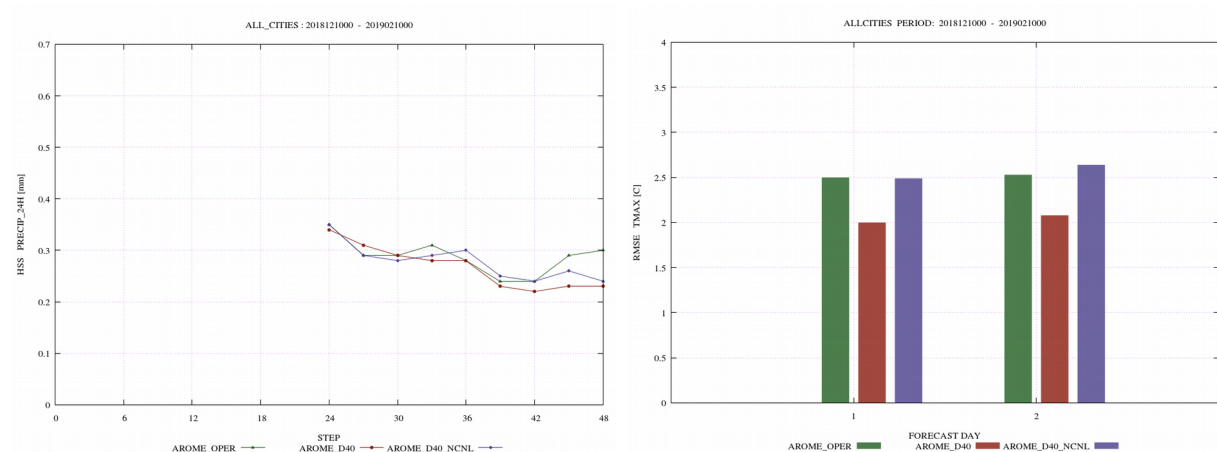


Figure 4: HSS of 24-hour accumulated precipitation (left) and RMSE of daily maximum temperature (right) AROME-MAD forecasts initialized at 00UTC, over a winter period (2018.1210-2019.02.10), using different setups: CY38-green; CY40(export)-red; CY40(changed)-blue.

3 Data assimilation activities

After the local installation of CY40 as described before, the migration of the DAsKIT setup for surface DA (originally created at Météo-France HPC platforms) has started to the IBM Power 7⁺. This setup consisted on a set of three scripts handling the workflow to perform the 12UTC surface analysis of AROME-PT2 (2,5km, 60 vertical levels), using as input the Iberian SYNOP observations under WMO BUFR format, and the consecutive model initialization and short-term forecast to prepare the background to the next network cycling. This set of scripts was adapted to the local HPC infrastructure taking advantage of an already existing ecflo scripts set, previously designed to accommodate a 3-hour cycling of a surface DA setup for AROME-PT2 under CY38T1 as described by Monteiro et al. 2018.

Before cycling the DAsKIT setup, the diagnostics jointly proposed for this migration were successfully performed (not shown).

A preliminary quality assessment over the same Winter and Summer periods used for CY40 validation of AROME-PT2 forecasts up to 40-hours, initialized at 00UTC was then possible (see previous section), by four different setups: i) the actual CY38 operational dynamical adaptation configuration; ii) the CY40 dynamical adaptation (export version without namelist changes downscaled from ARPEGE forecasts); with the DAsKIT analysis initialization (60 levels); and iv) with the DAsKIT analysis initialization but with 46 vertical levels (instead of 60 levels). Figure 5 illustrate some of the statistical scores obtained.

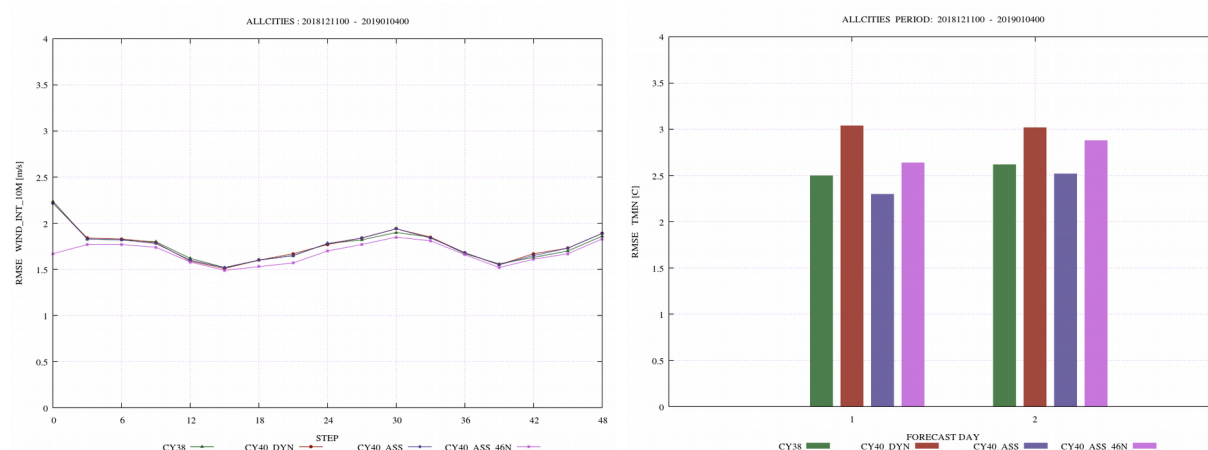


Figure 5: RMSE of 10-metre wind and of the daily minimum temperature of 48-hour AROME-PT2 forecasts, initialized at 00UTC, over a winter period (2018.1210-2019.02.10), using different setups: CY38-green; CY40(export)-red; CY40(DAsKIT_L60)-blue; CY40(DAsKIT_L46)-magenta.

Preliminary scores of AROME-PT2, when initialized by a surface DA cycling, have shown some extra work have still to be done on the local CY40 cycling setup; however, two basic remarks are immediately available from the panels of Figure 5: i) when initialised by the surface DA, 10-metre wind forecasts obtained with an AROME-PT2 configuration of 46 vertical levels show an added value over the configuration with 60 vertical levels; and ii) surface DA cycling has a positive impact over the daily minimum temperature. The first remark seems to recover a conclusion previously obtained with the CY38 cycling: with 46 vertical levels, the lowest AROME-PT2 model level is above 10-metre therefore the 10-metre wind field is computed by surface processes which take advantage of small scale features available after the surface DA, at the model initial state. The second observation is encouraging in terms of the potential added value of surface DA over the dynamical adaptation, since seems to indicate a positive impact of the daily minimum temperature (under Winter conditions).

In the meantime, further validation of the surface DA is expected, now with the adoption of the changes mentioned in Table 1. To follow the DAsKIT working plans (see for instance, http://www.umr-cnrm.fr/aladin/IMG/pdf/2019daskit_summaryreport_v20191016.pdf), during the first quarter of 2020 the porting of surface DAsKIT setup to CY43T2_bf10 should be initiated; moreover, a combined solution of surface+3D-Var DA for AROME-PT2 should be worked out. However, the CY43 activities should take place already at ECMWF HPC platforms, due to the actual obsolescence of the local operational HPC infra-structure.

Acknowledgements

To Alena Trojáková, Ryad El Khatib and Oldrich Spaniel, for their support on the successful installation of CY40T1_bf07 on the local HPC IBM Power 7⁺.

4 References

Masson, V. et Seity, Y., 2009: Including atmospheric layers in vegetation and urban offline surface schemes. *J. Appl. Meteor. Climatol.*, 48, 1377–1397.

Geleyn, J.-F., 1988: Interpolation of wind, temperature and humidity values from model levels to the height of measurement, *Tellus A*, Volume: 40A Issue 4.

Monteiro, M., Costa, V., Rio, J., Lopes, M.J., Moreira, N., 2018: 2017 ALADIN Highlights for IPMA, I.P. (Portugal), ALADIN-HIRLAM Newsletter, n^o10, available from <http://www.umr-cnrm.fr/aladin/IMG/pdf/nl10.pdf>.

ALADIN activities in Romania

Alina Dumitru, Simona Tascu, Alexandra Craciun

1 Introduction

National Meteorological Administration of Romania has purchased a new HPC system in 2019. The upgrade of the infrastructure represents an important achievement for the future plans within the NWP department, such as the possibility to increase the model resolution or new cycles.

2 Characteristics of the new HPC and ALARO operational suite

Characteristics of the new HPC

The new system is used for both operational and research purposes. HPC diagram is represented in figure 1. The main attributes are as follows:

- 5 chassis Lenovo ThinkSystem Modular Enclosure
- each chassis has 4 nodes Lenovo ThinkSystem SD530
- each node has 2 processors Intel Xeon Gold 6130
- each processor has 16 cores
- 2 login nodes Lenovo ThinkSystem SR650
- connectivity: infiniband, 10 GbE, GbE

The total number of cores on the new HPC is 640 which are shared with the COSMO group.

Characteristics of the ALARO operational suite

Currently, we are running ALARO-0 cy40t1 on the old HPC having the following settings:

- semi-implicit semi-Lagrangian 2TL, $\Delta t=240$ s
- $\Delta x=6.5$ km, 240 x 240 points, 60 vertical levels
- 3h frequency LBC from ARPEGE, DFI Initialization
- 4 runs /day 00, 06, 12, 18 UTC
- forecast range: 78/54/66/54 hours

For the time being, we performed some tests for the above ALARO configuration for cy43t2 on the new HPC.

Future plans

More tests with ALARO cy43t2 will be done in order to increase the model resolution.

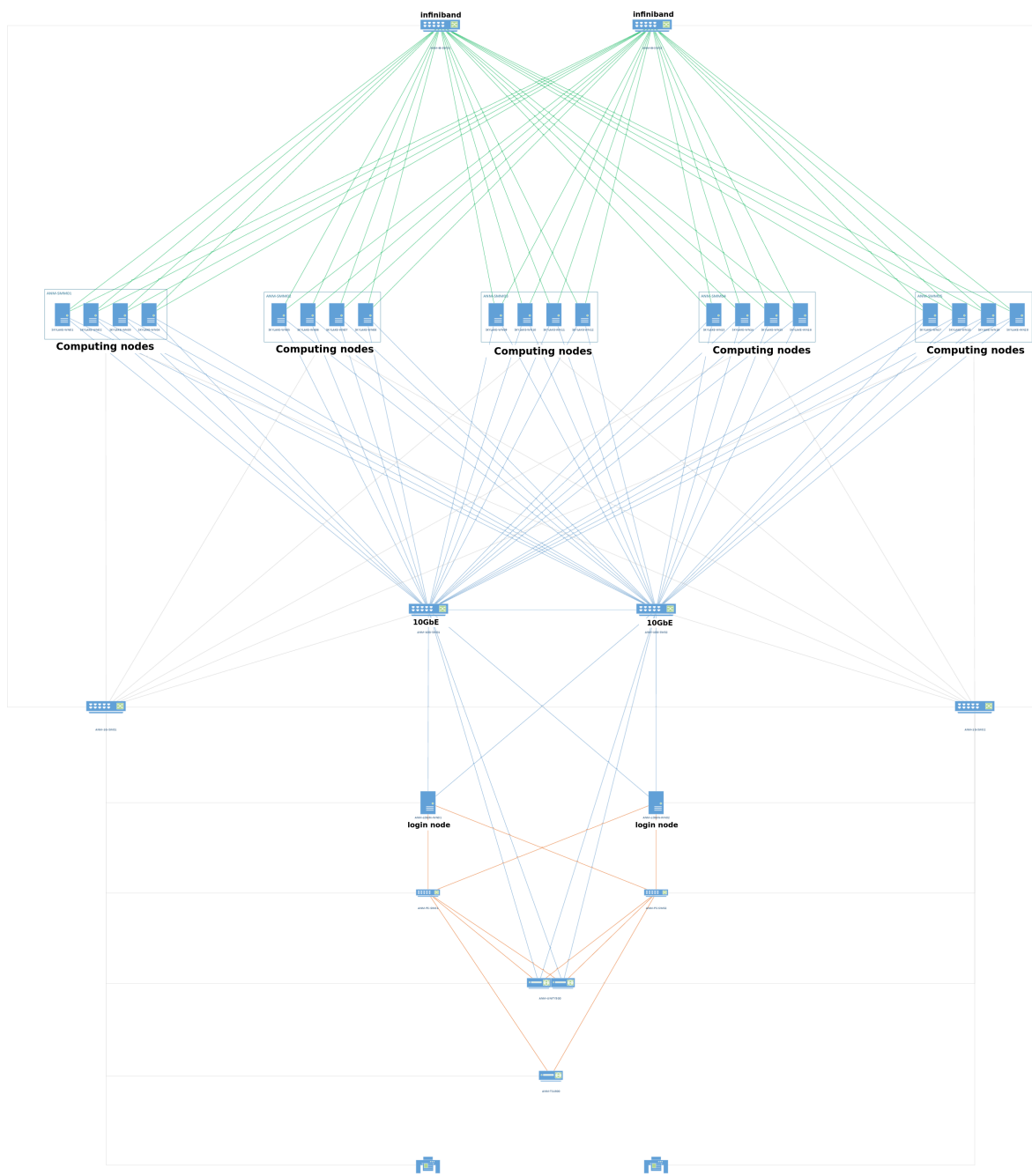


Figure 1: New HPC diagram

ALADIN related activities @SHMU (2019)

Mária Derková, Martin Belluš, Katarína Čatlošová, Martin Dian, Martin Imrišek, Michal Neštiak, André Simon, Oldřich Španiel, Viktor Tarjáni, Jozef Vivoda

1 Introduction

A summary of ALADIN related activities at Slovak Hydrometeorological Institute in 2019 is presented below. The setup of ALADIN operational system is described and some research and development activities are highlighted.

2 The ALADIN/SHMU NWP system

The ALADIN/SHMU system setup

The ALADIN/SHMU system is running on HPC IBM Flex System p460, 8 nodes, Power 7+ architecture, Red Hat Enterprise linux, gfortran. Its area covers so-called LACE domain with 4.5 km horizontal resolution and 63 vertical levels (see Figure 1, left panel). It is running 4 times per day up to 3 days. Current model version is based on CY40T1bf07 with ALARO-1vB physics and ISBA surface scheme, coupled to Arpege global model. The spectral blending by digital filter is applied for the upper-air pseudo-assimilation using Arpege analysis. For surface the CANARI data assimilation scheme including additional local observations is active. More ALADIN/SHMU details are given in Table 1. The ALADIN/SHMU domain is displayed on Figure 1 on the left.

Table 1: ALADIN/SHMU operational (left column) and experimental systems

CMC	ALARO	ALARO	AROME
<i>status</i>	operational	experimental	
<i>code version</i>	CY40T1bf07_export	CY43T2bf10	CY40T1bf07_export
<i>physics</i>	ALARO-1vB	ALARO-1vB	AROME-FRANCE
<i>resolution</i>	4.5 km	2.0 km	
<i>levels</i>	63	73	
<i>points</i>	625 x 576	512 x 384	
<i>boundaries</i>	ARPEGE, 3 h freq.	ALARO-1vB (4.5 km), 1 h freq.	
<i>initial conditions</i>	CANARI & upper-air spectral blending by DFI, 6 h cycling	downscaling	
<i>initialization</i>	none	DFI	none
<i>surface scheme</i>	ISBA	ISBA	SURFEX
<i>starting times</i>	00, 06, 12, 18 UTC	00 UTC and 12 UTC	
<i>forecast length</i>	+78 h/+72 h/+72 h/+60 h	+78h /+72h	

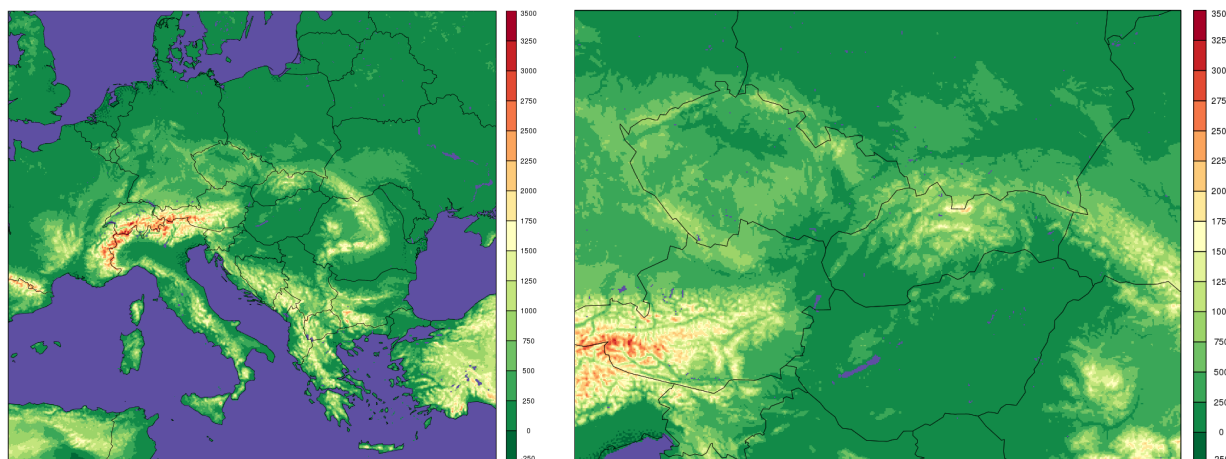


Figure 1: The domains and topography of ALADIN/SHMU operational system 4.5 km/L63 (left) and experimental convection permitting scale setup 2.0 km/L73 used for AROME and ALADIN systems (right).

3 Research and development activities

Most of research and development activities were ongoing within the RC LACE programme - stays or local work.

ALARO-1 Working days 2019

The ALARO-1 Working days have been organized in Bratislava, Slovakia, 11-13 March 2019 with 23 participants from 7 countries. Program, presentations and other documents can be found on the RC LACE web page <http://www.rclace.eu/?page=197>.



Figure 2: Participants of the ALARO-1 Working days, Bratislava, March 2019.

Test of a new numerical scheme for calculations over the vertical grid in the Integrated Forecasting System (IFS) (J. Vivoda, ECMWF stay)

The vertical scheme based on a finite-element discretisation method (VFE - vertical finite element), that was initially developed for ALADIN LAM NWP system, was tested in the IFS model within the research stay at ECMWF. Firstly, the VFE scheme was implemented in the hydrostatic IFS, and secondly, tested in its non-hydrostatic version. It was shown that the new scheme offers several benefits for the IFS at the same computational cost: higher accuracy in the vertical discretisation; smaller sensitivity to the model's vertical resolution and numerical precision; and the ability to use the same vertical discretisation in the modelling of hydrostatic and nonhydrostatic dynamics. (<https://www.ecmwf.int/en/about/media-centre/news/2019/tests-numerical-scheme-developed-member-states-are-promising>)

Mode-S data assimilation (K. Čatlošová)

Two months (January-February 2018) data sample of Mode-S data (EHS & MRAR) from four radars provided by Slovak ATC was analyzed in frame of diploma thesis at the Faculty of Mathematics, Physics and Informatics, Dpt. of the Atmospheric Physics. Statistical approach based on OMG departures using AROME/SHMU 2 km/L73 model was used to select reliable data. Then the aircraft whitelist was created based on ICAO addresses according to criteria listed in Table 2. Results for temperature are shown for illustration on Figures 3 and 4. Further evaluation and data assimilation experiments are ongoing.

Table 2: Criteria for the OMG Mode-S data selection and whitelisting

	OMG statistical thresholds		Whitelisting criteria		
			No. of OBS	mean value	σ
temperature	± 10 K	2σ	1000	1 K	2 K
wind speed	± 20 m/s	2σ	1000	1 m/s	5 m/s
wind direction	± 45 deg	2σ	1000	10 deg	100 deg

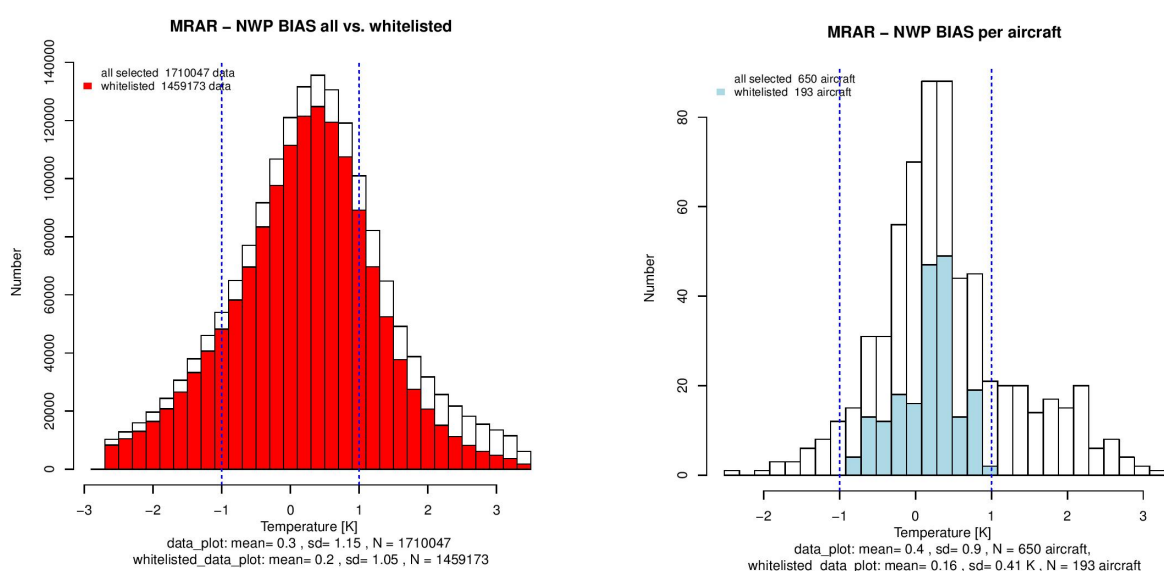


Figure 3: Distribution of the temperature OMG BIAS after whitelisting for all data (left) and data per aircraft (right).

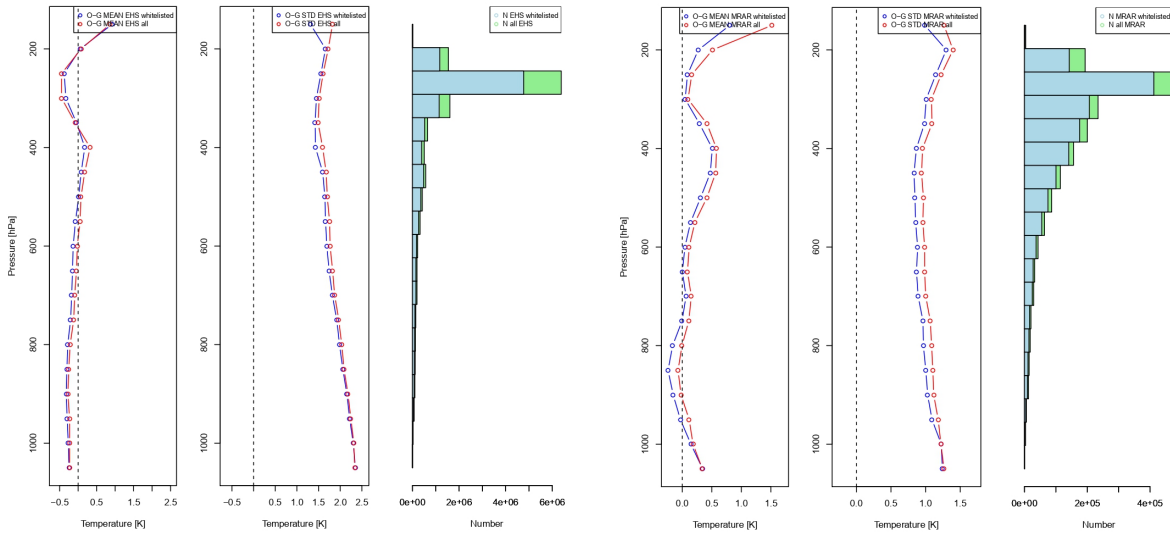


Figure 4: Vertical profile of the temperature OMG BIAS and STD after whitelisting for EHS (left) and MRAR (right) data.

Upgrade of the A-LAEF system (M. Belluš)

The new A-LAEF setup (5 km/L60, since 2018) contains ensemble of surface data assimilation (ESDA) with internally perturbed screen-level observations, upper-air spectral blending, stochastic perturbation of physics tendencies (SPPT) for ISBA prognostic fields and new ALARO-1 multiphysics (additionally to the model upgrade from cy36 to cy40t1, increased horizontal and vertical resolution and redefined domain). LBC files are prepared via c903 directly from ECMWF gribs on octahedral cubic grid. Everything is running in the ecFlow under TC user since July 2019. The components of the A-LAEF suite are sketched on the Figure 5.

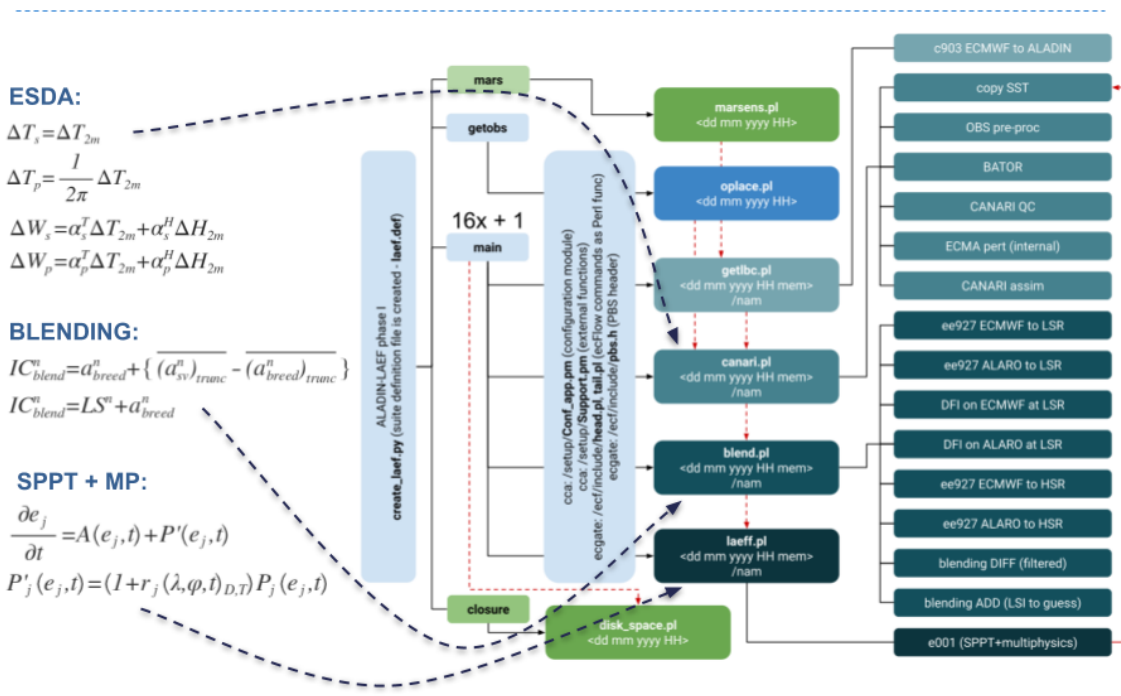


Figure 5: Components of the A-LAEF operational suite under ecFlow.

GNSS data assimilation (M. Imrišek)

Work on the assimilation of the ZTD data is carried out in cooperation with the Slovak University of Technology, Dpt. of Theoretical Geodesy, where the local independent near real-time processing system of GNSS network of permanent stations is running. GNSS ZTD data are experimentally assimilated into AROME/SHMU 2 km/L73 model version together with SYNOP, TEMP, AMDAR and AMV data. Simple white list method and static correction based on OMG statistics was applied for each permanent GNSS station. An example of absolute (left) and relative (right) degrees of freedom statistics (DFS) for various observation types is shown on figure 6 for two days of June 2018. Absolute DFS for GNSS ZTD is small, but relative is high, that is in accordance with studies at other NMSs.

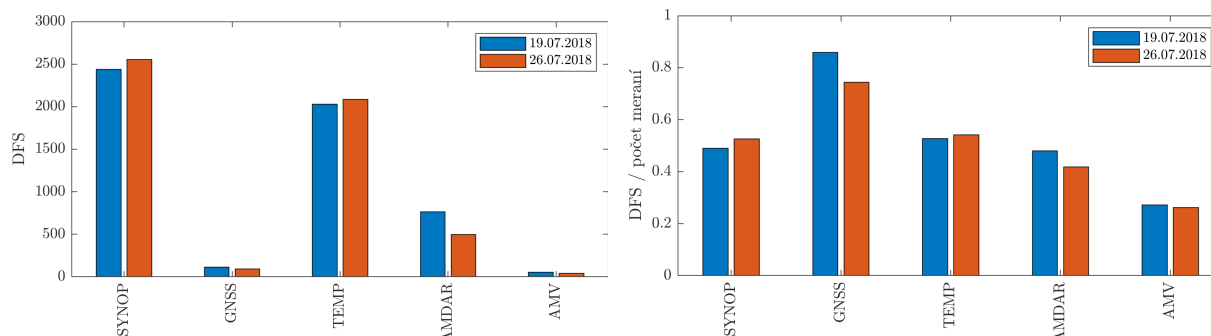


Figure 6: The absolute (left) and relative (right) DFS for various observation types.

Short 5 days e-suite (16-20/07/2018) of 3D-Var with (+ZTD) and without (-ZTD) was run. Neutral to slightly positive impact was noticed, as illustrated on specific humidity scores with respect to TEMPs. Figure 7 shows BIAS & RMSE for 850 and 700 hPa levels.

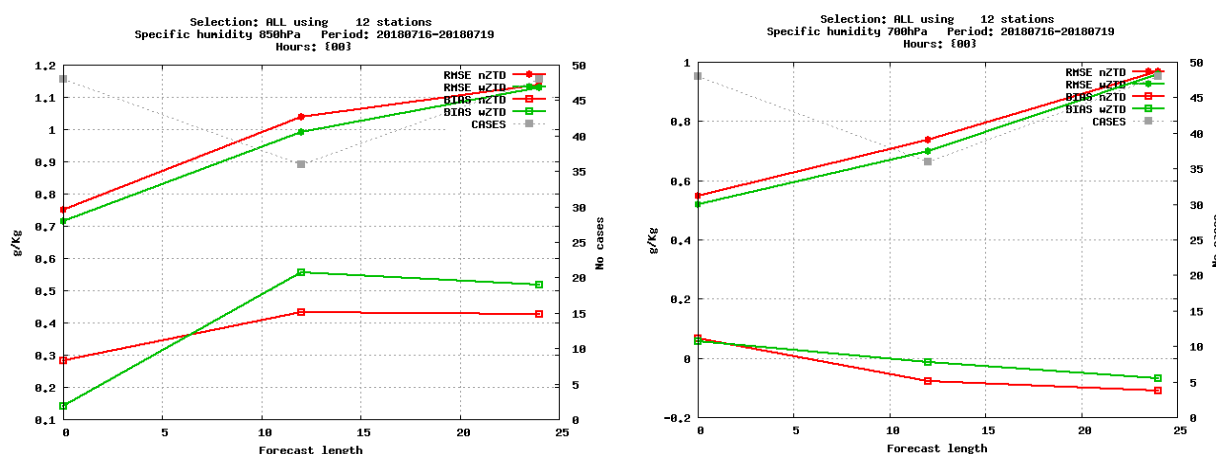


Figure 7: The BIAS and RMSE verification scores of specific humidity for 850 hPa (left) and 700 hPa (right) for data assimilation experiments with ZTD (green) and without ZTD (red).

Offline soil moisture analysis within the SURFEX-SODA framework (V. Tarjáni)

Offline surface assimilation cycling using the EKF method was implemented within SODA framework for two configurations denoted oper and inca (Table 3) using SURFEX V8.1. Outputs from CANARI or INCA analyses of T2M and HU2M are used as gridded observations, having the same regular mesh as the target domain. Forcing (upper boundary condition for SURFEX) is taken from the level at 20 m above the surface (via fullpos). EKF analysis cycling was carried out for 12 days of August 2019 with analyses performed daily at 12 UTC. The feasibility of cycled EKF analysis implementation was

demonstrated. Temporal evolution of analysis increments and observation innovation (Figure 8) show physical relevance. Thorough performance evaluation is planned.

Table 3: Setup of configurations used for SURFEX-SODA experiments

	oper	inca
grid size & dx	614 x 565 pts/ 4.5 km	501 x 301 / 1 km
gridded observations	CANARI analysis	INCA-SK analysis
forcing (@ 20 m height): TA, QA, WIND, DIR, P _s	ALARO/SHMU	
forcing CO ₂	0.000620=const.	
forcing surface radiation	ALARO/SHMU	ALARO/SHMU & GR_AVG
forcing surface precipitation	ALARO/SHMU	INCA-SK

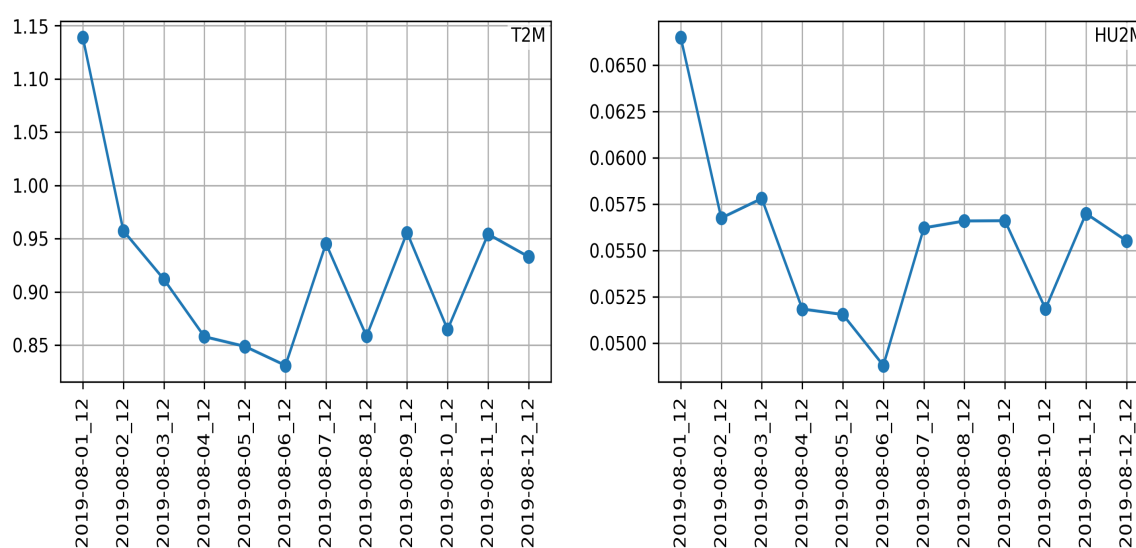


Figure 8: The RMSE of the observation innovations for T2m (left) and RH2m (right).

Implementation of local AWS in the CANARI in ALARO/SHMU (M. Derková)

In attempt to improve too high near surface moisture leading to unrealistic CAPE values that were reported by SHMU forecasters full set of local AWS measurements available from LACE countries was experimentally assimilated into ALARO/SHMU 4.5 km/L63 CANARI analysis over 13-21/06/2019 period. Neutral to slightly positive impact was noticed, notably for T2m_{min}, T2m_{max}. Results are illustrated on Figure 9.

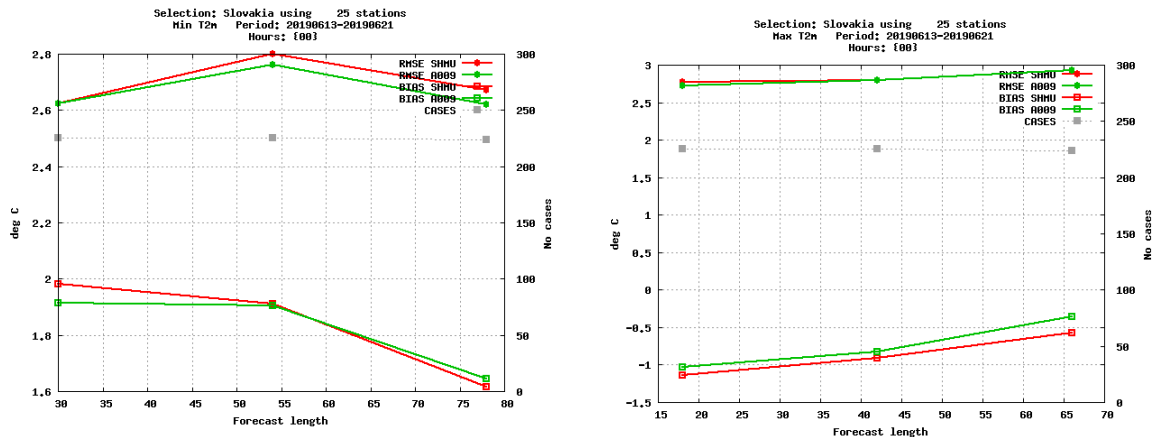


Figure 9: The BIAS and RMSE verification scores of Tmin (left) and Tmax (right) computed over Slovakia for experiment using all available LACE surface automatic weather stations in CANARI (A009 – green) and for the operational suite (SHMU – red).

Testing of parameterization of visibility in ALARO (A. Simon)

The visibility parameter originally coded for AROME (Meteo-France) and later implemented for ALARO (CHMI, ARSO) was tested in ALARO/SHMU 2 km/L73 in CY43t2. Both visibility with respect to cloud liquid water (fog) and precipitation were examined. Default parameters settings and their tuning according to literature review and real measurements (SYNOP, METAR) were evaluated in the case studies during 2017-2019. An illustration of the visibility as a function of the liquid water content for different tuning options is plotted on Figure 10. Preliminary conclusions revealed that obtained visibility seems to be reasonable, with some limitations. Further validation and tuning is welcome. For this work, a participation on the Training on code developments and validation, Toulouse 2019 is acknowledged. Results from the case of 06/01/2019 09 UTC are illustrated below for 9 h forecast of CLW based visibility (Figure 11, bottom left) and precipitation based one (top left), corresponding satellite picture (bottom right) and the real SYNOP measurements (top right). More details in the report Simon and Dian, 2019.

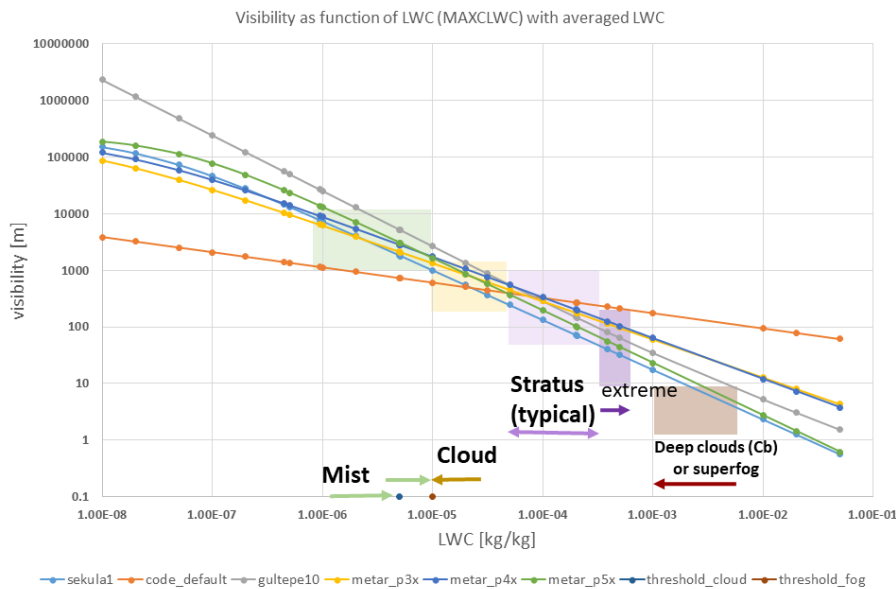


Figure 10: Visibility as a function of the LWC for various tunings.

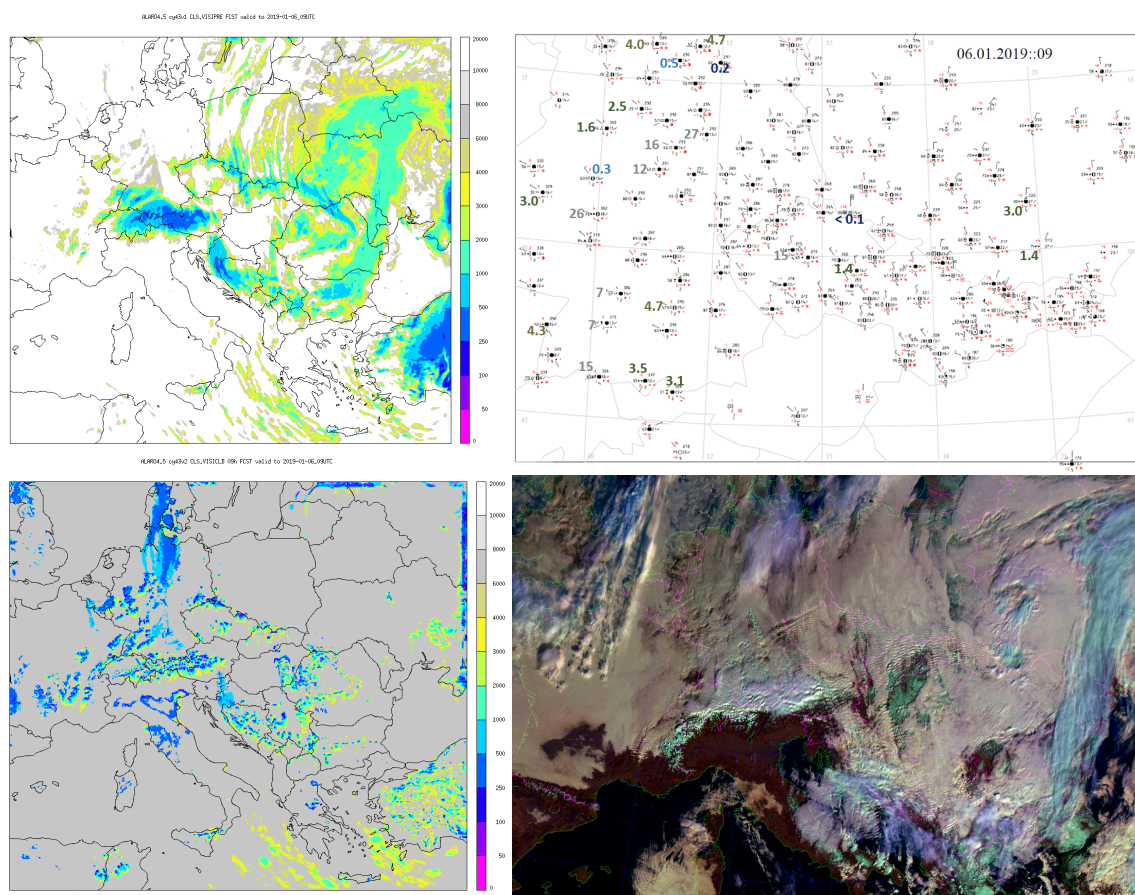


Figure 11: Case study for January 06, 2019 09 UTC: precipitation based visibility (top left), CLW based visibility (bottom left), SYNOP map (top right) and corresponding satellite picture (bottom right).

4 References

Wang, Y., Bellus, M., Weidle, F., Wittmann, Ch., Tang, J., Meier, F., Xia, F., Keresturi, E., 2019: *Impact of land surface stochastic physics in ALADIN-LAEF*. QJRMS, 2019, Vol 145, Issue 724, pp 3333-3350
DOI: 10.1002/qj.3623

Bellus, M., Weidle, F., Wittmann, Ch., Wang, Y., Tascu, S. and Tudor, M., 2019: *Aire Limitée Adaptation dynamique Développement InterNational – Limited Area Ensemble Forecasting (ALADIN-LAEF)*. Adv. Sci. Res., 16, 63-68, 2019. <https://doi.org/10.5194/asr-16-63-2019>

Belluš M., 2019: *Working Area Predictability Progress Report, RC LACE Document* (available on www.rlace.eu)

Bistak, A., Hulinova, Z., Nestiak, M., Gasparik, J., 2019: *The Use of Computer Simulation in Preparation of Construction Works Carried Out by Helicopters*. September 2019, IOP Conference Series Materials Science and Engineering 603:032037
DOI: 10.1088/1757-899X/603/3/032037

Katarína Čatlošová, 2019: [Slovak Mode-S data assimilation into AROME/SHMU](#), RC LACE stay report, Prague (available on www.rclace.eu)

Simon, A. and Dian, M., 2019: *Report on visibility tests with ALARO on cycle 43 t2 bf10 at SHMU* (available on www.rclace.eu)

Jozef Vivoda: *NH system as departure from HY system. Unification of HY and NH code*, RC LACE stay in Prague, 11/2019, (available on www.rclace.eu)

ALADIN highlights in Slovenia in 2019

Benedikt Strajnar, Peter Smerkol, Neva Pristov, Jure Cedilnik, Jure Jerman, Matjaž Ličar

1 Introduction

This contribution briefly presents selected development highlights of ALADIN-related activities at the Slovenian Environment Agency in 2019, mostly in the area of data assimilation.

1 Highlighted activities

Upgrade of operational suite

The operational ALADIN model and its assimilation system was upgraded to cy43t2, after a validation which showed neutral impact with respect to previously used cy40. Few updates were in physics package ALARO-1vB (modifications in shallow convection, exponential random cloud overlaps in radiation and cloud diagnostics). Additionally, observational data set was extended with Mode-S MRAR observations from Czech Republic.

Developments towards reflectivity data assimilation

Evaluations of OPERA/OIFS volume radar observations data were ongoing in 2019. The tool for homogenization of OPERA files (HOOF) was further upgraded upon requests by the users in the LACE and partly HIRLAM community. The preprocessed reflectivity data from 40 European radars was evaluated in a 14-day assimilation trial. The setting of preprocessing and assimilation followed choices made by Meteo France except that HOOF was applied to check the data homogeneity. Verification showed improvements of surface scores (bias of temperature, humidity) due to assimilated reflectivity. Impact on upper-air scores was mixed: temperature was somewhat improved while humidity at around 700 hPa was notably degraded (dry bias, Fig. 2). The latter is also in agreement with degradations seen in cloudiness. The experimentation needs to be extended to more cases and weather regimes.

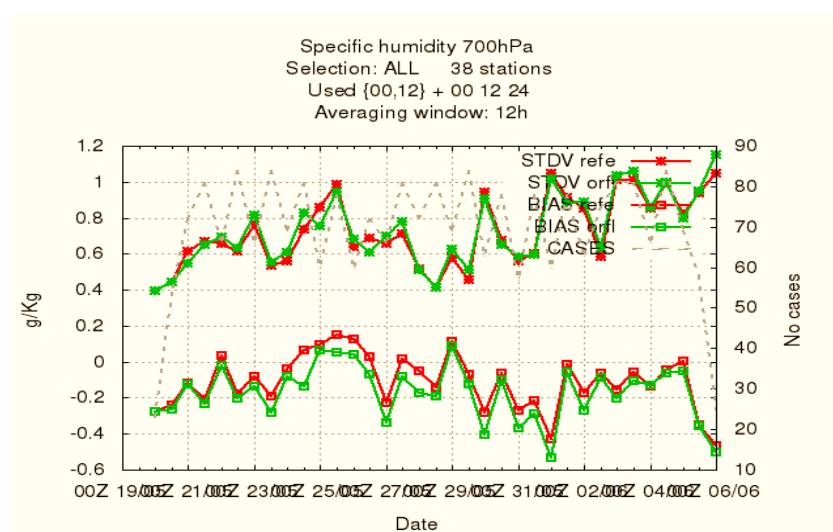


Figure 1: Systematic degradation of humidity bias at 700 hPa (green line) due to assimilated OPERA radar reflectivities with respect to reference (red line) in ALADIN/SI.

Dealiasing of radar radial winds

Remote sensing department of Slovenian Environment Agency started work on Doppler wind processing, with focus on NWP requirements. A survey of existing methods for dealiasing of wind field for radars with low Nyquist velocity was carried out, and a few relevant methods were implemented and tested on synthetic and real cases. It is planned that the most prominent method will be included to the HOOFF software in 2020. This activity may be partly coordinated with OPERA where de-aliasing is to be implemented in a later perspective.

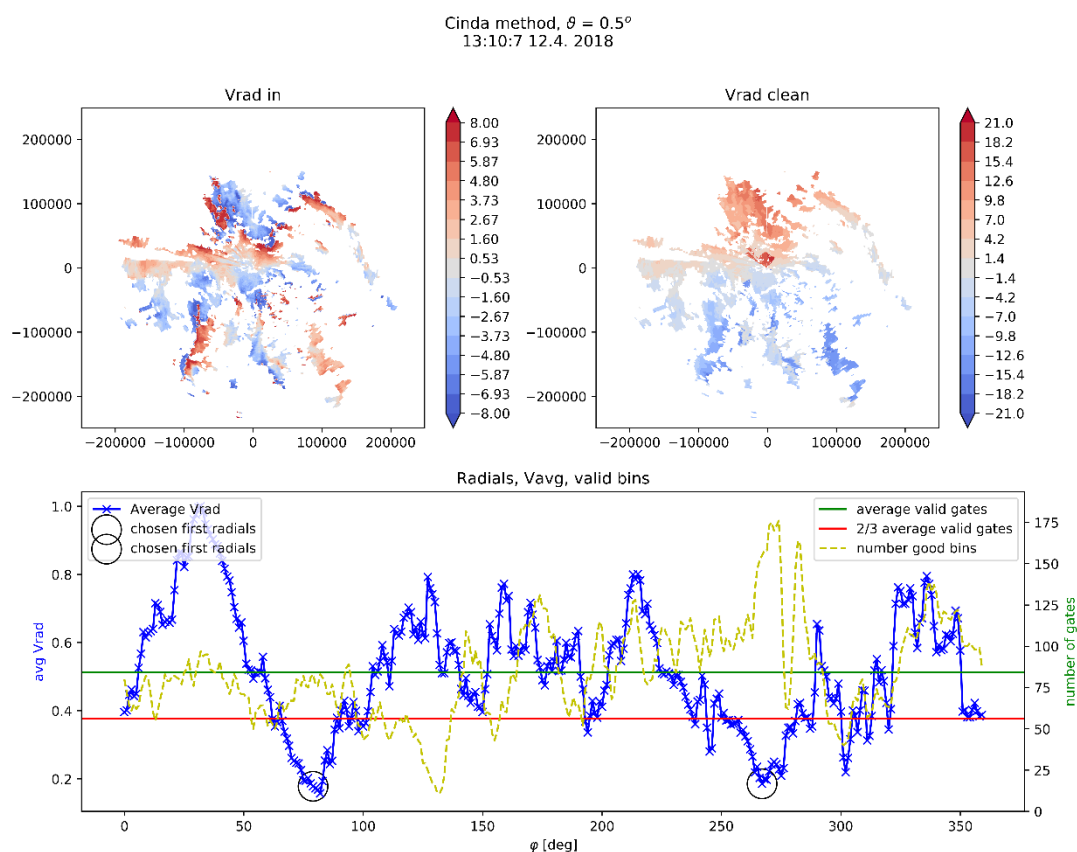


Figure 2: Example of raw (upper left) and dealiased (upper right) radial velocity field using the Cinda method (similar to the method by He et al.) and average radial velocity over a given azimuth (minima are base for dealiasing).

Evaluation of attenuation in telecommunication microwave links for data assimilation

The attenuation of telecommunication inter-antenna links in cellular networks due to rain is an attractive new observation data source. A feasibility study with an example test data from one of Slovenian mobile service provider continued in 2019. A first task was to efficiently separate attenuation data in rainy and dry conditions. This is not trivial because the emitted (and received) signal power change in time, so that the dry attenuation is not exactly known. Moreover, the attenuation can be increased also in non-rainy conditions if emitting/receiving antenna is wet. A solution based on histogram analysis was proposed (example in Fig. L1). The attenuation data marked as rainy was fitted against precipitation estimates (from INCA) in order to obtain a useful attenuation/rain rate relation.

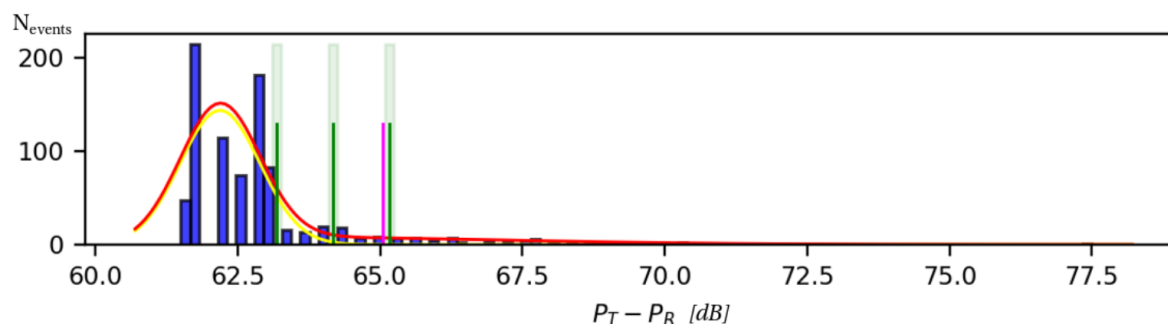


Figure 3: A fit to the distribution of total link attenuation (transmitted - received power) for 4 days of link data at 5 minute intervals. Fit is made to determine the attenuation baseline: the attenuation of the dry period, either via fit, where the baseline is determined as fit average + 3 * fit sigma (the third green line) or via calculation of IQR (interquartile range) of the histogram (violet line).

Implementation of precipitation type diagnostics

Precipitation type computation was prepared by Yann Seity and Ingrid Dombrowski-Etchevers (Meteo France), it is based on wet bulb temperature and snow, rain, ice and graupel/hail and their ratios. The code is already part of the Météo-France operational branch (AROME). Radmila Brožkova phased it in the local branch at CHMI and adopted it for the ALARO physics. Her pack was compiled and evaluated in Ljubljana and later in Krakow. Adaptations for the treatment of graupel and hail (due to differences in microphysics) still has to be validated.

Precipitation type in one point can be defined as most frequent and/or most severe type over a time period (figure 4). These products will be very useful for the end-users.

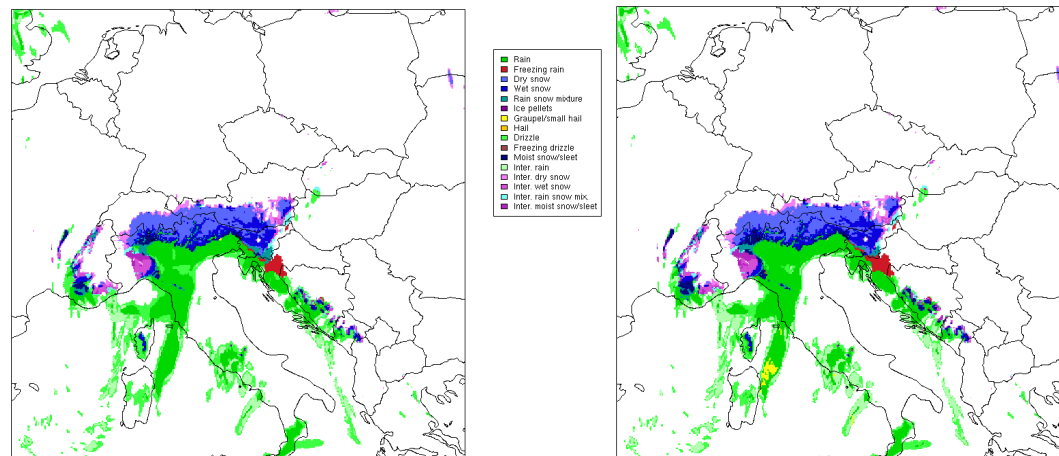


Figure 4: Most frequent (left) and most severe (right) precipitation type during last hour on 30.01.2014 20:00 UTC.

2 Conclusions

In 2019, ALADIN operational suite was upgraded to cycle 43, keeping the model resolution and domain unchanged. The R&D activities focused on radar assimilation, evaluation of potential of microwave links and to model diagnostic products. In 2020, we foresee implementation of 1.3 km nowcasting model version and operationalization of radar DA.

3 References

Smerkol P. (2019), Documentation for the Homogenization Of Opera files (HOOF) tool, ARSO, Ljubljana, <http://www.rclace.eu/forum/viewtopic.php?f=37&t=582&p=2079&hilit=hoof#p2079>, ongoing updates.

Sekula P, (2019), [Testing of new diagnostic fields: precipitation type in cy43t2 in ALARO](#), ALADIN flat-rate stay report, Ljubljana, 19 August - 13 September 2019 (<http://www.rclace.eu/?page=12>)

A major update in AEMET operational suite including radar reflectivity, ASCAT data, humidity in the large scale blending and assimilation of screen level variables in 3DVar

J. Sánchez-Arriola¹, P. Escribà¹, I. Monteiro², J. Campins¹, M. Díez¹, D. Martín¹, V. Costa²,
B. Navascues¹ and J. Calvo¹

¹Agencia Estatal de Meteorología (AEMET)

²Instituto Português do Mar e da Atmosfera (IPMA)

1 Introduction

The current HARMONIE-AROME (Bengtsson et al., 2017) operational suite in AEMET that runs on the local HPCF, is based on a 3DVar data assimilation with a 3h cycle. It assimilates conventional observations from SYNOP, SHIP, DRIBU, AMDAR, and TEMP reports, GNSS ZTD data, and ATOVS satellite radiances from AMSUA and AMSUB/MHS instruments.

A major update of this system has been carried out by updating the handling of ATOVS and GNSS observations and introducing radar reflectivities, scatterometer winds, assimilation of T2m and RH2m in upper air and activating the large scale mixing for humidity. A detailed description of these changes as well as the results and a case study are explained in this document.

2 ZTD GNSS updates

The operational run assimilates GNSS Zenith Total Delay (ZTD) observations from EGVAP (EUMETNET GPS water vapour programme). A selection of the best combination of Station-Analysis Centre (AC) is updated periodically through a White List of observations to take into account the changes in the satellite systems or in the processing of each Analysis Centre itself.

This selection of station-AC has been updated in July 2019 and a list of 625 station-AC combination has been obtained, according with a pre-fixed criteria. The GNSS ZTD observations are selected with a cut-of time of one hour and 10 minutes and both a temporal and spatial thinning are performed. The temporal thinning consists in selecting the observation closest to the analysis time that is every three hours. Currently, a spatial thinning of 50 km is applied resulting in a selection of 207 stations from the total 625 station-AC combinations (Figure 1).

It is important to mention that GNSS ZTD observations have biases that must be corrected prior to their assimilation. The bias correction has been performed using the Variational Bias Correction scheme (VarBC), with a constant offset as the only predictor and a cycle of 3 hours to update the bias coefficients. When a significant model change is implemented, a training period is needed to adjust the bias correction coefficients and in our case the period needed has been around one month.

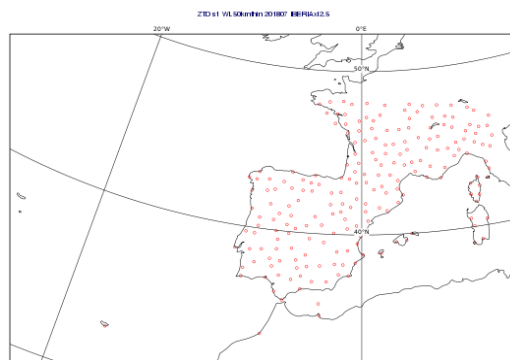


Figure 1: GNSS ZTD observations used in the analysis with the updated White List thinned 50 km.

3 ATOVS updates

Since early 2017, the operational run of HARMONIE-AROME assimilates microwave radiance from the so-called Advanced TIROS Operational Vertical Sounders (ATOVS) on board of several polar-orbiting satellites. ATOVS comprise AMSU-A, AMSU-B (Advanced Microwave Sounding Unit A and B) and MHS (Microwave Humidity Sounder; which has replaced the old AMSU-B) instruments. In particular the operational suite uses radiances from NOAA-18, NOAA-19, METOP-A and METOP-B (Campins et al., 2017).

These polar satellites describe sun-synchronized orbits, and so they pass over a given region at about the same local time, twice each day. However, for NOAA18 and NOAA-19 the local time of the ascending (or descending) node is slowly retarded in time. For short periods (days or weeks) this delay does not suppose any problem, but for long periods (months or years) it implies a change in the number of available observations for each assimilating cycle. As an example, at early 2017 the operational run assimilated radiances from NOAA-18 at 06 and 18 UTC but actually very few or no observations are collected into these assimilating cycles. Similarly, NOAA-19 radiances have progressively shifted from 03 and 15 UTC to 06, 15 and 18 UTC.

ATOVS radiances must also be bias corrected before their assimilation. In HARMONIE, bias correction is carried out using the Variational Bias Correction scheme (VarBC), which is a particular adaptive scheme that is embedded inside the assimilation system. Bias correction is estimated by means of a linear combination of predictors, the so-called bias coefficients, that are continuously updated as part of the assimilation. As the update is daily and they are different for each cycle, when ATOVS radiances moved from a assimilating cycle to another one, the VarBC bias coefficients must be calculated from the beginning. For NOAA-18 and NOAA-19, VarBC coefficient were calculated in September 2018 from a cold-start and for a 1-month spinup period. During this period, radiances were passively assimilated and monitored to ensure un-biased background and analyses departures. From mid-October onwards ATOVS radiances for NOAA-18 and 19 were assimilated as active. For METOP-A and METOP-B warmed-up coefficients were used from the, in that moment, operational suite.

So, the main difference between the old and the new operational suite is that the new one assimilates again radiances from NOAA-18 and NOAA-19, while those from METOP-A and B have no changed. Due to the poorly quality of AMSU-B channels for NOAA-18 only AMSU-A channels are assimilated (Calvo et al., 2019).

4 Radar assimilation

The data from Portuguese (2), Spanish (17) and French (23) radars pre-processed by OPERA (Saltikoff et al., 2019) are ingested in the 3DVar data assimilation. The OPERA data are received from BALTRAD Advanced Weather Radar Networking (Michelson et al., 2018) and only some minor changes have been needed to adapt the reference cycle 40 HARMONIE-AROME code to the operational context in AEMET to be able to assimilate these observations. Concerning the pre-processing, only the observations with an elevation angle higher than 1 degree have been selected. With the ones whose quality "flag" assigned in the OPERA pre-processing exceeded a fixed threshold, a reduction of resolution has been performed. Therefore, superobservations are generated, avoiding the effects of spatially correlated observation errors (Ridal et al., 2017). The assimilation procedure and some results can be found in Sánchez-Arriola et al. (2019).

The relationship between the model variables and the reflectivities is non-linear and therefore it is complex, since it takes into account the microphysics parameterization. Furthermore, reflectivity errors show non-Gaussian distributions. For these reasons, in the HARMONIE-AROME system, the reflectivity variable is not directly assimilated in the model but is previously transformed into a 1D vertical profile of relative humidity as described in Caumont et al. (2010). This procedure includes the comparison between the simulated reflectivity by the model and the observation. The humidity profiles assimilated may contribute then to wet or dry the first guess.

As it can be seen in the results, the impact of these observations has been similar to other studies performed in AEMET, which is positive in precipitation forecast mainly by decreasing the false alarm rate of precipitation and being in general more accurate on the place the storms are located as it can be seen in the case study described below.

5 Ascatt assimilation

Positive impact of the assimilation of scatterometer winds in HARMONIE-AROME were reported for in several forecasting centres (Valkonen et al., 2016; Marseille and Stoffelen, 2017; Monteiro and Marseille, 2018) and encouraged the implementation described herein.

Moreover, domains that include large areas covered by oceans, such as AEMET operational domain or IPMA's pre-operational domain, require initialization over areas sparsely covered with conventional observations.

Space-borne scatterometers provide a large number of near surface wind estimations over the ocean. Scatterometers are satellite radar instruments, which provide a measure of wind speed and direction near the sea surface. ASCAT, is European C-band (rain insensitive) scatterometer on-board the Metop-A, Metop-B and Metop-C satellites, which were launched into a sun-synchronous orbit in October 2006, September 2012 and November 2018 respectively. Satellite overpass time, expressed as Local Time at Ascending Node (LTAN), is 21:30 on the Metop reference orbit. The sun synchronous reference orbit ensures that the local solar time of observations for a geographic location is the same time (at night on ascending orbits and during the morning for descending orbits). Metop-A is now drifting to an earlier LTAN.

ASCAT data used at both AEMET and IPMA, are on a 12.5 km grid provided by the EUMETSAT Ocean and Sea Ice Satellite Application Facility (OSI SAF). The data are generated from the EUMETSAT global data service (GDS) 30–60 min after the measurements are taken. Currently, for AEMET and IPMA operational domains, ASCAT wind observations can be used by the 3D-Var assimilation system at the 09UTC or 12 UTC analysis and at the 21 UTC analysis.

A data thinning to every 4-th ASCAT wind vector cell is performed (currently, the default setting in HARMONIE-AROME) in order to avoid spatially correlated errors. These settings correspond, for the ASCAT-coastal product, to a 50 km thinning spacing. Before thinning, all available ambiguous wind solutions are presented to the assimilation system and the most likely solution is selected to be used. For the selected wind solutions observation errors for zonal wind u and meridional wind v components are set to 1.39 and 1.54 m/s.

Some previous tests have been performed in AEMET to check the availability, the quality of the data and the impact of assimilating this observation and a slightly positive impact has been found. At IPMA, several Observation System Experiments (OSEs) have been conducted to assess the impact of ASCAT winds IPMA's local HARMONIE-AROME configuration. OSEs considering assimilation of conventional observations with/without scatterometer wind observations and testing different options of thinning were performed. Noticeable was the improvement found for the 10 m wind over sea at the first 10 hours forecast of (more details in Monteiro and Marseille, 2018).

The scatterometers data have been included in the HARMONIE-AROME configuration described in this paper since 21st November 2019, when this new setup was already running in real time. Overall the impact of these data is neutral with a slight improvement in wind fields as can be seen in Figure 2.

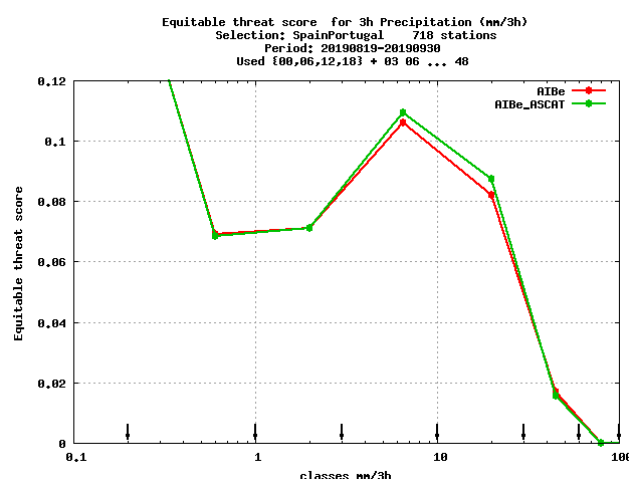


Figure 2: Impact of assimilating ASCAT data. Equitable Threat Score for 3h accumulated precipitation (mm/3h) against SYNOP observations for the period 19 August to 30 September 2019.

6 Assimilation of T2m and RH2m

The previous operational version has used screen level observations of temperature and humidity only in the surface analysis only. From our experience with the LETKF algorithm we thought that these observations may have also a positive impact in the upper air 3DVar analysis. The main concern could be the arguable erroneous double counting if doing so. On the other hand it is reasonable to think that using screen level observations in upper air may lead to a smoother transition between surface and upper air.

A parallel run was performed with the operational 3DVar configuration for a month with many cases of large and extreme precipitation over Iberian Peninsula (October 2018). Main conclusions were that the assimilation of these observations has a positive impact in reducing screen level humidity bias and it improves slightly the RMSE of humidity for low and middle levels (Figure 3). Besides, a small

positive impact in precipitation is seen (not shown). Another interesting feature is that the lowest level analysis increments are more realistic in orographic and coastal areas.

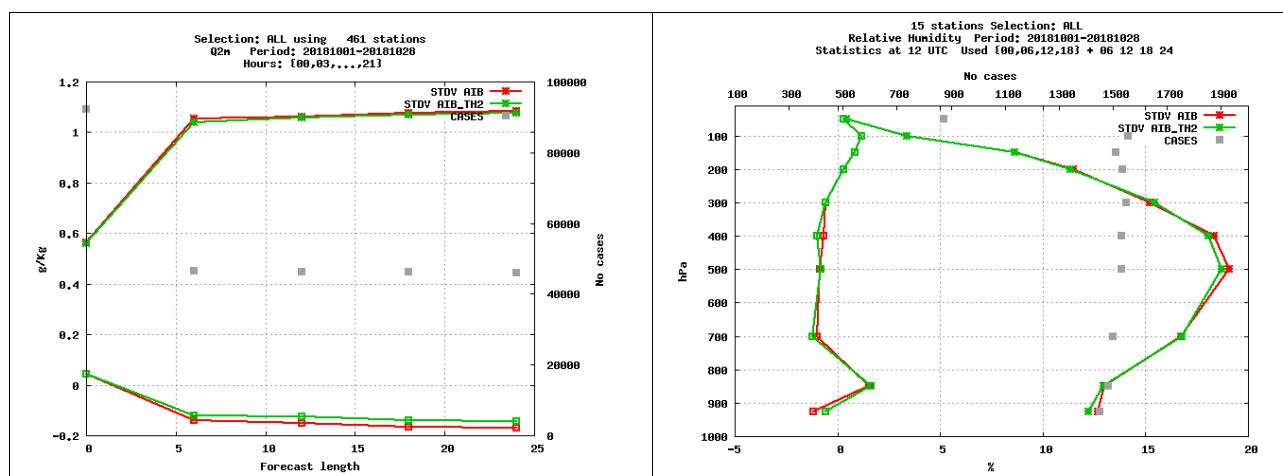


Figure 3: Impact of assimilating screen level temperature and humidity in 3DVar for the period October 2018. Verification against observations for 2 m specific humidity function of the forecast length (left) and upper air relative humidity at 12 UTC, both up to H+24. In red the operational version and in green the version including screen level assimilation. Bias are empty square marks and standard deviation full square marks.

7 Humidity large scale mixing

Large scale mixing of the HARMONIE-AROME first guess with the IFS short-range forecast was first introduced in the HIRLAM framework with the aim of taking advantage of the high quality IFS analysis (Vignes, 2011). This methodology mixes the local and global first guesses in spectral space which results in an analysis of better quality. This mixing is applied just before the upper air 3DVar analysis and the outcome is a modified first guess that will be the input for the analysis. The standard practice in HIRLAM community is to apply this large scale mixing only to wind components and the temperature because there is a concern that this blending applied to humidity fields could destroy the small scale humidity features produced by our non-hydrostatic high resolution model.

Also based in previous LETKF experiments, we thought that the model forecasts could be improved particularly for humidity if we extended the mixing to the vertical humidity. As the large scale information is only used for scales above 100 km we think that small scale information can be preserved through the blending process. Besides, it is reasonable to think that mixing only 3 variables supposes some lack of coherence since the atmospheric state for large scales is defined by 5 variables: temperature, two wind components, humidity and surface pressure.

In Figure 4 we show the objective verification for a 48 hours forecast over a two month period (October and November 2018). The improvement in vertical humidity and precipitation is clear. The impact in other variables is neutral or slightly positive.

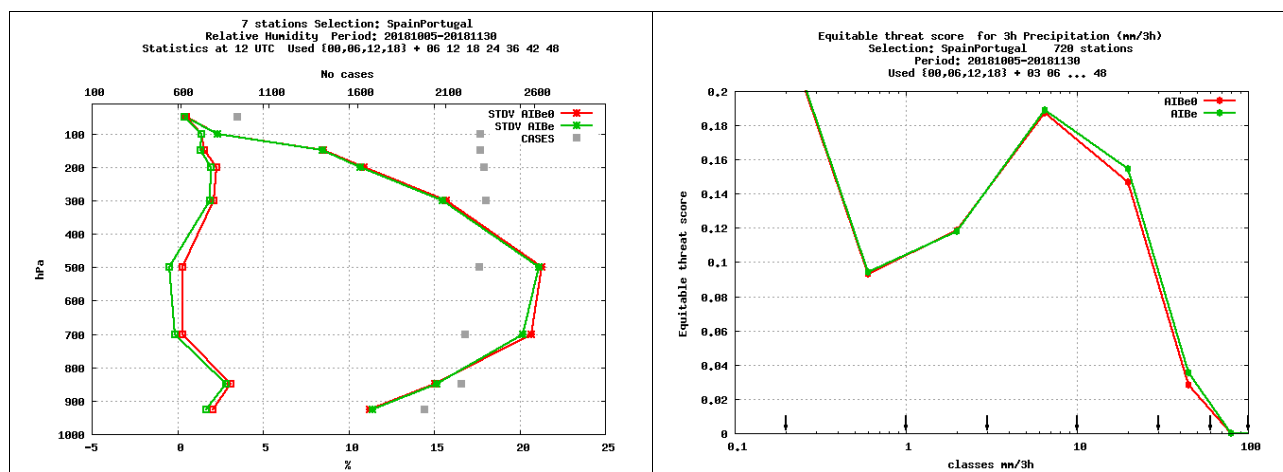


Figure 4: Impact of large scale humidity mixing for the period October-November 2018. Verification against observations for upper air relative humidity (left) and Equitable Threat Score 3-hr precipitation (right). In red the version described in this article mixing wind components and temperature, and in green including also the humidity mixing. Bias are empty square marks and standard deviation full square marks.

8 Tuning of the wind drag

Operational 10 m wind forecasts show a clear positive bias that can be alleviated by increasing the momentum drag coefficient in the canopy scheme from $C_D=0.01$ to 0.02 as can be seen in the objective verification (Figure 5). Nevertheless, the bias, around 0.9 m/s is still large and there are indications that some kind of orographic drag could be needed.

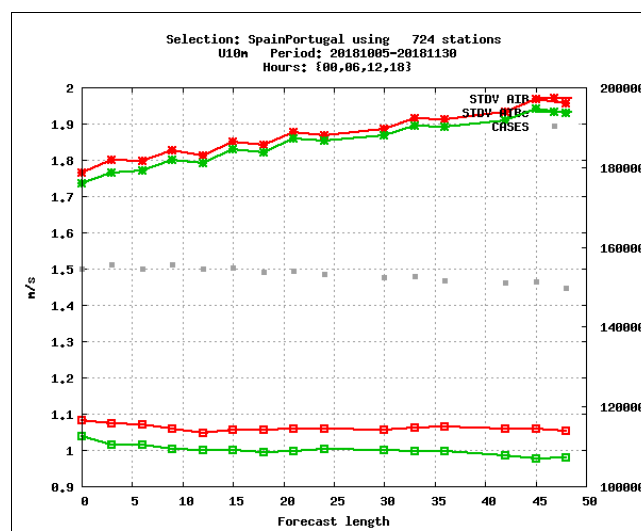


Figure 5: Objective verification of 10 m wind function of the forecast length for the period October-November 2018. In red the operational version and in green the updated version including an enhanced momentum drag. Bias are empty square marks and standard deviation full square marks.

9 Case study: 9 October 2018

On 9 October 2018 a flash flood devastated the village of Sant Llorenç des Cardessar, in the northeast of Mallorca (Balearics Islands, Spain). The episode provoked thirteen deaths and high economic damages. The flash-flood was caused by a torrential precipitation event, from a convective origin, that fell into a very small catchment. A train of convective cells moving from South to North organized as a quasi-stationary line in NE. The episode recorded torrential rainfall with a highest intensity of 89.6 mm in 1 hour, and total rainfall amount of 232.8 mm in less than 6 hours (Figure 6a). Radar 24-hour accumulated rainfall (Figure 6b) shows the small spatial scale of the event, although underestimate the intensity.

The operational forecast from HARMONIE-AROME did not forecast neither the location nor the intensity of this episode. Thereby, the forecast reflectivity at 15 UTC (Figure 7a) from the integration initialized at 00 UTC shows intense precipitation at the south of Mallorca, but far from the affected region. The precipitation forecast from AIBe (Figure 7b) improves both the intensity and location but is not able to reproduce the small stationary system that produced the torrential rain. The improvement in the humidity initial state seems to point out to an improvement of the precipitation forecasts.

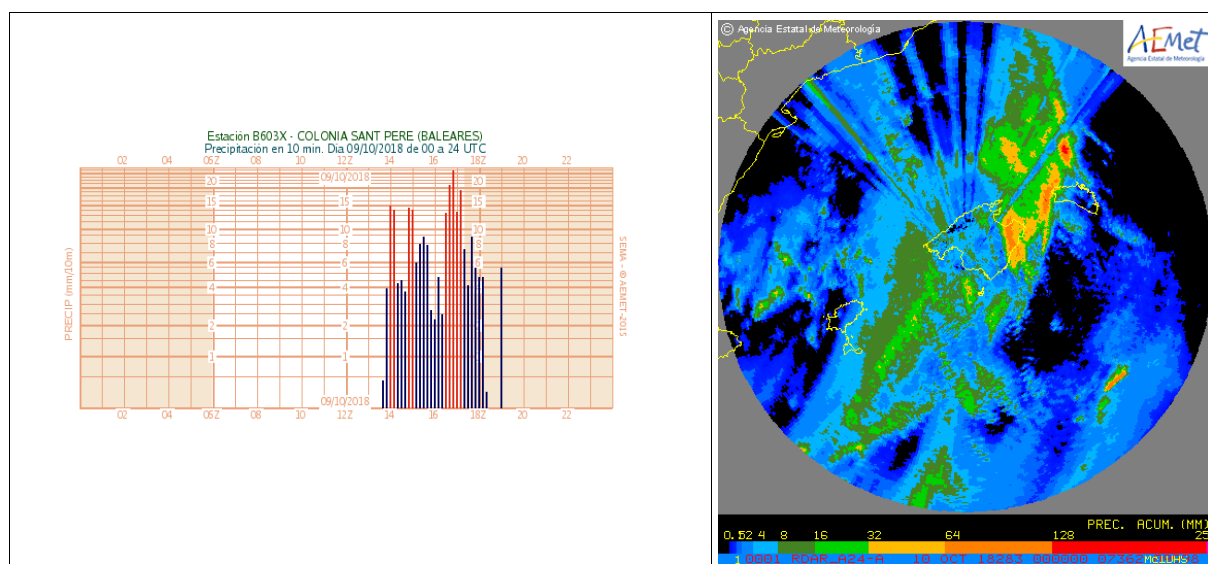


Figure 6: (a) Precipitation intensity (mm/10m) on 9 October 2018 at Colonia de S.Pere, and (b) 24-hr radar accumulation (mm) showing the maxima at the NE of Mallorca.

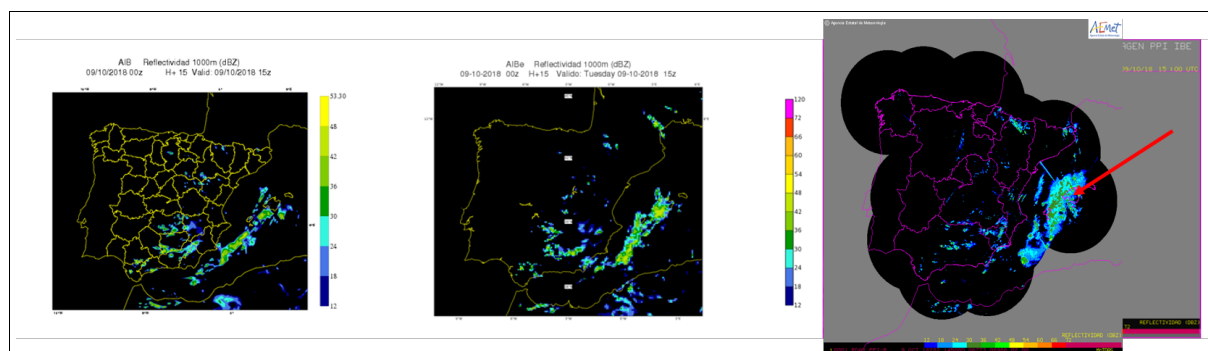


Figure 7: Simulated model reflectivities (dBZ) at 15 UTC: Operational (left) new versión (middle) compared with radar observation (right).

10 Verification results

The new setup has been running for several test periods of different seasons and in real time since September 2019. The ASCAT data have been added since the 21st November 2019.

A general improvement is found in all the variables being more significant in the humidity profiles and in the precipitation as can be seen in Figures 8 and 9. Only for the period 19 August-30 September 2019 we found a neutral impact on precipitation.

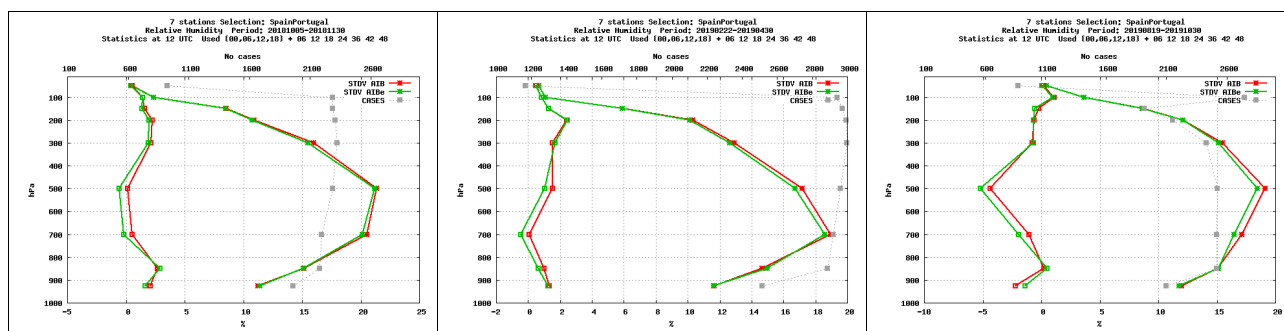


Figure 8: Relative Humidity verification against soundings for the period Oct-Nov2018 (left), Mar-Apr2019 (middle) and Ago-Sep2019 (right). In red the reference operational suite and in green the new version described in this article. Bias are empty square marks and standard deviation full square marks.

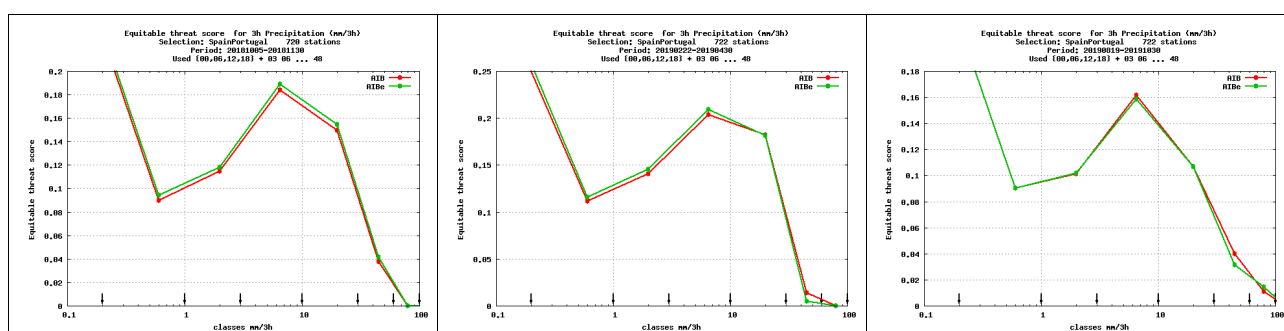


Figure 9: Equitable Threat Score for 3-hr precipitation against rain gauges for the period Oct-Nov2018 (left), Mar-Apr2019 (middle) and Sep-Nov2019 (right). In red the reference operational suite and in green the new version described in this article. Bias are empty square marks and standard deviation full square marks.

11 Conclusions

A major update has been implemented in AEMET operational suite. Most of enhancements concern to the data assimilation. The new suite includes an update in the handling of ATOVS and GNSS observations, the assimilation of new data sources (radar reflectivities, scatterometer winds, T2m and RH2m observations in upper air), and activation of the large scale mixing for humidity. Additionally, some tuning of the wind drag has been performed. All these updates result on an overall improvement of all model variables in all seasons. The most significant impact is found in the humidity profiles and precipitation.

Although it has been demonstrated the positive impact of all the new components together, we think that the radar assimilation and the humidity large scale blending may be the ones with major impact.

In the future, we expect to incorporate also Doppler radar winds in the assimilation as well as other scatterometers data. Besides, we are in the process of introducing SEVIRI and IASI data. Other aspects that we will tackle are the reduction of the 10 m wind overestimation, the decrease of the minimum temperature overestimation in stable conditions and the improvement of the gust estimation associated with deep convection.

12 References

- Bengtsson, L., Andrae, U., Aspelién, T., Batrack, Y., Calvo, J., de Rooy, W., Gleeson, E., Hansen-Sass, B., Homleid, M., Hortal, M., Ivarsson, K.-L., Lenderink, G., Niemelä, S., Nielsen, K. P., Onvlee, J., Rontu, L., Samuelsson, P., Muñoz, D. S., Subias, A., Tijm, S., Toll, V., Yang, X., and Køltzow, M. Ø., 2017: The HARMONIE-AROME Model Configuration in the ALADIN-HIRLAM NWP System, *Monthly Weather Review*, 145, 1919-1935
- Caumont, O., V. Ducrocq, E. Wattrelot, G. Jaubert & S. Pradier-Vabre, 2010: 1D+3DVar assimilation of radar reflectivity data: a proof of concept. *Tellus A: Dynamic Meteorology and Oceanography*, Volume 62, Issue 2
- Calvo, J., Calvo C., Callado A., Campins J., Díez M., Escribà P., Geijo G., Hernández A., Jiménez A., Martín D., Morales G., Viana S. and Sánchez-Arriola J., 2019: Highlights of the NWP activities at the Spanish Meteorological Agency. ALADIN-HIRLAM NewsLetter No. 12.102-111
- Campins, J., Sánchez-Arriola J., Díez M., Calvo J. and Navascués B., 2017: Assimilation of ATOVS and GNSS ZTD data in the HARMONIE-AROME model configuration run at AEMET. ALADIN-HIRLAM NewsLetter No. 8, 40-50
- Marseille, G.J. and A. Stoffelen, "Toward Scatterometer Winds Assimilation in the Mesoscale HARMONIE Model," IEEE J. Sel. Top. Appl. Earth Obs. Remote Sens., 10 (5), 2017.
- Michelson, D., Henja, A., Ernes, S., Haase, G., Koistinen, J., Ośródko, K., Peltonen, T., Szweczykowski, M. and Szturc, J., 2018. BALTRAD Advanced Weather Radar Networking. *Journal of Open Research Software*, 6(1), p.12. DOI: <http://doi.org/10.5334/jors.193>
- Monteiro, I and G.J. Marseille, 2018. Scatterometer Assimilation Experiments with HARMONIE-AROME Mesoscale Model over south-western Europe. EUMETSAT Meteorological Satellite Conference, 17-21 September 2018. [Online].
- Ridal, M., and M. Dahlbom, M., 2017: Assimilation of Multinational Radar Reflectivity Data in a Mesoscale Model: A Proof of Concept. *Journal of Applied Meteorology and Climatology*, 56(6), 1739-1751
- Sánchez-Arriola J., Navascués B., Calvo J., 2019: Radar Reflectivity Impact study with HARMONIE-AROME in AEMET. ALADIN-HIRLAM Newsletter No.12, 112-118
- Saltikoff, E. & Haase, Günther & Delobbe, Laurent & Gaussiat, Nicolas & Martet, Maud & Idziorek, Daniel & Leijnse, Hidde & Novák, Petr & Lukach, Maryna & Stephan, Klaus. 2019. OPERA the Radar Project. *Atmosphere*. 10. 320. 10.3390/atmos10060320.

Valkonen, T., H. Schyberg, and J. Figa-Saldaña, Assimilating Advanced Scatterometer Winds in a High-Resolution Limited Area Model Over Northern Europe. *IEEE J. Sel. Top. Appl. Earth Obs. Remote Sens.*, 2016.

Vignes, O. (2011). Short presentation on LSMIX option in HIRLAM/HARMONIE systems.
<https://hirlam.org/trac/attachment/wiki/HarmonieSystemDocumentation/lsmixbc.ppt>

SMHI ALADIN/HIRLAM 2019 Main Activities

Magnus Lindskog, Ulf Andrae, Jelena Bojarova, Nils Gustafsson, Susanna Hagelin, Karl-Ivar Ivarsson, Åke Johansson, Heiner Körnich, Tomas Landelius, Paulo Medeiros, Esbjörn Olsson, Martin Ridal, Per Undén, Daniel Yazgi

1 Introduction

The philosophy of the Swedish Meteorological and Hydrological Institute (SMHI) numerical weather prediction section is to carry out research and developments in close collaboration with our partners. The collaborating partners are our colleagues within the ALADIN/HIRLAM consortium and also our partners in other national and international projects. Through collaboration with others SMHI have achieved progress during 2019 in a wide range of areas. We acknowledge all our collaborating partners and their contributions, but highlight here the main areas of SMHI contributions within the main areas of collaboration.

2 Upper-air data assimilation and modelling

SMHI contributions to methodology developments for upper-air data assimilation have been attributed to evaluation and further development of HARMONIE 4D-VAR, as well as phasing of HARMONIE 4D-Var between cycles 40 and 43. The evaluation concerned both single observation experiments and full scale data assimilation experiments. The experiments highlighted the importance of a proper handling of lateral boundary conditions within the data assimilation process. The present handling can be improved both through application of a wider extension zone and through application of inclusion of lateral boundary conditions within the 4D-VAR control vector. A system with possibility to apply a wider extension zone in data assimilation than in model forecast has been designed.

Upper-air observation handling activities at SMHI include preparation of the HARMONIE-AROME system for assimilation and monitoring of satellite based winds from the Aeolus instrument as well as microwave radiances from the AMSU-A and MHS instruments on-board the METOP-C satellite as well as from the MWHS-2 instrument onboard the FY3-C and FY3-D satellites.

Together with MET Norway, we have investigated the impact of the wind profiles from the Aeolus satellite in the MetCoOp domain. The Aeolus satellite is a polar orbiting satellite and on average there are two or three passages over the MetCoOp domain per day. During the test period recommended by ESA (14 Sept. to 14 Oct. 2018), we found that the overall impact of the satellite data was neutral. This is in agreement with results obtained from global models by other centres, such as ECMWF and Météo-France which saw improvements in the tropics and the Southern hemisphere, but neutral or degradations of the forecasts when using Aeolus data in the Northern hemisphere.

For this project we also cooperate with IRF (the Swedish Institute for space physics) in Kiruna, where we compare our HARMONIE-AROME simulations with the data from their wind profiler ESRAD and to Aeolus data. While the Aeolus data has a neutral impact in the standard verification scores we have seen that the Aeolus data changes the model analysis in the data assimilation. Figure 1a shows the difference in wind speed at 10 km in the analysis between two experiments, one actively assimilating the Aeolus data and the other using the Aeolus data in passive mode for 06 UTC on 17 Sept. 2018. Figure 1b shows the satellite tracks for the same day.

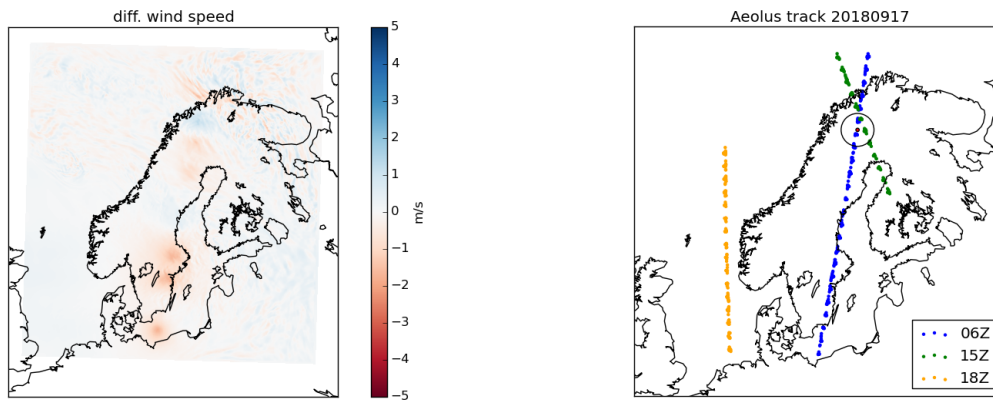


Figure 1: Left (a): The difference in wind speed at 10 km height at analysis time for the 06 UTC cycle of HARMONIE-AROME when assimilating Aeolus winds in active mode and in passive mode. Right (b): The satellite tracks for Aeolus on the same day. The red dot show the location of ESRAD, the IRF wind profiler, and the black circle 1 degree distance to ESRAD.

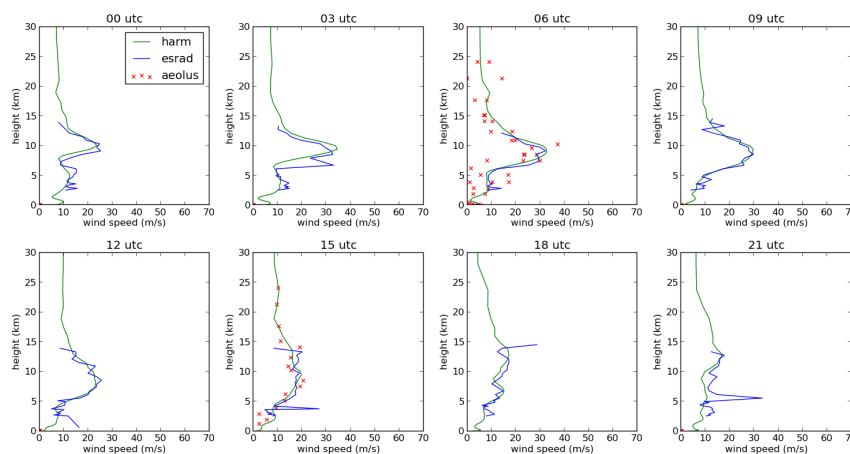


Figure 2: Wind speed profiles for horizontal line of sight for HARMONIE-AROME (green lines), ESRAD wind profiler (blue lines) and Aeolus (red crosses).

We have found the satellite passes near the location of the wind profiler twice per week during the test-period, and while further analysis of the data is still ongoing, there seems to be a good agreement in the wind speed measurements from ESRAD and Aeolus with the model values (see Fig.2).

Regarding modelling, there have been some progress in microphysics during the last year. Common complains about the forecasts that are addressed here are the following:

- Too much fog, especially in spring and over sea
- Too small amounts of low clouds, except very low clouds (below 100 or 200 metres)
- Too small amounts of middle level clouds
- Occasionally, super cooled rain was not forecast properly.

Currently, the active cloud condensation nuclei concentration (CCNC) is hard-coded to 300 cm^{-3} over land and 100 cm^{-3} over sea. Several studies .e.g Mazoyer et al (2019) suggests that this concentration may be lower in fog due to less mixing and other processes. A pragmatic approach is just to allow a lower CCNC in the lowest model level. This reduces that occasions of fog in the model. Another change is to let the relative humidity for which condensation can start be dependent of the model level thickness, since a thicker model level means a larger variation of relative humidity within the grid box. This is achieved by letting the tuning parameter VSIGQSAT be a little larger for thick layers than for thin ones. The result of this change is less clouds, including fog near the ground and somewhat more above 200 metres with the current set-up of model levels.

Missing super-cooled rain has been related to occasions with layers near the ground having temperatures below freezing, such that some clouds contain a tiny part of ice. By setting a threshold for the amount of ice for which ice should have an impact on turning supercooled rain into graupel, the supercooled rain is properly forecast in those cases. A cross section over northern Sweden is shown in Fig. 3, without (left) and with the modified tuning parameter, respectively. In the reference (left) we see that rain freezes near ground into graupel due to thin clouds containing very tiny amounts of ice in the cold layer near ground. The result with the modified microphysics scheme is seen in the right part of Fig. 3. The threshold for the amount of ice causing freezing is higher and prevents freezing which shows much better agreement with observations.

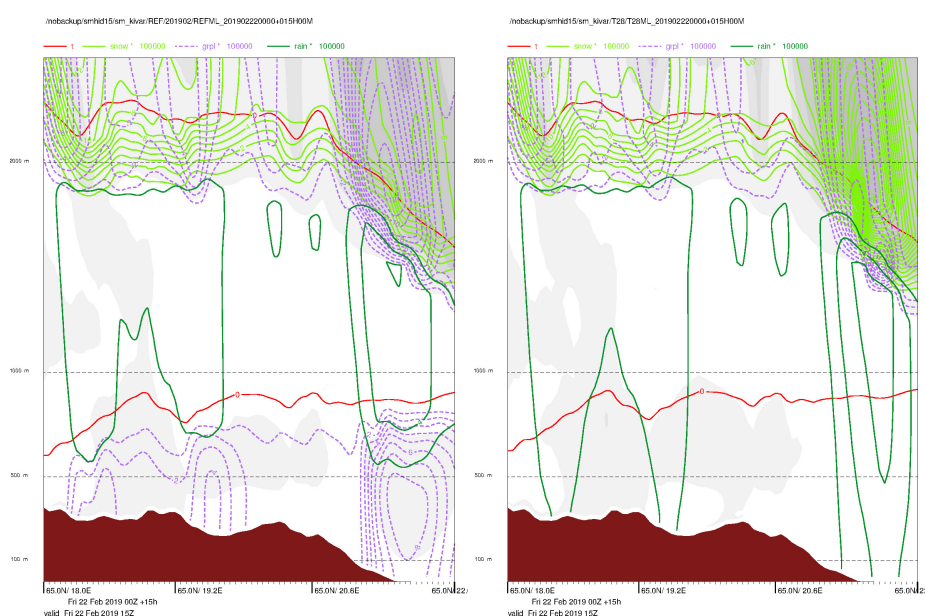


Figure 3: Cross section at 65 degrees N over northern Sweden. The result are with the operational forecast (left) and with the forecast produced with a modified tuning parameter (right). Zero degrees isotherm in red, snow in light green, rain in dark green and graupel in purple.

3 Surface data assimilation and modelling

The ambition of the European Union's Horizon 2020 project IMPREX was to enhance forecast quality of extreme hydro-meteorological conditions and their impacts. SMHI numerical weather prediction contribution to IMPREX focused on the effects of surface data assimilation on short-range (days ahead) weather forecasting. A refined surface data assimilation (Lindskog and Landelius, 2019), as compared to the baseline (based on cy 38h1.2) was applied. The refinements includes assimilation an simplified extended Kalman filter (Mahfouf et al.

2009), MESCAN background error correlations (Soci et al., 2013a and 2013b) based on the Swedish MESAN analysis system (Häggmark et al., 2000), and assimilation of satellite-based soil moisture information.

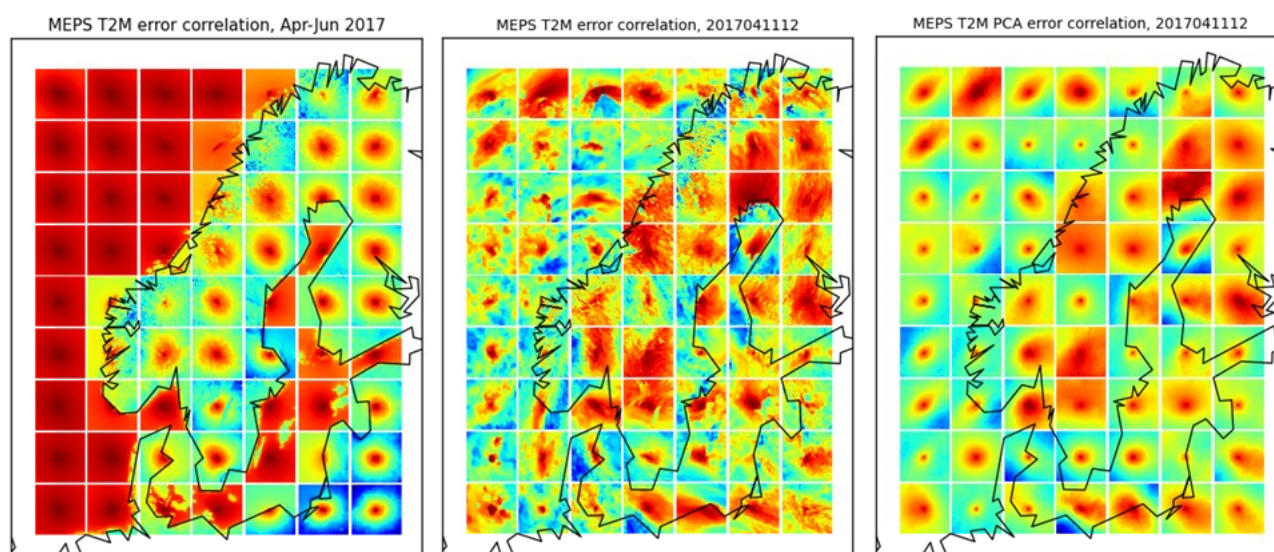


Figure 4: Background error correlations for two-metre temperature. Left: Estimates based on HARMONIE ensemble members from a four month summer period. Middle: Estimates based on ensemble data from a single day. Right: Regularized single day estimate obtained by projection of the data in the middle panel onto a PCA basis derived from the data in the left panel (also using data from overlapping regions not shown for reasons of clarity).

Here the inhomogeneities were modelled by introducing a horizontal dependency of land-sea mask and of height of orography. Since then, work has continued to study the possibility of modelling the inhomogeneities directly based on the data using Ensemble Kalman Filter (EnKF) techniques.

The challenge is that the number of ensemble members is very low (approx 10) compared to the rank of the matrix describing the background error in a region influenced by the observation (approx 1 0000). As a result ensemble based error matrices often show spurious correlations at distances far away from the observation. A common way to tackle this problem is to multiply the ensemble based error matrix with a localization matrix (point-wise Shur product) and hence force the correlations to be small far away from an observation.

This method has however a number of drawbacks. Here we study a possible alternative where the background error matrix is instead modelled with a small set of basis vectors. So far we only have very preliminary results. The basis is obtained from a principal component analysis (PCA) of the error matrices in different regions of the model area. A number of non-overlapping regions are illustrated in 4. However, also somewhat overlapping regions could be included to extend the data set as long as the data can be considered to be independent enough.

The error matrix in each region is first calculated for a sufficiently long time period (e.g. for a season) using all ensemble members for that period, see left panel of 4. Note that here the correlation length is very long over sea which to some extent an artefact from how the surface parameters are perturbed in the HARMONIE system. Only areas centred around surface points should be included in the analysis.

Next a PCA is done on the regional error matrices to come up with a small number (same order as the number of ensemble members) of basis vectors that can be used to model the horizontal variation in the background error. The results when modelling the error correlation based on the ensemble members from a given date as is and projected on the PCA basis are illustrated in the middle and right panels of 4.

Results are preliminary but promising and work will continue and involve tuning of the PCA procedure and

comparisons with the Shur product approach. For the longer term the idea is to arrive at a consistent surface assimilation system where EnKF techniques also are employed for the vertical part of the data-assimilation where information from the surface observations is propagated into the deeper soil layers.

In addition, the refined system discussed earlier also included assimilation of satellite based snow information based on both Cryoland and on NOAA IMS (ICE Mapping System) daily products. The Cryoland fractional snow cover used is a visible sensor product with 500 m horizontal resolution and the NOAA IMS snow cover used is multi-sensor product with 4 km horizontal resolution. A pre-processing and quality step prior to assimilation was found important for forecast quality.

SMHI has furthermore in collaboration with European Centre for Medium-Range Weather Forecasts (ECMWF) carried out an evaluation of ECMWF and HARMONIE-AROME snow analysis products and this comparison is as well relevant for identifying model strengths and weaknesses and needs for further developments. In the study, we were focusing on evaluation of these products in the predominantly boreal regions of Sweden and Finland. In this region the knowledge of snow depth is crucial for predicting potential for flooding during the melting season and also for hydro-power applications. For this evaluation we have accessed two data sets of snow depth, snow water equivalent (SWE), and density from SMHI and the Finnish Environment Institute (YMPARISTO). The evaluation was done for the winters of 2016/17 and 2017/18 at a total of 146 locations. Histogram of observed values as compared with HARMONIE-AROME and ECMWF operational snow analyses are shown in Fig. 5. One interesting result is that HARMONIE-AROME overestimates the snow density and has a maximum threshold of snow density that prevents it from an accurate modelling in cases of high snow densities. More recent studies focused on HARMONIE-AROME and ECMWF next generation snow schemes. The next generation HARMONIE-AROME snow scheme has more vertical levels and seems to have a more realistic representation of snow density than the currently used scheme.

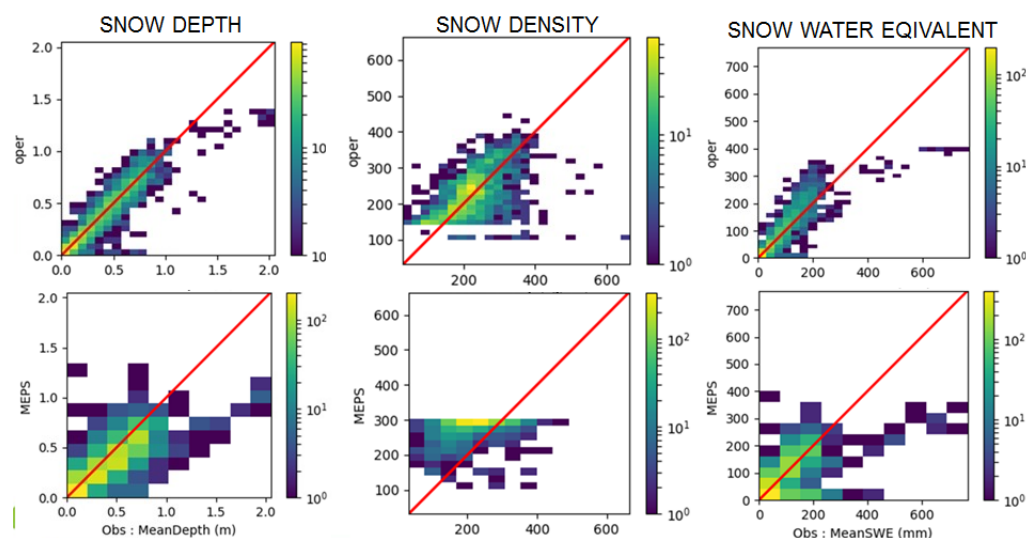


Figure 5: Histogram of observed snow depth (left column), snow density (middle column) and snow water equivalent (right column) as compared to ECMWF (upper row) and HARMONIE-AROME lower row operational analyses.

4 Re-analyses

SMHI is the Contractor for the Copernicus Service for Regional Reanalyses over Europe, C3S_322_Lot1. Météo-France and MET Norway are partners (or sub-contractors). During this service the regional reanalysis that was started during the UERRA (Uncertainties in European Regional Re-analyses, <http://www.uerra.eu/>)

project has been extended to July 2019. In the mean time a new system has been developed in close collaboration with Météo-France and MET Norway and also with the Arctic Reanalysis Service, Lot2, (CARRA) lead by MET Norway. The new system, Copernicus European Regional ReAnalysis (CERRA), is run at a horizontal resolution of 5.5 km with 106 model levels. As for UERRA an offline surface model (SURFEX) is also run with the same horizontal resolution. There is an off line precipitation analysis with off -line Canari with MESCAN but in CERRA the 2m temperature and humidity analysis is part of the coupled analysis (with 3D-VAR) since MESCAN is used in the new system and the grid resolution of the 3D-VAR and model is at 5.5 km. A lot of the development has been in cooperation with CARRA that runs regional re-analyses over two domains in the Arctic region. Some of the development can be transferred in to the HARMONIE/ALADIN systems such as, for example, a new black list procedure, tests of different methods to blend with large scale information from the driving model and GRIB2 parameter definitions as all output and archiving is in GRIB2 format.

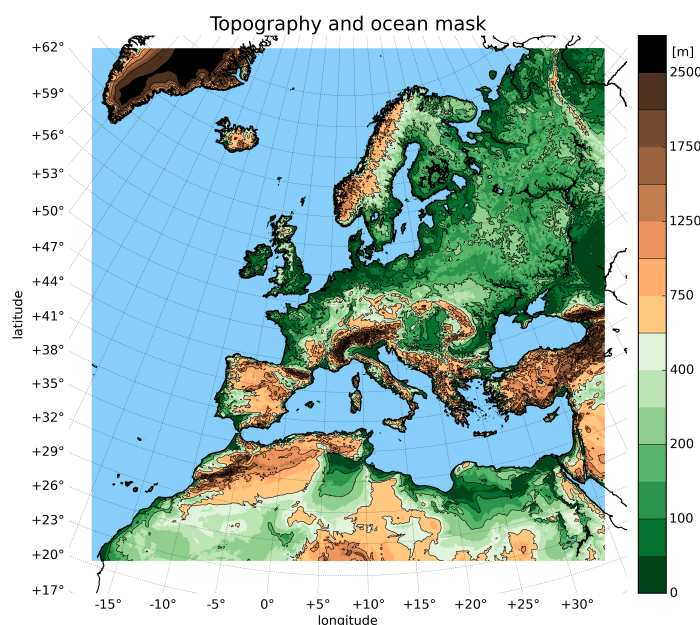


Figure 6: Horizontal domain of the CERRA Service (same as CORDEX 11 and UERRA).

The CERRA Reanalysis system extends from the previous UERRA system in several ways: The model code is based on HARMONIE cy40h1.1 instead of cy38h1.2. The horizontal and vertical resolution have been increased from 11 to 5.5 km and 65 to 106 levels (thereby reaching 1 hPa rather than 10) and there is a 3 hourly cycling rather than 6 hourly. There is extensive use of remote sensing data in CERRA which were not used in UERRA. Finally, there is an ensemble component with data assimilation and it provides both uncertainty estimations and an update of the background error covariances ('error of the day'). In addition there is more emphasis on user support and the data are published in the C3S Climate Data Store (CDS) and thereby much more accessible to general users than before in Mars or Webmars.

Observations included are conventional observations from the MARS archive at ECMWF but also additional conventional observations from local sources covered by the model domain. Apart from the conventional observations, satellite radiances from MSU, AMSU-A and B, MHS and IASI. In addition a few other non-conventional observations are used such as ground based GNSS, GNSS radio occultation, atmospheric motion vectors as well as wind observations from scatterometers.

Within CERRA an ensemble setup is run together with the deterministic run. The ensemble consist of 10 members of which one is an unperturbed control member. The remaining 9 are run with an ensemble data assimilation (EDA) to create the differences between members. It is run with 11 km horizontal resolution but with the same number of vertical levels as the deterministic version. The same observations are used. The

ensemble is used to create the background error statistics for the deterministic run. The background error statistics is updated every second day and consist of three parts. One part is from and EDA run from a winter period, one part from an EDA run from a summer period and the third part consists of statistics from the last two days counted from the deterministic run. The weight of the first two is dependent of the time of year while the weight of the 'EDA of the day' is always 20%.

The new re-analysis will run from 1981 until 2021 when the project ends with planned production start in January 2020.

5 Ensemble forecasting

The work around Ensemble Prediction Systems this year have been focused on the implementation of a continuous EDA based ensemble forecasting system described in Andrae et al. (2020) and further development of BRAND scheme (Frogner et al., 2019) for the generation of initial conditions perturbations.

BRAND based forecasting ensemble was used for the generation of the background error statistics for the CARRA production. Figure 7 shows schematically differences between EDA based and BRAND based approaches for the generation of short range ensemble forecasts.

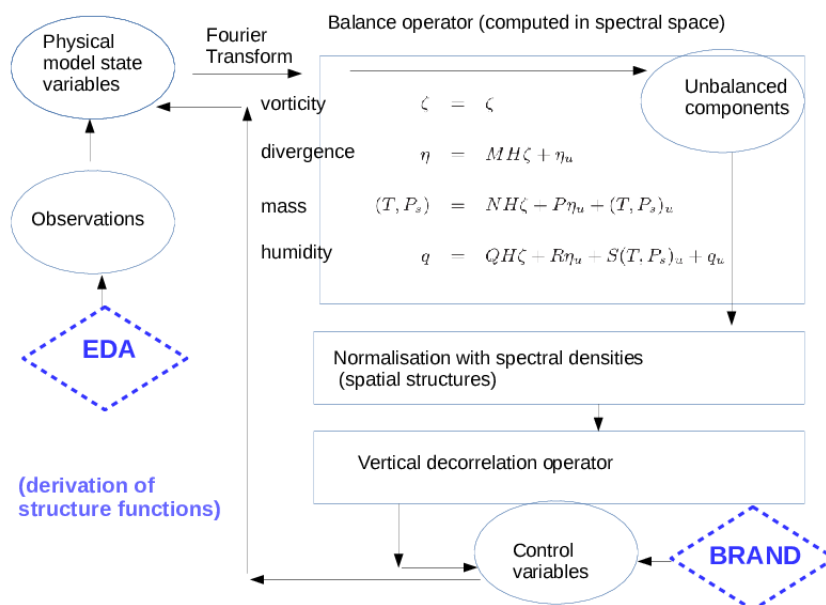


Figure 7: Schematic representation of the EDA based and BRAND based schemes for the sampling of initial conditions uncertainty in HARMONIE-AROME forecasting system

EDA based scheme inserts uncertainty in observation space, on scale of the observing system, by perturbing observed quantities randomly with the assumed observation error standard deviation and uses data assimilation as a device to form ensemble of analysis increments; in this way the uncertainty from the observation space is propagated into the physical model space. BRAND based scheme does not perturb observations at all. Instead it samples the uncertainty directly in the control vector space perturbing the whole range of scales. Afterwards the uncertainty in the control vector space is transformed into the physical model space using the background error covariance model. The amplitude of such perturbation is a tunable factor. In both cases the obtained perturbation in physical space is added to the high-resolution short-range forecast fields to form the initial fields for the ensemble forecasts. BRAND scheme can be applied to two different modes: the BRAND-DET

(deterministic mode) and the BRAND-EPS (EPS mode). In the deterministic mode the perturbation is added to the control forecast, while in the EPS mode the small amplitude perturbation, dependent on the ensemble size, is added to the own first-guess of the ensemble member. This approach allows each ensemble member to develop its own memory in the same way as the EDA based ensemble does.

The background error covariance model is an efficient diagnostic tool that helps to get a better insight into the properties of the ensemble generation approach (Bojarova and Gustafsson, 2019). At early forecast ranges the behaviour of the ensemble might be contaminated by the ensemble generation approach and might impact the inference drawn from such ensemble. The detailed analysis of the structure functions performed shows that EDA based structure functions overestimate the balanced rotational component of the flow. Figure 8 shows diagnostic plots of structure functions derived from EDA (blue) and BRAND-EPS (grey) based ensembles of the short range forecasts. Plot to the left shows the domain and time averaged vertical profile of the standard deviation of the temperature error and contribution to it of balanced (explained from vorticity (Pb) and by unbalanced divergence) and unbalanced part. As one can see the EDA based structure functions suggest much larger standard deviation of the temperature error around 850 hPa than the BRAND-EPS based structure functions do. Such structure function will lead to the overfit of the observations in the lower troposphere. Diagnostics shows that increase in the temperature error standard deviation is mainly due to balanced contribution explained by vorticity. The plot to the right shows percentage of the explained temperature variance by vorticity (a proxy of rotational flow) and by the unbalanced divergence (a proxy of divergent flow). EDA based structure functions indicate stronger contribution of rotational flow and weaker contribution of divergent flow. In particular one can see a peak of the contribution by vorticity on scales of (400 km-600 km) that roughly correspond to the scales of observing system (the conventional observations only were used in these experiments). The stronger balance between temperature and vorticity on meso-scales in the EDA based ensemble, at scales where vorticity has most of energy, leads to the larger standard deviation of the temperature error. We speculate that this strong balance between temperature and vorticity at meso-scales seen in the EDA based ensemble is an artefact of the ensemble generation approach and is not a genuine feature of the flow.

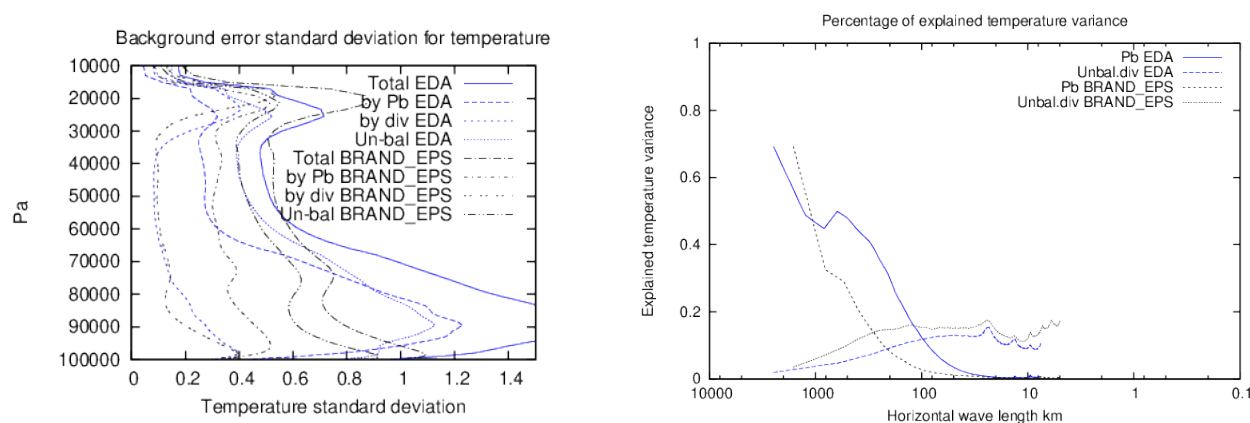


Figure 8: Diagnostic plots of structure functions derived from EDA (blue) and BRAND-EPS (grey) based ensembles of short range forecasts. Left plot : Domain and time averaged vertical profile of background error standard deviation for temperature as a function of pressure levels and contribution from balanced and unbalanced components. Right plot : the percentage of the explained temperature variance by balanced contributions as a function of the horizontal length-scales

Figure 9 shows the percentage of the explained humidity variance by balanced contributions (by vorticity (Pb), by unbalanced divergence and by unbalanced mass) as a function of the horizontal length-scales derived from the EDA based (blue) and the BRAND-EPS based (grey, left plot) and the BRAND-DET (grey, right plot)

ensembles. As one can see that ability to preserve the memory is important in order to develop meso-scale features by ensemble, the stronger contribution from the unbalanced mass field to the variability of the humidity field. The BRAND-DET ensemble with no memory in ensemble members lacks the capacity of doing so. The unbalanced mass field explains only about 15 percent percent of variability for the humidity field on meso-scales for the BRAND-DET based ensemble and up to 30 percent for the EDA based ensemble (Figure 9, right plot). On contrary in the BRAND-EPS based ensemble the unbalanced mass field explains about 30 per cent of the variance for the humidity through entire range of meso-scales, and not only over the range of scales corresponding to observing system as this happens for the EDA based ensemble. The variability inserted at scales of the observing system in the EDA based ensemble is not able to propagate to the entire range of meso-scales in the HARMONIE forecasting system.

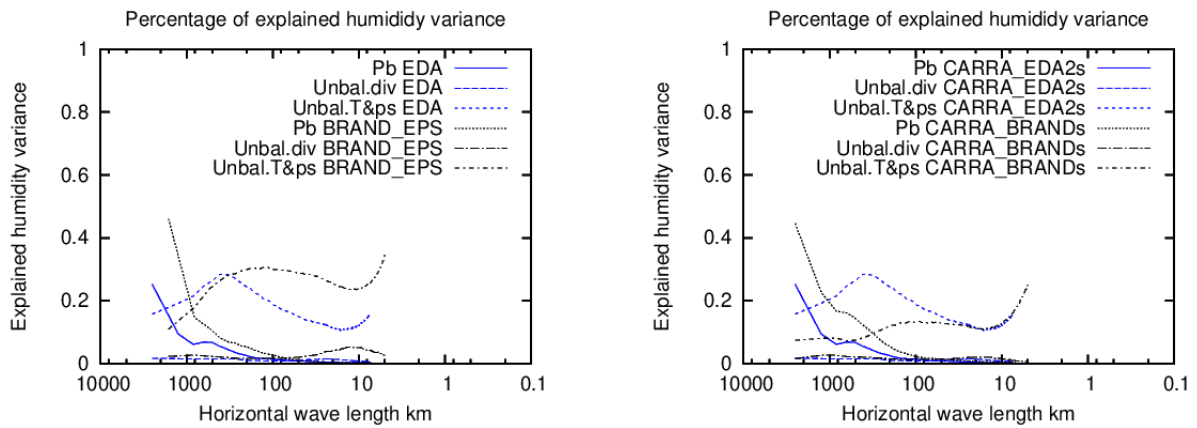


Figure 9: The percentage of the explained humidity variance from balanced contributions derived from EDA based (blue) and BRAND-EPS based (grey, left plot) and BRAND-DET based (grey, right plot) ensembles of short range forecasts as a function of the horizontal length-scales.

6 Verification

In the sciences we do not prove anything, but we do try to establish, with various degree of certainty, how nature works and operates. Newtonian gravitation is as well established as anything in physics. Another phenomenon which in the last half century has proven to be of fundamental importance and relevance to the atmosphere is chaos. Since chaos is a ubiquitous feature of the atmosphere it therefore has direct consequences for numerical weather prediction (NWP). In chaotic systems the uncertainty in a forecast increases exponentially with time. However, the uncertainty cannot grow forever and have an upper limit, or saturation value, which is equal to the difference between two random states. Lorenz (1982) proposed as a prototype error growth model a logistic curve, which ever since it was introduced has been found very appropriate for NWP. A form of the logistic error growth model appropriate to NWP is

$$e(t) = \frac{E}{1 + \frac{E - e_0}{e_0} e^{-at}}$$

where e is the forecast error, a is the growth-rate of small errors, e_0 is the error at the initial time of the forecast and E is the asymptotic, saturation error at very large forecast lead time. That this error growth model is indeed appropriate to NWP is indicated by the closeness of the blue and red curves in Fig. 10. The blue curve is the root mean square error (RMSE) of the Z500 field in the Northern Hemisphere Extratropics of ECMWF HRES global model as verified against radiosonde observations during the month of February 2018. The red curve is

a best fit to the above logistic curve model of error growth.

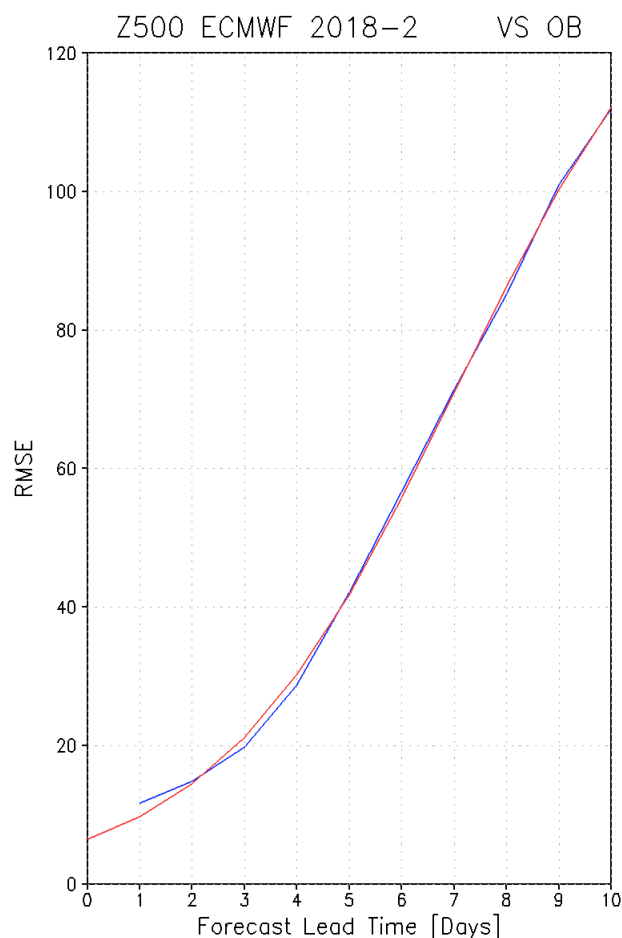


Figure 10: Error growth for medium range forecasts when verification is made at the same point in the daily cycle, in this case 00 UTC. The blue curve is the root mean square error (RMSE) of the Z500 field in the Northern Hemisphere Extratropics of ECMWF HRES global model as verified against radiosonde observations during the month of February 2018. The red curve is a best fit to the logistic curve model of error growth.

When verifying short-range forecasts, with forecast lead times from 0 to around 48 hours, we do not normally observe the above monotonically increasing error evolution closely following a logistic curve with increasing forecast lead time. What is observed is instead undulating non-monotonically increasing error curves like the one displayed in Fig. 11. A key difference between the error curves in Figs. 10 and 11 is that the errors in Fig. 10 are all evaluated at the same point in time of the daily cycle, 00 UTC in this case. Looking closely in Fig. 11 one can observe that the error for any specific point in time of the daily cycle actually increases monotonically with increasing forecast lead time. This fact indicates that one possible explanation for the observed undulating error growth is that one or several of the parameters in the logistic error growth model varies with the daily cycle. We here hypothesize that this parameter is the asymptotic upper limit, or saturation error E , which is equal to the difference between two random states. From statistics we know that this difference is exactly $\sqrt{2}$ times the observed climatological standard deviation of the variable which is verified. This statement is strictly true only if the model have the same variability as the atmosphere. The aim of the present study is to demonstrate that the observed variability indeed varies substantially through the course of the daily cycle and

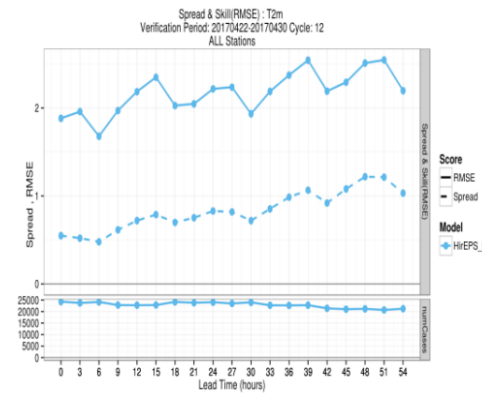


Figure 11: Verification of short-range forecasts at forecast lead times of 0, 3, 6, 9, ... , 54 hours produced by the HIRLAM EPS. The uppermost blue solid curve shows the evolution of the RMSE of 2m temperature over a limited area domain centered over Scandinavia for the time period 22 April - 30 April 2017.

therefore possibly could be the main reason for the observed undulation of the error growth on intra-daily time scales. Furthermore, it will be shown that the daily cycle changes during the course of a year.

Hourly observations of 2m temperature, T2M, at Norrköping, Sweden, for the 21 year period 1997-2017 was used to calculate how the daily cycle varies throughout the yearly cycle. The result is shown in Fig. 12 and reveals that there are indeed substantial differences between the variability at different times of the daily cycle. Furthermore, these differences vary in a complicated fashion with the annual cycle.

Figure 13 demonstrates how these intra-daily differences in variability can produce an undulating error growth

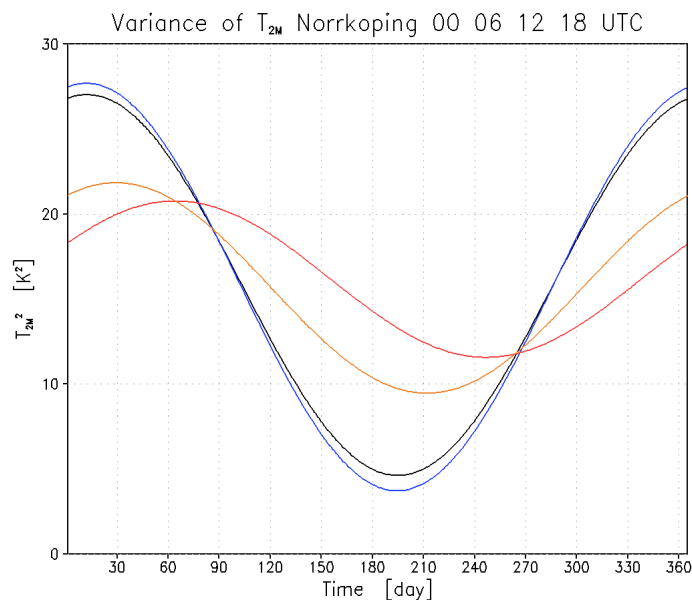


Figure 12: Yearly cycle of the variance of 2m temperature at four different times of the daily cycle, based on hourly data for the 21 year period 1997-2017, at Norrköping, Sweden. Black curve is for 00 UTC, blue curve 06 UTC, red curve 12 UTC and yellow curve 18 UTC.

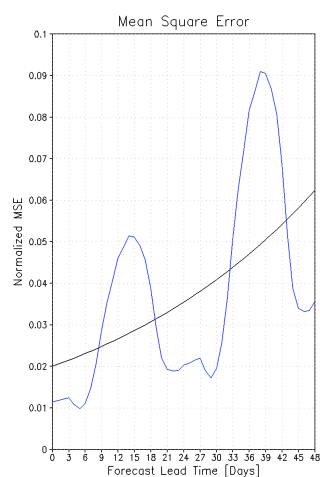


Figure 13: Error growth of T2M at Norrköping, Sweden. The black curve represents error growth according to the logistic error growth model with realistic fixed values of the three parameters a , e_0 and E . The blue curve represents error growth according to the same logistic error growth model with the same fixed values of the two parameters a and e_0 , but with varying values of E commensurate with the daily cycle of variability at 1 July as shown in Fig. 12.

similar to the ones observed. The black curve represents the error growth according to the logistic error growth model with realistic fixed values of the three parameters a , e_0 and E . The blue curve represents error growth according to the same logistic error growth model with the same fixed values of the two parameters a and e_0 , but with varying values of E commensurate with the daily cycle of variability at 1 July as shown in Fig. 12.

The observed daily cycle of variability has been shown to be substantial and this fact alone has the potential to explain the undulating, non-monotonic, error growth that is observed when verifying on intra-daily time scales.

7 Conclusions

SMHI ALADIN/HIRLAM activities during 2019 have all benefited from a fruitful collaboration within different research contexts. Major achievements for SMHI obtained through such collaborations and expected to be ready for production early 2020 are the CERRA regional re-analysis system and a continuous EDA based ensemble forecasting system.

8 References

- Andre U., Frogner I-L., Vignes O., A continuous EDA based ensemble in MetCoOp, ALADIN-HIRLAM Newsletter No. 14, 2020.
- Bojarova, J. and Gustafsson, N., Relevance of the climatological background error statistics for mesoscale data assimilation., *Tellus A: Dynamic Meteorology and Oceanography*, **71:1**; doi:10.1080/16000870.2019.1615168
- Frogner, I.-L., Andrea, U., Bojarova, J., Callado, A., Escribà, P.A., Feddersen, H., Hally, A., Kauhanen, J., Åandriamampianina, R., Singleton, A., Smet, G., van der Veen, S. and Vignes, O. HarmonEPS-The HARMONIE Ensemble Prediction System., *Weather And Forecasting*, **34**; doi:10.1175/WAF-D-19-0030.1
- Hägmark, L., Ivarsson, K.-I., Gollvik, S. and Olofsson, P.-O. Mesan, an operational mesoscale analysis system, *Tellus A. Dynamic Meteorology and Oceanography*, **52**, Iss. 1, 2000.

- Lindskog, M. and Landelius, Short-Range Numerical Weather Prediction of Extreme Precipitation Events Using Enhanced Surface Data Assimilation. *Atmosphere*, 10, 587; doi:10.3390/atmos10100587, 2019.
- Lorenz, E. N., 1982: Atmospheric predictability experiments with a large numerical model. *Tellus*, 34 505-513.
- Mazoyer M., Burnet F., Denjean C. , Roberts G.C., Haeffelin M., Dupont J-C., and Elias T. Experimental study of the aerosol impact on fog microphysics. *Atmos. Chem. Phys.*, **19**, 4323-4344, 2019.
- Soci. C. and E. Bazile, 2013: New MESAN-SAFRAN downscaling system. EURO4M deliverable D2.5. http://www.euro4m.eu/downloads/D2.5_New_MESAN-SAFRAN_downscaling_system.pdf. Retrieved September 11, 2019. 2013a.
- Soci, C., E. Bazile, F. Besson, T. Landelius, J-F. Mahfouf, E. Martin and Y. Durand. Report describing the new system in D2.5. EURO4M deliverable D2.6. http://www.euro4m.eu/downloads/D2.6_Report_describing_the_new_system_in_D2.5.pdf. Retrieved September 11, 2019. 2013b.

Implementation of CANARI in AROME TURKEY

Yelis Cengiz, Meral Sezer

1 Introduction

In fall 2019, Arome Turkey cy43t2-bf10 was installed and first steps of 3h Rapid Update Cycle (RUC) were taken with the implementation of CANARI. Following the data assimilation activities performed by DAsKIT programme, firstly surface assimilation tests were prepared in Arome Turkey cy43t2-bf10 using Global Telecommunications System (GTS)-Synop observations with 3h cycling. The verification scores were calculated using HARMONIE verification monitor (Yang, 2008) and in this paper the first results of CANARI optimal interpolation test are represented.

2 Implementation of CANARI

The first implementation test of CANARI in AROME Turkey was done for the period of 2019110300-2019111200. An experiment ARM_ASSIM was conducted with the following steps. ARM_ASSIM has the same features as the operational Arome Turkey (Table 1) except for ARM_ASSIM was run with CANARI surface assimilation.

Firstly the surface fields which do not exist in the upper air guess file were added into the guess file from coupling file which is obtained from global model ARPEGE. Afterwards surface temperature in the guess was replaced by the one in the analysis file which is produced by the previous CANARI run. In the final step before running CANARI, sea surface temperature analysis is replaced with the one in the coupling file which is at AROME resolution.

After these steps the CANARI software is utilized to produce the analysis of temperature and relative humidity of 2 meters. In this current test study CANARI was run with single processor using rh2 and t2m data in bufr format obtained from GTS Synop observations. The duplication of observations was eliminated by using bufr_filter from eccodes (<https://confluence.ecmwf.int/display/ECC/BUFR+tools>) An example of the observations used by CANARI is shown in Figure 1. In several network times, there was no synop observation available, in that case 001 configuration utilized the +3 forecast from previous network time as the initial file for surface.

Table 1: The features of operational AROME Turkey

Model version	Cy43t2.bf10
Resolution	1.7 km
Levels	72
Boundaries	Arpege
Starting times	00 UTC ,06 UTC ,12 UTC, 18UTC

20191106 06 UTC SYNOP GTS OBSERVATIONS
USED IN CANARI T2M ANALYSIS



Figure 1: The locations of GTS Synop Observations used in CANARI in the analysis of 2 meter temperature at 2019110606 UTC

The analysis increments of the surface parameters are represented in Figure 2. The increment of X001TG1 varies between 3.481 and -1.848 and the increment of X001WG1 is changing between 0.1025 and -0.180.

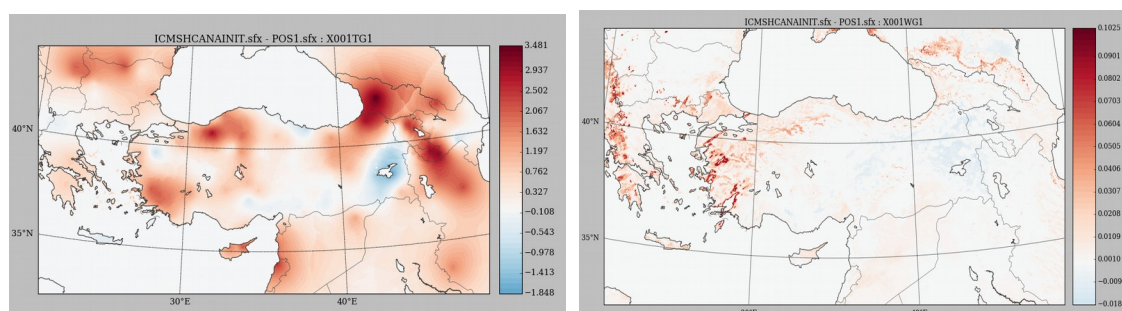


Figure 2: Analysis increments of surface parameters X001TG1 (on the left) and X001WG1 (on the right) for the time of 2019110606.

3 Verification Results

Verification results of the study are shown in the Figure 2. The bias and standard deviation of 2 meter temperature is represented on the left. The improvement in 2 meter temperature forecast is observed in ARM_ASSIM experiment results at the beginning and in the middle of the forecast length. However regarding the BIAS of 2 meter relative humidity forecast scores the operational AROME Turkey-ARM experiment performs better than ARM_ASSIM experiment.

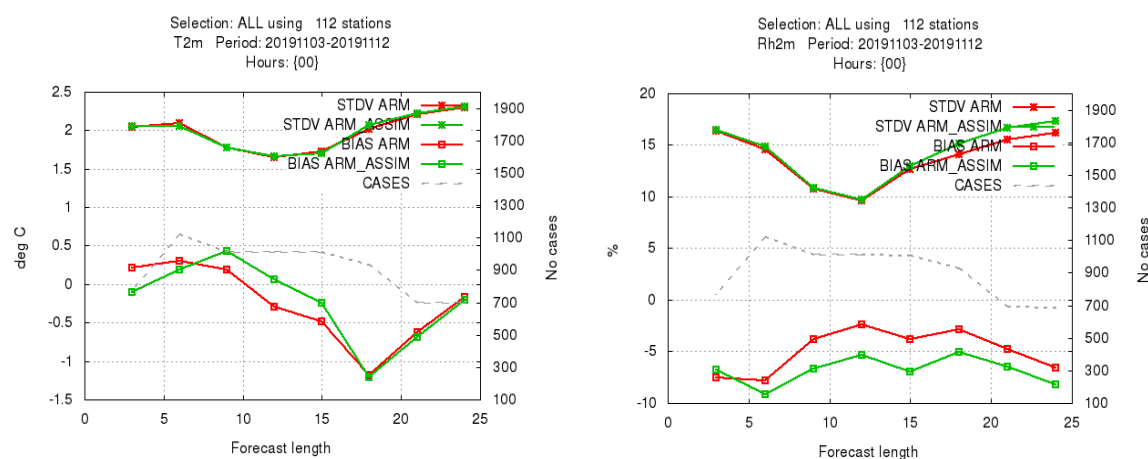


Figure 3: The verification scores of T2m (on the left) and Rh2m (on the right). ARM_ASSIM indicates the experiment conducted with CANARI surface assimilation and ARM indicates the operational AROME Turkey without surface assimilation.

The current study was the first assimilation activity tested in Arome-Turkey. Further studies and investigations will be done and as a next step will be the implementation of 3d-Var in Arome-Turkey.

4 Acknowledgement

The authors would like to thank Maria Monteiro and Alena Trojakova for their help and support and would like to thank all participants of DAsKIT for their valuable contributions.

5 References

Yang, X. 2008, Development of Hirlam/Harmonie monitoring system. HIRLAM Newsletter no 54, 62-65.

HIRLAM experience with ECOCLIMAP Second Generation

Samuelsson Patrick¹, Kourzeneva Ekaterina², de Vries John³ and Viana Samuel⁴,

¹Swedish Meteorological and Hydrological Institute (SMHI)

²Finnish Meteorological Institute (FMI)

³Royal Netherlands Meteorological Institute (KNMI)

⁴Spanish Meteorological Agency (AEMET)

1 Introduction

ECOCLIMAP SG (ECO-SG) is a new version of the land cover map and database of surface parameters available for SURFEX (Masson et al., 2013), which is planned to be used operationally in Harmonie-Arome Canonical Model Configuration (Bengtsson et al., 2017) of the ALADIN-HIRLAM NWP system. It is built by applying a semi-automatic classification algorithm to the ESA CCI Land Cover product (Version 1.6.1, 28/01/2016), combined to other high-resolution databases for towns, rivers, height of trees, etc., resulting in a global classification of 33 ECOCLIMAP SG land cover types (see list in Table 1) at appr. 330m resolution. It is three times finer than the resolution of previous ECOCLIMAP versions (see e.g. Faroux et al., 2013). In ECOCLIMAP SG, the previous notion of cover classes has changed to cover types. The difference between them is the following. The land cover classes defined land use and vegetation types with characteristic phenological annual cycle and consisted of fractions of different tiles (sea, water, urban and nature). The land cover types define only land use and vegetation types. They do not reflect phenological annual cycle and belong only to one tile each. It is expected that ECOCLIMAP SG will be easier to maintain and improve (for instance with newest versions of ESA-CCI products). Primary land parameters (LAI, root/soil depth, soil/vegetation albedos, etc.) are provided as separate files allowing for an easy substitution of physiographic data with local databases.

Before operational use in Harmonie-Arome, ECOCLIMAP SG should be evaluated via comparison with previous ECOCLIMAP versions and other sources of physiographic data, to understand the potential benefits and issues and identify regions where the new physiography data is substantially different to the previous one. The use of ECOCLIMAP SG in SURFEX is only possible from version 8.1, which has been introduced in the current cy43h development branch of Harmonie-Arome. Tests with ECOCLIMAP SG in different domains and seasons have been conducted as part of the validation experiments to reach the first cy43h release of Harmonie-Arome, cy43h2.1. Using the results from the comparison between new and old physiography and by analyzing the main differences in model performance with respect to experiments with old ECOCLIMAP, it is possible to critically evaluate ECOCLIMAP SG and determine what changes in the physiography have the strongest impact in verification results of near-surface model variables.

The objective of this work is to summarize the main findings from our work in evaluating and testing ECOCLIMAP SG. Section 2 covers the evaluation of the distribution of the water cover types (types 1, 2 and 3 in Table 1), the main changes in the distribution of total open land / forested cover types, town fraction and the cycle of Leaf Area Index (LAI). In section 3 the meteorological impact of the new physiography in Harmonie-Arome is analyzed. In section 4 a modification of the roughness length formulation for crops and grass land cover types is proposed to lessen the observed increase in

Table 1: Land cover types represented in ECOCLIMAP-SG land cover map.

1. sea and oceans	18. tropical grassland
2. lakes	19. winter C3 crops
3. rivers	20. summer C3 crops
4. bare land	21. C4 crops
5. bare rock	22. flooded trees
6. permanent snow	23. flooded grassland
7. boreal broadleaf deciduous	24. LCZ1: compact high-rise
8. temperate broadleaf deciduous	25. LCZ2: compact midrise
9. tropical broadleaf deciduous	26. LCZ3: compact low-rise
10. temperate broadleaf evergreen	27. LCZ4: open high-rise
11. tropical broadleaf evergreen	28. LCZ5: open midrise
12. boreal needleleaf evergreen	29. LCZ6: open low-rise
13. temperate needleleaf evergreen	30. LCZ7: lightweight low-rise
14. boreal needleleaf deciduous	31. LCZ8: large low-rise
15. shrubs	32. LCZ9: sparsely built
16. boreal grassland	33. LCZ10: heavy industry
17. temperate grassland	

wind bias in Harmonie-Arome tests with ECOCLIMAP SG. Finally some final conclusions are reported in section 5, and references are given in section 6.

2 Evaluation of ECOCLIMAP SG

2.1 Materials and methods

The physiography of SURFEX consists of: (i) the map of covers, (ii) the land surface parameter tables for each cover, and (iii) the software to combine them, to aggregate and to project the results onto the atmospheric model grid. In this study, we evaluated both the original data from the land cover maps and the projected data to investigate the land/water distribution, and only projected data for LAI evaluation.

Both ECOCLIMAP and ECOCLIMAP SG land cover maps use plain LON-LAT coordinate system and WGS84 datum. The resolution of ECOCLIMAP and ECOCLIMAP SG land cover maps are 30 and 10 arc sec. respectively. To study the land/water distribution in the original maps, the ECOCLIMAP version 2.5_plus was used. This is the version 2.5 corrected in the following (i) changes in some cover classes, to get rid of the inland water fraction within covers, according to Table A1 (ii) using of the flood-filling algorithm, to remove the miss-classification of fjords and coastal lagoons as lakes. These corrections were applied to achieve the best possible consistency between the lake database GLDB (Choulga et al., 2014) and the ECOCLIMAP land cover map to run the parameterization of lakes operationally (Fortelius et al., 2018). Table A1 contains also corrections which were applied for the parameter tables, to change the partition between tiles. The original land cover maps were evaluated globally, but focusing on problematic regions (see the method later on in this section). For reference information, satellite images from GoogleMaps were used.

Before the comparison of the land cover maps, ECOCLIMAP was re-projected to the resolution of ECOCLIMAP SG (from 30 arc sec. coarse to 10 arc sec. fine resolution). This was done just by repeating the same pixel information for several times, which is possible due to the fact that the pixel size of ECOCLIMAP is multiple to the pixel size of ECOCLIMAP SG (with the factor of 3), and both are integer values. One pixel of ECOCLIMAP corresponds exactly to 9 (3 x 3) pixels of

ECOCLIMAP SG. Re-projection was done by repeating each pixel of ECOCLIMAP 3 times in longitude, and then 3 times in latitude direction, totally 9 times.

Table 2.1.1: Contingency table for agreement between the ECOCLIMAP and ECOCLIMAP SG land cover maps in 1 x 1 degree grid box. In the table, n_{ij} is a number of corresponding pixels

		ECOCLIMAP SG		
		land	sea	inland water
ECOCLIMAP	land	n_{11}	n_{12}	n_{13}
	sea	n_{21}	n_{22}	n_{23}
	inland water	n_{31}	n_{32}	n_{33}

Since the reference GoogleMap information is non-digital, the land cover map may be evaluated only visually, and only for some problematic regions. The problematic regions were selected through the comparison between ECOCLIMAP and ECOCLIMAP SG. The idea behind is the following: if ECOCLIMAP and ECOCLIMAP SG show the same cover (class or according type) over some territory, it is likely that this cover is true. But if over some region ECOCLIMAP and ECOCLIMAP SG show different covers, this region is problematic and should be checked by the visual comparison with GoogleMaps.

Cover type is a categorical value. Categorical values may be compared using contingency tables. A result of comparison between covers in ECOCLIMAP and ECOCLIMAP SG was considered as a random value. The whole globe was covered by a coarse regular LON-LAT grid, and the statistics was collected by sampling over each grid box of this grid. The grid-box size was selected to be 1 arc deg., which is large enough to collect the reliable statistics and fine enough to see the regional differences between the two maps. For this study, three cover classes and types were considered: land, sea and inland water (including both lakes and rivers). Only cover classes containing 100% of water were considered in ECOCLIMAP. So, for each 1x1 degree grid box, the contingency table represented by Table 2.1.1 was calculated. First, each pixel of the ECOCLIMAP land cover map was compared with the corresponding pixel of the ECOCLIMAP SG land cover map. Then, the statistics was calculated over 1x1 grid box: n_{11} is the number of pixels which are land both in ECOCLIMAP and ECOCLIMAP SG, n_{12} is the number of pixels which are land in ECOCLIMAP but sea in ECOCLIMAP SG, and so on. In an ideal case of totally corresponding maps, all n_{ij} should be zero, except for the diagonal values, when $i=j$. The larger are the diagonal values and the smaller are the non-diagonal values, the better.

Contingency tables allow to quantify the agreement and disagreement in all possible misclassification situations. However, absolute numbers are difficult to interpret, partly because the frequency of pixels of different covers may vary a lot between grid boxes. For example, in a grid box located in Mongolia, the number of lake pixels is much smaller than of land pixels, and there are no sea pixels at all. So, the relative values were calculated using the following formulae:

$$f_{ij} = n_{ij} / ((\sum_{i=1}^3 n_{ij} + \sum_{j=1}^3 n_{ij}) / 2)$$

(absolute values are normalized to the mean sum of pixels in the appropriate column and line). If the denominator is zero (e.g., for the case of Mongolia, there are no sea pixels in any map), f_{ij} is undefined. For easier use, the normalized (fractional) values were expressed in per cents.

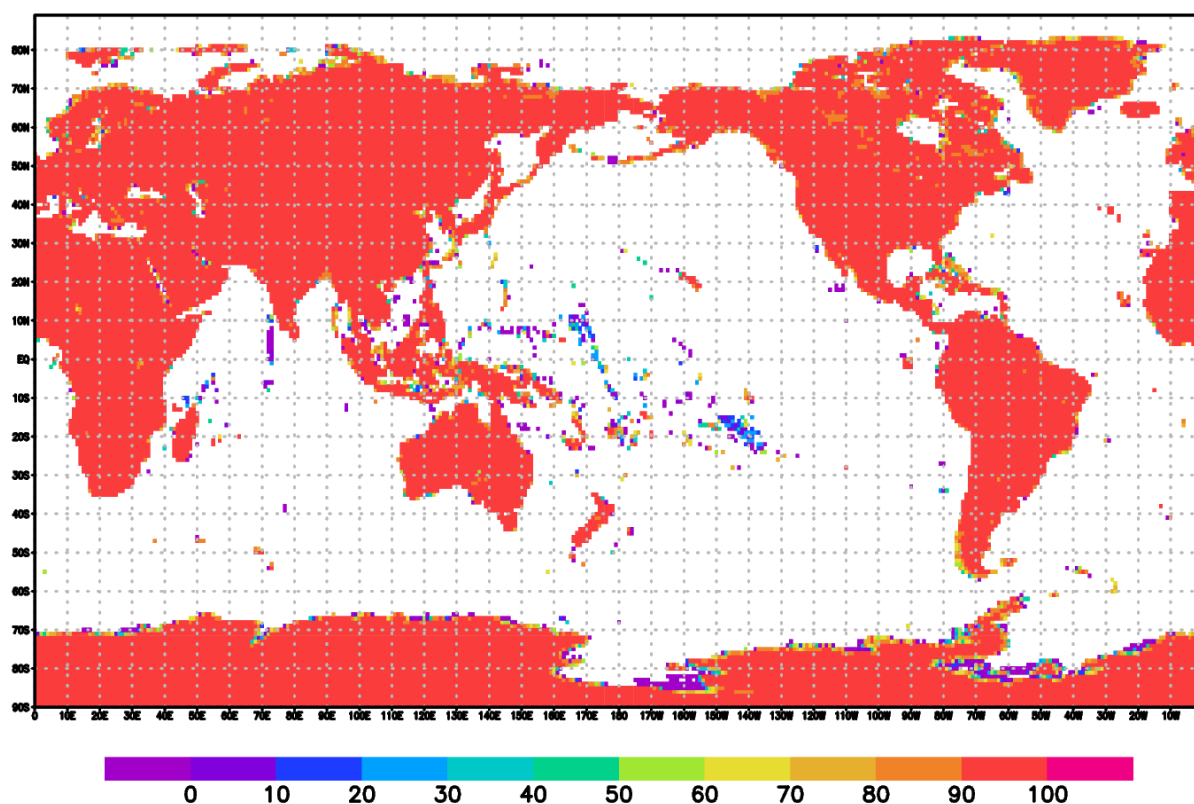


Figure 2.2.1: Agreement f_{11} map for the “land” cover types between ECOCLIMAP and ECOCLIMAP SG, %

For the evaluation of the projected and aggregated content of the ECOCLIMAP data sets, off-line simulations were performed with Open SURFEX V8.1 using PGD to project the physiography onto the Harmonie domains for The Netherlands, Spain (IBERIA_2.5) and MetCoOp (METCOOP25B) and aggregate the data to 2.5km resolution. PREP was used to create a start file for a specific date and time including the climatological information on LAI. The first guess fields for SURFEX on all three domains were obtained from cold starts with Harmonie branch CY40h1.2_tg2, configured for each of the domains. The +3H forecast output from SURFEX was used in GRIB format as the start file that needs to be specified in the Fortran namelist NAM_PREP_SURF_ATM [2]. For this comparison, ECOCLIMAP_v2.2 (ECO-II) was used.

The projected and aggregated physiographic fields were evaluated visually. Geographic maps were produced for relevant physiographic fields based on both ECOCLIMAP versions. For a particular physiographic field, the two maps were incorporated in a PowerPoint presentation slide. Changedetection was made possible by alternating between both maps operating the arrow keys. This approach was also used to study the annual cycle of LAI.

2.2. Evaluation of the land-water distribution

To evaluate land-water distribution in the land cover map of ECOCLIMAP SG, contingency tables were calculated for 1x1 grid boxes all over the globe, and the maps of each table element were built, totally 9 maps. These maps show the regions of agreement and disagreement between two physiography data-sets. From these contingency table maps, the problematic regions were identified as the regions with low agreement (0-10%) or with high disagreement (more than 50%). For each problematic region, ECOCLIMAP and ECOCLIMAP SG maps were compared visually with GoogleMaps. If needed, photos and street views from GoogleMaps were also considered, as well as

Table 2.2.1: Regions with low agreement and high disagreement from the comparison between ECOCLIMAP and ECOCLIMAP SG (ECO SG) by contingency tables. For agreement, the less percentage, the worth. For disagreement, the higher percentage, the worth.

	Regions
Agreement f_{11}	Canada (70-80%), Chile (50%-70%), Oceania (20%-30%)
Disagreement f_{12} (less land in ECO SG)	The Netherlands (up to 20%), the southern coast of Chile (up to 30%), the Greenlandian coasts (20%-30%), the Arctic Canada coast
Disagreement f_{13} (more lakes in ECO SG)	Siberia (thermokarst lakes, up to 30%), Canada (up to 30%), Australia (40%), Northern Poland (10%)
Disagreement f_{21} (more land in ECO SG)	The southern coast of Chile (up to 30%), the Caspian Sea (up to 30%), Greenland coast (up to 30%)
Agreement f_{22}	The south of Chile (appr. 20%), the southern coast of Norway (50%), the Pacific coast of Canada (appr. 20%), Grenadian coasts (appr. 40%)
Disagreement f_{23} (sea => lake in ECO SG)	The Pacific coast of Canada (up to 60%), the southern coast of Chile (up to 70%)
Disagreement f_{31} (less lakes in ECO SG)	Finland and Karelia (up to 15%), Canada (up to 10%)
Disagreement f_{32} (lake => sea in ECO SG)	no
Agreement f_{33}	Everywhere except large lakes

additional information about lakes, rivers, bays, etc. Examples of contingency table maps are given for the land agreement f_{11} (land on both land cover maps) by Figure 2.2.1, lake agreement f_{33} (lake on both land cover maps) by Figure 2.2.2 and disagreement f_{31} between lakes (on ECOCLIMAP) and land (on ECOCLIMAP SG).

According to Figure 2.2.1, the agreement between ECOCLIMAP and ECOCLIMAP SG for land pixels f_{11} for the inland areas is good (more than 90%), with the exception of Canada, due to lakes. However, for the complicated coastline, the agreement drops, sometimes to 0%. The most problematic areas, where the agreement is low, are given in Table 2.2.1. This table shows the results of analysis for all types of agreement and disagreement. The agreement for the sea pixels f_{22} (not shown) is also good (more than 90%) for the sea areas, but drops close to the coastline, sometimes down to 0%. Disagreements between land and sea f_{12} and f_{21} (not shown) are in general up to 10% close to the coastline. However due to resolution, on ECOCLIMAP SG small islands became even smaller, but some new small islands appeared. Also some bays became smaller or even disappeared and some islands merged. In general, the amount of land in ECOCLIMAP SG remains the same as in ECOCLIMAP (only decreasing in the Netherlands and the Grenadian coasts), but the location of islands and bays may be slightly different. The special case is the Antarctica. For the Antarctic coast, agreement both for the land and sea pixels is very poor everywhere, very often goes down to 0%. The disagreement is very high, in some places up to 100%, and there is less land in ECOCLIMAP SG compared to ECOCLIMAP. additional information about lakes, rivers, bays, etc. Examples of

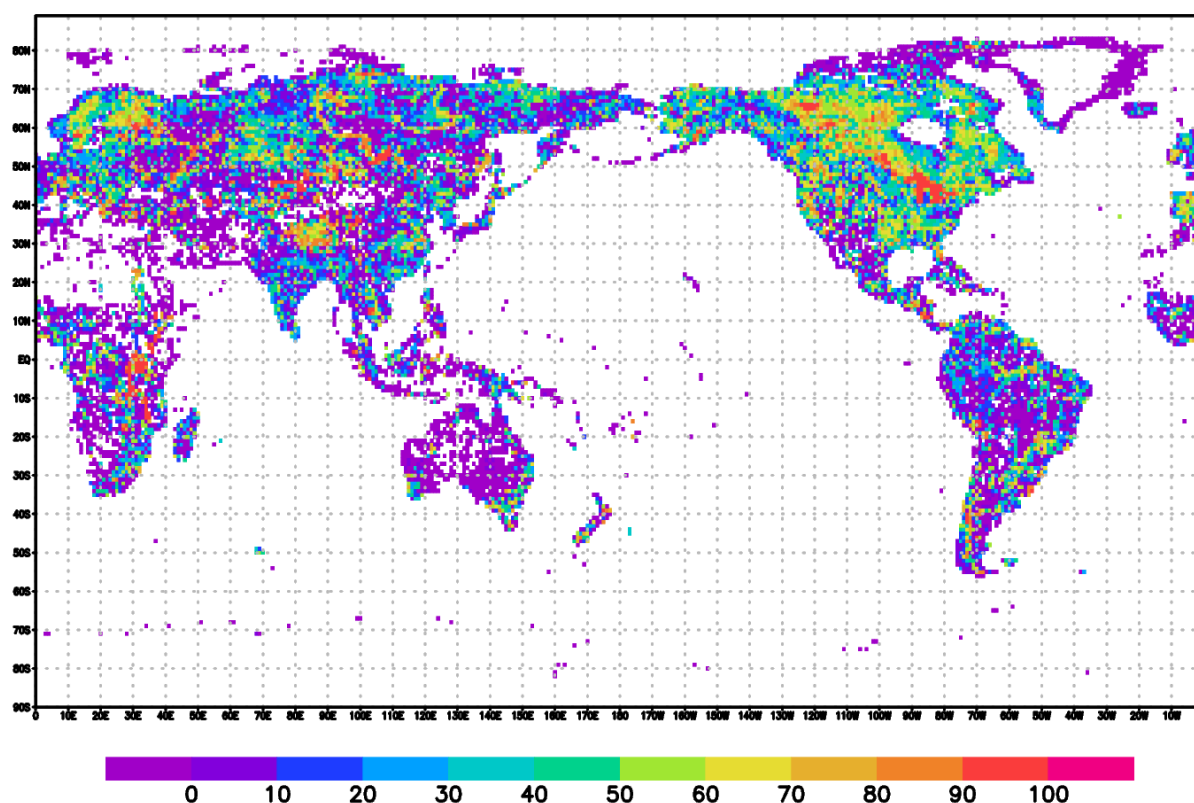


Figure 2.2.2: Agreement f_{33} map for the “lake” cover types between ECOCLIMAP and ECOCLIMAP SG, %

contingency table maps are given for the land agreement f_{11} (land on both land cover maps) by Figure 2.2.1, lake agreement f_{33} (lake on both land cover maps) by Figure 2.2.2 and disagreement f_{31} between lakes (on ECOCLIMAP) and land (on ECOCLIMAP SG).

According to Figure 2.2.1, the agreement between ECOCLIMAP and ECOCLIMAP SG for land pixels f_{11} for the inland areas is good (more than 90%), with the exception of Canada, due to lakes. However, for the complicated coastline, the agreement drops, sometimes to 0%. The most problematic areas, where the agreement is low, are given in Table 2.2.1. This table shows the results of analysis for all types of agreement and disagreement. The agreement for the sea pixels f_{22} (not shown) is also good (more than 90%) for the sea areas, but drops close to the coastline, sometimes down to 0%. Disagreements between land and sea f_{12} and f_{21} (not shown) are in general up to 10% close to the coastline. However due to resolution, on ECOCLIMAP SG small islands became even smaller, but some new small islands appeared. Also some bays became smaller or even disappeared and some islands merged. In general, the amount of land in ECOCLIMAP SG remains the same as in ECOCLIMAP (only decreasing in the Netherlands and the Grenadian coasts), but the location of islands and bays may be slightly different. The special case is the Antarctica. For the Antarctic coast, agreement both for the land and sea pixels is very poor everywhere, very often goes down to 0%. The disagreement is very high, in some places up to 100%, and there is less land in ECOCLIMAP SG compared to ECOCLIMAP.

The agreement for the lake cover type (Figure 2.2.2) is much lower. It reaches 90% only for the large lakes (the Great Lakes, Lake Victoria, Lake Baikal, Lake Ladoga, etc). For the regions with only a few small lakes, it goes down to 0% (lakes are absent, they are at different places and so on). For large lake regions such as Canada and Finland, the agreement reaches 60%. Due to the large dispersion, the lake agreement map is difficult to analyze. From the disagreement f_{13} map (not shown), there are several

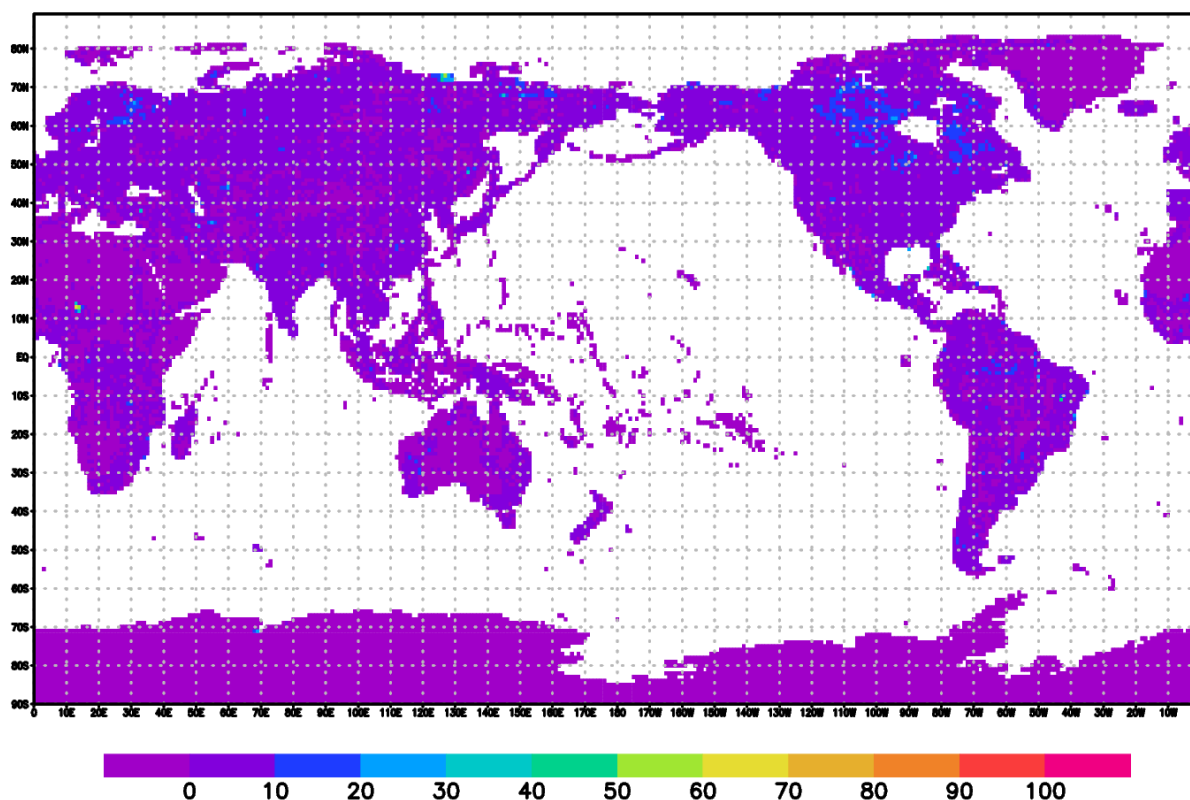


Figure 2.2.3: Disagreement f_{31} map: the “lake” cover type in ECOCLIMAP and “land” cover type in ECOCLIMAP SG, %

regions with more lakes in ECOCLIMAP SG than in ECOCLIMAP, see Table 2.2.1. The disagreement f_{31} map is represented on Figure 2.2.3. It shows regions with less lakes in ECOCLIMAP SG (see also Table 2.2.1). For Canada, there are both increase and decrease of lake pixels in ECOCLIMAP SG, which means that lakes are in different places, however increase is larger than decrease.

Disagreement described by f_{23} and f_{32} maps (not shown, results are only in Table 2.2.1) is connected with miss-classification of lake and sea water. The situation, when the lake pixels in ECOCLIMAP became the sea pixels in ECOCLIMAP SG is a seldom occurring case: the f_{32} disagreement only reaches 10% along the coastline.

For the very low local agreement and/or very high local disagreement situations, the visual comparison with Google maps was performed. Sometimes the large disagreement may result from purely mathematical reasons, e. g. when the coastline is located so that a small piece of land in the corner of 1x1 grid box exists on one map, but not on the other. These cases were looked through, but are not listed in the conclusions. General conclusions from the comparison are given in Section 2.6. Specific details of the comparison with illustrations are listed in List A1 in Annex.

Land-water distribution maps for projected and aggregated data for the Netherland domain are shown in Figure 2.2.4. The geographic maps have been made with *matplotlib* in Python. For coastline plotting *matplotlib* utilizes the Global Self-consistent Hierarchical High-resolution Geography (GSHGG) Database also used to create the cover map of ECO-II and ECO-SG. The coastline is therefore considered as reference.

On The Netherlands domain it can be seen that for coastlines at high zoom factors in The Netherlands like the river deltas (Zeeland) and for areas with large tidal flow (northern Netherlands, Bretagne), SG shows better adherence to the coastline database. For rocky coasts with islands (Croatia) and for

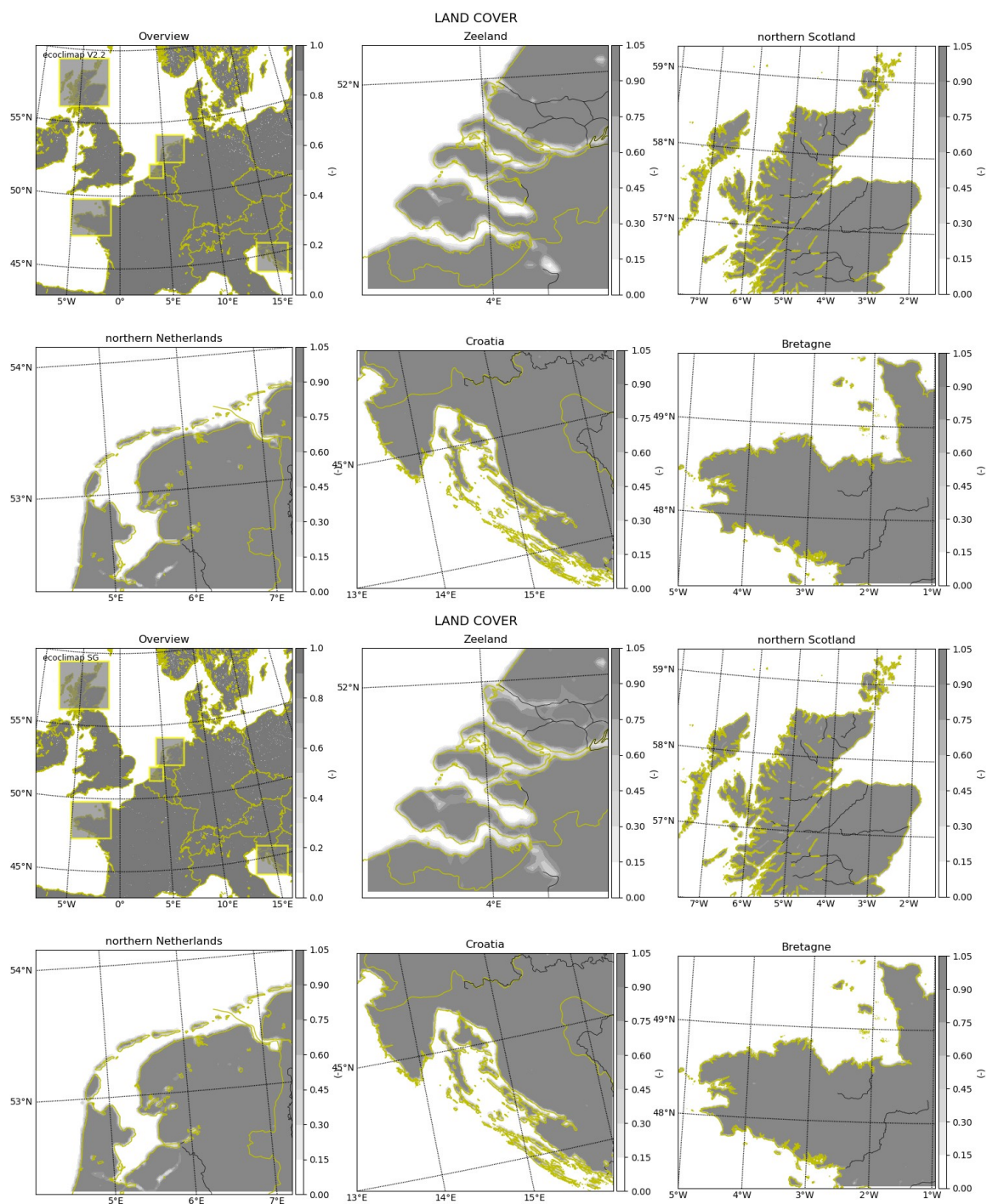


Figure 2.2.4 Land-water fraction maps for the Netherland domain. Coastlines are drawn in yellow, rivers in black. The upper six plots are for ECO-II, the lower six for ECO-SG. The upper left plot gives an overview of the whole domain and depicts five frames over areas of interest as yellow rectangles. The detail maps are plotted at full resolution with no area details left out.

intricately detailed coastlines with fjords (northern Scotland) differences are small between ECO-II and ECO-SG. The domain overview also shows shifts in in-land lake positions when going from ECO-II to ECO-SG. The latter gives a better description of the river Rhine.

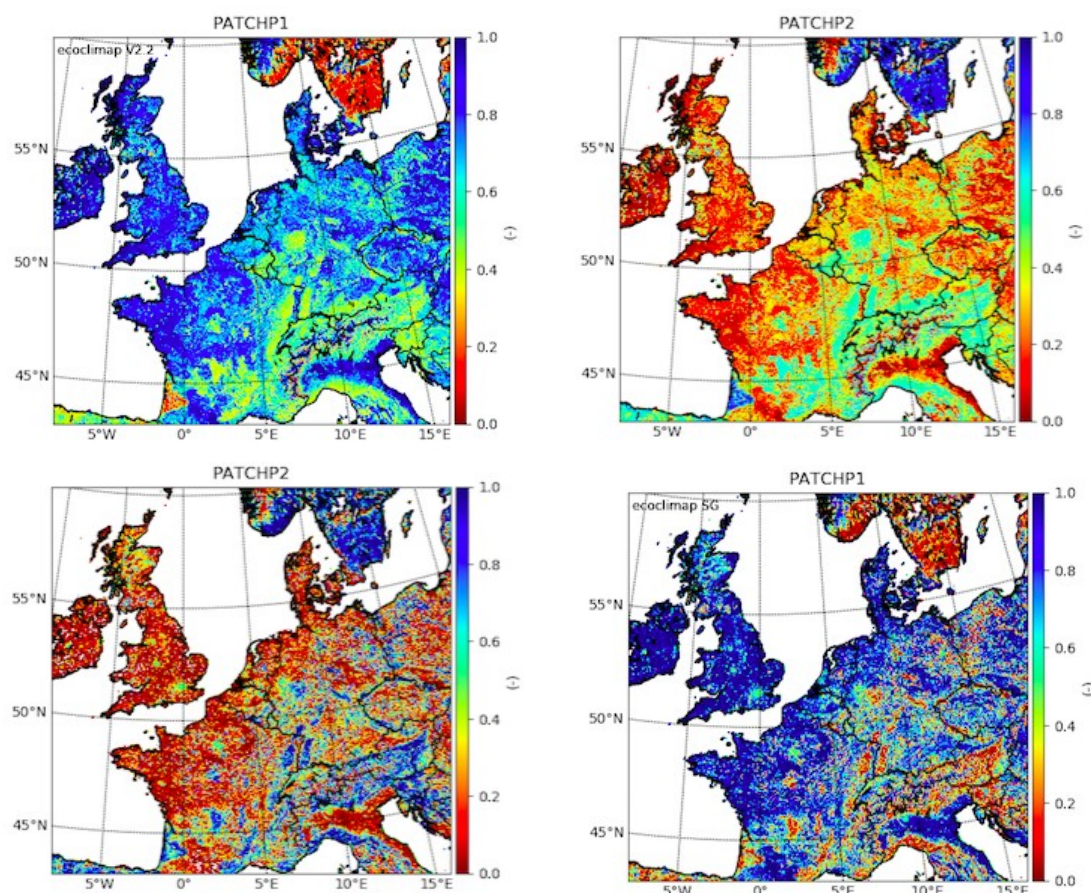


Figure 2.3.1: Spatial distribution of vegetation patches on The Netherlands domain.

2.3. Evaluation of open-land and forest distribution

The default setup of cy43h will use two patches on the nature tile, i.e. a subdivision between open land and forest, respectively. Therefore, in Figures 2.3.1-2.3.3 we evaluate the differences in the distribution of open land and forest between ECO-II and ECO-SG, respectively, on the three domains at 2.5km resolution.

On the Netherlands domain in Figure 2.3.1 the difference between ECO-II (upper plots) and ECO-SG is apparent for continental Europe. In ECO-II we see substantial areas in green signifying a 50-50 distribution between open land and forest areas. In ECO-SG the green areas have been replaced mostly by areas of open land in the middle and western part of the continent. In and around the Alps however, they have been replaced mostly by forest patches. Also, in the western part of the continent, on the British Isles and Ireland open land areas have become more open.

On the IBERIA_2.5 domain in Figure 2.3.2, areas exist in ECO-II with small fractions of high vegetation that in ECO-SG are completely void of high vegetation, such as in the north-west of Spain and north and south of the Pyrenees. In North-Africa areas without high vegetation in ECO-II are present more in-land in the Saharan Desert whilst in ECO-SG these areas are scattered more along the Mediterranean coast. There is also more high vegetation in the region north of Valencia in ECO-SG.

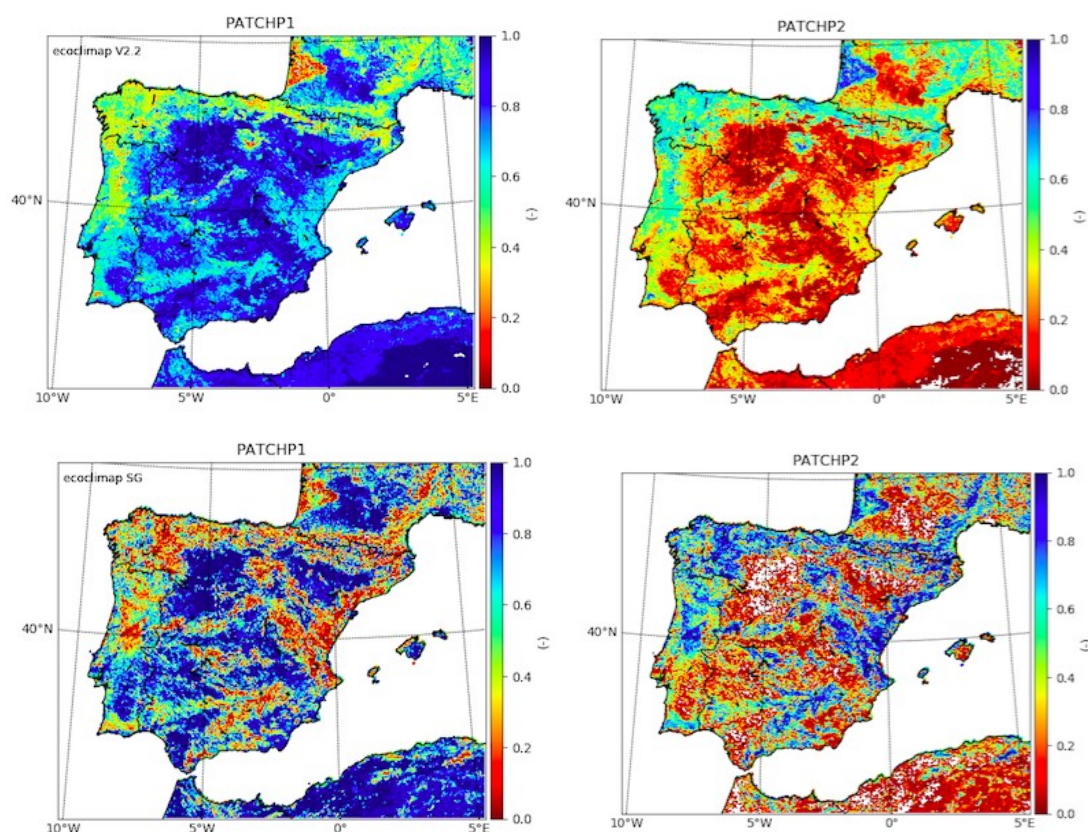


Figure 2.3.2: As Figure 2.3.1 for the IBERIA_25 domain.

On the METCOOP25B domain in Figure 2.3.3 a sharp demarcation exists between open land patches in Norway and forest patches in Sweden and Finland. In ECO-II there is a transitional area (color coded in green) in north Scandinavia that is mostly considered high vegetation in ECO-SG.

2.4. Evaluation of town distribution

Based on a comparison with ECO-I, ECO-II is suspected to have too little urbanization, especially over the Netherlands area (not shown). Therefore, a comparison was made between ECO-II and ECO-SG to see if any improvement may be expected. Figures 2.4.1-2.4.3 show the town fraction of both ECOCLIMAP versions.

With the garden option activated in TEB parks and gardens are considered as part of the urban tile instead of as part of the nature tile in the aggregation. In all domains as a whole, the general trend is that with the garden option switched off, the town fraction is higher in ECO-SG than in ECO-II, both in spatial extent and in terms of density. If the garden option is switched on the town density generally increases further in both respects, more so in ECO-SG than in ECO-II. In urban areas the situation is subtly different. On the Netherlands domain, increases in town density in the connected urban areas of the cities of Amsterdam, The Hague, Rotterdam and Utrecht (Randstad), mostly affect town density and not so much spatial extent. On the IBERIA_2.5 domain the town fraction for the city of Madrid increases spatially and in density more in ECO-SG than in ECO-II and progressively when the garden option is switched on. On the METCOOP25B domain the town fraction of the city of Copenhagen increases only moderately going from ECO-II to ECO-SG when the garden option is switched off and mostly in terms of spatial extent. When the garden option is switched on the town density increases significantly but the spatial extent not so much. The difference between ECO-II and ECO-SG in that case are relatively small as well.

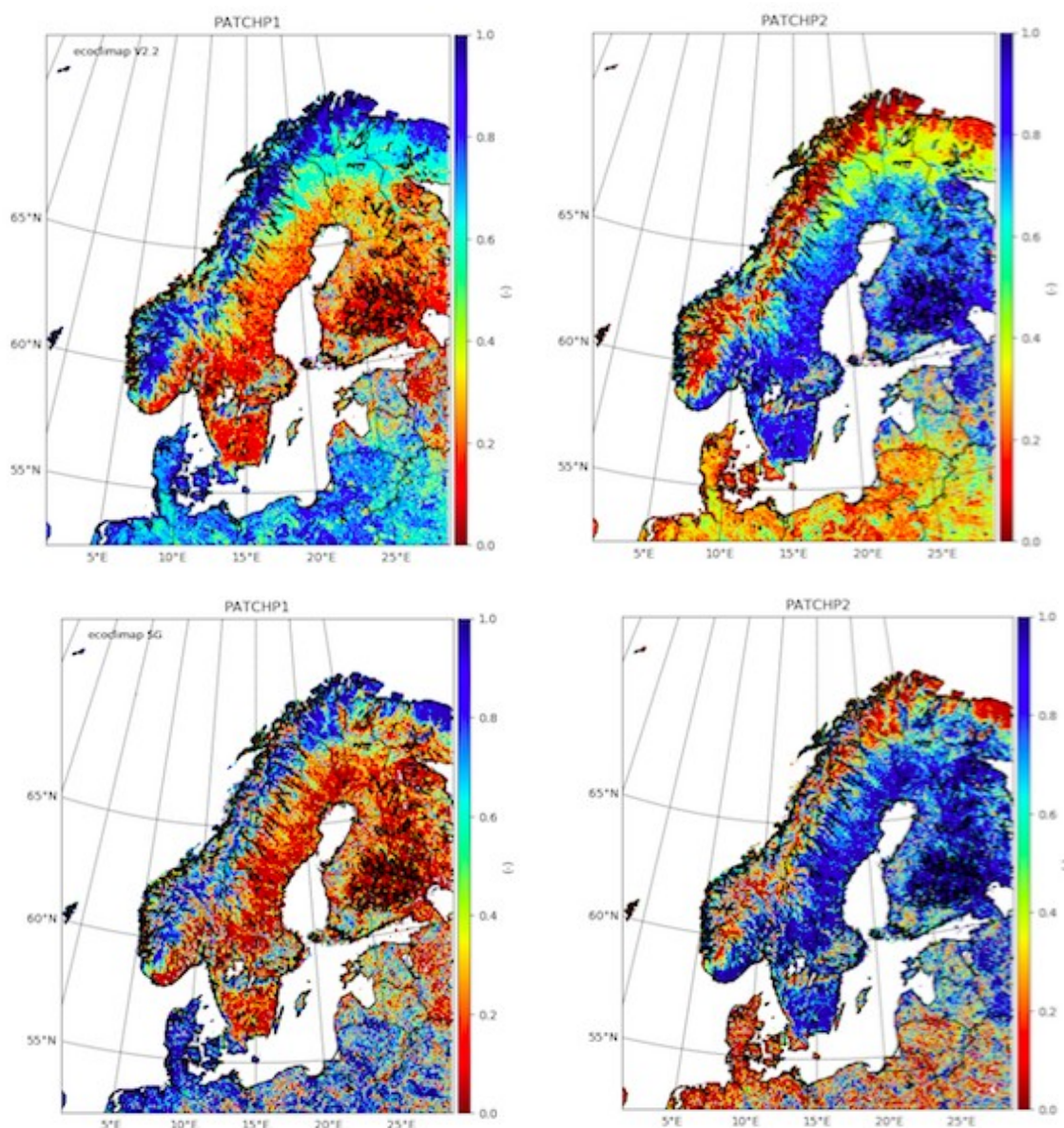


Figure 2.3.3: As Figure 2.3.1 but for the METCOOP25B domain.

2.5. Evaluation of Leaf-Area Index distribution

Figures 2.5.1-2.5.3 present the geographic aggregation of samples of the leaf area index (LAI) climatology for ECO-II and ECO-SG and their difference (SG-V2). For a large part of the Netherlands domain a reduction in LAI can be seen in ECO-SG compared to ECO-II from winter into early spring and from autumn into winter (0215). Early in the growing season (0415) local reductions in LAI going from ECO-II to ECO-SG are prominent in areas such as The Netherlands, Ireland, the South of Sweden and Norway and parts in the south of France) During the summer the differences are small only to increase again later in the year (not shown). In the south of Sweden a strong reduction in LAI can be seen year round.

On the IBERIA_2.5 domain a widespread year round reduction in LAI can be seen in central Spain and North Africa in ECO-SG and ECO-II and vast areas that seemed to be subject to increased desertification in ECO-SG. In the growing season an increase in LAI occurs in ECO-SG in the Pyrenees mountains and the mountains at the Spanish North coast compared to ECO-II.

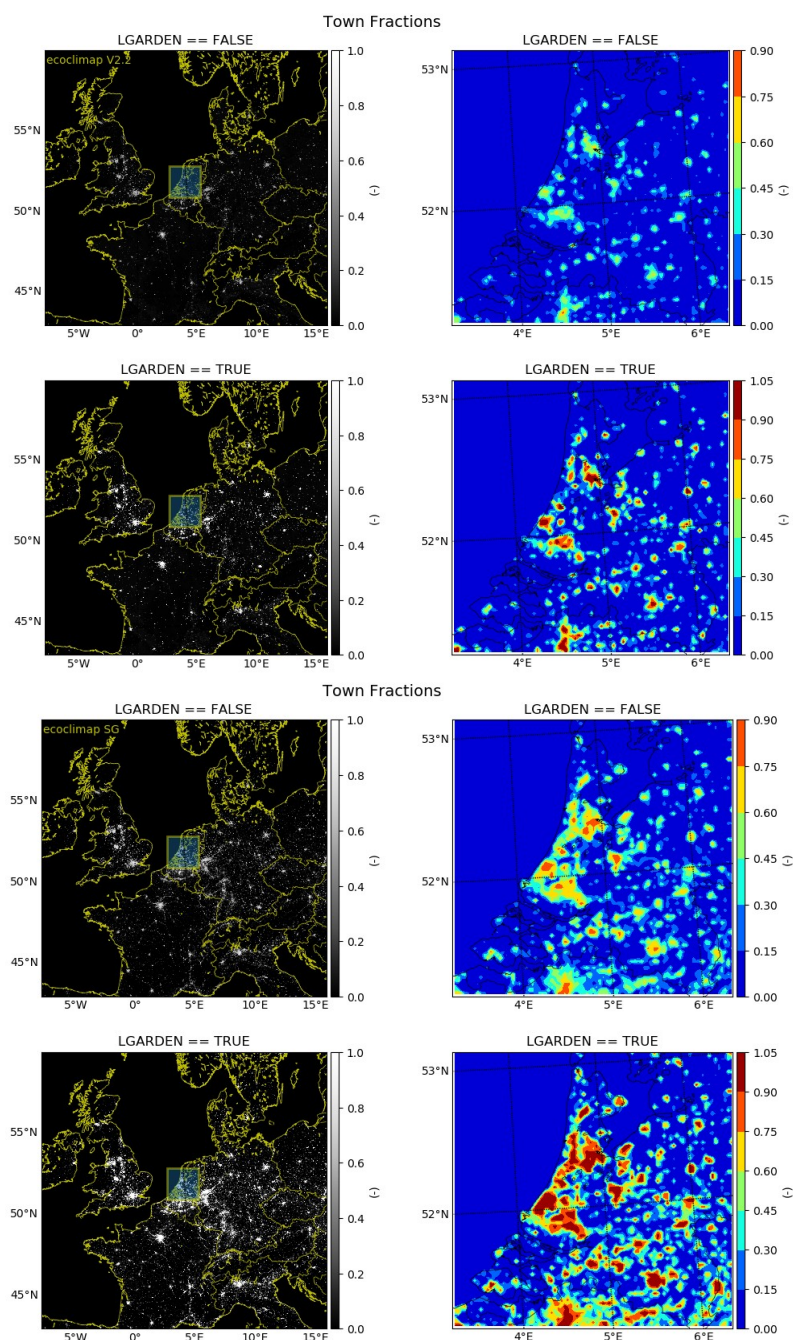


Figure 2.4.1: Town fractions on the Netherlands domain. The upper four plots are for ECO-II while the lower four plots are for ECO-SG. Plots to the left give an overview of the whole domain and plots to the right give a detailed view of a major urban area. For each ECOCLIMAP version the upper (lower) plots show the magnitude of the urban density with `TEB_GARDEN` switched off (on). With garden option switched on, the color coding is slightly different because town fractions between 0.9 and 1.0 are present. No town fraction above 1.0 is present and the color bar values up to 1.05 are triggered by round-off errors leading to values slightly above 1.0.

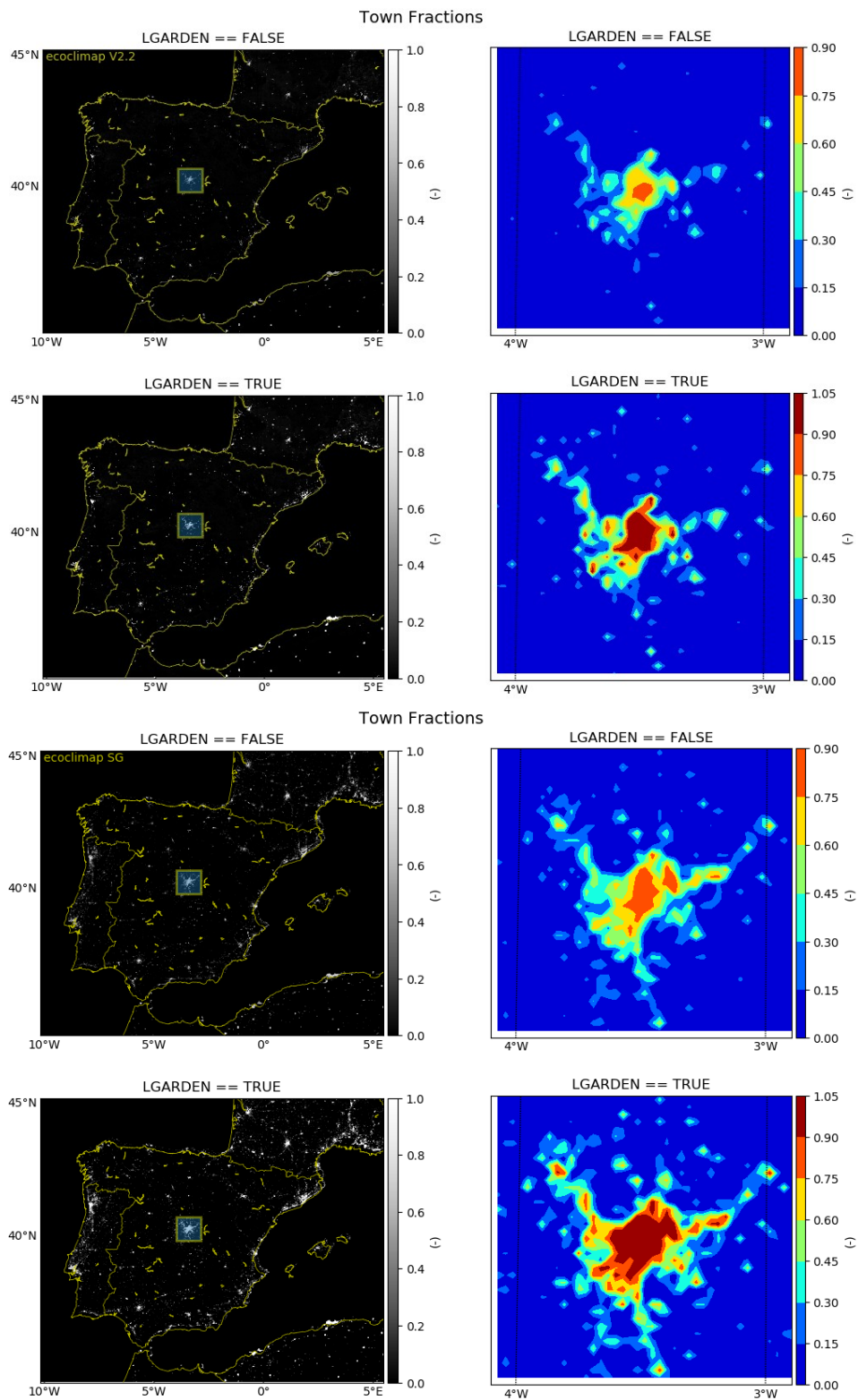


Figure 2.4.2: As Figure 2.4.1 but on the IBERIA_25 domain.

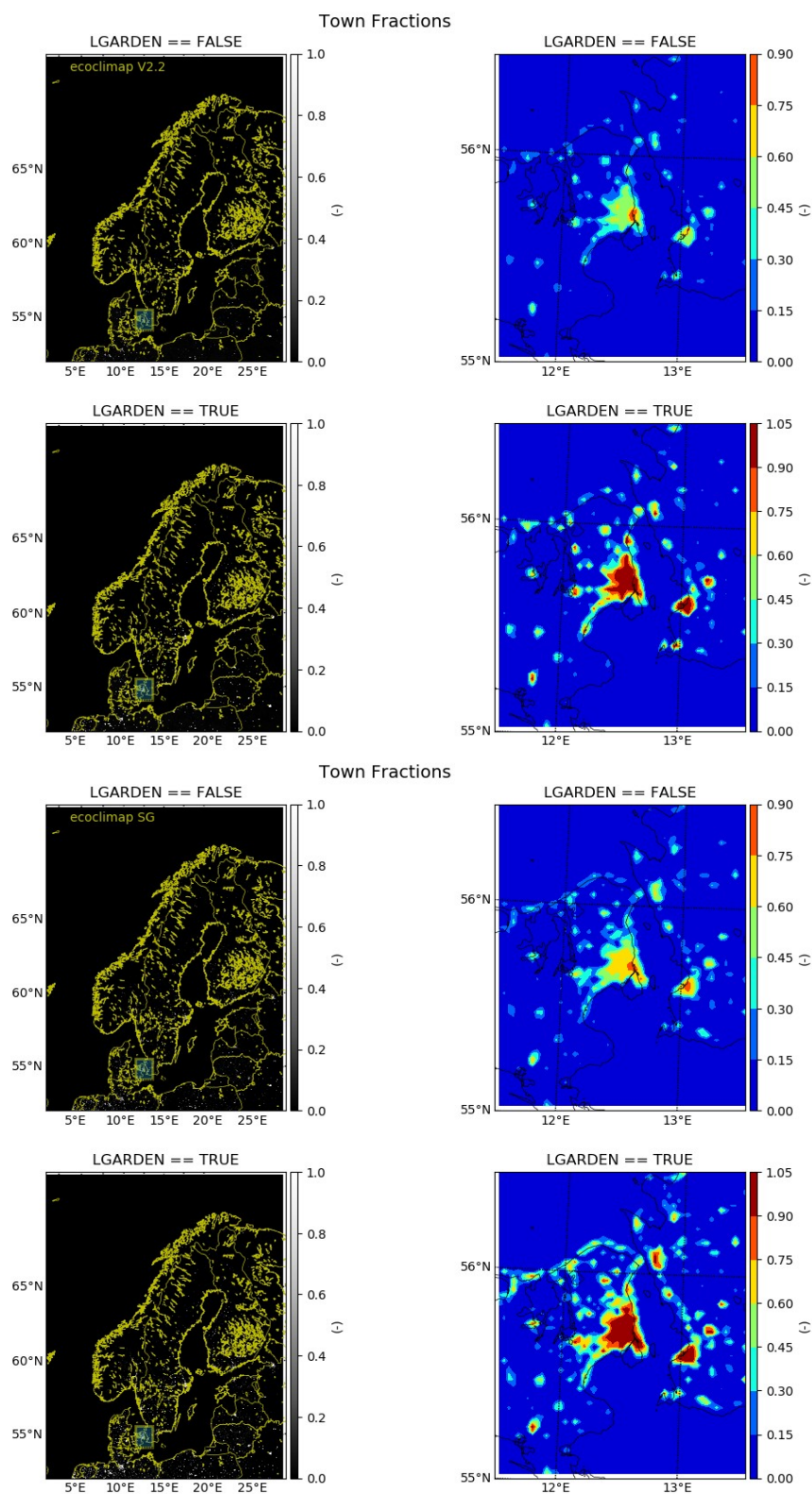


Figure 2.4.3: As Figure 2.4.1 but for the METCOOP_25B domain.

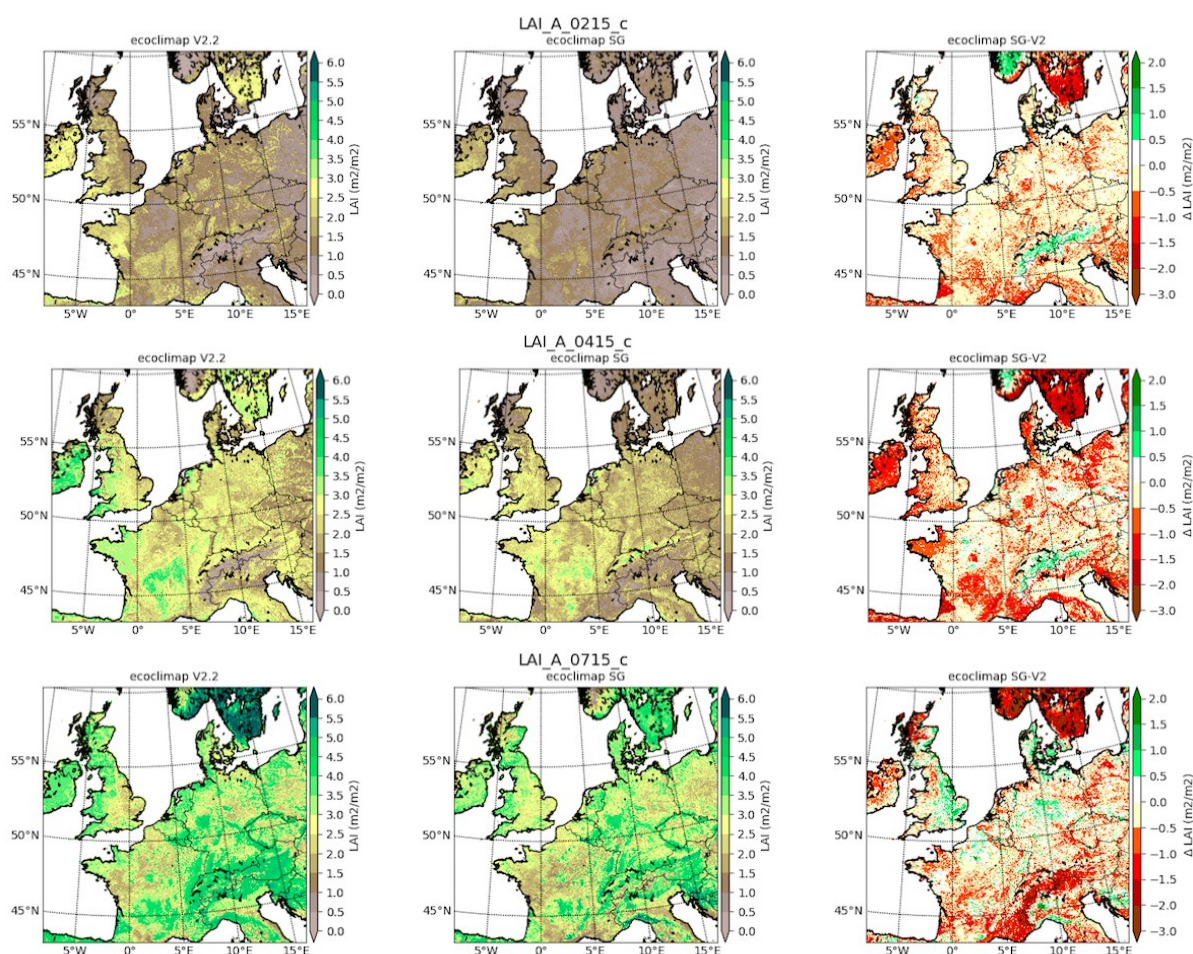


Figure 2.5.1: LAI climatology on the Netherlands domain. The columns represent ECO-II (left), ECO-SG (middle) and the difference (ECO-SG - ECO-II) (right). The rows represent different times, February 15th (top), April 15th (middle) and July 15th (bottom).

On the METCOOP25B domain there is a considerable difference in the seasonality of the LAI-cycle in the latitudinal direction in Sweden and Finland. ECO-II has a much stronger LAI signal than ECO-SG ever increasing from winter towards summer. An increase in LAI in ECO-SG can be seen in the Copenhagen area in the growing season

2.6. General conclusions on evaluation of ECOCLIMAP SG

General conclusions based on the evaluation of the land-water distribution

- Shift. ECOCLIMAP and ECOCLIMAP SG are shifted against each other. In some regions, this shift reaches 20 km. The direction is different in different regions. For ECOCLIMAP, the shift (e.g., against CORINE) is a well-known problem (Matti Hortanainen, personal communication). The comparison allows to hope that ECOCLIMAP SG got rid of this shift problem. This is an **improvement** in ECOCLIMAP SG comparing with ECOCLIMAP.
- Many new reservoirs appeared in ECOCLIMAP SG, but some of them became much smaller. The information is more updated. This is an **improvement** in ECOCLIMAP SG.

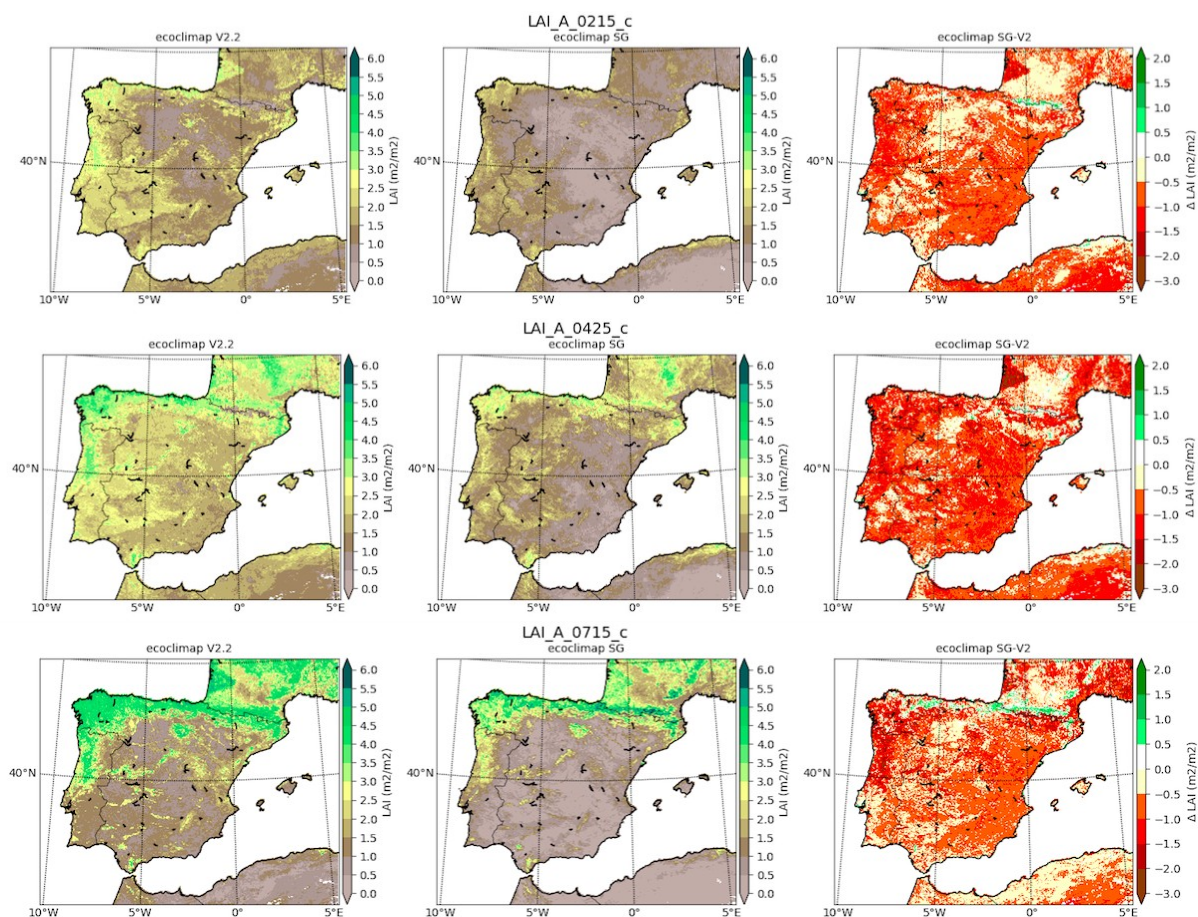


Figure 2.5.2: As Figure 2.5.1 but for the IBERIA_25 domain. The rows represent February 15th (top), April 25th (middle) and July 15th (bottom).

- Bays and fjords miss-classified as lakes exist in ECOCLIMAP SG (in ECOCLIMAP v2.5_plus, they were corrected). Correction is needed.
- Lakes miss-classified as sea water exist in both maps along the sea coast, but in ECOCLIMAP SG there are much more of them. Correction is needed. The most serious case is Lake Tustumena in Alaska with a surface area of 300 km² (not shown).
- Rivers in ECOCLIMAP SG are in general good. All the most large rivers are marked on the map. No deep penetration of the sea water into the continent is noticed. However, there are quite many artifacts connected with rivers. The most serious case is over Lake Great Slave (not shown).

What may be expected when Harmonie-Arome converts to ECO-SG are the following:

- More open land patches over continental Europe and more forest areas in the Alps and northern Scandinavia in ECO-SG is going to affect screen level variables.
- The increase in town fraction in ECO-SG both spatial extent and in urban density will have local effect on T2m and U10.
- The decrease in LAI in ECO-SG over continental Europe, the British Isles and Ireland in the growing season and somewhat less in summer may be beneficial to help reduce problems with excessive evaporation in Harmonie-Arome.
- The decrease in LAI in central Spain will have an effect on wind speed.
- The considerable reduction in seasonality of LAI in ECO-SG over Sweden and Finland should have an effect on snow cover, soil moisture and evaporation.

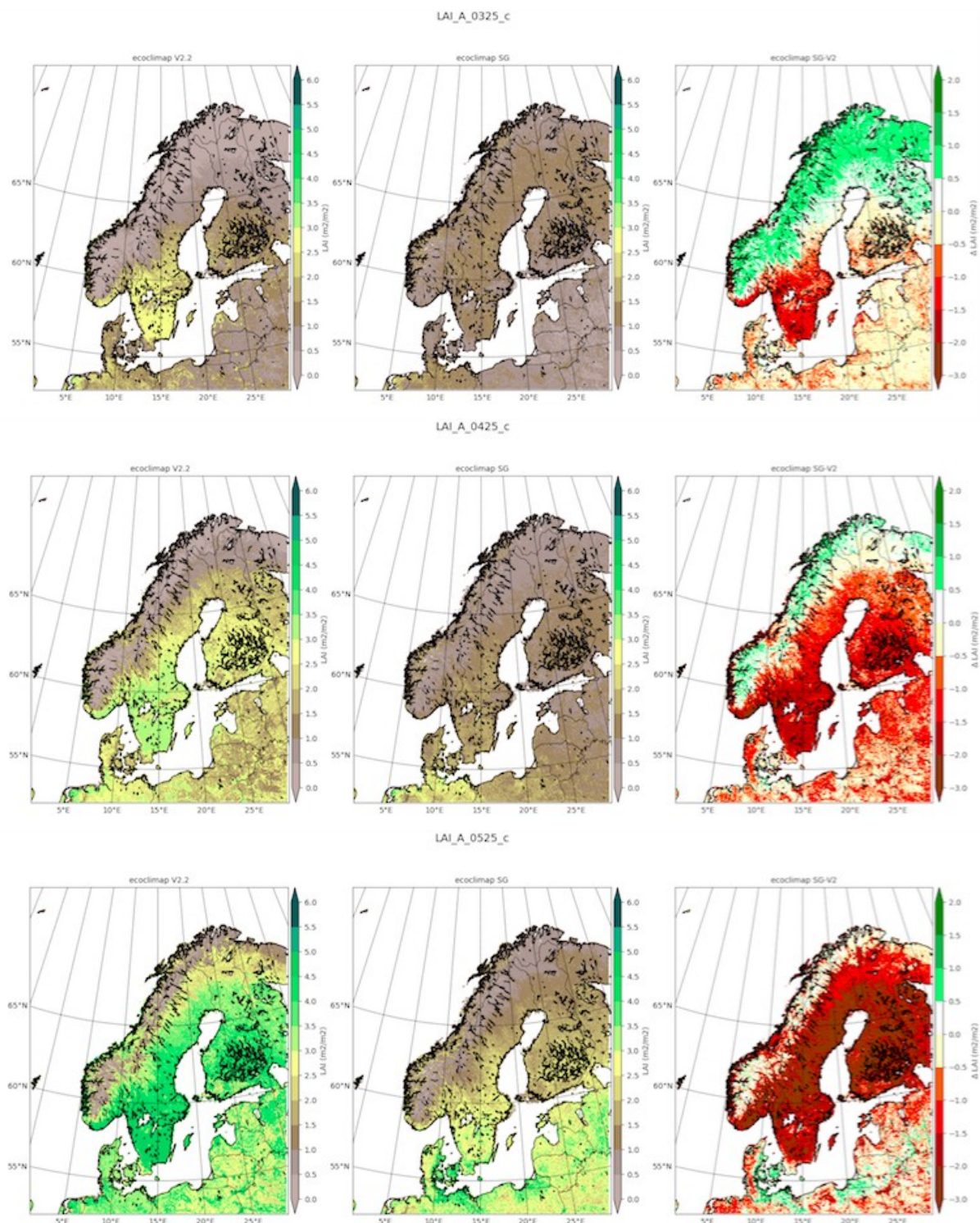


Figure 2.5.3: As Figure 2.5.1 but for the METCOOP_25B domain. The rows represent March 25th (top), April 25th (middle) and May 25th (bottom).

Table 3.1: Target experiments.

Domain	Period of analysis	Experiments (legend in figures)
AEMET	Winter: 20181223-20190202	AIBxl_43tg1cca AIBxl_43tg2cca
AEMET	Summer: 20180801-20180830	AIBxl_43tg1cca AIBxl_43tg2cca
METCOOP	Winter: 20190201-20190228	43tg1_WINTER 43tg2_WINTER
METCOOP	Summer: 20190701-20190731	43tg1_summer 43tg2_summer
KNMI	Winter: 20181205-20190201	KNMI_D18J19_tg1 KNMI_D18J19_tg2
KNMI	Summer: 20160705-20160901	KNMI_JA16_tg1 KNMI_JA16_tg2

3 Meteorological impact study

One of the main motivations for HIRLAM to consider ECOCLIMAP SG as an alternative to ECOCLIMAP2.5_plus at this moment is that Leaf-Area Index (LAI) has been identified as a suspicious parameters for a bad performance of HARMONIE-AROME over e.g. the Netherlands during the spring and summer seasons (Tijm and Bloemendaal, 2016). Sensitivity studies with cy40h over the KNMI domain have shown that reduced LAI (*0.5) in combination with increased stomatal resistance (*1.25) and reduced soil moisture increments in OI assimilation (*0.33) lead to improved forecast performance (Tijm, 2018). Of course, a simple division of LAI by two cannot be used as a general solution in model development. So, in our search for a more robust solution we looked into LAI in ECOCLIMAP SG and found that it gives decreased LAI values on the same order as suggested by the sensitivity tests. Therefore, in our development plan for a release of cy43h2.1, ECOCLIMAP SG has been one of the ingredients in what we call target tests.

In this publication we do not provide all the details about the differences between the test targets of cy43h2.1, but simply point out that the most important difference is the versions of ECOCLIMAP. For the target one (tg1) ECOCLIMAP SG, and for the target two (tg2) ECOCLIMAPv2.5_plus are used. Other differences between the targets are related to the cloud droplet concentration specified for the lowest model level. However, this is believed to have no significant impact on the results discussed here.

Experiences by Météo-France in testing of ECOCLIMAP SG in AROME-France showed that the default tree height had to be decreased to achieve good wind speed over forested areas (Faroux and Le Moigne, 2018). Based on this experience we compared the ECOCLIMAP SG tree height to a laser-estimated tree height data set available over the MetCoOp area (Samuelsson et al., 2018). The mean ratio between the laser-estimated tree height data set and the ECOCLIMAP SG tree height over this area was 0.658. Thus, the ECOCLIMAP SG tree height has been scaled with this factor for all HARMONIE-AROME domains.

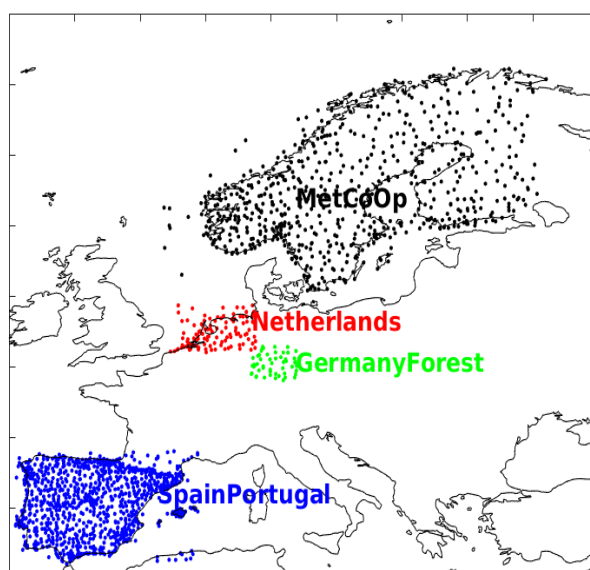


Figure 3.1: Subregions and their names used in the discussion of results. The regions are indicated by the positions of the screen-level stations. The MetCoOp subregion belongs to the METCOOP domain, the Netherlands and GermanyForest subregions belong to the KNMI domain and the SpainPortugal subregion belongs to the AEMET domain.

The main objective here is to show and discuss the differences in meteorological impact due to different ECOCLIMAP versions. Thus, with the exception for wind speed, there will be less emphasis on how the two targets compare with observations. During the target tests we have concluded that some parameters affecting near-surface temperature and moisture conditions need some tuning. This will be mentioned briefly but is not the main focus of discussion.

3.1. Experiments

A number of experiments with different combinations of domains and periods have been performed to evaluate the cy43h targets. A subset of these experiments are used to illustrate the main outcome of the results in this analysis. Table 3.1 lists these different combinations used. All experiments are done with 2.5 km grid spacing and 3D-VAR upper air data assimilation using conventional observations. For the surface 3-layer Force-restore and D95 snow scheme have been used in combination with OI data assimilation using screen level observations. All experiments are based on 48 hours forecasts from 00Z and 12Z with three hours cycling and use a spinup period of 15 days prior to the start date specified in the table. For the discussion of results four subregions are selected as shown in Figure 3.1. Also, most figures are presented as mean diurnal cycles, which are based on forecast hours 25-36 while statistics presented in the text is based on all 48 forecast hours.

3.2. Wind speed

The biggest differences between tg1 and tg2 are seen in wind speed, U10m (Figure 3.2). In general wind speed is higher in tg1 for all seasons and for all domains and also often too high compared to observations.

For some reason, not yet fully understood, the SpainPortugal region has a positive bias in U10m in tg2 of 0.3 ms^{-1} which becomes even higher, 0.6 ms^{-1} , with tg1. An examination of the KNMI results show that this increased bias in tg1 is mainly connected to open-land areas with an increase in bias of 0.5 ms^{-1} (from 0.2 ms^{-1} in tg2 to 0.7 ms^{-1} in tg1) for the Netherlands subregion while the forested region

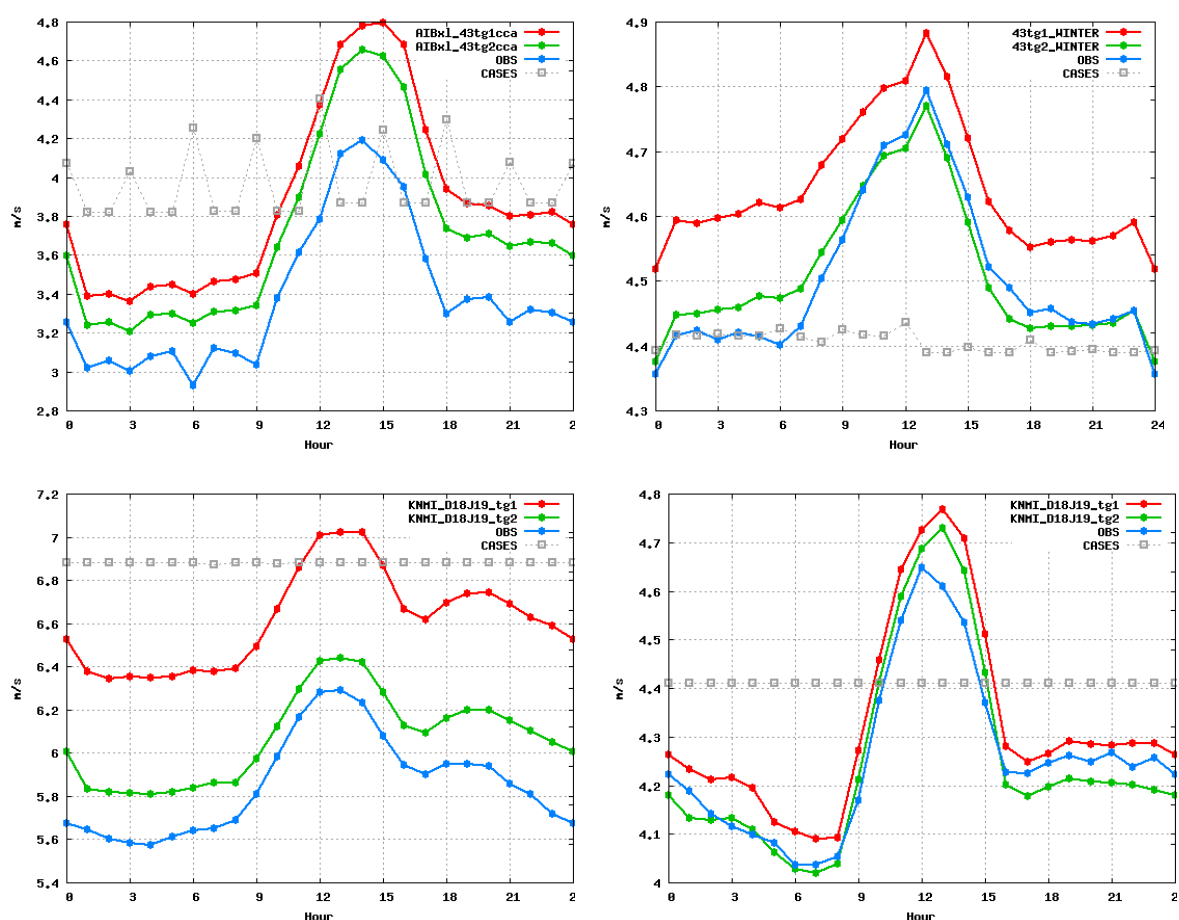


Figure 3.2: Mean diurnal cycle of wind speed (U_{10m} in ms^{-1}) for the winter periods for AEMET/SpainPortugal (upper left), METCOOP/MetCoOp (upper right), KNMI/Netherlands (lower left) and KNMI/GermanyForest (lower right). The lines represent tg1 (red), tg2 (green) and observations (blue). Please note that the wind-speed scales are different.

represented by GermanyForest shows an increase of only $0.1 ms^{-1}$ (from $0.0 ms^{-1}$ to $0.1 ms^{-1}$) which also corresponds to a $0.1 ms^{-1}$ increase over the MetCoOp subregion.

The reason for increased U_{10m} bias over open-land regions can be connected to a considerable reduction in LAI in ECOCLIMAP SG which has a direct impact on the vegetation roughness length. See Section 4 for sensitivity tests with modified roughness length formulations.

One exception from the general increase in wind speed in tg1 exist and that is for the Northern Scandinavia area during winter time (not shown). Here an increased LAI seems to be compensated by a redistribution of open-land and forest in such a way that the overall effect on U_{10m} is small.

3.3. Temperature and humidity

In general T_{2m} is warmer for tg1 than for tg2 by $0.2^{\circ}C$, especially during daytime (see Figure 3.3). The exception is in winter time over the MetCoOp domain which gives colder T_{2m} daytime conditions in tg1 than in tg2. Night time T_{2m} in tg1 is also somewhat warmer than in tg2 in general. The warmer daytime conditions are expected due to the lower LAI values in tg1 (see Section 2.5).

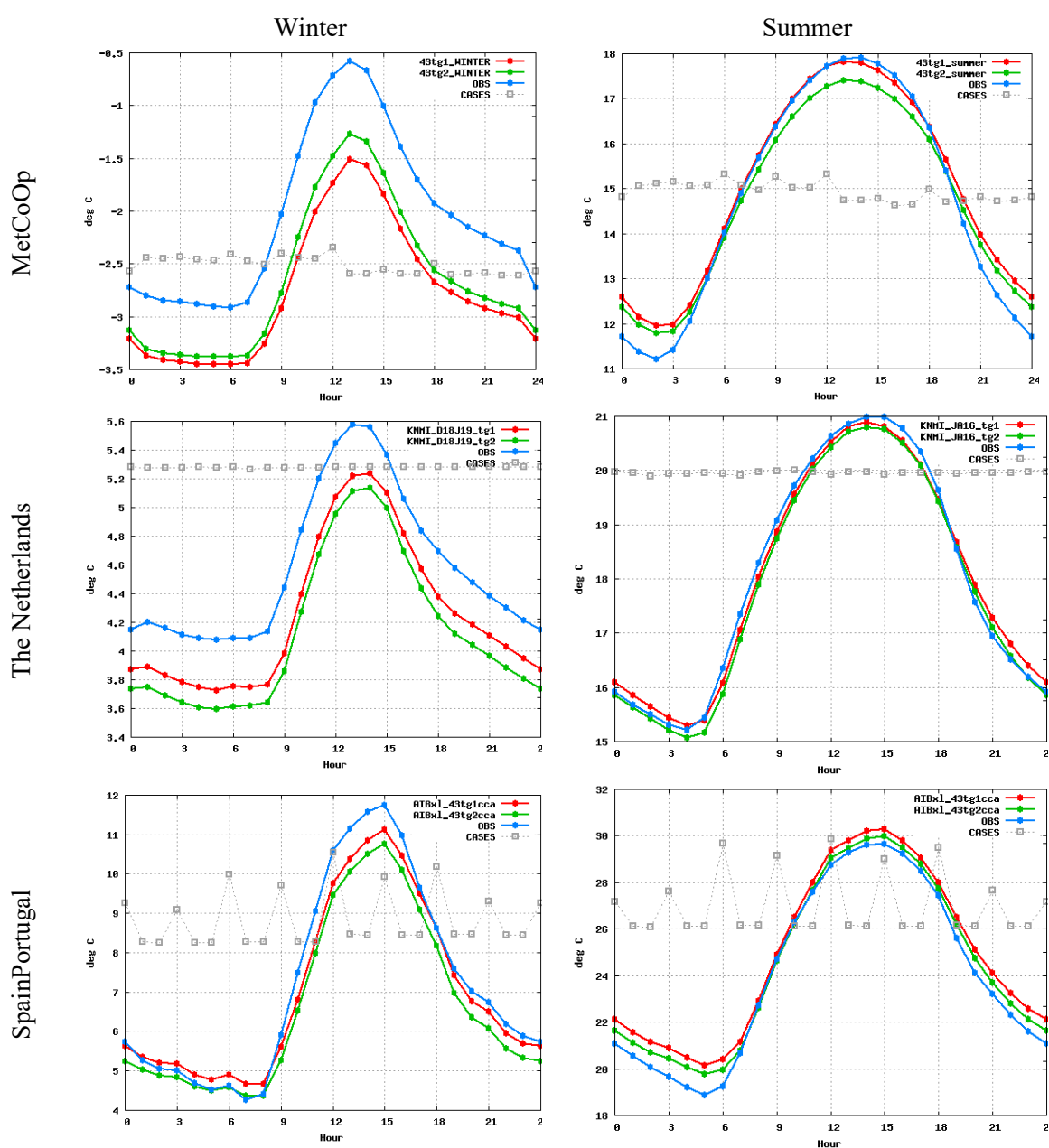


Figure 3.3: Mean diurnal cycle of near-surface air temperature (T_{2m} in $^{\circ}\text{C}$) for two seasons, winter and summer, and three subregions, MetCoOp, Netherlands and SpainPortugal. Please note that the temperature scales are different.

Looked over all seasons (not shown) Q2m is in general drier in tg1 than in tg2 although the numbers behind Figure 3.4 actually show slightly more humid conditions in tg1 (0.01 gkg^{-1}). However, an exception is over the KNMI domain which shows almost no difference between the targets or somewhat more moist conditions in tg1 (0.07 gkg^{-1} over the Netherlands), especially in summer. In general we have a dry bias in Q2m, especially in summertime (-0.3 gkg^{-1} in tg1). This is probably due to a combined effect of different factors which together gives drier conditions, like reduced LAI in combination with too high minimum stomatal resistance (R_{smin}). The investigation of this dry bias, and tuning of parameters, is an ongoing process right now.

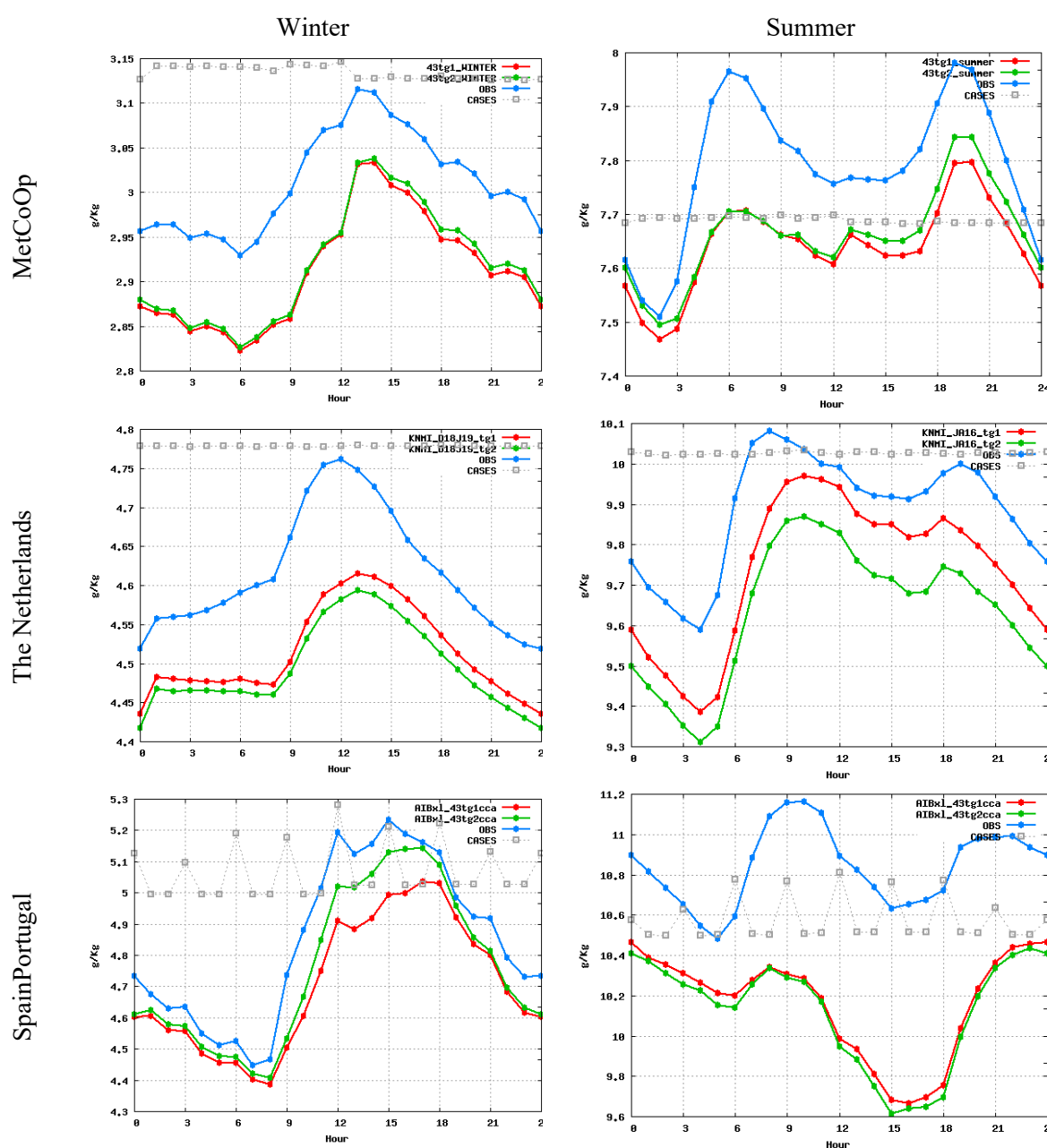


Figure 3.4: As Figure 3.3 but for near-surface specific humidity (Q_{2m} in $g\,kg^{-1}$). Please note that the humidity scales are different.

4 Experiments with roughness

Results from the previous section show that one of the main problems with the new physiography in cy43h's tg1 experiments is an increase in U10m which induces a considerable positive bias over many sub-domains (Iberia outside forested regions, the Netherlands, Ireland, etc.). This is especially a problem over AEMET's domain (IBERIA_25), where the wind bias in cy40h and in cy43h's tg2 is larger in general than in other domains. The increase in wind bias is mainly produced by the

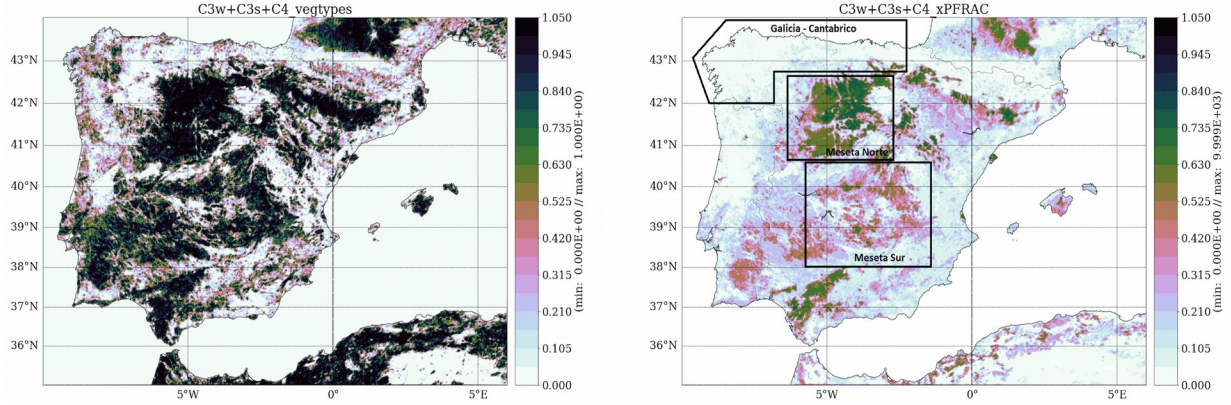


Figure 4.1: Total fraction of crops cover types in ECOCLIMAP SG (left) and ECOCLIMAP 2.2 (right) in the Iberian peninsula. Data comes from physiographic files on the IBERIA_25 domain at 2.5km resolution. Polygons on the right figure delimit subregions used for verification.

combination of several changes in the physiography. In Spain and Portugal, the global weight of crops in ECOCLIMAP SG (land cover types 19-21 from Table 1) has increased noticeably, as shown in Figure 4.1. Similarly, in other domains the amount of grass (covers 16-18) has increased as well. In SURFEX, the roughness length z_0 of both land types is a function of the Leaf Area Index (LAI):

$$z_{0_{grass}} = 0.13 LAI / a \quad (4.1)$$

$$z_{0_{crops}} = 0.13 \min(1.0, z_{allen}) \text{ for } LAI < b, \quad (4.2)$$

$$z_{0_{crops}} = 0.13 \quad \text{for } LAI > b \quad (4.3)$$

$$\text{where } z_{allen} = \exp\left[\frac{LAI - b}{1.3}\right], \text{ } a=6 \text{ and } b=3.5. \quad (4.4)$$

Therefore, the reduced LAI cycle all year round in ECOCLIMAP SG over Spain which was noted in Section 2.5 reduces in general the effective roughness length for crops and grass covered areas; as a consequence, the vertical flux of momentum decreases and the wind speed close to the surface increases. The overall effect in U10m wind bias for a specific area where grass or crops are predominant in ECOCLIMAP SG will depend also on whether these cover types substitute different land cover types from ECOCLIMAP-II with larger (i.e. forests) or smaller (i.e. bare land) roughness lengths. In Spain and Portugal, many areas have $LAI < 0.5$ in summer and early autumn in ECOCLIMAP SG, which in the current formulation means a z_0 similar or lower than that of the bare land (0.013 m). Therefore, the increase of crop covered areas will mainly tend to increase the wind and wind bias in those regions.

We propose here a simple modification in the roughness height formulation for crops and grasslands, to be used in combination with ECOCLIMAP SG, aimed to alleviate the increase in wind bias observed in tg1 experiments. This is achieved simply by defining $a=3$ and $b=2.5$ in Equations 4.1-4.3. The difference between both formulations is shown in Figure 4.2.

The proposed modification has been tested over the AEMET domain for the first 10 days of the summer period specified in Table 3.1. The results show, as expected, a general decrease in wind speed and wind speed bias over Spain and Portugal (Figure 4.3, upper left) with respect to the values with the original roughness length formulation (tg1 experiment). It can be seen that values are also lower than for tg2. Results for different subregions with contrasting physiography are also included in these figures. “Meseta Norte” comprises stations along the Duero basin, which covers most part of the large cluster of crops centered in 42°N, 5°W as shown in Figure 4.1.; “Meseta Sur” is also a region with crops centered in 39.5°N, 5°W, and “GaliciaCantabrico” is the region in NW Spain where the fraction

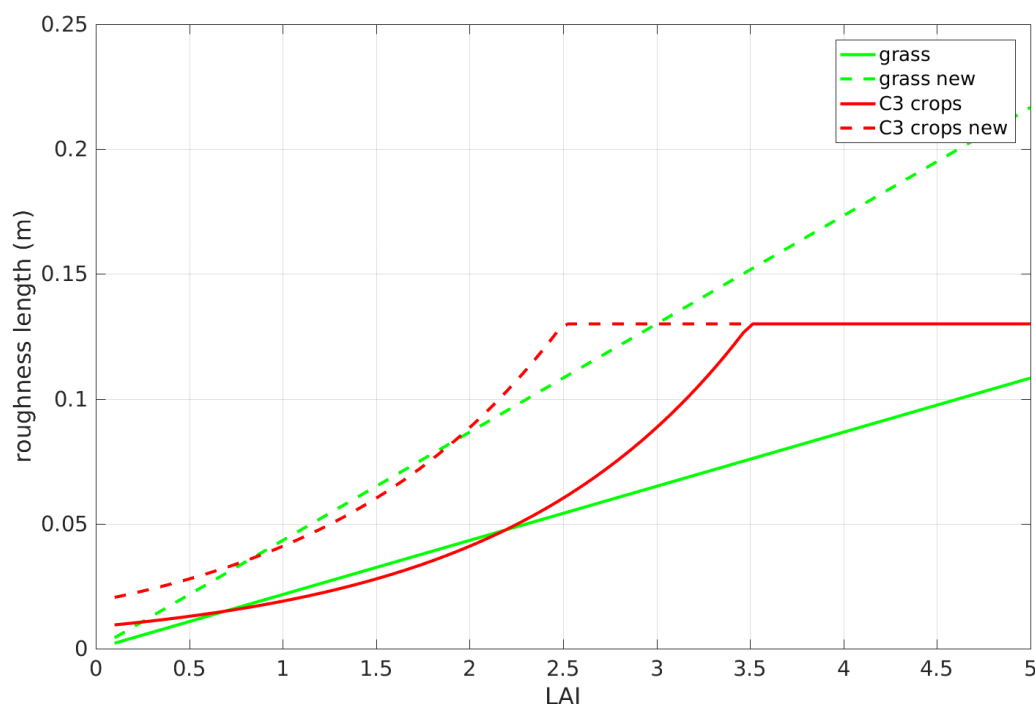


Figure 4.2: Original (solid) and modified (dashed) formulation of roughness length for grass (green) and crops (red) land cover types.

of crops is quite low in general, specially in ECOCLIMAP-II (forested cover types are predominant in this region). The new roughness length formulation decreases the U10m bias around $0.15\text{-}0.2\text{ ms}^{-1}$ in Meseta Norte and Meseta Sur subregions, while the decrease is more limited in the more forested GaliciaCantabrico region, as expected. In “Meseta Sur”, where the average crop fraction in ECOCLIMAP SG is nearly twice the average value for ECOCLIMAP-II as shown in Figure 4.1, the wind bias with the tuned roughness length has values similar to the tg2 experiment. On the other hand, it should be noted that in Meseta Norte, where it is also noticeable an increase in the crop fraction in ECOCLIMAP SG, tg1 and tg2 showed a similar wind bias. This should mean that the effective roughness length in this area is similar in both experiments, which indicates that the increase in the crop fraction in ECOCLIMAP SG was at the expense of a decrease in land types with a similar roughness length such as bare land or grasslands, rather than a decrease in the presence of other land types with higher roughness lengths, like “forest” cover types.

A decrease in near-surface wind speed can impact other near surface variables such as humidity and temperature, mainly through the reduction of evaporation from the soil surface and the canopy layer due to less ventilation. However, it has been checked that the impact of the modified roughness length formulation in T2m and RH2m is quite small. Therefore the proposed modification seems an adequate way to address the wind bias increase observed when using ECOCLIMAP SG. Nevertheless, given the different physiographic factors which can induce changes in the effective roughness length in tg1 experiments with ECOCLIMAP SG, the proposed tuning should be taken as a pragmatic solution which will work in different degrees over different zones depending on the specific physiographic changes over each zone and how they interact together (i.e.; areas/seasons where the open land patch increases but LAI is larger in ECOCLIMAP SG will be less affected by the tuning).

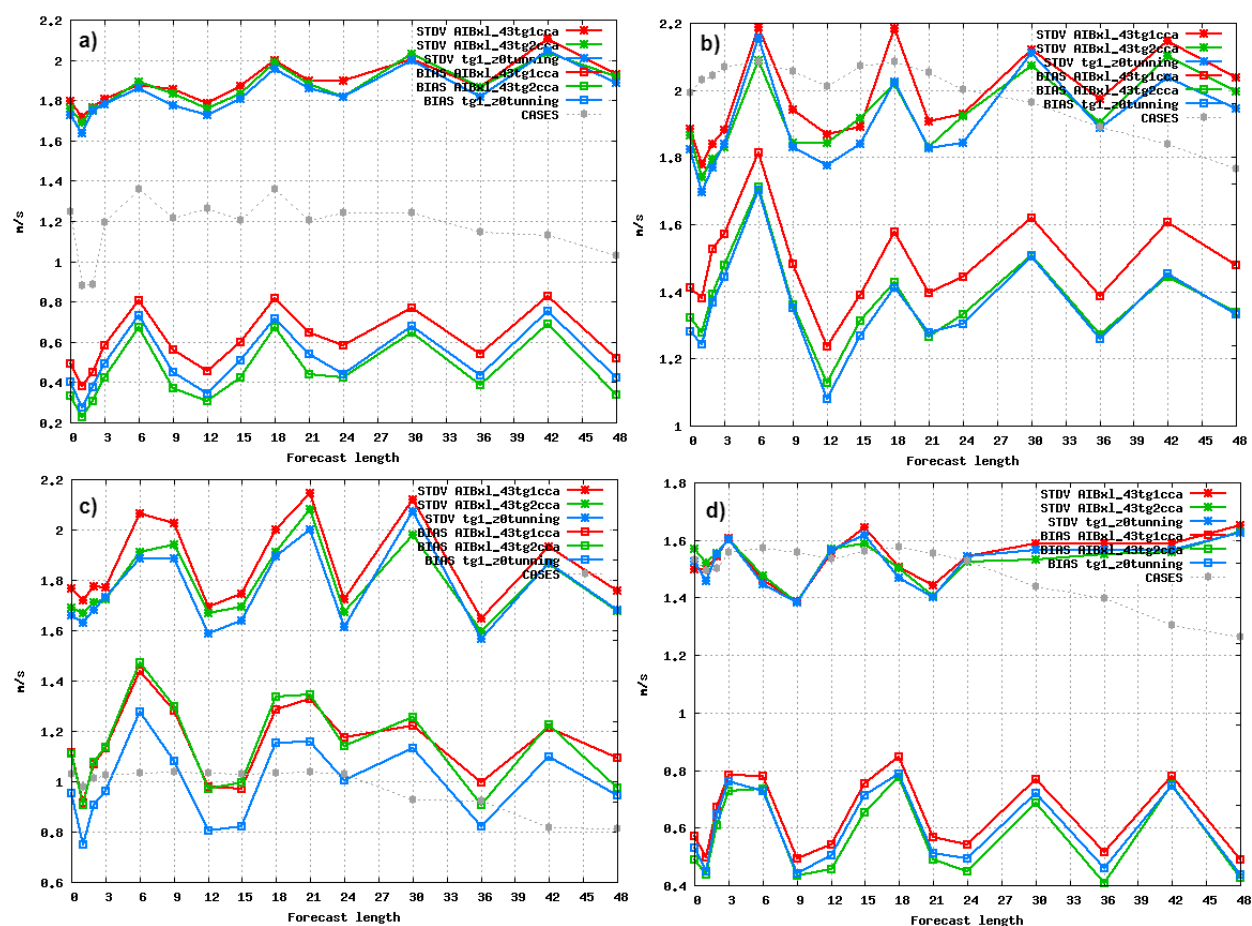


Figure 4.3: Mean U10m bias and standard deviation vs forecast length from 1 to 10 August, 2018 in a) Spain and Portugal, b) Meseta Sur, c) Meseta Norte and d) Galicia - Cantabrico. The lines represent target 1 (red) and target 2 (green) experiments with original formulation of z_0 , and target 1 with modified z_0 for crops & grass vegetation types (blue).

5 Conclusions

In this study, the new physiography map ECOCLIMAP SG with the increased resolution developed within the SURFEX community was compared with the current map ECOCLIMAP. Comparison was performed for the distribution of land and water covers, fractions of open land and forest, urban areas and Leaf-Area Index. To compare the land-water cover maps, a new method was developed. The method is based on statistics from contingency tables and allows to find the problematic regions with low agreement or high disagreement between two maps.

It was found that in addition to the increased resolution, ECOCLIMAP SG contain many improvements in comparison with ECOCLIMAP. First, there is no shift in ECOCLIMAP SG, as it was in ECOCLIMAP. Information on reservoirs is more correct. Improvements are in terms of representation of lakes and sea water (large lagoons, thermocarst and oxbow lakes, removed artifacts). Still, deterioration also exists, mainly for endorheic lakes, which are very difficult to map, because their surface area varies in time. False lakes appears in Chile and Greenland. These errors may come from mis-classification between mountain shadows and water; also there can be supraglacial lakes, which exist temporarily. Some small islands are omitted in ECOCLIMAP SG. Flooded areas such as paddy (rice) fields or mangroves are also problematic. Perhaps, they need special representation (parameterization) in NWP and climate models. The found problems need corrections (where it is

possible and easy to correct). Technically, at the moment ECOCLIMAP SG is not consistent with GLDB, but the SURFEX software provides technical consistency, for the price of physical errors. For Europe, the errors are not large. Physically, ECOCLIMAP SG gives approximately the same amount of sea water as ECOCLIMAP, with exception for the Netherlands, where it increases. The amount of lake water due to resolution generally decreases in ECOCLIMAP SG in Finland and Karelia, with approximately 15% and increases in Canada and in Northern Poland.

We see a change in distribution of land cover types between ECOCLIMAPv2.2 and ECOCLIMAP SG. ECOSG shows more open land patches over continental Europe and more forest areas in the Alps and northern Scandinavia. Also, spatial extent and density of urban areas increases. A general decrease of LAI, especially for open land vegetation types, is seen over continental Europe, the British Isles and Ireland in the growing season but somewhat less in summer. Over Sweden and Finland a reduction in the seasonality of LAI is seen.

The increase of open land areas in ECOSG in combination with decreased LAI have a considerable effect on wind speed in Harmonie-AROME simulations. U10m generally increases over the Netherlands and Spain/Portugal areas. For T2m we see in general a warming of daytime conditions and for moisture, Q2m, many times drier conditions although the response is more variable for moisture than for temperature.

Finally, a modification in the formulation of roughness length for crops and grass vegetation types has been tested over AEMET's domain for correcting the increase in 10m wind speed with the new physiography, with positive results. The proposed modification barely impacts other variables.

6 References

Bengtsson, L., U. Andrae, T. Aspelien, Y. Batrak and co-authors (totally, 23), 2017: The HARMONIE-AROME Model Configuration in the ALADIN-HIRLAM NWP System, *Mon. Weather Rev.*, **145**, 1919–1935, <https://doi.org/10.1175/MWR-D-16-0417.1>

Choulga, M., E. Kourzeneva, E. Zakharova and A. Doganovsky, 2014: Estimation of the mean depth of boreal lakes for use in numerical weather prediction and climate modeling. *Tellus A* 2014, **66**, 21295, <http://dx.doi.org/10.3402/tellusa.v66.21295>

ECO-SG: ECOCLIMAP-SG: technical documentation. Available from https://opensource.umr-cnrm.fr/attachments/download/2059/doc_ecosg.pdf

Faroux, S., A. T. Kaptué Tchuenté, J.-L. Roujean, V. Masson and co-authors (totally, 6), 2013: ECOCLIMAP-II/Europe: a twofold database of ecosystems and surface parameters at 1 km resolution based on satellite information for use in land surface, meteorological and climate models, *Geosci. Model Dev.*, **6**, 563–582, <https://doi.org/10.5194/gmd-6-563-2013>

Faroux, S and P. Le Moigne, ECOCLIMAP Second Generation, Presentation at Joint 28th ALADIN Workshop & HIRLAM All Staff Meeting, Toulouse, France, 2018.

Fortelius, C., E. Gregow, E. Kourzeneva, L. Rontu and K. Hämäläinen, 2018: Highlights of NWP activities at FMI. *ALADIN-HIRLAM Newsletter* no.10, January 2018. Available from <http://www.cnrm-game-meteo.fr/aladin/>

Masson, V., P. Le Moigne, E. Martin, S. Faroux and co-authors (totally, 41), 2013: The SURFEX7.2 land and ocean surface platform for coupled offline simulation of Earth surface variables and fluxes. *Geosci. Model Dev.*, **6**, (4), 929-960, DOI: 10.5194/gmd-6-929-2013

Samuelsson, P., M. Homleid, T. Aspelien and U. Andrae, Two patches in cy40h HARMONIE-AROME and modified tree height and snow roughness length for the MetCoOp domain, *ALADIN-HIRLAM Newsletter* no.10, January 2018. Available from <http://www.cnrn-game-meteo.fr/aladin/>

Tijm, S. and N. Bloemendaal, SURFEX fluxes in Spring and Summer, Presentation at Joint 26th ALADIN Workshop & HIRLAM All Staff Meeting, Lisbon, Portugal, 2016.

Tijm, S., Forecast model progress, Presentation at Joint 28th ALADIN Workshop & HIRLAM All Staff Meeting, Toulouse, France, 2018.

Annex

Table A1: Correction for the cover classes in the land cover map ECOCLIMAPv2.5_plus.

	Cover class	Current partition	Correction	Remarks
124	Warm tropical wetlands	nature – 80% inland water – 20%	nature – 100 %	-
125	Subpolar wetlands	nature – 80% inland water – 20%	nature – 100 %	-
176	Rice fields	nature – 80% inland water – 20%	-	“False” cover, does not exist on the land cover map
238	Temperate wetlands	nature – 80% inland water – 20%	-	“False” cover, does not exist on the land cover map
239	Subpolar wetlands	nature – 80% inland water – 20%	nature – 100 %	Exists only in Iceland
240	Peat bogs	nature – 80% inland water – 20%	-	“False” cover, does not exist on the land cover map
241	Salines and salt marshes	nature – 50% inland water – 50%	-	“False” cover, does not exist on the land cover map
242	Intertidal flats	nature – 50% sea water – 50%	-	“False” cover, does not exist on the land cover map
243	Coastal lagoons	sea water – 100%	-	“False” cover, does not exist on the land cover map
249	INLAND WATERS1	inland water – 100%	sea water – 100%	Polders and coastal lagoons

550	UNDEFINED1	nature – 45% inland water – 55%	Fixes in the land cover map: from 550 to 2 or from 550 to the major cover class in the vicinity. For the rest: nature – 45% sea water – 55%	In Europe: sea water near the coast, coastal lagoons, river estuaries. In Ukraine and Turkey: lakes. In Asia: land.
551	INLAND WATERS2	nature – 5% inland water – 95%	-	“False” cover, does not exist on the land cover map
552	POLAR WETLANDS1	nature – 100%	Fixes in the land cover map: from 552 to 1 or from 552 to 2	In Europe: sea water near the coast, coastal lagoons. In Asia: lakes and land.
553	INLAND WATERS3	nature – 1% inland water – 99%	Fixes in the land cover map: from 553 to 2 or from 550 to the major cover class in the vicinity. For the rest: nature – 1% sea water – 99%	In Europe: glaciers, sea water near the coast, coastal lagoons, river estuaries. In Asia: lakes, sea water near the coast and land.
554	INLAND WATERS4	nature – 2% inland water – 98%	Fixes in the land cover map: from 554 to 2 or from 554 to the major cover class in the vicinity. For the rest: nature – 2% sea water – 98%	In Europe: land, sea water near the coast, coastal lagoons, river estuaries. In Ukraine: lakes. In Asia: lakes, sea water near the coast and land.
555	INLAND WATERS5	nature – 3% inland water – 97%	nature – 3% sea water – 97%	Sea water near the coast, coastal lagoons, river estuaries.

556	INLAND WATERS6	nature – 25% inland water – 75%	Fixes in the land cover map from 556 to 2. For the rest: nature – 25% sea water – 75%	Sea water near the coast, coastal lagoons, river estuaries, one lake.
-----	----------------	------------------------------------	---	---

List A1: Results of the detailed comparison between ECOCLIMAP and ECOCLIMAP SG for the land-sea-inland water cover types

1. Resolution issues
 1. In Western Africa, more rivers and lakes appeared on ECOCLIMAP SG
 2. In Canada, more lakes appeared on ECOCLIMAP SG. Illustrated by Fig. A1
 3. In Finland and Karelia, number of lake pixels decreased in ECOCLIMAP SG. Illustrated by Fig. A2
2. Coastal lagoons
 1. The Wadden Sea in The Netherlands changed from land on ECOCLIMAP to sea on ECOCLIMAP SG (illustrated by Fig. A3). Actually, for the Wadden Sea ECOCLIMAP contained cover classes 549-550 and 553-556, which contain quite large percentage of water. But in ECOCLIMAP SG this is pure water: **improvement**
 2. Szczecin (Oder) lagoon is a lake in ECOCLIMAP SG, while in ECOCLIMAP it was land: **improvement**
 3. River Mississippi delta: dramatic changes. More sea and lake water in ECOCLIMAP SG: **improvement**
3. Endorheic lakes
 1. The Aral Sea is the sea in ECOCLIMAP SG, with some artifact in the Northern part. Also, it is too large both in ECOCLIMAP and ECOCLIMAP SG: **deterioration**
 2. Dry Lake Merlhir in Sahara desert, with the surface area of 6800 km² exists as a lake in ECOCLIMAP SG, but not in ECOCLIMAP: **deterioration**
 3. Dry Lake Namak in Iran with the surface area of 1800 km², as well as many other dry lakes in this region is land on ECOCLIMAP SG but was lake on ECOCLIMAP: **improvement**
 4. In Australia, many dry lakes are “water” on ECOCLIMAP SG: **deterioration**
 5. Lake Tuz in Turkey decreased a lot on ECOCLIMAP SG: **improvement**
 6. Big bay in the North-Eastern part of the Caspian Sea is sea water on ECOCLIMAP, but lake water on ECOCLIMAP SG. Actually, it is dry.
 7. Lake Rann of Kutch in India became partly sea on ECOCLIMAP SG, and increased in size: **deterioration**
 8. Dry lake Etosha Pan in Africa is “water” on ECOCLIMAP SG: **deterioration**
 9. Lake Chad in Africa decreased a lot on ECOCLIMAP SG: **improvement**
4. Thermokarst lakes: their number increased a lot on ECOCLIMAP SG (as illustrated by Fig. A4). There is also some local decrease, however, overall increase is larger: **improvement**
5. Oxbow (fluvial) lakes: many of them appeared on ECOCLIMAP SG. Mostly noticeable are from River Ob (see Fig. A5 for illustration), River Ganges, River Taz, River Lena, River Mackenzie, River Parana, River Amazon, small rivers in Australia: **improvement**
6. River estuaries for rivers in UK and for River Garonne, which are tidal areas, from land on ECOCLIMAP (yet, cover classes with some percentage of water) became sea on ECOCLIMAP SG: **improvement**
7. Paddy (rice) fields in Vietnam (as illustrated by Fig. A6), India, China: due to them, there is much more water in ECOCLIMAP SG in these areas. Paddy (rice) fields can be sea,

- lake and river water! In reality, they contain water but can't be treated by the lake parameterization, due to totally different physics.
8. Australia: there are dramatic changes in the sea coast and lakes in the Northern part on ECOCLIMAP SG. In the Western part, many lakes disappeared or became smaller, and Lake Macleod appeared (1500 km²): **improvement**
 9. Small islands:
 1. Rat islands (around 175.0,55.0), Vanua Levu (around 175.0, -15.0, the surface area is 5580 km²) appeared on ECOCLIMAP SG: **improvement**
 2. Amsterdam (77.555, -37.848) and Saint-Paul (77.521, -38.728); Fatu Hiva (around -135.0, -15.0, the surface area is 84 km²); Isla Socorro with the surface area 132 km², Isla Clarion, Revillagigedo islands (around -115.0, 15.0); Arrecife Alacarnes (around -85.0, 25.0); Malpelo (around -85.0, 5.0); Isla de la Plata (around -85.0, -5.0); Abrolhos islands with the surface area 50 km² (around -35.0, -15.0) disappeared on ECOCLIMAP SG: **deterioration**
 10. Artifacts
 1. In Arctic Russia, the peninsular close to River Pechora delta (around 53.0,68,0), false sea pixels disappeared on ECOCLIMAP SG: **improvement**
 2. In Arctic Siberia, River Jana delta: the false bay disappeared on ECOCLIMAP SG: **improvement**
 3. In Papua, the sea-type artifact disappear on ECOCLIMAP SG: **improvement**
 4. On Lake Rukwa in Africa, the land artifact disappeared on ECOCLIMAP SG: **improvement**
 5. In River Lena delta, the artifact lake disappeared on ECOCLIMAP SG: **improvement**
 6. In River Amur delta, the artifact lake disappeared on ECOCLIMAP SG: **improvement**
 7. In Greenland, many false lakes appeared on ECOCLIMAP SG (as illustrated by Fig. A7): **deterioration**
 8. Along Chile coast, many false small lakes appeared on ECOCLIMAP SG (as illustrated by Fig. A8): **deterioration**
 9. On Severnaya Zemlya island, the big bay disappeared on ECOCLIMAP SG. In reality, there is a glacier.
 11. On Java island, many lakes appeared on ECOCLIMAP SG: **improvement**
 12. In New Zealand, changes are dramatic: rivers disappeared totally, some lakes as well. However it is difficult to classify it as improvement or deterioration, due to resolution issues. More studies are needed.
 13. Lake Tengiz in Kazakhstan, with the surface area of 1382 km², was absent on ECOCLIMAP, but appeared on ECOCLIMAP SG: **improvement**
 14. On Cuba and the Bahamas, number of lake pixels increased on ECOCLIMAP SG, which were land on ECOCLIMAP (although actually they are sea/mangrove and should be corrected): **improvement**
 15. In Chile, a big lake appeared on ECOCLIMAP SG (around -74.0, -49.0), however it is most likely a glacier: **deterioration**
 16. Lake Mar Chiquita increased a lot on ECOCLIMAP SG: **improvement**

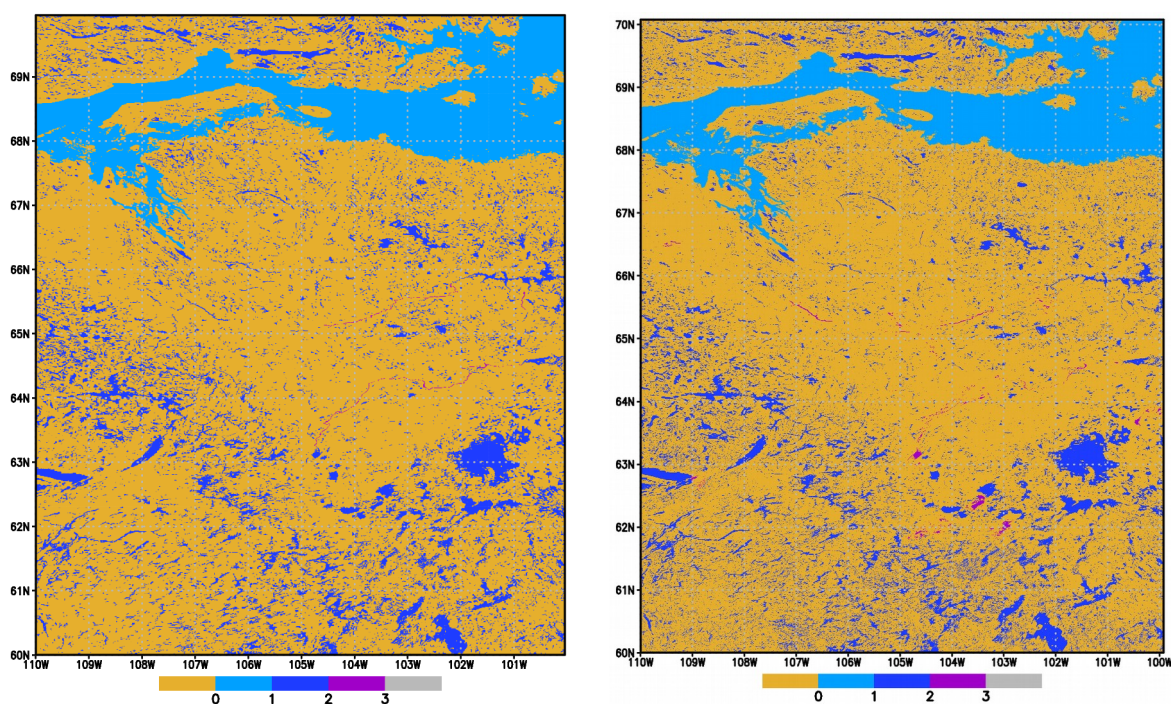


Figure A1: Canada: distribution of land, sea and inland water (lakes and rivers) cover types on ECOCLIMAP (left) and ECOCLIMAP SG (right). Colors are: yellow for land, light blue for sea, blue for lakes and magenta for rivers.

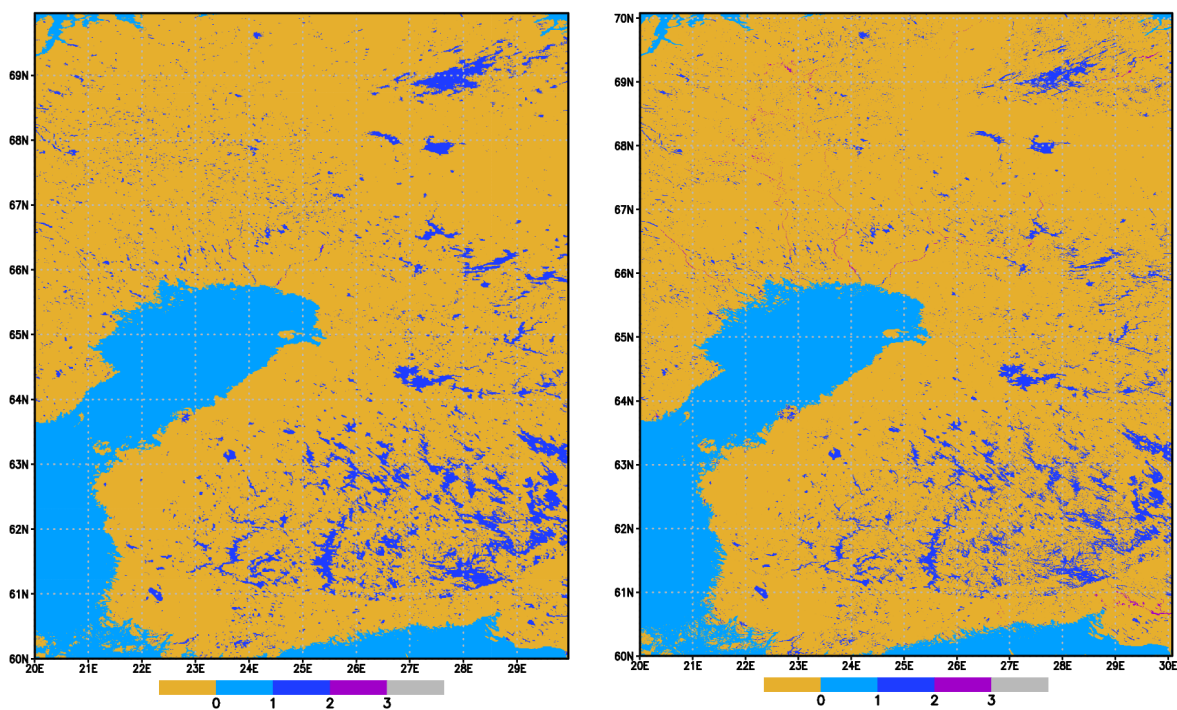


Figure A2: Same as Fig. 2.2.4, but for Finland and Karelia.

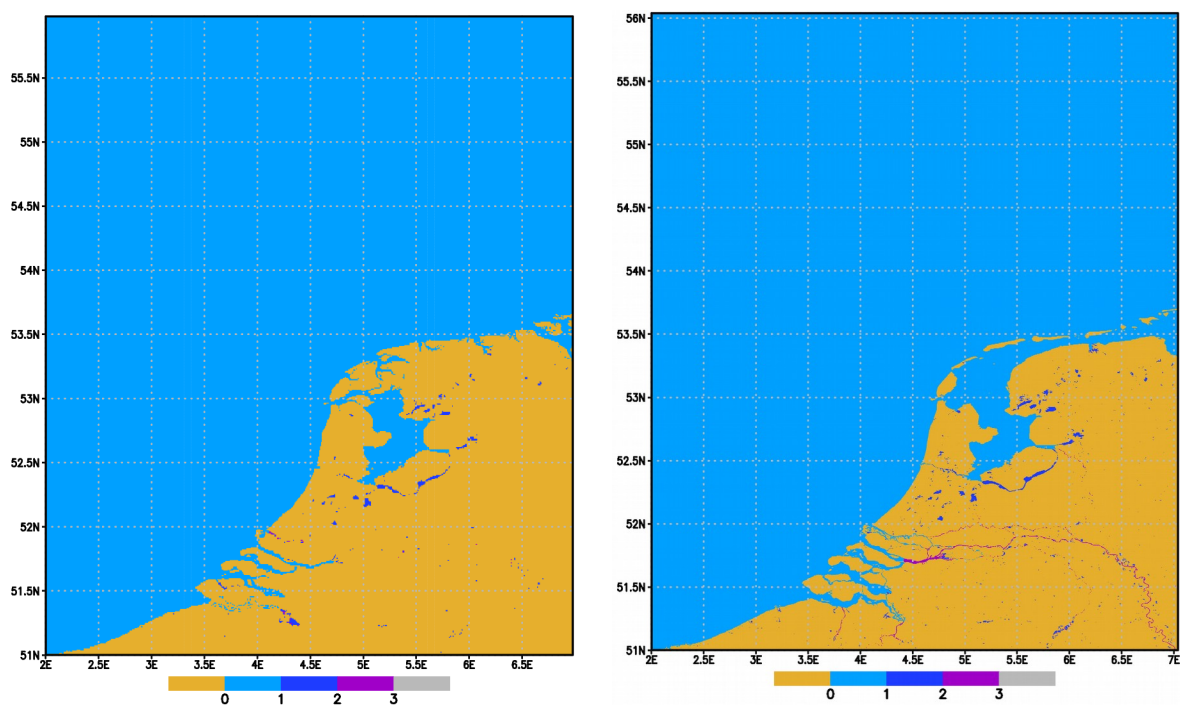


Figure A3: Same as Fig. 2.2.4, but for the Netherlands.

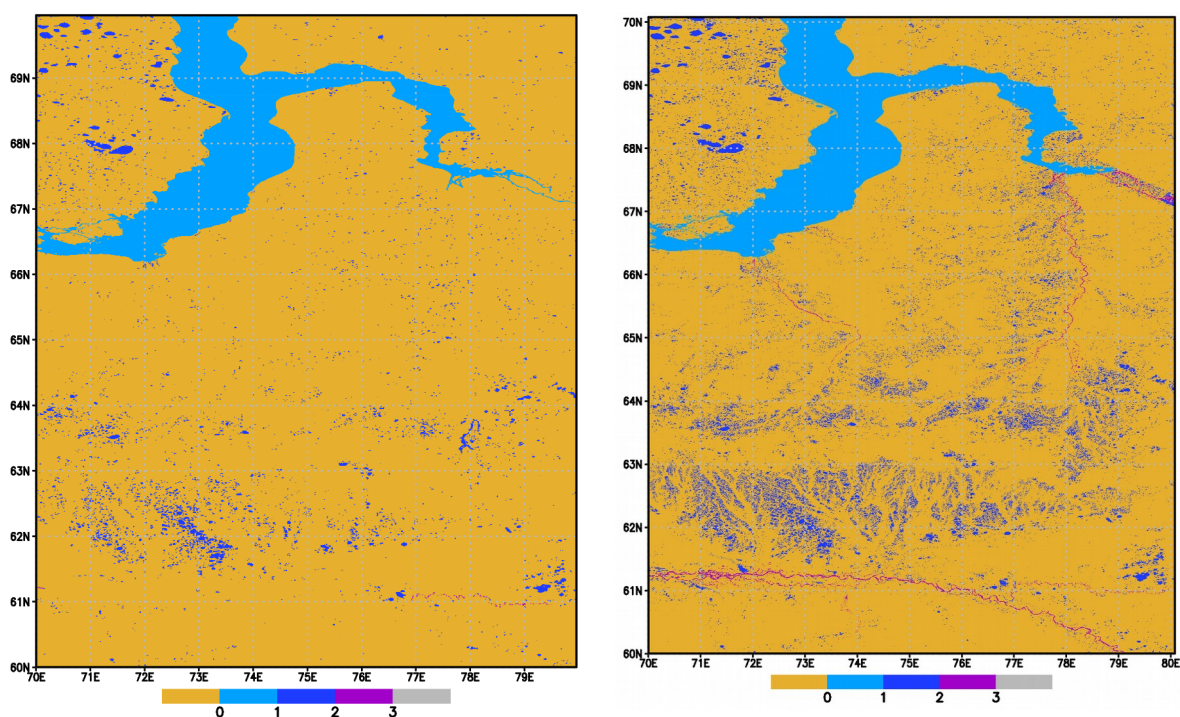


Figure A4: Same as Fig. 2.2.4, but for thermocarst lakes in Western Siberia.

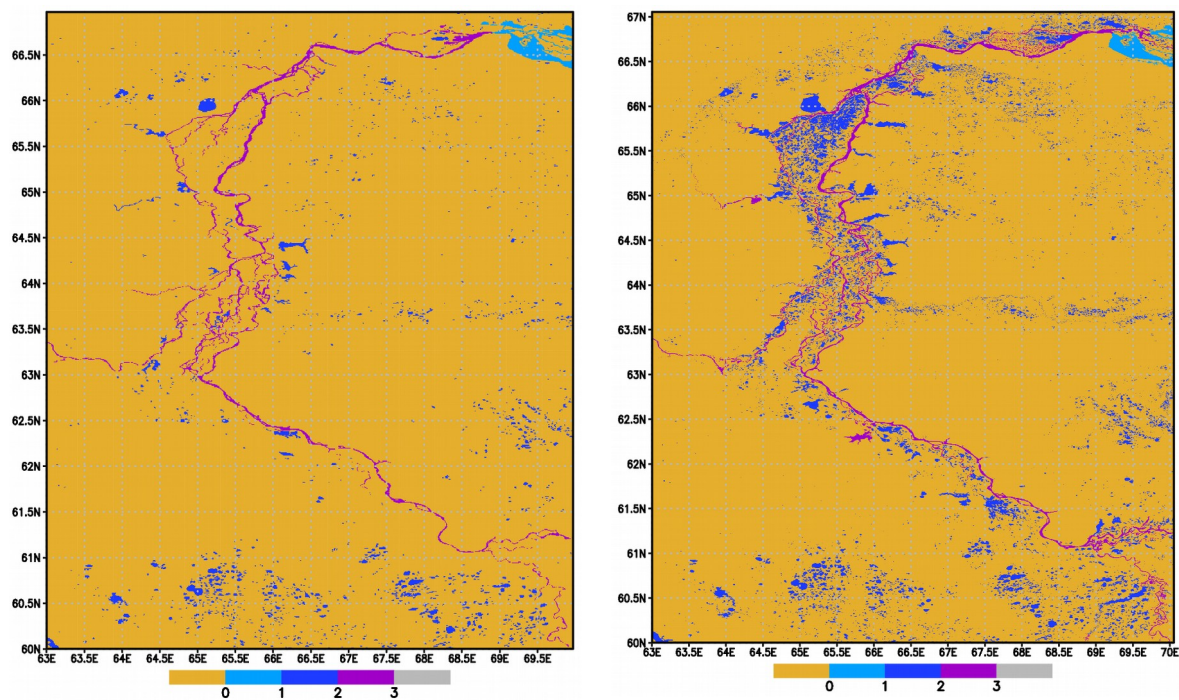


Figure A5: Same as Fig. 2.2.4, but for oxbow (fluvial) lakes along River Ob.

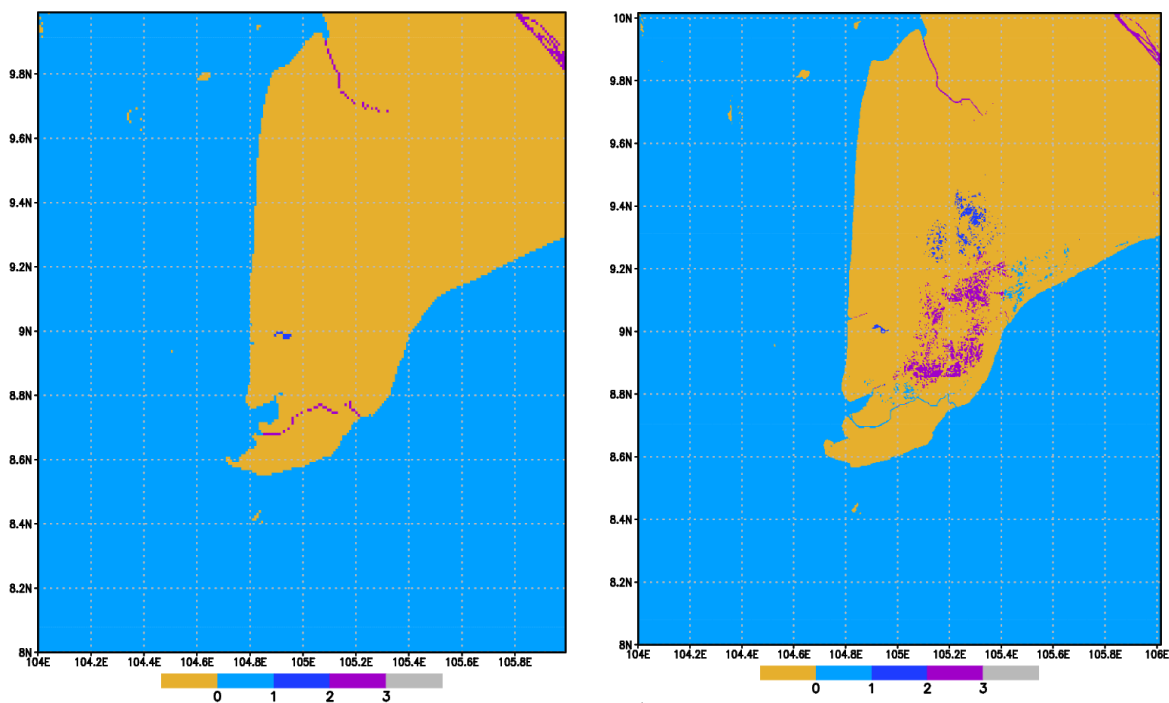


Figure A6: Same as Fig. 2.2.4, but for paddy (rice) fields in Vietnam.

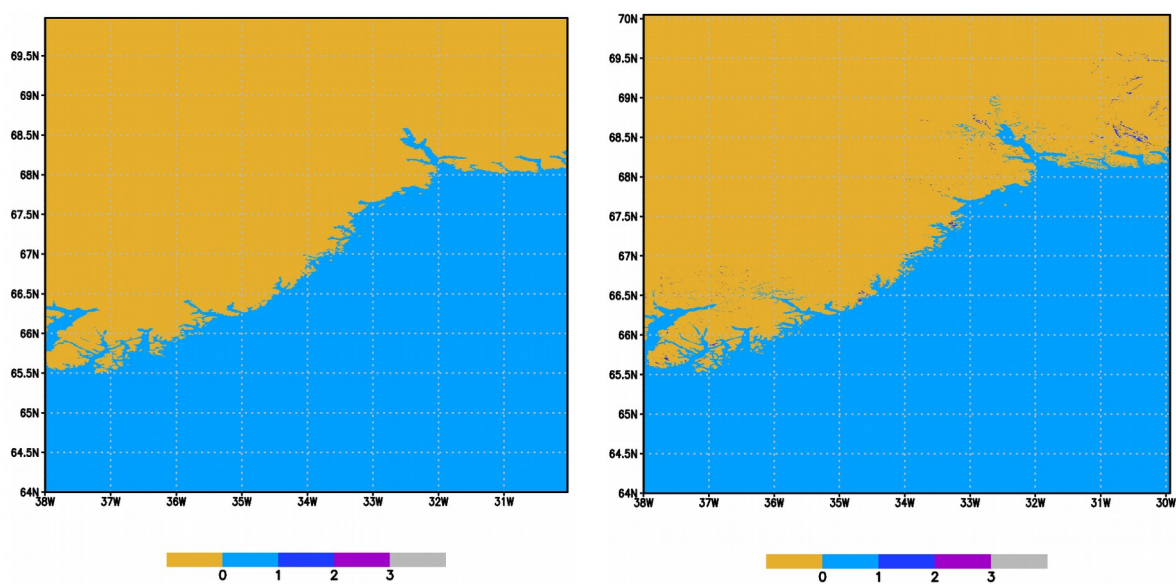


Figure A7: Same as Fig. 2.2.4, but for artifact lakes in Greenland.

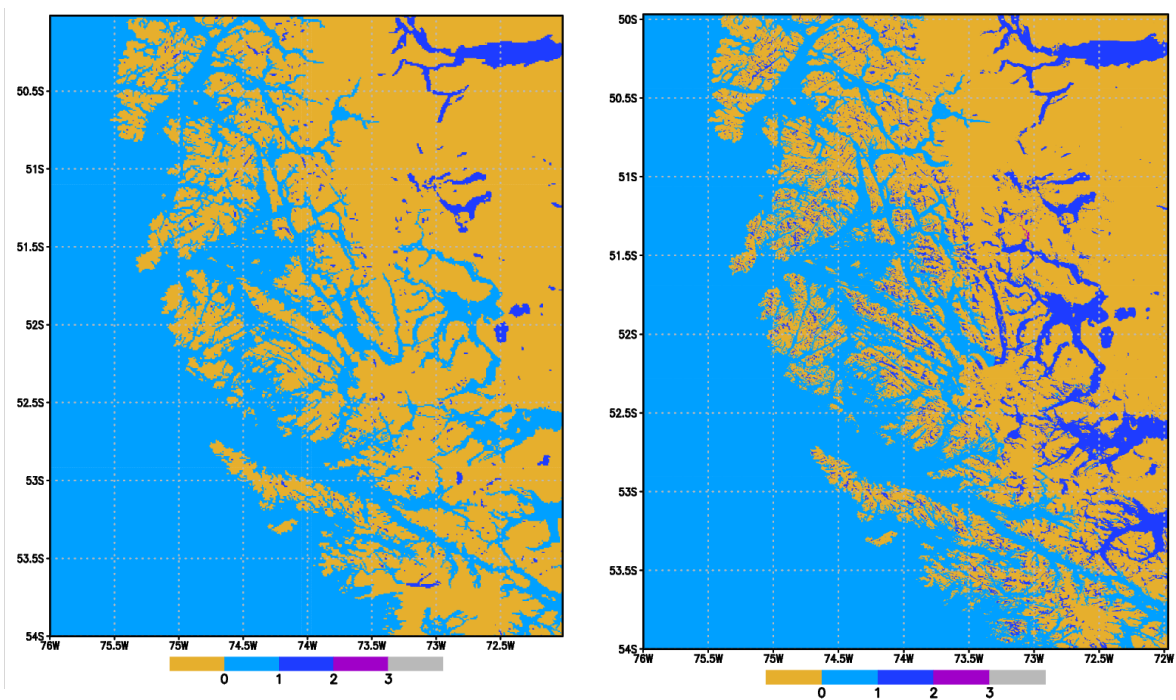


Figure A8: Same as Fig. 2.2.4, but for artifact lakes along Chile coast.

A continuous EDA based ensemble in MetCoOp

Ulf Andrae¹, Inger-Lise Frogner², Ole Vignes², Andrew Singleton², Roohollah Azad², Mikko Partio³, Niko Sokka³

1. Swedish Meteorological and Hydrological Institute (SMHI)
2. Norwegian Meteorological Institute (MET Norway)
3. Finnish Meteorological Institute (FMI)

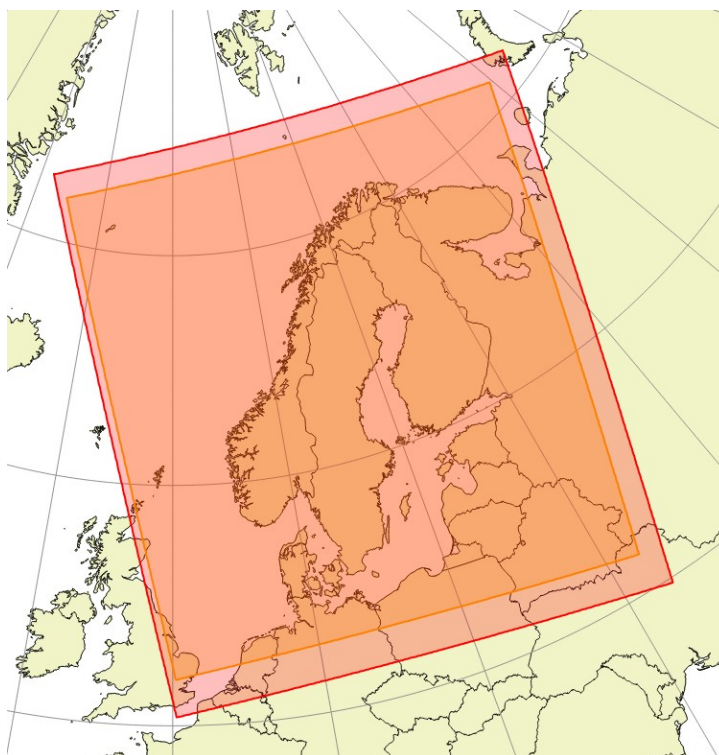


Figure 1. Current and future domain

1 Introduction

The MetCoOp ensemble prediction system, MEPS, has been operational since late 2016 and is today an important component in the daily forecasting at the institutes. The increased computational capacity made available in early 2019 offered the possibility to introduce a parallel, close to full scale, experimental ensemble system. In the following we describe the properties and limitations of the current system, the reasoning behind the design of the new setup and a comparison of the performance of the two systems. The new ensemble will replace the current one as the operational ensemble for MetCoOp in February 2020.

2 Properties of the current ensemble

The current operational system, MEPS (Andrae 2017), is based on the harmonie-40h1.1.1 version of the HARMONIE-AROME model (Bengtsson et.al. 2017) with perturbation methods as in HarmonEPS (Frogner et.al. 2019b). The model runs over the inner domain shown in Figure 1 with a

horizontal resolution of 2.5km and 65 levels in the vertical. For the first three members, control and pseudo-control members, the assimilation cycle is 3h and a large variety of conventional and non-conventional observations are assimilated. For the additional members the assimilation cycle is 6h and only surface assimilation is applied. The generation of the ensemble members is distributed over three HPCF, two in Sweden and one in Finland, which runs 5, 4 and 1 members respectively. MEPS serves as the primary source of uncertainty information for the first two days at the MetCoOp institutes and has been shown to add forecast skill on e.g. precipitation for scales not described well by the ECMWF ensemble IFSSENS (Frogner et.al. 2019a). We can however identify a few problems and limitations in the current system:

- The number of members are limited by two factors. The first is the total computational capacity available when we run all members simultaneously and constrained by a delivery time of about one hour. The second limiting factor is the SLAF methodology where we use two IFS HRES forecasts from 6h apart to generate the perturbations, with hourly nesting. In practise it means that the boundary file for member nine at +54h uses the difference from +84h and +90h. From +90h the data is only available every 3h, hence, there is no room for further expansion with the current method.
- Attempts to use MEPS for nowcasting of precipitation have failed due to an overestimation of precipitation during the first forecast hours. Further it has been noted that the wind field during the first hours has an undesirable high noise level. Both aspects suggests that the current initial perturbations are too imbalanced.
- A general feedback from duty forecasters is a lack of spread in e.g. clouds making the ensemble less useful for e.g. aviation forecasting.

3 Designing a new ensemble

The continuous approach

The most straightforward and common way to produce an ensemble is to launch all members at the same time and as in the current MEPS configuration perturb the initial state around a control analysis. This approach leads to a very unbalanced usage of the computer resources and, as mentioned above, a strong constraint on the numbers of members. To construct probability products by lagging of several forecasts with different initial time is not a new approach (Hoffman and Kalnay 1983). However, to distribute the generation of ensemble members in time as described by Yang et. al. (2017) and Porson et.al. (2020) is fairly new. The approach has several appealing properties. Spreading the generation of members in time not only evens out the workload on the computer, it also allows us to increase the number of members for a given maximum computer capacity. For the forecaster we are able to present frequent updates and an ensemble with less jumpiness, due to the lagging. In our setup we've distributed the members in time, and over our three HPCF as shown in table 1. The results presented here are based on 9 unique members whereas the operational setup will have 6 more members meaning that we will produce 5 new members each hour. Hereafter we will call this suite CMEPS. The ensemble related configuration differences between MEPS and CMEPS are summarized in table 3. The settings for IFSSENS are included as a reference.

Table 1: Distribution of members in time and over the MetCoOp computers for the results described in the report. Numbers in parentheses are additional members in the operational setup

	Time (UTC)	Cirrus	Stratus	Voima
Stream 1	00,03,...,21	0, (12)	1,2	(9)
Stream 2	01,04,...,22	7,(13)	3,4	(10)
Stream 3	02,05,...,23	8,(14)	5,6	(11)

Ensembles of Data Assimilation (EDA) properties

Describing the initial uncertainty through perturbation of observations within their observations error limit is a well established method used e.g. by ECMWF (Isaksen et.al. 2010). The method is also implemented in the HarmonEPS system and has been shown to improve the spread of e.g. near surface variables without loss of skill (Frogner et.al. 2019b). For a system that is distributed in time and over several HPCs it's also appealing not to have to relate to a single control analysis. Another aspect is the potential usage of the operational ensemble to generate background error statistics for the data assimilation discussed later. Either as climatological statistics from different seasons or in a more continuous manner. Following Frogner et.al. (2019b) we have combined EDA with perturbations derived from IFSSENS but scaled by 0.5 as compared to the SLAF based perturbations in MEPS. Running with EDA only does not provide a satisfactory spread (result not shown).

Distributing the different streams in time, like shown in table 1, naturally has an impact on the number of observations available for assimilation. The result is summarized in table 2 and we note that for most observations types the difference is small. The most striking difference is the number of radiosondes (TEMP T) which mainly launched at synoptic hours and which results in 85% less observations in stream 2 compared to stream 0. However, when comparing the mean absolute error of e.g. MSLP from perturbed member forecasts we see no differences in quality (not shown) suggesting that all members have similar quality despite the variations in observation density.

Table 2. Typical number of observations at different hours (UTC)

	Stream 0 (00,03,...,21)	Stream 1 (01,04,...,22)	Stream 2 (02,05,...,23)
TEMP T	250-300	150-200	40
AIRCRAFT T	105	130	120
SYNOP Z	530	530	445
GNSS	70	70	70
RADAR	1100	1100	1100
ASCAT	600	750	600
IASI (METOP1)	300	300	300
SYNOP SNOW	>650	>650	>650
SYNOP T2M	850	760	760

In the default HARMONIE-AROME setup snow is assimilated once a day at 06Z since this is when the majority of the snow observations are reported. This would of course leave the members not running at 06Z without any snow assimilation or at least with much less observations. To overcome this the snow assimilation has been shifted to be done at 07/08/09Z using a longer time window to maximize the number of snow observations used. An example of the impact in observation usage is shown in figure 2.

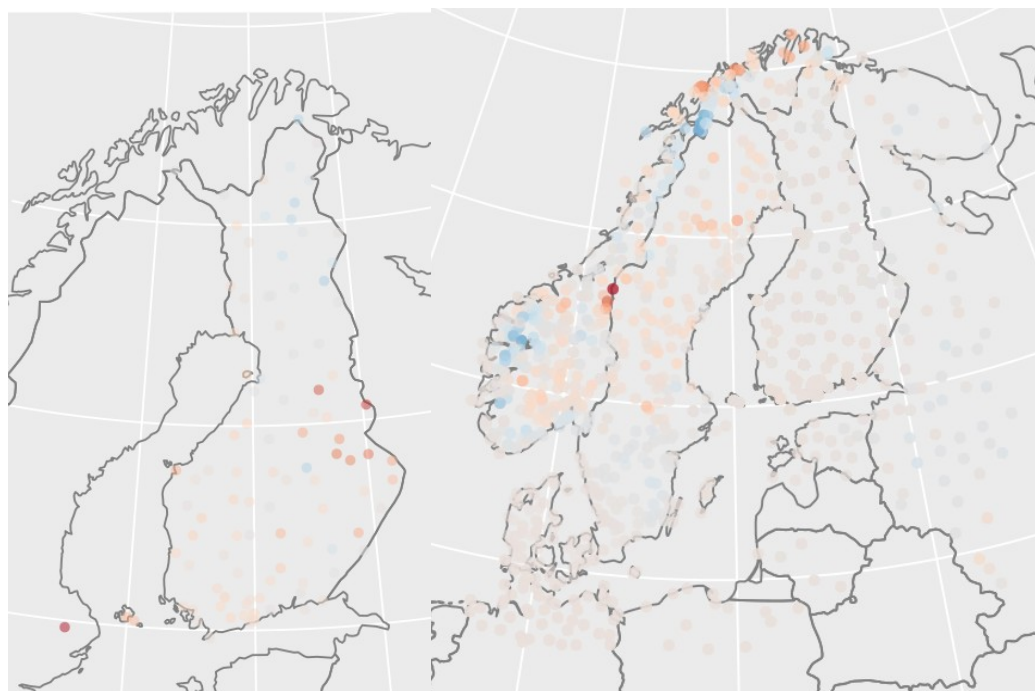


Figure 2. Snow increments at 2019-03-04 08Z before (left) and after (right) the extended observation usage.

Using IFSENS boundaries

Generating lateral boundary perturbations through the SLAF method has been an efficient way to introduce an operational ensemble without any extra requirements on the dissemination of data from the global model (IFS). However, as mentioned earlier we are, with the current method, limited by the maximum available forecast length of the forcing model. Frogner et. al. (2019b) showed that by using IFSENS it's possible to maintain a larger spread throughout the forecast compared to SLAF. It was also shown that with a clustering method maximizing the spread (Molteni et. al. 2001) it's possible to select IFSENS members and increase the spread even more. For simplicity this is not pursued further but we pick the first 28 members so that each CMEPS member uses different IFSENS members seen over a time window of 6h. The control member is still coupled to IFS HRES from which we also take the SST and ice cover for all members since the coarser resolution in IFSENS degrades T2M scores along coastlines. Note that the perturbation of SST maintains the variability in the lower boundary forcing over sea.

Technical aspects

Although the three streams in table 1 are in principle independent they only differ by a few configuration settings. Running a continuous setup of course poses challenges when it comes to updates and maintenance, especially for a setup running simultaneously on three different platforms. Using HARMONIE terminology we've therefore introduced the concept of STREAM to allow several forecast cycles to run in parallel in the same experiment setup. Each STREAM has an independent set of binaries, scripts and config files.

To allow us to grow the ensemble with a factor of three without increasing the cost for data transfer and storage too much we introduced GRIB2 using the lossless CCSDS algorithm with an accuracy of 16 bits for all fields. The algorithm provides a reasonable balance between reduced size and increased cost in packing/unpacking, figure 3. As a result the size reduced with 59% for a typical history file and 56% for a fullpos file.

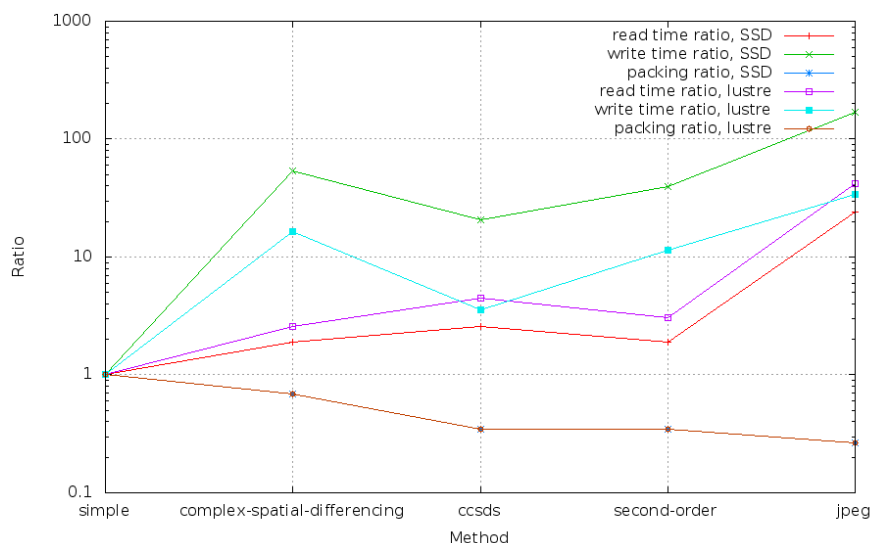


Figure 3. Comparison of various packing methods available in ecCodes.

Table 3: Summary of properties of the current and next generation ensemble. The ECMWF ensemble, IFSSENS, is included as a reference

	MEPS	CMEPS	IFSSENS
Availability and members	10 members up to 54h every 6h	5 members up to 66h every 1h	51 members up to 90h every 6h
Initial uncertainty	Perturbed control analysis using SLAF (+/-) Perturbed surface state variables	EDA + perturbation from IFSSENS Perturbed surface state variables	EDA Singular vectors
Model uncertainty	Perturbed surface properties	Perturbed surface properties	SPPT
Lateral boundary uncertainty	Perturbed ECMWF HRES using SLAF (+/-)	Use the first 28 ECMWF IFSSENS members. HRES is used for member 0.	

4 Results

The continuous setup has been running in real time since February 2019 and in early May the domain was extended to the red area in figure 1. In the following we focus on the results from 15th of May to 13th of August 2019.

Ensemble performance

In figure 4 we compare only the first three members from MEPS and CMEPS. These members are the only ones running at the same hours and allows to examine the differences without any influence of

lagging. It's clear that CMEPS has a much smaller spinup with less excessive initial winds and precipitation, suggesting that the EDA based perturbations are more balanced than the ones based on SLAF used in MEPS. The bias signature for precipitation resembles the deterministic model for CMEPS whereas for cloud cover the spinup is larger.

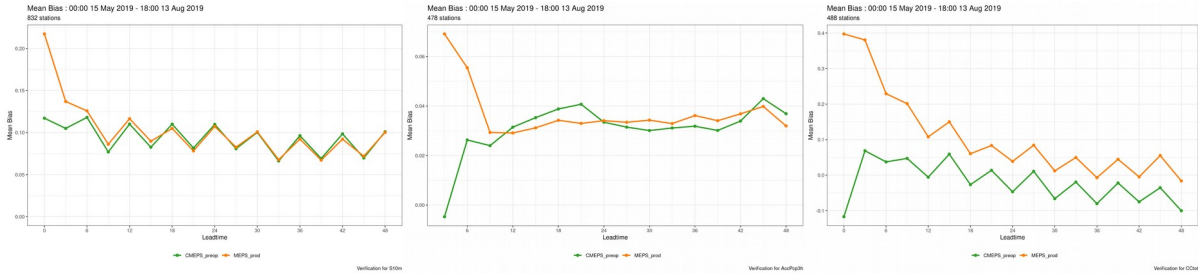


Figure 4: Bias for 10m wind, 3h precipitation and total cloud cover respectively. The comparison is done for member 0-2 only to avoid the influence of lagging. MEPS is shown in orange and CMEPS in green.

With the continuous approach we have the possibility to generate a new ensemble every hour. It's therefore interesting to compare the maximum benefit of CMEPS compared to MEPS by including a 6h old version of MEPS in the verification. In figure 5 we see that for PMSL CMEPS is somewhere in between a fresh and an old MEPS. The penalty compared to a fresh MEPS comes from a combination of using older boundaries and from the larger error growth in IFSSENS as compared to IFS HRES due to the lower resolution. This is in line with Parson et.al. (2020) and they suggest that a slightly larger ensemble is required in a continuous setup to compensate for this effect. The 10m wind speed shows an overall improvement although small. Both clouds and precipitation has an improvement in terms of CRPS although for precipitation the spread at longer lead times is a bit too large, figure 6.

In CMEPS we've managed to increase the spread for T2M although the impact on CRPS is not very large. RH2m is the only parameter where we see an overall degradation in CMEPS as compared to MEPS, figure 7. This is related to an increased dry bias in CMEPS as compared to MEPS, figure 8. In shorter sensitivity tests during the summer season, figure 8, we have seen that switching off the perturbation of soil moisture reduces the dry bias somewhat. However, switching off the perturbations for soil moisture over a 20 day period in December 2019 to January 2020, figure 9, does not cure the dry bias compared to MEPS.

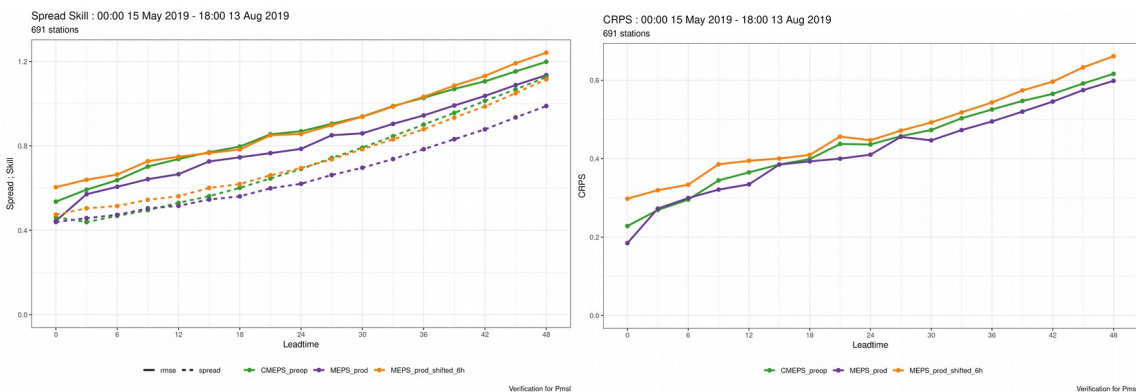


Figure 5: PMSL spread/skill (left) and CRPS(right) for CMEPS (green), MEPS (purple) and a 6h old MEPS (orange).

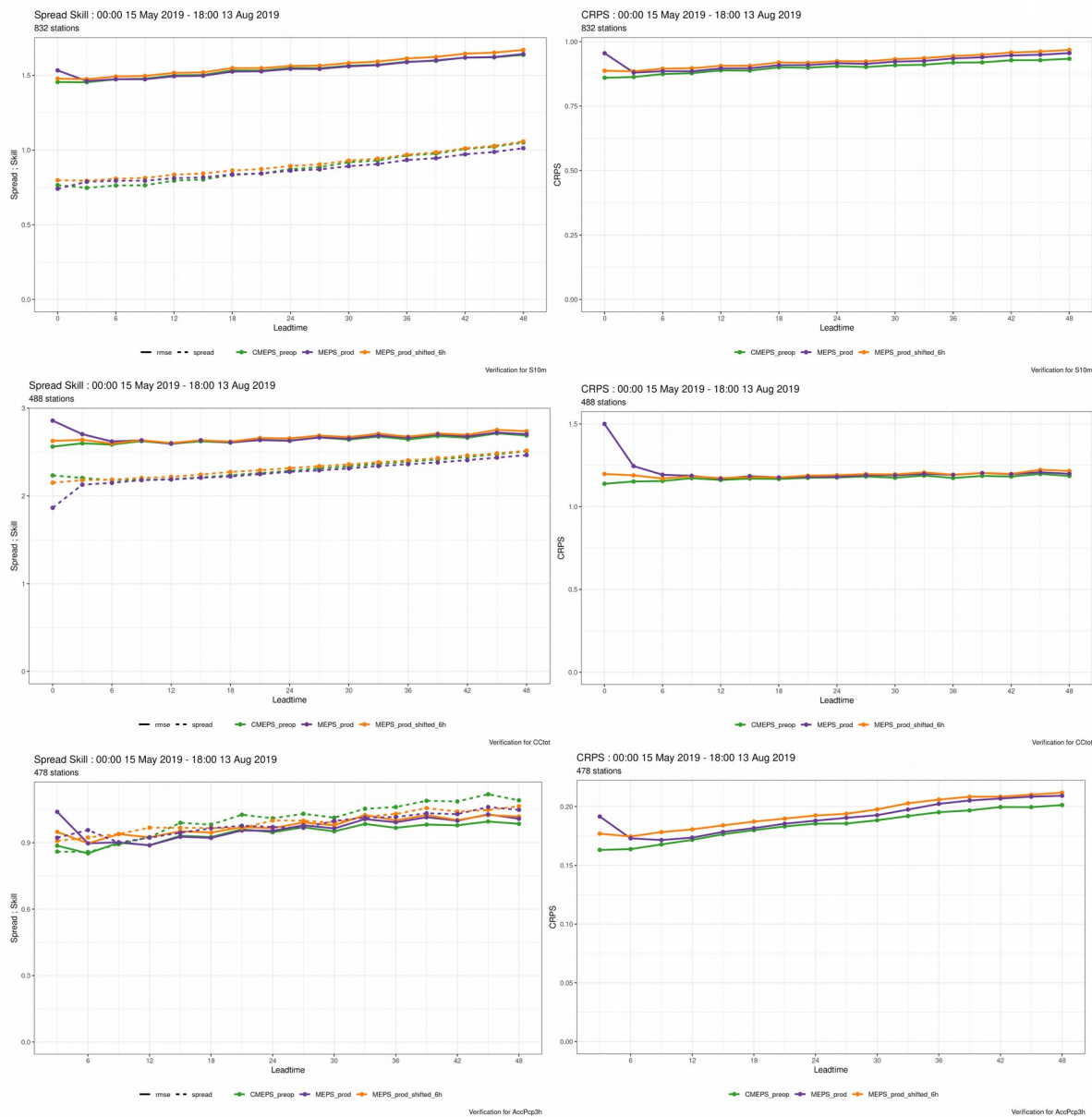


Figure 6: Spread/skill (left) and CRPS(right) for CMEPS (green), MEPS (purple) and a 6h old MEPS (orange). From top to bottom: 10m wind, total cloud cover and 3h precipitation.

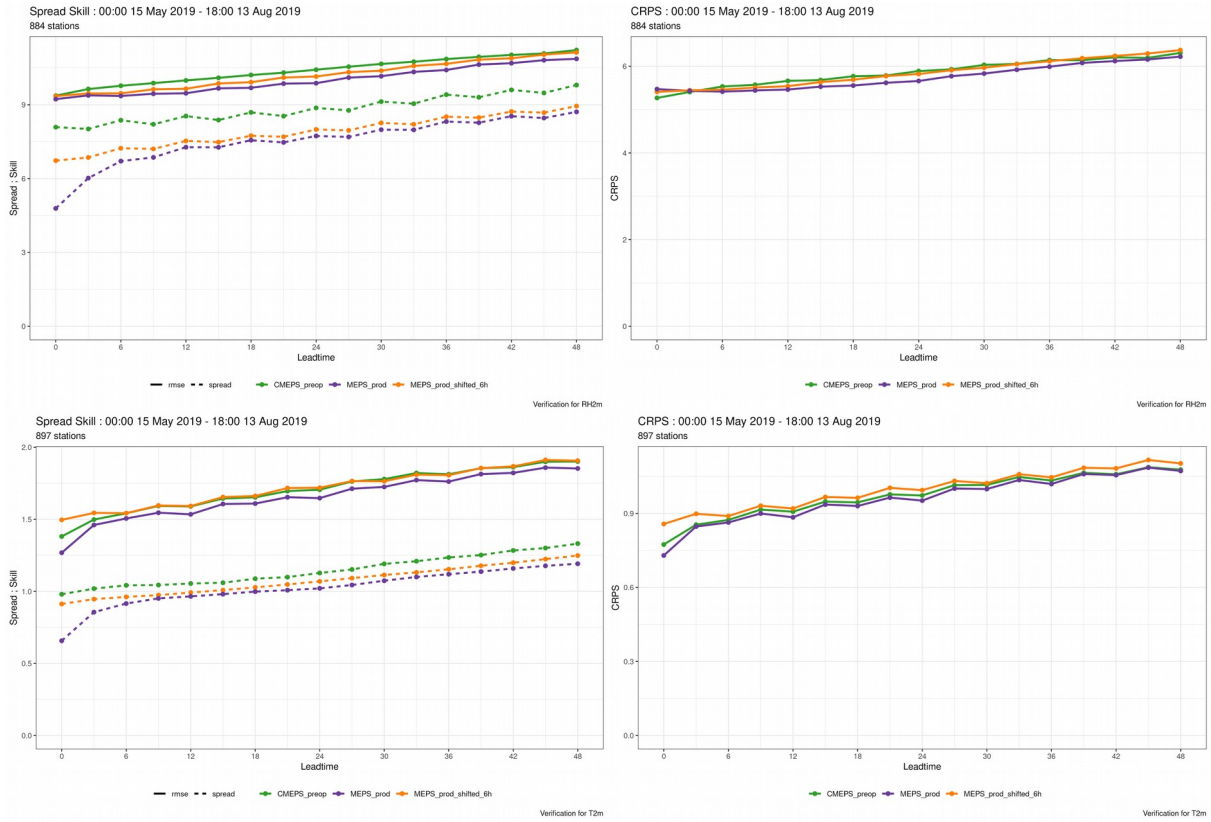


Figure 7: Spread/skill (left) and CRPS(right) for CMEPS (green), MEPS (purple) and a 6h old MEPS (orange). From top to bottom: RH2m and T2m.

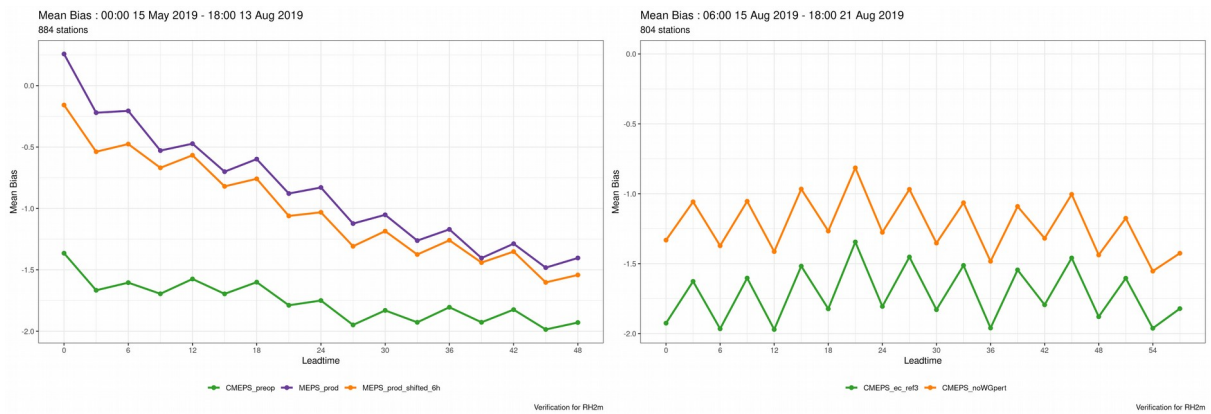


Figure 8: RH2m bias for CMEPS (green), MEPS (purple) and a 6h old MEPS (orange).

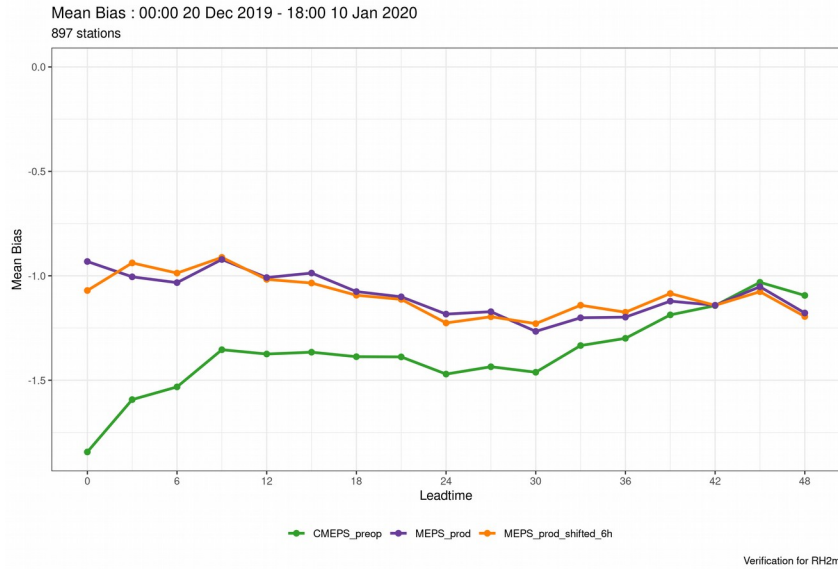


Figure 9: RH2m bias for CMEPS (green), MEPS (purple) and a 6h old MEPS (orange) for the 10 last days in December 2019.

Use CMEPS for generation of background errors

The background error statistics currently used for assimilation in MEPS are based on statistics derived from dedicated offline EDA experiments for a winter a summer season. Since then not only the forecast model characteristics have changed but also the model domain. Using data from the CMEPS archive is thus an appealing approach to generate new statistics. It would allow us to do more frequent updates without any extra cost. Sampling from 14 May 2019 to 29 Nov 2019 every 5 days and 3 times per day gives us 348 differences between pairs of archived 6h range forecasts. Comparing the spectral density with the currently used statistics we note that we have more energy on larger scales, figure 10. The result of a single temperature observation 1K warmer than the corresponding background value and with an observation error standard deviation of 1K placed in the center of the domain at 500 hPa (lev=24) is shown in figure 11. The response with the new structure function are slightly larger increments with a larger spatial scale. In addition to the pure EDA perturbations CMEPS has additional ones coming from the surface perturbations and the use of IFSSENS member derived perturbations which may contribute to the larger scales. Further experimentation is required to see whether data from CMEPS is suitable for generation of background errors or not.

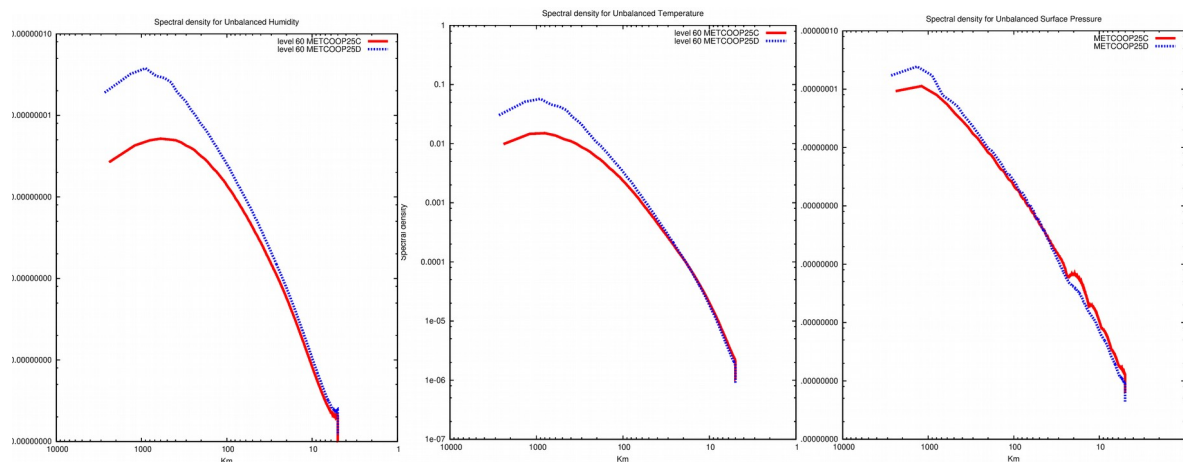


Figure 10. Spectral density functions for humidity, temperature and surface pressure. MEPS in red and CMEPS in blue.

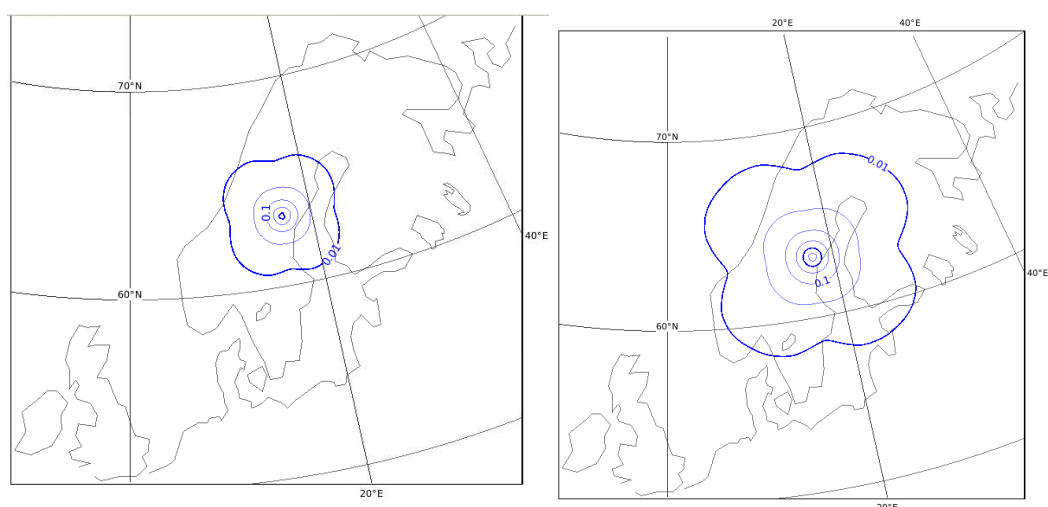


Figure 11. Impact of single obs experiment for old (left) and new (right) structure functions.

5 Conclusions and outlook

The MetCoOp ensemble have been redesigned to address two out of three mentioned shortcomings in the current setup. By a continuous EDA based approach driven by IFSSENS on the boundaries we have been able to construct a three times larger ensemble with less spinup problems offering the forecasters hourly updates. There are however remaining problems such as a pronounced dry near surface bias for perturbed members. Neither is the lack of spread in cloud variables improved by the above mentioned changes and it's clear that a representation of the internal model uncertainty is still missing. In operational like setups HarmonEPS is implemented both with multiphysics and even multimodel (Frogner et. al. 2019b). Stochastically perturbed physical tendencies (SPPT) is also available and stochastic physics perturbations (SPP) is under development. The two latter options seems like the next natural steps to improve the uncertainty representation on short and longer development time scale. In Figure 12 the impact of adding model perturbations (SPP) on total cloud cover is shown for a one month long experiment in June 2019. The SPP experiment is compared to a reference experiment (black) using default HarmonEPS perturbations, SPP (orange) is the same except SPP perturbations are also used. SPP clearly improves the scores for total cloud cover, with higher spread and lower RMSE.

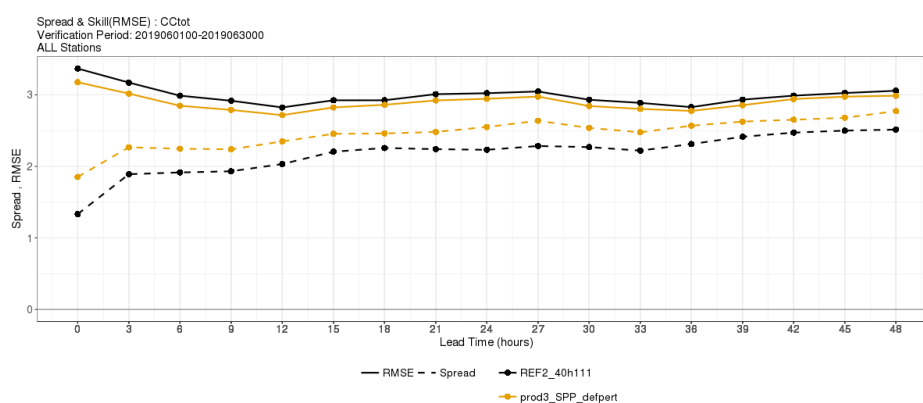


Figure 12: Spread and skill for total cloud cover for June 2019, reference experiment (black) and with SPP added (orange).

6 References

Andrae U., The MetCoOp ensemble MEPS, ALADIN-HIRLAM Newsletter No. 8, pp. 98–103, 2017. Available at: <http://www.cnrm.meteo.fr/aladin/IMG/pdf/nl8.pdf>.

Bengtsson, L., U. Andrae, T. Aspelien, Y. Batrak, J. Calvo, W. de Rooy, E. Gleeson, B. Hansen-Sass, M. Homleid, M. Hortal, K. Ivarsson, G. Lenderink, S. Niemelä, K.P. Nielsen, J. Onvlee, L. Rontu, P. Samuelsson, D.S. Muñoz, A. Subias, S. Tijm, V. Toll, X. Yang, and M.Ø. Køltzow, 2017: [The HARMONIE-AROME Model Configuration in the ALADIN-HIRLAM NWP System](https://doi.org/10.1175/MWR-D-16-0417.1). *Mon. Wea. Rev.*, **145**, 1919–1935, <https://doi.org/10.1175/MWR-D-16-0417.1>

Frogner, I-L, Singleton, AT, Køltzow, MØ, Andrae, U. Convection-permitting ensembles: Challenges related to their design and use. *Q J R Meteorol Soc.* 2019a; 145 (Suppl.1): 90–106. <https://doi.org/10.1002/qj.3525>

Frogner, I., U. Andrae, J. Bojarova, A. Callado, P. Escribà, H. Feddersen, A. Hally, J. Kauhanen, R. Randriamampianina, A. Singleton, G. Smet, S. van der Veen, and O. Vignes, 2019b: [HarmonEPS—The HARMONIE Ensemble Prediction System](https://doi.org/10.1175/WAF-D-19-0030.1). *Wea. Forecasting*, **34**, 1909–1937, <https://doi.org/10.1175/WAF-D-19-0030.1>

Hoffman, R.N. and Kalnay, E. (1983) Lagged average forecasting, an alternative to Monte Carlo forecasting. *Tellus A*, 35A(2), 100–118. <https://doi.org/10.1111/j.1600-0870.1983.tb00189.x>.

Isaksen, L., M. Bonavita, R. Buizza, M. Fisher, J. Haseler, M. Leutbecher, and L. Raynaud, 2010: Ensemble of data assimilations at ECMWF. Research Department, Tech. Memo. 636, 48 pp., <https://www.ecmwf.int/en/elibrary/10125-ensemble-data-assimilations-ecmwf>.

Molteni, F., R. Buizza, C. Marsigli, A. Montani, F. Nerozzi, and T. Paccagnella, 2001: A strategy for high-resolution ensemble prediction. I: Definition of representative members and global-model experiments. *Quart. J. Roy. Meteor. Soc.*, **127**, 2069–2094, <https://doi.org/10.1002/qj.49712757612>.

Porson, A. et.al., 2020: Recent upgrades of the Met Office convective-scale ensemble: an hourly time-lagged 5-day ensemble, *Submitted to Quart.J. Roy. Meteor. Soc.*

Yang, X., Feddersen, H., Hansen Sass, B., Sattler, K., 2017: [Construction of a continuous mesoscale EPS with timelagging and assimilation on overlapping windows](#), *ALADIN-HIRLAM Newsletter*, 8, 112-118

Previous issues of the joint ALADIN-HIRLAM NL



[No.13 August 2019](#)

ALADIN-HIRLAM Newsletter
No. 13, August 23, 2019



Joint 29th ALADIN Wk & HIRLAM ASM 2019
Madrid, 1-5 April 2019

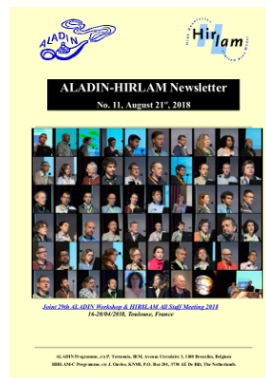
ALADIN Programme, c/o P. Termonia, IRM, Avenue Circulaire 3, 1180 Bruxelles, Belgium
HIRLAM-C Programme, c/o J. Onville, KNMI, P.O. Box 201, 3730 AE De Bilt, The Netherlands

[No.12 January 2019](#)



ALADIN Programme, c/o P. Termonia, IRM, Avenue Circulaire 3, 1180 Bruxelles, Belgium
HIRLAM-C Programme, c/o J. Onville, KNMI, P.O. Box 201, 3730 AE De Bilt, The Netherlands

[No.11 August 2018](#)



ALADIN Programme, c/o P. Termonia, IRM, Avenue Circulaire 3, 1180 Bruxelles, Belgium
HIRLAM-C Programme, c/o J. Onville, KNMI, P.O. Box 201, 3730 AE De Bilt, The Netherlands

[No. 10. January 2018](#)



ALADIN Programme, c/o P. Termonia, IRM, Avenue Circulaire 3, 1180 Bruxelles, Belgium
HIRLAM-C Programme, c/o J. Onville, KNMI, P.O. Box 201, 3730 AE De Bilt, The Netherlands

[No. 9. September 2017](#)



ALADIN Programme, c/o P. Termonia, IRM, Avenue Circulaire 3, 1180 Bruxelles, Belgium
HIRLAM-C Programme, c/o J. Onville, KNMI, P.O. Box 201, 3730 AE De Bilt, The Netherlands

No. 8. January 2017.



No. 7. September 2016



No. 6. February 2016.



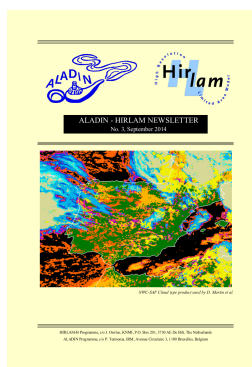
No. 5. August 2016



No. 4. February 2015



No. 3. September 2015



No. 2. April 2014



No. 1. September 2013

